MULTIFUNCTIONAL ORIGAMI: FROM ARCHITECTED METAMATERIALS TO UNTETHERED ROBOTS

A Dissertation
Presented to
The Academic Faculty

By

Larissa Simoes Novelino

In Partial Fulfillment
of the Requirements for the Degree
Doctor of Philosophy in the
School of School of Civil and Environmental Engineering

Georgia Institute of Technology

May 2021

MULTIFUNCTIONAL ORIGAMI: FROM ARCHITECTED METAMATERIALS TO UNTETHERED ROBOTS

Approved by:

Dr. Glaucio H. Paulino, Advisor
School of Civil and Environmental Engineering
Georgia Institute of Technology

Dr. Abdul-Hamid Zureick
School of Civil and Environmental Engineering
Georgia Institute of Technology

Dr. Jerry Qi
The George W. Woodruff School of Mechanical Engineering
Georgia Institute of Technology

Dr.-Ing. Yves Klett
Institute of Aircraft Design
University of Stuttgart

Dr. Paolo Gardoni
School of Civil and Environmental Engineering
University of Illinois at Urbana-Champaign

Date Approved: December 16, 2020

“But you know, happiness can be found even in the darkest of times,

if one only remembers to turn on the light.”

Albus Dumbledore,

Harry Potter and the Prisoner of Azkaban

Dedicated to my parents,

Lilia Simoes and Ubiraci Novelino

ACKNOWLEDGEMENTS

First, I would like to thank my advisor, who supported me along this challenging journey. Prof. Glaucio H. Paulino, your passion for novel and exciting problems is fully reflected in this thesis. I am thankful for all the opportunities and unique experiences you allowed me to have during my graduate studies. Those experiences had a significant impact on my professional and personal life.

To my committee members, I would like to express my gratitude to you for taking the time to be part of my thesis defense and the insightful comments you provided. Prof. Abdul-Hamid Zureick, Prof. Jerry Qi, Prof. Yves Klett, and Prof. Paolo Gardoni, your comments and insight improved this thesis significantly.

I want to thank my colleagues: Xiaojia Shelly Zhang, Emily Sanders, Ke (Chris) Liu, Tuo Zhao, Evgueni Filipov, Heng Chi, Pradeep Phanisri, Fernando Senhora, Yang Jiang, Weichen Li, Erol Unal, Oliver Giraldo, Javier Vila Moran, Emily Alcazar, Madelyn Kosednar, Alex Tong, Yipin Si, and Tomás Zegard. I cannot express how much I learned from you.

I want to thank my collaborators: Dr. Ke (Chris) Liu, Prof. Manos M. Tentzeris, Dr. Syed Nauroze, Prof. Paolo Gardoni, Prof. Horacio D. Espinosa, Prof. Sridhar Krishnaswamy, Nicolas A. Alderete, Zhaowen Lin, Dr. Heming Wei, Prof. Diego Misseroni, Prof. Renee Zhao, Dr. Qiji Ze, and Shuai Wu. I would like to express my gratitude for all the knowledge that you have shared with me.

I am grateful for all my mentors at the Federal University of Para. Prof. Sandoval Rodrigues, thank you for all the advice and conversations that guided my academic and professional path. Probably without noticing, you gave me the guidance and encouragement that I needed to get here. Prof. Remo Magalhaes, thank you for all the conversations and sharing your own experience; those were fundamental to my decisions. Prof. Gerson Miranda, thank you for all the conversations, encouragement, and advice.

I am grateful for my Master's degree advisor at PUC-Rio. Prof. Ney Dumont, you introduced me to research and pointed me in the right direction. The skills that I developed under your guidance are reflected in this thesis.

I am grateful for my professors and mentors at Georgia Tech. Prof. Lauren Stewart, thank you for all the conversations on research, teaching, and career path. You were a mentor to me in many ways. Thank you for the opportunity to co-teaching with you and for taking the extra mile to make sure that I had a wonderful experience. I am thankful for having the opportunity to learn from such a unique professor. Prof. Abdul-Hamid Zureick, thank you for your support; you helped me in many stages of my graduate studies, from my qualifying exam to guidance with experiments shown in this thesis. For that, I am incredibly grateful.

To my friends from home and to the friends I made at Tech, you were the light in the darkest times. I am incredibly grateful for your friendship. Maria, Debora, Gustavo, Fiuk, Philipe, Patrick, Helvio, Caroline, and Ana Claudia, thank you for the friendship and support over those years. Larissa and Graciele, I will never be able to express how thankful I am to you both. You helped me to make this work possible. No words can describe how grateful I am for everything you have done for me. Giorgio, thank you for helping me survive grad school; you help me be a stronger person. I would not make it without you. Fernando, thank you for dealing with me in the most stressful times and always trying to help me. I could not be more grateful for having you on this journey with me. Asta, you came towards the end of the journey; nonetheless, you significantly made it brighter. Thank you for all the origami fun when I needed help.

I want to thank Dr. Robert Simon, who helped me in different stages of my graduate studies. I also want to thank the help from the School of CEE machine shop, especially Andy Udell and Blake Baklini.

I want to acknowledge the support that I received from the Brazilian National Council for Scientific (CNPq), which allowed me to pursue my graduate studies. I would also like to acknowledge the Raymond Allen Jones Chair endowment at Georgia Tech.

Finally and most importantly, I would like to thank my mother, who may not have necessarily agreed with my choices, but supported me in each one of them. She is the best role model I could ever wish for.

TABLE OF CONTENTS

LIST OF TABLES

LIST OF FIGURES

SUMMARY

Origami has unfolded engineering applications in various fields, such as electrical, civil, aerospace, biomedical, and materials engineering. Those applications take advantage of the origami shape change capabilities to create tunable, deployable, and multifunctional systems. Although origami has catalyzed innovative solutions for such systems, its feasibility is challenged by pervasive pragmatic aspects. Thus, this thesis focuses on practical aspects that must be addressed for multifunctional origami applications, such as geometric imperfections, manufacturing, multiphysics considerations, and actuation strategies across scales. Specifically, it provides an in-depth study of geometric imperfections that may occur during the fabrication or service of origami systems and investigates how such inevitable imperfections impact both geometric and mechanical properties of origami patterns. Regarding manufacturing, we bring origami to the micro-scale and create architected metamaterials with remarkable mechanical properties, e.g., stiffness and Poisson's ratio tunable anisotropy, a significant degree of shape recoverability, and reversible auxeticity. On the multiphysics front, we examine the coupling of mechanical and electromagnetic fields by using origami to fabricate spatial filters – frequency selective surfaces with dipole resonant elements placed across the pattern fold lines. The electrical length of the dipole elements changes as the pattern changes folding states, facilitating tunable frequency responses. Finally, we propose an untethered actuation solution with direct applications to origami robotics. Our solution couples geometric bi-stability and magnetic-responsive materials, allowing for instantaneous shape locking and local/distributed actuation with controllable speed, which can be as fast as a tenth of a second. The proposed actuation leads to direct application to robots capable of shape-changing, computing, and sensing.

CHAPTER 1

INTRODUCTION AND BACKGROUND

Origami, the Japanese art of paper folding, has been of interest to artists, mathematicians, educators, and engineers. The study of the mathematics of paper folding led to essential design principles that allowed for creating complex geometries and an intuitive way of visualizing mathematical concepts and principles. Over the past decade, origami has also unfolded engineering applications in various fields. We can find such applications in material [1, 2, 3, 4], electrical [5, 6, 7, 8], civil [9, 10], aerospace [11, 12, 13], and biomedical [14, 15] engineering. Those applications take advantage of origami shape change capabilities to create tunable, deployable, and multifunctional systems.

Although Origami has proven to be a great design solution for unique systems, further investigations are still needed to make those systems practical. This need created a new research field called Origami Engineering. Origami Engineering involves studying the interaction between geometry and mechanics, the pattern's manufacturing, the influence of imperfections during the fabrication or service, and actuation strategies (Fig. 1.1).

In this thesis, we focus on the practical aspects that must be addressed for many origami applications. For example, origami structures demonstrate great theoretical potential for creating metamaterials (materials with exotic properties). However, there is a lack of understanding of how inevitable imperfections that occur during fabrication or service influence the mechanical behavior of origami-based metamaterials. For conventional materials, imperfection plays a profound role in shaping their behavior. Thus, we need to investigate how geometric imperfections impact the origami patterns' geometric and mechanical properties. We use experiments and numerical simulations to quantitatively demonstrate how geometric imperfections impede the Miura-Ori's foldability while increasing its compressive stiffness.

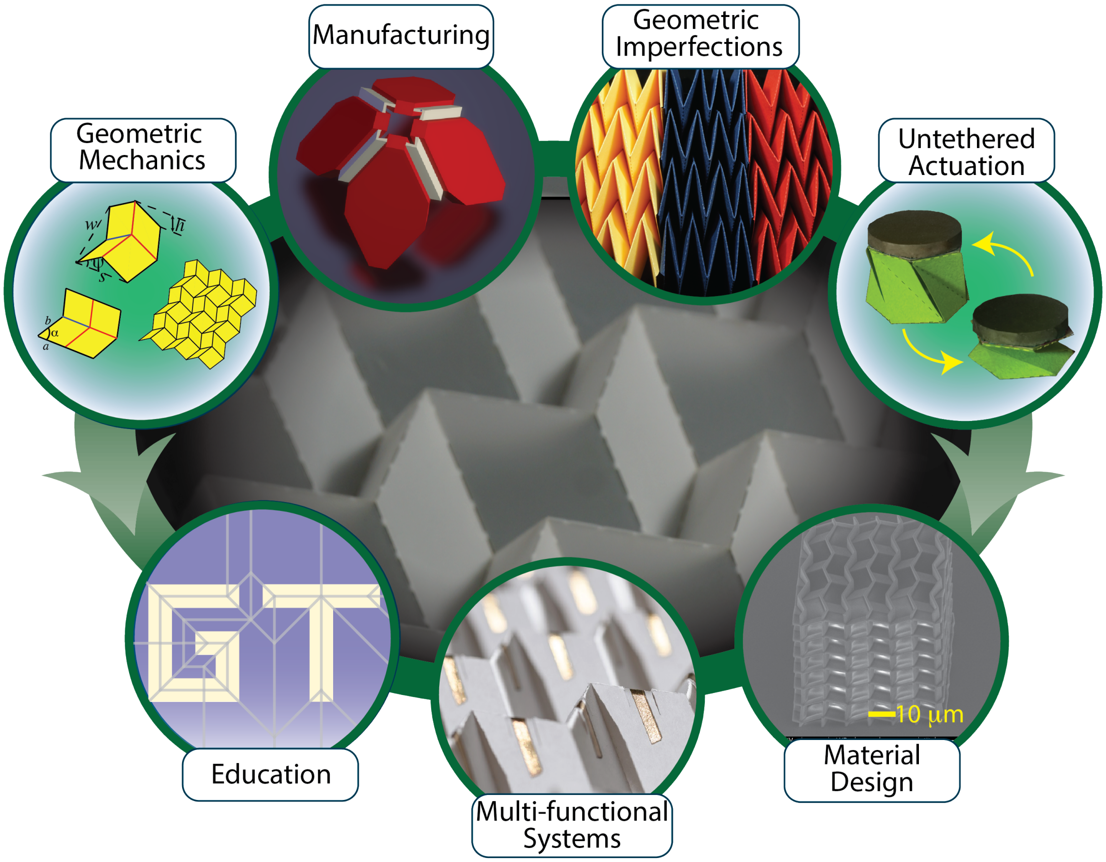

Figure 1.1: Origami Engineering Overview: From theory, design, and fabrication to applications.

Another important practical aspect addressed in this thesis relates to the actuation of the origami-inspired systems, which currently rely on the use of actuation methods that are pneumatic [16, 17, 18, 19], mechanical [20], stimuli-responsive [21, 22, 13, 23, 24], etc. These actuation strategies commonly lead to bulky actuators, extra wiring, slow speed, or fail to provide a local and distributed actuation. In this thesis, we couple geometrical and mechanical properties of the bi-stable Kresling pattern with a magnetically responsive material to realize the untethered and local/distributed actuation with controllable speed, which can be as fast as a tenth of a second with instantaneous shape locking.

Throughout the thesis, we focus on the geometric design, fabrication and test of multi-functional origami systems across scales: (1) architected materials that display remarkable mechanical properties (e.g., stiffness and Poisson's ratio tunable anisotropy, large degree of shape recoverability, and reversible auxeticity), (2) tunable electromagnetic systems, and (3) untethered robots capable of computing and sensing.

1.1 Origami Design Principles, Properties, and Terminology

In this section, we discuss the main properties of origami patterns and important theorems for origami design. The properties and concepts explained here will be used through out this thesis.

1.1.1 Developable Pattern

Developability is a property that allows for a pattern to be folded from a single (uncut) piece of paper. A pattern is developable if and only if all its vertices are also developable. For a vertex to be developable, a necessary and sufficient condition is that the sum of all the angles in a vertex must be equal to $360°$. That is, $\sum_i^n \alpha_i = 360°$, where α_i is the angle between creases i and $i+1$, and *n* is the total number of angles surrounding the vertices.

1.1.2 Flat-Foldability

A flat-foldable pattern is a pattern that can be folded flat without creating additional creases. A necessary condition (not sufficient) for a pattern flat-foldability is that all the vertices in the pattern also have to be flat-foldable. For vertex flat-foldability, four conditions need to be satisfied: (1) *Even Degree Theorem*, (2) *Maekawa-Justin Theorem*, (3) *Local Minimum Theorem*, and (4) *Kawasaki-Justin Theorem.*

Even Degree Theorem:

The Even Degree theorem states that a flat-foldable vertex always has an even degree (i.e., an even number of creases meeting at the vertex).

Maekawa-Justin Theorem

The Maekawa-Justin theorem states that a flat-foldable vertex always has a ± 2 difference between the number of mountain (*M*) and valley (*V*) folds. That is, $M - V = \pm 2$. Fig. 1.2(A) show an example of a generic four-degree vertex that satisfy this theorem.

Local Minimum Theorem

The local minimum theorem states that a flat-foldable vertex always has (1) all strict local minimum angles delimited by one mountain and one valley fold and; (2) at least one non-strict local minimum angle among neighbor angle(s) that is also non-strict local minimum is delimited by one mountain and one valley fold. An angle is defined as a strict local minimum when it is smaller than both of its neighboring angles (i.e., $\alpha_{i-1} > \alpha_i < \alpha_{i+1}$). An angle is a non-strict local minimum either when it is equal to one of its neighbors and smaller than the other (e.g, $\alpha_{i-1} > \alpha_i = \alpha_{i+1}$), or when it is equal to both neighbors (e.g, $\alpha_{i-1} = \alpha_i = \alpha_{i+1}$).

For example, in Fig. 1.2(B) we show an example of a flat-foldable vertex. The $45°$ angle shaded in blue is the only angle that is a strict local minimum ($50° > 45° < 85°$). Because this is a flat-foldable vertex, this angle is delimited by one mountain and one valley fold. The two $45°$ angles shaded in orange are non-strict local minimums, because $90° > 45° = 45°$ and $85° > 45° = 45°$. Because those two angles are non-strict local minimums, only one of them needs to be delimited by one mountain and one valley fold in order to satisfy the local minimum theorem.

Kawasaki-Justin Theorem

The Kawasaki-Justin theorem states that a vertex is flat-foldable if and only if the alternating sum of the angles (α_i) between creases is equal to zero. That is, $\alpha_1 - \alpha_2 + ... + \alpha_{n-1} - \alpha_n = 0°$. For example, the generic four-degree vertex in Fig. 1.2(A) is flat-foldable if and only if $\alpha_1 - \alpha_2 + \alpha_3 - \alpha_4 = 0°$.

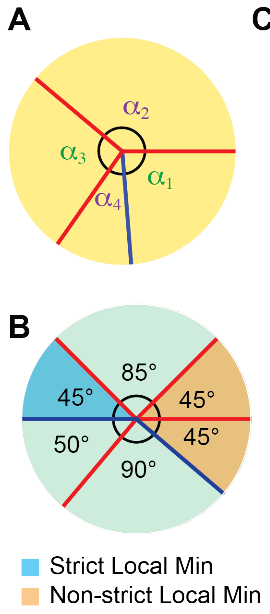

C

Theorem	Statement	
Maekawa-Justin Theorem	The difference between the number of mountain and valley folds in a flat foldable vertex is always 2, i.e.: $M - V = \pm 2$	Necessary conditions
Even Degree Theorem	A flat foldable vertex has even degree, i.e. even number of creases.	
Local Min Theorem	Any strict local min (i.e., $\alpha_{i-1} > \alpha_i < \alpha_{i+1}$) of a flat foldable vertex is delimited by one mountain and one valley fold. For non-strict local min that are neighbors, at least one of them is delimited by one mountain and one valley fold.	
Kawasaki-Justin Theorem	A vertex is flat foldable if and only if the alternating sum of the angles between the creases is zero $\alpha_1 - \alpha_2 + \alpha_3 - \alpha_4 + \ldots + \alpha_{n-1} - \alpha_n = 0°$	Sufficient condition

Figure 1.2: (A) Generic single vertex (B) Flat-foldable vertex. (C) Table summarizing the conditions for vertex flat-foldability. Red and blue lines represent mountain (M) and valley (V) folds, respectively.

Note that from all the four stated theorems, only the Kawasaki-Justin Theorem is a necessary and sufficient condition for flat-foldability. Fig. 1.2(C) summarizes the four conditions for vertex flat-foldability. For further information and proof of those theorems, we refer to [25, 26, 27].

1.1.3 Rigid Foldable Pattern and Rigid Origami

A pattern is *rigid foldable* if it can be folded such that all the deformation can be restricted to the folding at the hinges (i.e., crease lines). That is, a pattern that with deformation at the panels (regions between creases) and no stretching of the crease lines. The eggbox (Fig. 1.3) is an example of a rigid foldable pattern. This pattern can fold between its two flat-foldable states without any deformation of the panels. This property allows for the fabrication of rigid origami. A *rigid origami* is an origami pattern made of rigid (or semi-rigid) material connected by compliant hinges. In Fig. 1.3, we show the eggbox pattern, which is a rigid foldable patter, in a non-rigid (paper model) and a rigid origami model (3D printed). The multi-material 3D printed model has panels made of a semi-rigid material (PLA) connected by compliant material (Filaflex).

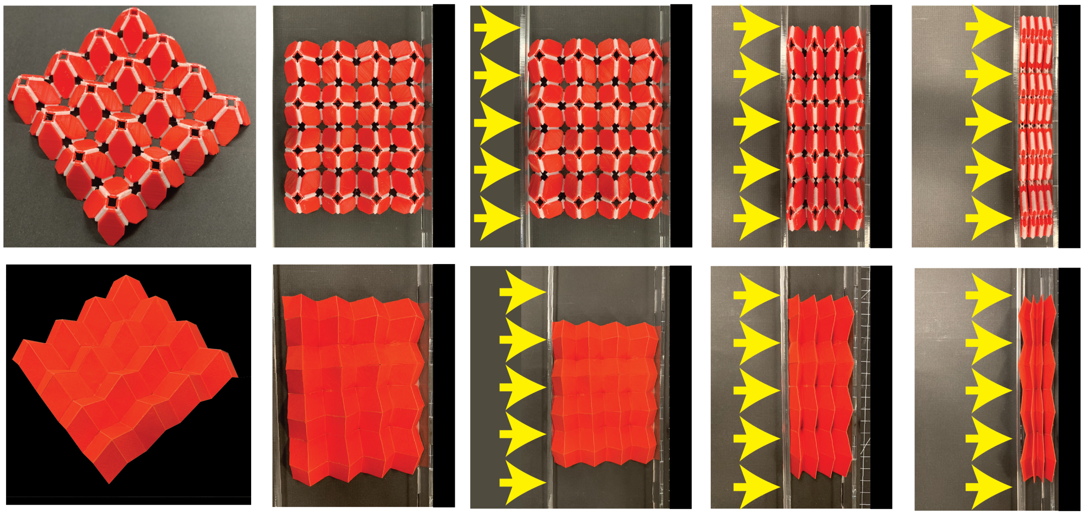

Figure 1.3: Origami: From art to engineering. Multi-material 3D printed model (top) and paper model (bottom) of the eggbox origami pattern. Origami 3D printed by the author and Emily D. Sanders. Panels are made of a semi-rigid material (PLA) connected by compliant material (Filaflex).

In the example in Fig. 1.3, we observe that an origami pattern can be a rigid foldable pattern without being a rigid origami (paper model). However, rigid origami is only possible for rigid foldable patterns. The key idea is that rigid foldability is a purely geometric property, while a rigid origami behavior depends on material properties. In general, the behavior of a rigid foldable pattern can be approximated to a rigid origami. This allows us to describe the kinematic in a purely geometrical manner. Such approximation is valid as long as the stiffness of the hinges is considerably smaller than the stiffness of the panels. This will be the case of some of the patterns studied in this thesis.

1.2 Thesis Organization

This thesis has one educational chapter and four research chapters. The subsequent chapters are organized as follows: *Chapter 2* introduces the fold-and-one-cut problem in an educational form. *Chapter 3* investigates the mechanical properties (e.g., anisotropy, reverse auxeticity) of an origami-architected metamaterial (Fig. 1.4). This metamaterial has a microstructure composed of multiple Miura-Ori tubes assembled in a zipper/aligned fashion. *Chapter 4* presents an application of the Miura-Ori for tunable electromagnetic structures. *Chapter 5* presents an untethered actuation solution that couples geometric bi-stability and a magnetic-responsive material. *Chapter 6* investigates the mechanical properties of the Miura-Ori under the presence of geometric imperfections (Fig. 1.5). *Chapter 7* concludes and summarizes the main contributions of this thesis.

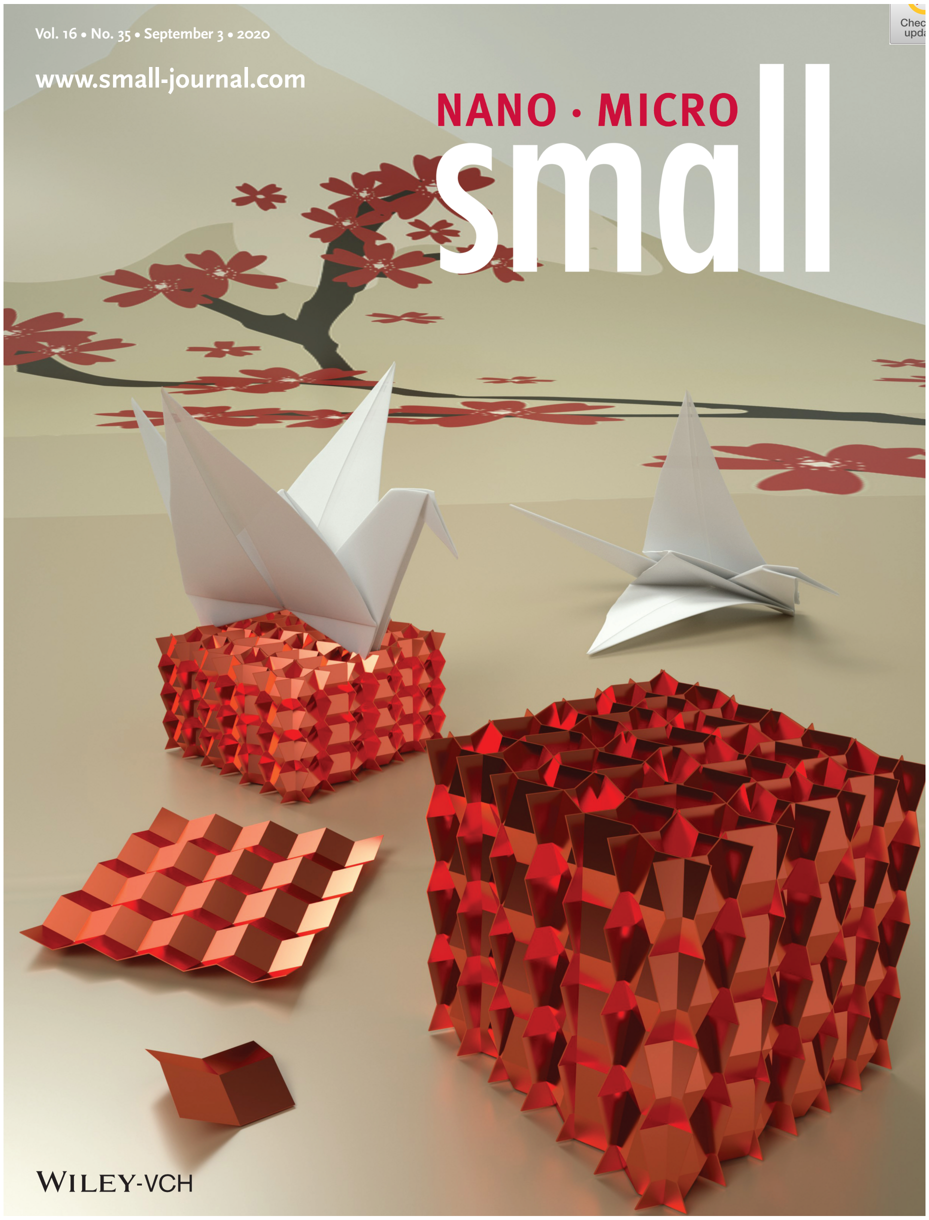

Figure 1.4: Inside front cover of *Small* 35/2020 [28]. Origami foldability, naturally realizable at the micro- and nanoscale, provides a pathway to enlarge the design space of mechanical metamaterials [3].

ISSN 1364-5021 | Volume 476 | Issue 2241 | September 2020

PROCEEDINGS
OF THE ROYAL SOCIETY A

MATHEMATICAL, PHYSICAL AND ENGINEERING SCIENCES

Proc. R. Soc. A | Volume 476 | Issue 2241 | September 2020

Rapid indirect solar responses observed in the lower atmosphere

Big influence of small random imperfections in origami-based metamaterials

Review of smoothed particle hydrodynamics: towards converged Lagrangian flow modelling

THE
ROYAL
SOCIETY
PUBLISHING

Figure 1.5: Cover of the *Proceedings of the Royal Society A*, Volume 2020, Issue 2241: The foreground displays three origami sheets, under compressive load, folded from perfect and slightly misaligned Miura-Ori patterns. The small geometric imperfections induced by the misalignment could have a big impact on the mechanical behavior of origami folded metamaterials. The background displays a perfect Miura-Ori tessellation [29].

CHAPTER 2

FOLD-AND-ONE-CUT

In this educational chapter, we use a didactic approach to explain the fold-and-one-cut problem. This problem has a history in child puzzles and magic books [30, 31]. As a puzzle, children cut a polygon out of a piece of paper with a single straight cut. As a magic trick, magicians fold a piece of paper into a flat configuration followed by a single straight cut. The cut separates the paper into multiple pieces that reveal unexpected geometric shapes when unfolded. Fig. 2.1 shows the crease pattern for the fold-and-one-cut of Houdini's famous five-point star. Mathew Gardner was the first to state the fold-and-one-cut as an open problem [32]. That is, *which shapes can we obtain via folding and one single straight cut?* Demaine et al. [33] proved that any shape (or a collection of disconnected shapes) composed of only straight lines can be folded into a flat configuration that aligns all (and only) the edges of the polygon, resulting in the following theorem:

> **Theorem:** Given any collection of straight edges, there exists a flat-folding that aligns all the edges (and only the edges) into a single line, such that cutting along this line results in the desired cutout.

Two methods have been proposed to find the set of creases that allows for cutting the polygon(s) with a single cut: (1) the straight skeleton method [33], which works almost always and; (2) the disk packing method [34], which always works but it is not as practical. In this chapter, the focus will be on the first method.

Although the fold-and-one-cut problem and the straight skeleton method have been introduced and mathematically explored in many works [33, 27, 26], we present here a comprehensive explanation in which we apply the mathematical principles to explain the series of steps, via the straight skeleton method, for the development of the crease pattern

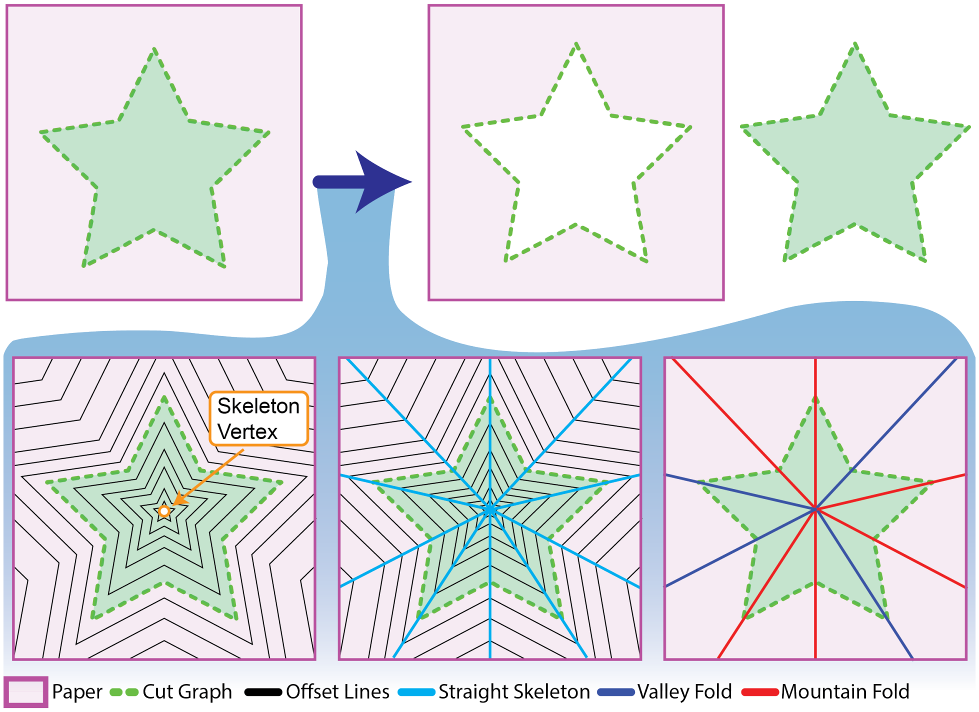

Figure 2.1: Fold-and-one-cut of Houdini's famous five-point star.

needed for single cut a given shape.

2.1 Introduction

The main idea of the fold-and-one-cut problem is that we want to collapse all (and only) the lines in the cut graph (faces of the polygon) into a single line. To bring all the edges together, we need to create fold lines along the bisector angles between two edges. To find the location of the bisectors, we create a straight skeleton [35], which is generated by shrinking/expanding the faces of the polygon(s).

While generating the offset faces, the first crease lines and vertices of the pattern will start to appear in the form of (1) *Skeleton Parallel Lines:* formed when two offset faces collapse into one and (2) *Skeleton Vertices:* formed either when an edge of the polygon disappears or when more than two offset faces collapse to the same point. Fig. 2.2(A) shows the offsetting of the polygon faces (black lines), the skeleton vertices, and skeleton parallel lines that appear in the shrinking/expanding process. After the shrinking/expanding process is completed, we connect all the vertices of the shrunk/expanded polygons with the already formed skeleton lines and vertices (Fig. 2.2(B)). Those new lines bisect the edges of the cut graph and are called bisector lines. Note that while the straight skeleton of the letter “A” is composed of both parallel and bisector lines, Houdini’s five-point star is composed only of bisector lines.

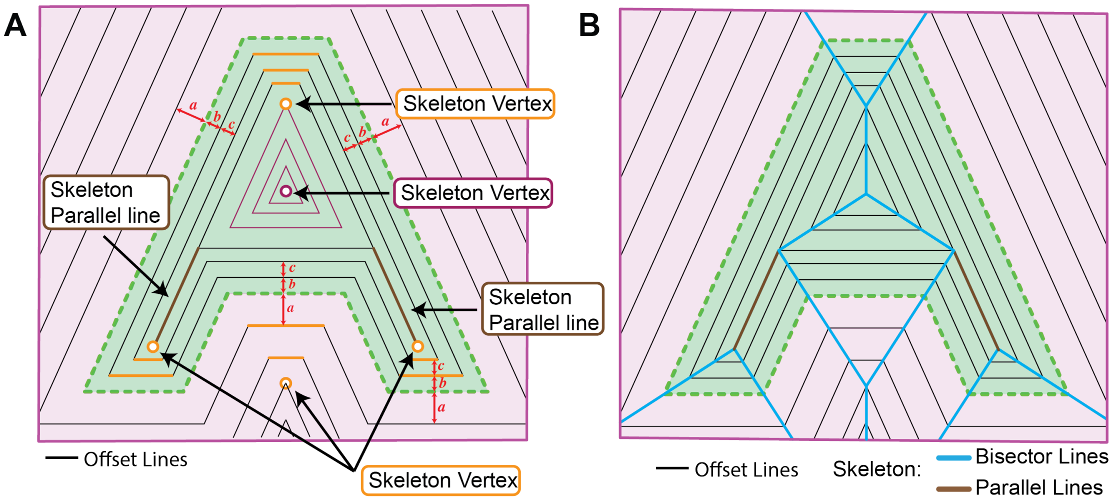

Figure 2.2: Straight skeleton of a polygon in the shape of the letter “A”.

For simple shapes, such as Houdini’s five-point star [30] (Fig. 2.1), the straight skeleton is sufficient to provide a flat-foldable crease pattern. However, for most cases, this set of creases are not enough to create a flat-foldable pattern. For example, Fig. 2.3(A) shows the straight skeleton of a rectangle, which is composed of two three-degree vertices. Because the even degree theorem states that a flat-foldable vertex has an even degree, we need to make this vertex even by adding extra creases. However, the new creases cannot miss-align the cut graph in the flat-foldable configuration (i.e., we need to add crease lines that bisect the cut edges). Those extra creases are called *perpendicular lines* because they bisect the cut edges with an angle of $90°$. Typically, each skeleton vertex presents multiple choices of perpendiculars. In Fig. 2.3(B), we provide all the possible perpendiculars for the skeleton of a rectangle. Although each vertex has three perpendiculars, we only need to select one of them to create a flat-foldable pattern (Fig. 2.3(C)).

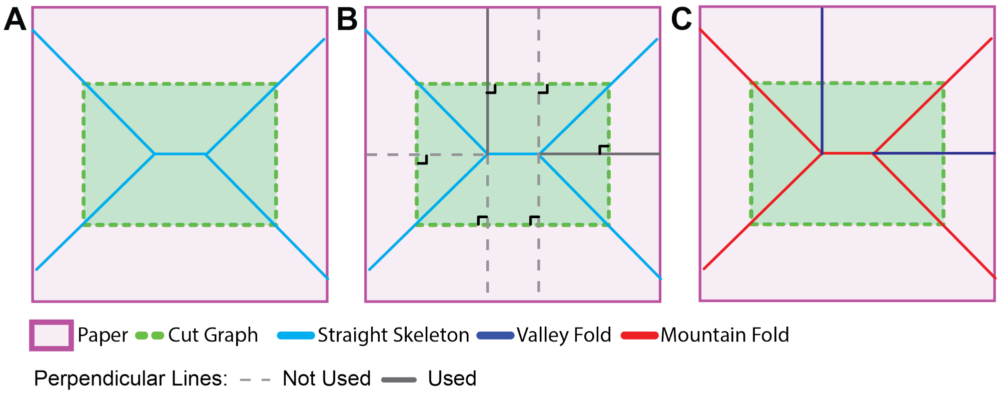

Figure 2.3: fold-and-one-cut of a rectangle: (A) Straight Skeleton, (B) perpendicular lines, and (C) one of the possible solutions for perpendiculars and mountain/valley assignment.

After adding perpendiculars to satisfy the even degree theorem in every vertex, we still need to provide a mountain/valley assignment for the crease lines and ensure that the resulting pattern is flat-foldable. Demaine et al. [33] showed that if all the vertices in the crease pattern satisfy the flat-foldability conditions, then global flat-foldability is guaranteed. Therefore, we must guarantee that the following conditions for flat-foldability are satisfied in every vertex: (1) *Even Degree Theorem*, (2) *Maekawa-Justin Theorem*, (3) *Local Minimum Theorem*, and (4) *Kawasaki-Justin Theorem*. Those flat-foldability conditions are summarized in Fig. 1.2.

The last step for the generation of a valid pattern is the crease line assignment. That is, we need to assign the creaseS as either mountain or valley folds such that the provided assignment results in a flat-foldable pattern. For that, we will use both the *Maekawa-Justin Theorem* and *Local Minimum Theorem* to guide our assignment. At this stage, we no longer need to verify if the vertices satisfy the *Even Degree Theorem* and the *Maekawa-Justin Theorem*, both were satisfied when we added perpendicular lines.

To make the steps for the fold-and-one-cut clear, we show a series of examples, starting with single polygons and followed by multiple disconnected polygons. Each example presents a particular event, that we use to clarify all the aspects of the Straight Skeleton method.

2.2 Example 1: “T” letter

To explain the method, we start using a simple polygon in the shape of the letter “T”. This polygon will be folded into a flat configuration that aligns only the cut graph (i.e., all the faces of the polygon) into a single line. By cutting along this line, we are able to extract the letter “T”, leaving the negative of the “T” on the remaining of the paper (Fig. 2.4).

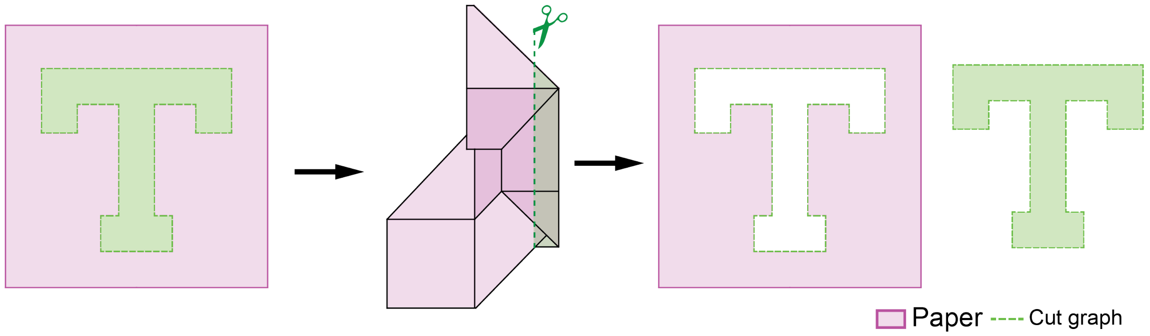

Figure 2.4: Paper with a single polygons in the shape of the letter “T”. By folding the crease pattern, we have a flat configuration that allows for the polygon to be extracted with a single straight cut.

2.2.1 Step 1: Straight skeleton

The first step consists of building the straight skeleton by shrinking and expanding the polygons faces (Fig. 2.5A), creating offset lines. While generating the offset lines, the first crease lines and vertices of the pattern will start to appear in the form of *skeleton parallel lines* and *skeleton vertices*. After finding all the parallel lines, we need to create the *skeleton bisector lines*, which connect the vertices of the cut graph with their respective vertices formed by the offset faces (Fig. 2.5B). The process to find the straight skeleton (i.e., skeleton parallel lines, bisector lines and vertices) is shown in Fig. 2.5. Note that whenever we refer to ”skeleton lines” we are referring to both parallel and bisector lines.

After the construction of the straight skeleton, we no longer need the offset lines. Thus, we can remove them, and work with the straight skeleton alone. In Fig. 2.6, we removed the offset lines and showed the straight skeleton of the letter “T”. In addition, we indicate

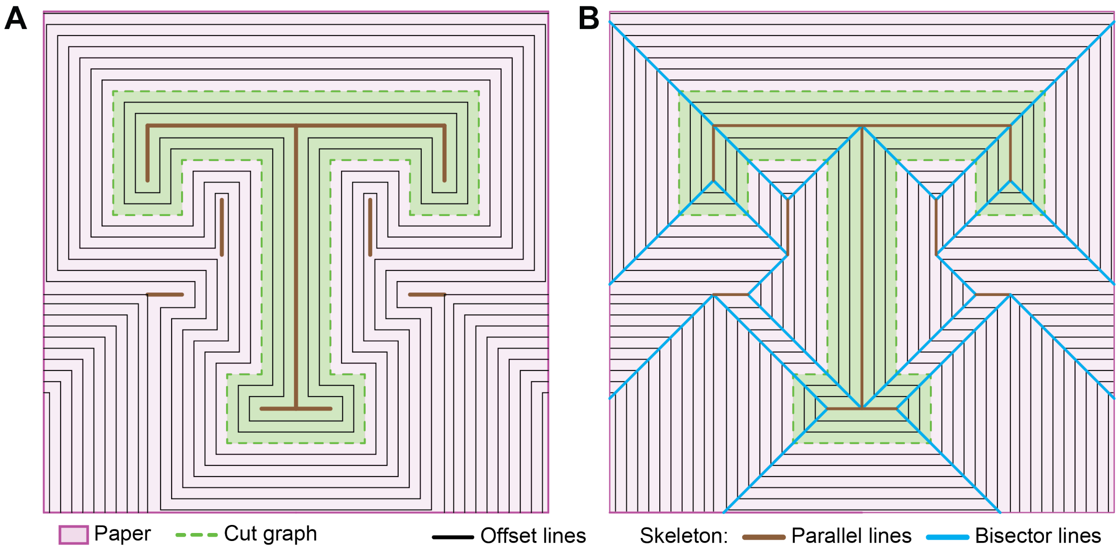

Figure 2.5: (A) Shrink/Expansion of the polygon in the shape of the letter “T” (B) Straight skeleton generated from the overlap of the offset lines (parallel lines) and the connection of the offset vertices (bisector lines).

the fold-and-one-cut terminology, as follows:

- Vertices and faces in the cut graph are called *cut vertices* and *cut edges* (or cut lines), respectively.
- Vertices and lines in the skeleton are called *skeleton edges* (or Skeleton lines) and *skeleton vertices*, respectively.
- The regions formed by the skeleton edges are called *skeleton regions*. Each cut edge belongs to a single skeleton region and that each region has only one cut edge (one-to-one correspondence).

2.2.2 Step 2: Perpendiculars

By inspecting the crease pattern generated from the straight skeleton, we observe that most vertices violate the even degree theorem. Because of these violations, the straight skeleton by itself does not generate a flat-foldable pattern. Therefore, we need to add *perpendicular*

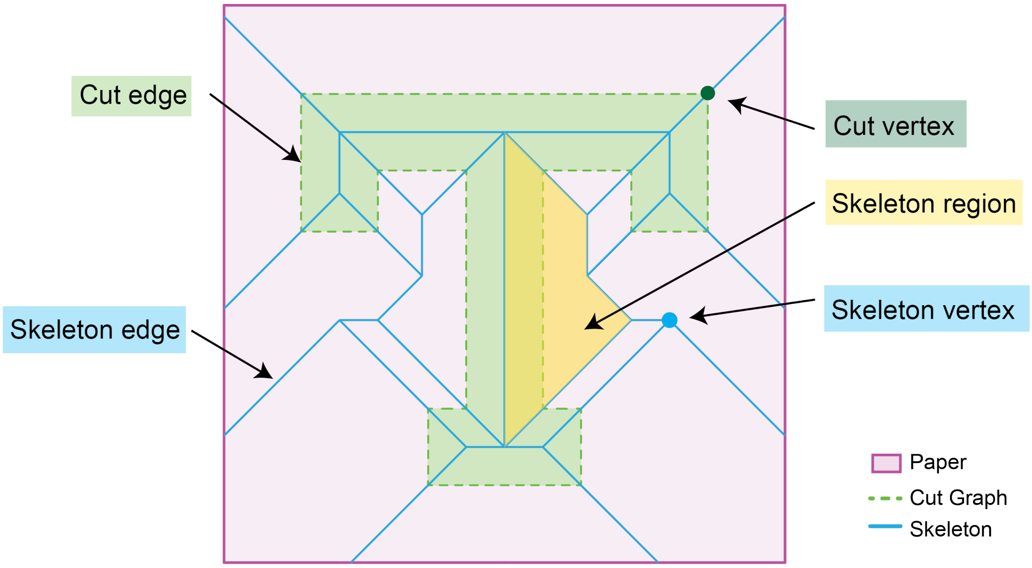

Figure 2.6: fold-and-one-cut terminology.

lines. That is, creases that will not miss-align the cut graph in the flat-foldable configuration. Perpendicular lines start at a skeleton vertex and end either in the paper boundary or in another skeleton vertex. If those lines meet a skeleton edge, they are reflected. For example, the skeleton vertex SV1 (Fig. 2.7) is surrounded by three skeleton regions (represented by red, orange and blue), and we have three perpendiculars (one per region). The perpendicular P1 meets the paper boundary without crossing any skeleton line. Perpendicular P2 meets a vertex also without crossing any skeleton line. However, P3 meets two skeleton lines before reaching the paper boundary. Each time P3 meets a skeleton line, P3 is reflected, which guarantees that the line will be perpendicular to the cut edge of the current region.

Degenerate cases occur in other skeleton vertices, such as the skeleton vertex SV2 (Fig. 2.7). The perpendicular lines P1 and P3 enter a distinct region from the one that has the edge they are perpendicular to. Those perpendiculars are degenerated cases and cannot be used. The only possible perpendicular for vertex SV2 is P2.

In Fig. 2.8(A), we show all the possible perpendiculars for each vertex. However, we do not need all of them to guarantee flat-foldability. By choosing the perpendicular that intersects the smallest number of skeleton lines, a much simpler crease pattern is created (Fig. 2.8(B)). In addition, because of the reduction in the number of fold lines, the final

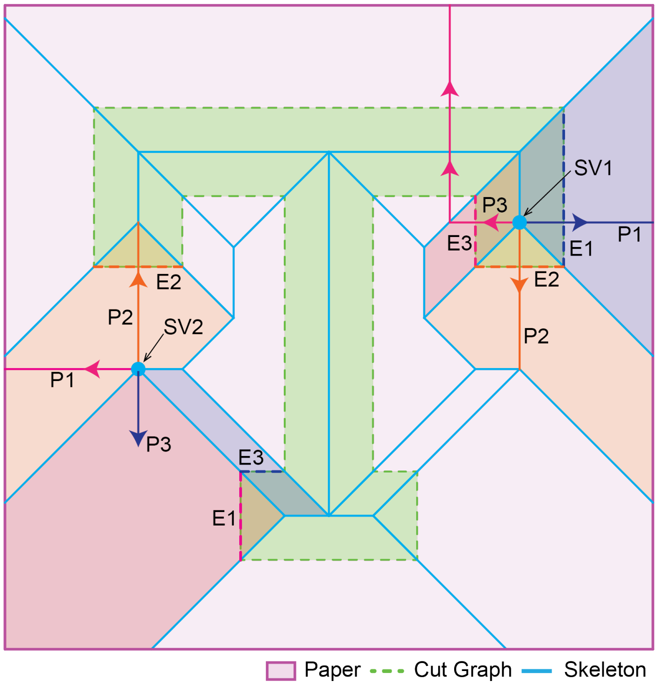

Figure 2.7: Schematics of the perpendiculars incident from skeleton vertex SV1 and SV2, where arrows indicate the direction of the perpendicular.

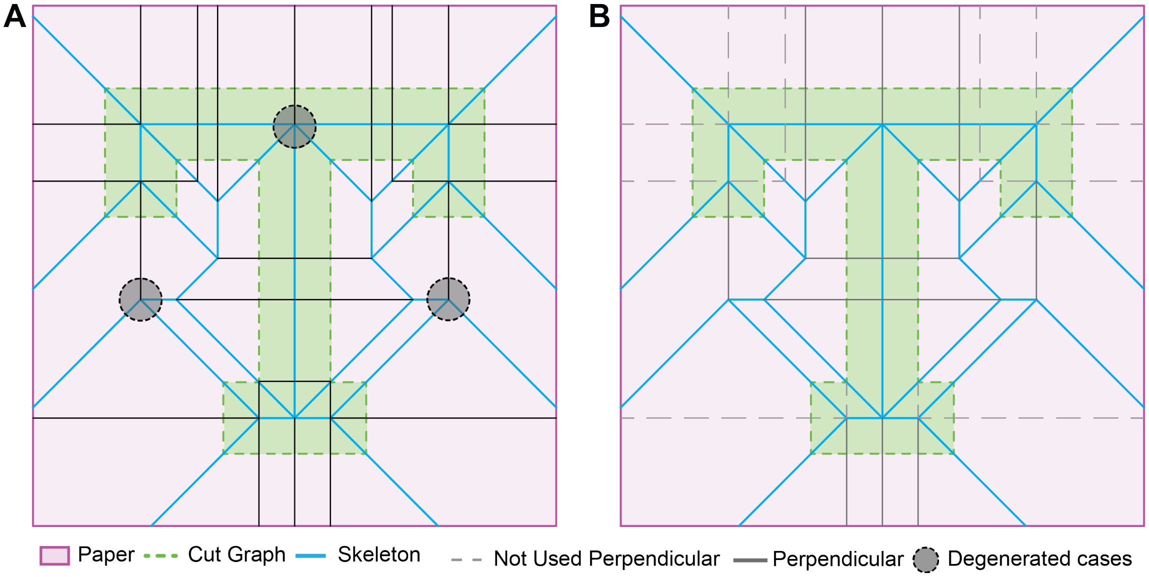

Figure 2.8: Paper with a single polygons in the shape of the letter “T”. (A) Crease pattern with all the possible perpendiculars. (B) Crease pattern showing the chosen perpendiculars (solid black) and the extra (and unnecessary) creases (dashed gray).

thickness of the flat-folded configuration is also reduced, making it easier to perform the single cut.

We cannot always choose the perpendiculars with the shortest path. Suppose the vertex has one of its angles $\geq 180°$. In that case, we have to split this angle by including a perpendicular line; otherwise, the Kawasaki-Justin Theorem will be violated, and flat-foldability will not be possible at this vertex. Remember, as long as all the vertices are even and obey this rule, the Kawasaki-Justin Theorem will always be satisfied.

To satisfy the even degree theorem and the Kawasaki-Justin theorem, we only need to add one perpendicular to odd vertices. For even degree vertices with all the angles $< 180°$, we do not need to add perpendiculars unless a perpendicular from another vertex is connected to it (making it an odd vertex) or to satisfy the Maekawa-Justin Theorem. This will be clarified in the following examples.

2.2.3 Step 3: Mountain/valley assignment

In the same way that the crease pattern for the fold-and-one-cut is not unique, the mountain/valley assignment is also not unique. Distinct assignments can generate a flat-foldable pattern. Our goal is to find a crease assignment that allows us to align the cut edges and nothing else. Meaning that we need the region inside the polygon (green) to be folded in one side and the remaining paper (magenta) in the opposite side with respect to the final cut line. If this is not respected, we may have cut lines that do not belong to the cut graph. Here we propose a simple method for the assignment of the crease lines. Unless we are taking advantage of the polygon symmetry, all the parallel lines inside the cut graph will almost always have the same assignment. In contrast, the ones outside will have the opposite assignment. Therefore, we propose an *initial guess* to start the mountain/valley assignment: *parallel lines inside the polygon are assigned as mountain folds and parallel lines outside the polygon are assigned as valley folds* (Fig. 2.9(A,B)). This initial guess will leave a few of the crease patterns without assignment.

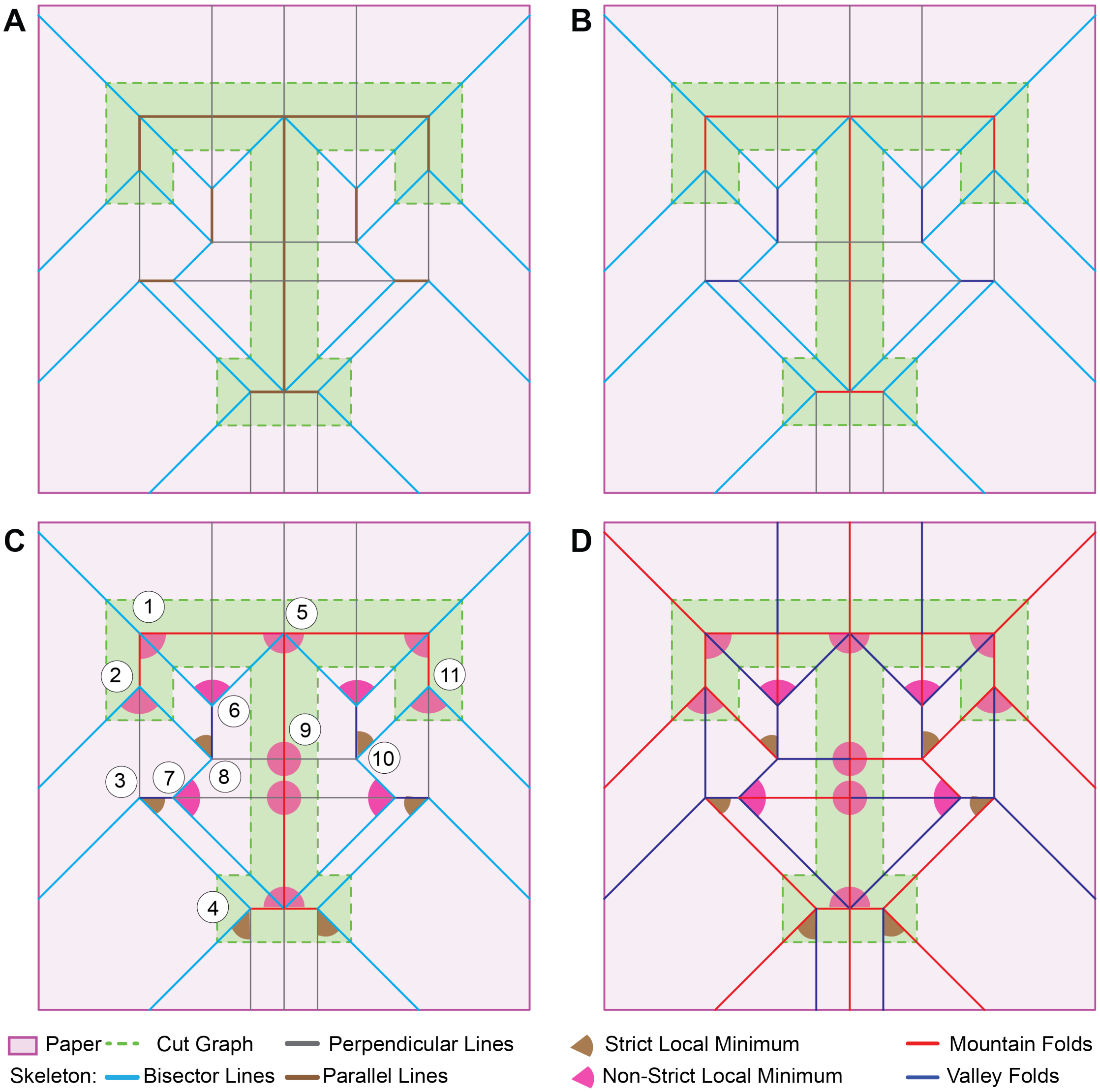

Figure 2.9: Mountain/valley assignment of the crease pattern for the letter “T”. (A) Skeleton (bisector and parallel) lines and perpendiculars. Steps for the mountain/valley assignment: (B) First step: the parallel lines inside and outside of the polygon are assigned as mountain and valley, respectively. (C) Second Step: Recognize the angles that are local minimums, and assign the the creases such that both the local minimum and the Kawasaki-Justin theorem are satisfied. (D) Crease pattern for the letter “T” with the mountain and valley assignment.

The next step is to check for vertex flat-foldability. Because, at this point, we know that both the even degree and the Kawasaki-Justin theorems are satisfied in all vertices, we only need to check the vertices for the Maekawa-Justin theorem and the local minimum theorem. By satisfying those two theorems, we find a mountain/valley assignment that leads to a flat-foldable pattern. At this point, all the vertices have at least one crease line with an assignment. To exemplify, we examine Vertices #1 to #7 in Fig. 2.9(C):

- *Vertex #1* is a four-degree vertex that has two non-strict local minimum angles, each one bounded by a mountain fold. To satisfy the local minimum theorem, we need to assign the crease line between the two angles as a valley fold. Because of Maekawa-Justin theorem, we know that the other non-assigned crease has to be a mountain.

- *Vertex #2* is a four-degree vertex with one pre-assigned mountain fold and two non-strict local minimum angles. Because the assigned mountain fold bounds the two largest angles, we know that this vertex will have three mountains and one valley. Because smaller angles are non-strict local minimum, the valley can be assigned to any one of the remaining creases. Thus, we assign the crease between the two non-strict local minimums as a valley fold.

- *Vertex #3* is a four-degree vertex with a pre-assigned valley fold, bounding a strict local minimum. This vertex also shares a crease with *Vertex #2*, which has already been assigned as a valley fold. Thus, to satisfy the Maekawa-Justin theorem, this vertex has to be a one-mountain and three-valley type. To satisfy the local minimum theorem, we assign the mountain fold to the crease bounding the strict local minimum angle.

- *Vertex #4* is a four-degree vertex with a pre-assigned mountain fold. This vertex also shares a crease with *Vertex #3*, which has already been assigned as a mountain fold. To satisfy the Maekawa-Justin theorem, this vertex has to be a three-mountain and one-valley type. Thus, the two creases without assignment will be assigned as one mountain and one valley fold. We also satisfy the local minimum theorem at the non-strict local minimum angle. In the crease assignment in Fig. 2.9(D), we assigned the left crease as a mountain and the right as a valley. The two creases could be assigned the other way around and still satisfy all the theorems.

- *Vertex #5* is a six-degree vertex with three mountain folds pre-assigned and four non-strict local minimum angles. Because of the Maekawa-Justin theorem, we know that this has to be a four-mountain and two-valley vertex. Also, we know that at least one of the valley folds has to be bounding a non-strict local minimum angle. The remaining mountain fold can be assigned to any of the unassigned creases and satisfy all the flat-foldability theorems. To simplify the folding, in Fig. 2.9(D), we opt to assign the mountain to the crease shared by the two $90°$ angles.

- *Vertex #6* is a four-degree vertex with a pre-assigned valley fold. This vertex also shares a crease with *Vertex #1* and *Vertex #5*, which have been both assigned as valleys. Because of the Maekawa-Justin theorem, we know that the non-assigned crease has to be a mountain fold. With this assignment, we also satisfy the local minimum theorem at the non-strict local minimum angles.

- *Vertex #7* is a four-degree vertex with a pre-assigned valley fold not bounding the two non-strict local minimum angles. Thus, we know that this vertex is a three-valley and one-mountain type. We can assign the missing mountain to any of the remaining creases and satisfy all the flat-foldability theorems. To simplify the folding, in Fig. 2.9(D), we opt to assign the mountain to the crease shared by the two non-strict local minimum angles.

- *Vertex #8* is a four-degree vertex with a pre-assigned valley fold bounding a strict local minimum angle. Thus, we know that this angle needs to be bounded by a mountain and a valley fold. The crease line shared with Vertex #2 has to be a mountain, which is consistent with the assignment we made for Vertex #2. Finally, because of the Maekawa-Justin theorem, the two un-assigned creases can be either mountain or valley folds while satisfying all the flat-foldability theorems. In Fig. 2.9(D), we assign them as valleys.

- *Vertex #9* is a four-degree vertex with four non-strict local minimum angles. This vertex has two pre-assigned mountain folds. The vertex also shares a crease line with *Vertex #8*, which has been assigned as a valley. Thus, we know that the non-assigned crease has to be a mountain fold because of the Maekawa-Justin theorem.

- *Vertex #10* is a four-degree vertex with a pre-assigned valley fold bounding a strict local minimum angle. Because of the local minimum theorem, we know that the crease line shared with Vertex #11 has to be a mountain, and because of the Maekawa-Justin theorem, we know that the other non-assigned crease has to be mountain fold. Although this vertex is similar to *Vertex #8*, the assignment of those vertices is not the same, which is needed to guarantee compatibility among connecting/neighboring vertices.

By inspecting all the remaining vertices in the same form as described above, we reach the crease assignment shown in Fig. 2.9(D). Sometimes, we may need to re-assign some creases to ensure compatibility between vertices. Therefore, it is good practice to work the assignment from one corner vertex to its neighbors. For example, following the same procedure described above for the other vertices, we see that although the crease pattern itself is symmetric, the mountain and valley assignment is not. If you work on vertices on both sides simultaneously, you would probably not guarantee assignment compatibility with all the vertices and would need to adjust the assignment of some lines. As previously mentioned, the mountain/alley assignment is not unique. For example, in Fig. 2.10, we show three possible mountain/valley assignments for the same crease pattern.

2.3 Example 2: "K" letter - *split event*

We use a polygon in the shape of the letter "K" (Fig. 2.11(A)) to show an example of a *split event*. This type of event occurs during the shrinking process of the polygon and results in the offset polygon being split into two (see the yellow region in Fig. 2.11(B)). After this event, we keep shrinking the two split polygons until they result in skeleton parallel

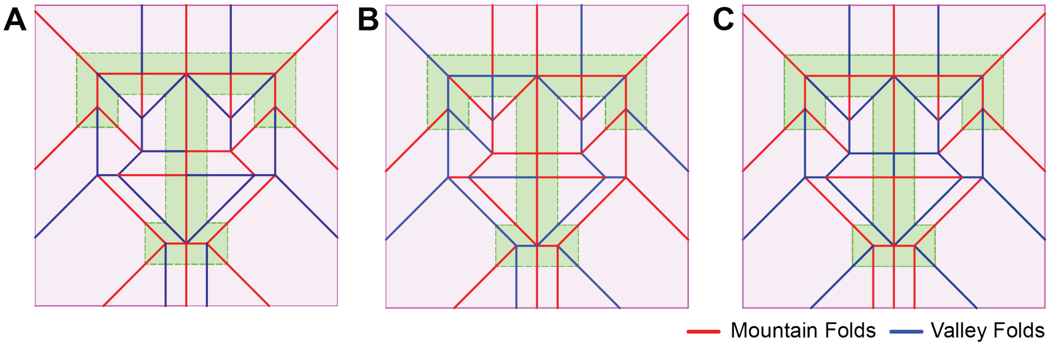

Figure 2.10: Mountain/valley assignment of the crease pattern for the letter "T". (A) Assignment created using the initial guess explained in this section. (B) Assignment created taking advantage of the symmetry of the letter. Note that the creases in the right and the left side have opposite assignments. (C) Assignment created such that the resulting assignment is symmetric. That is, right side is the mirror image of the left side.

lines. Because of the splitting event, the two parallel lines inside the polygon have no direct connection (Fig. 2.11(B)).

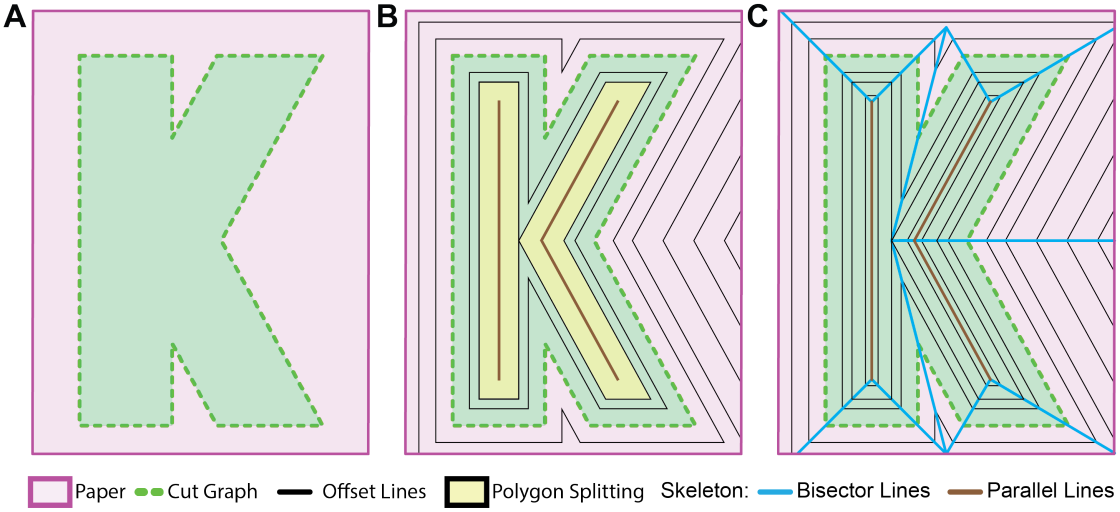

Figure 2.11: Fold-and-one-cut of a polygon in the shape of the letter "K" (A) Polygon to be cut. (B) Split event during the shrinking/expanding process (yellow polygons). (C) Skeleton lines

Although we have a split event, the procedure to create the crease pattern is still the same as described in the previous example. That is, once the shrinking/expanding process is done and we have all the parallel lines and some of the skeleton vertices, we find all the bisector lines by connecting the vertices of the cut edge and vertices between offset lines

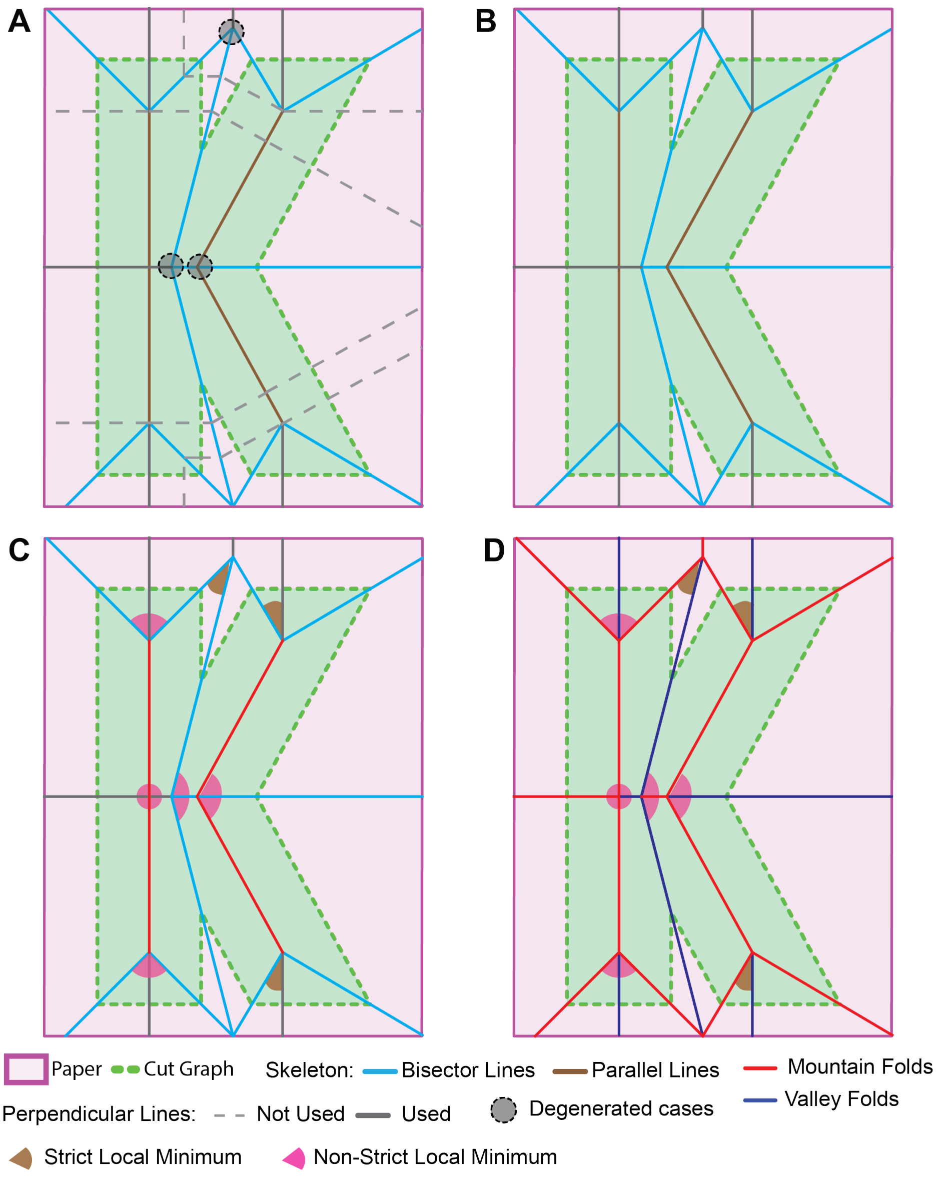

Figure 2.12: Fold-and-one-cut of a polygon in the shape of the letter "K" (A) Skeleton lines and all possible perpendicular lines. (B) Crease pattern without assignment. (C) Initial guess assignment. (D) Crease pattern.

(Fig. 2.11(C)). Next, we add perpendiculars to the vertices, such that all of them satisfy the even degree theorem and Kawasaki-Justin theorem. Fig. 2.12(A) shows all the possible perpendiculars for each vertex. All of them are valid choices, but we use the perpendiculars that do not cross any skeleton line for simplicity.

After we choose the perpendiculars that we will use (Fig. 2.12(B)), we need to assign the creases as either mountain or valley folds. Once again, we use our proposed initial guess: *parallel lines inside and outside the polygon are mountain and valley folds, respectively* (Fig. 2.12(C)). Next, we visit each vertex and assign the mountains and valleys such that the Maekawa-Justin Theorem and local Minimum Theorem are satisfied in every vertex. In Fig. 2.12(C)), we identify all the local minimums, which helps with the assignment choices. As previously mentioned, the mountain and valley assignment is not unique. In Fig. 2.12(D)), we show one of the possible solutions for the mountain/valley assignment.

2.4 Example 3: “GT”

In this example, we increase the complexity of the problem and we will show that the same approach described for a single polygon also applies for multiple polygons. To exemplify, we demonstrate how we can fold and single cut a simplified version of the Georgia Tech “GT” (Fig. 2.13).

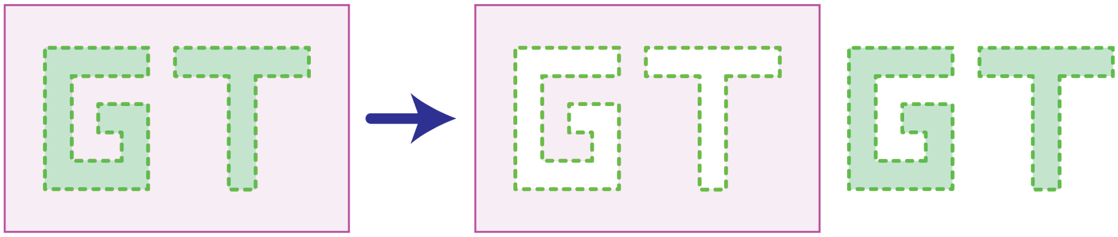

Figure 2.13: Simplified version of the Georgia Tech “GT” to be folded and single cut.

2.4.1 Step 1: Straight skeleton

Similar to a single polygon, the first step consists of building the straight skeleton. While shrinking/expanding the polygons, we observe an interaction between the offset lines of the letter “G” with itself and with the letter “T”. This interactions result in *parallel lines* outside the polygons (Fig. 2.14(A)). After finding all the parallel lines, we connect all the vertices between offset lines and their respective vertices in the cut edges. The process to find the straight skeleton (i.e., skeleton parallel lines, bisector lines, and vertices) is shown in Fig. 2.14(B).

2.4.2 Step 2: Perpendiculars

After we find the straight skeleton, we no longer need the offset lines. Therefore, we can remove them. Next, we need to satisfy the even degree theorem in all the vertices. For that, we add a perpendicular line at all (and only) the odd degree vertices. Fig. 2.14(C) shows all the possible perpendiculars and the degenerated cases. For a simplified crease pattern, we choose perpendiculars that intersect the straight skeleton the least (Fig. 2.14(D)).

2.4.3 Step 3: Mountain/valley assignment

Once we have all the crease lines defined, we need to assign them as mountain or valley folds. For that, we start by using the proposed initial guess: *parallel lines inside and outside the polygon are mountain and valley folds, respectively* (Fig. 2.14(E)). With this initial assignment, all the vertices have at least one pre-assigned crease. Following, we need to assign the remaining creases such that both the Maekawa-Justin theorem and the local minimum theorem are satisfied in all the vertices.

Vertices #1 to #6 (Fig. 2.15(A)) already have two out of four creases pre-assigned as both mountains or both valleys folds that bound two non-strict local minimum angles. Because of the Maekawa-Justin theorem, we know that we need to assign one mountain and one valley. Because of the local minimum theorem, we know that for vertices #1 to #4, the valley fold has to be between the non-strict local minimum, and for vertices #5 and #6, the mountain fold has to be between the non-strict local minimum (Fig. 2.15(B)).

Vertex #8 is a four-degree vertex with three-mountains (Fig. 2.15(B)). Consequently, the unassigned crease is a valley. Now we can follow Vertex #8 perpendicular line that was just assigned as a valley. This perpendicular line forms vertex #9 and vertex #10, which have two valleys and two mountains already assigned, respectively. Because of the Maekawa-Justin theorem, we know that between vertex #9 and #10, this perpendicular is

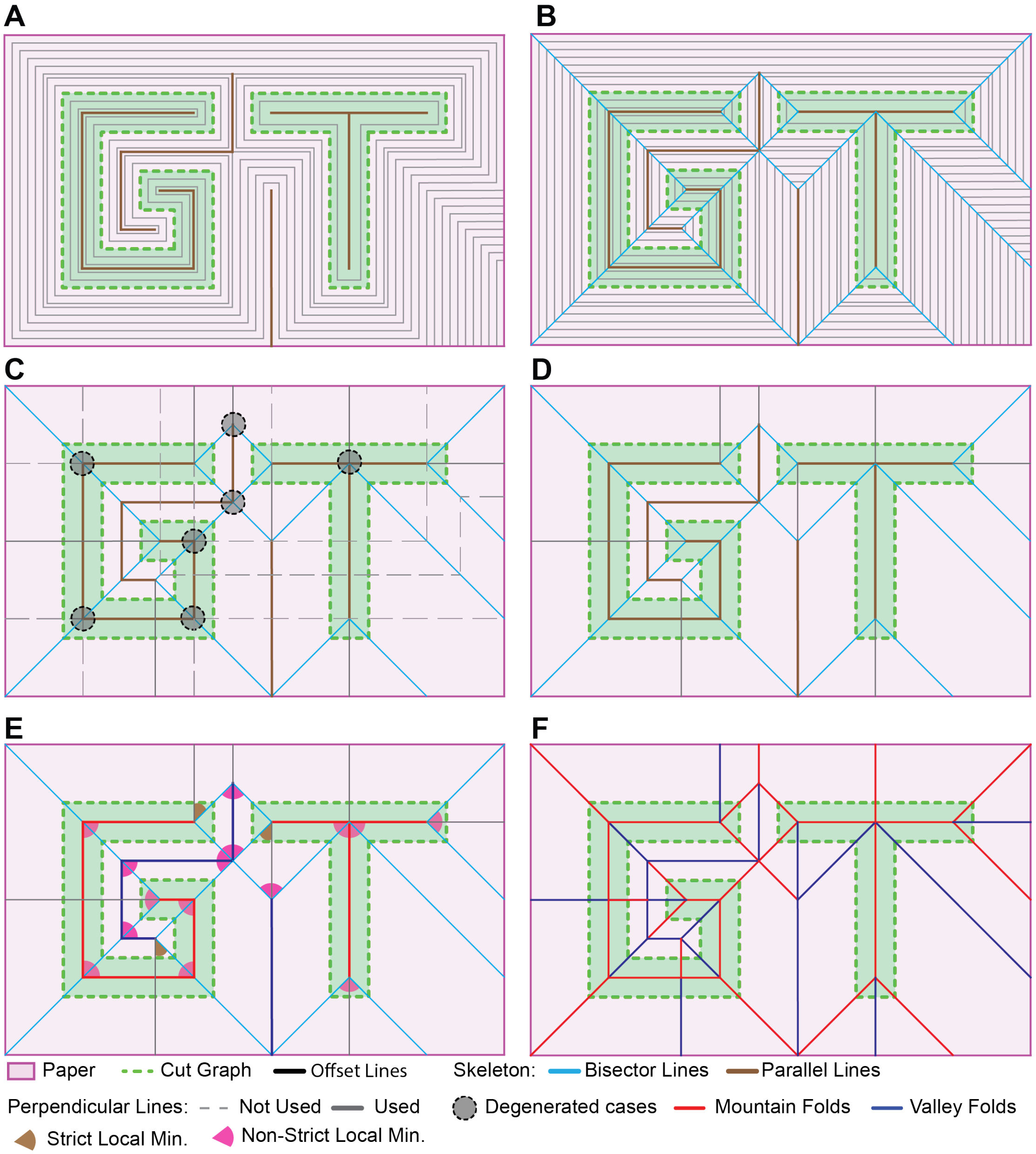

Figure 2.14: Steps for the fold-and-one-cut of “GT”: (A) Shrunk/Expanded polygon faces and parallel lines. (B) Shrunk/Expanded polygons with all the skeleton (parallel and bisector) lines. (C) Skeleton lines with all possible perpendiculars (D) Skeleton line and chosen perpendicular lines. (E) Initial guess for assignment and local minimum angles marked. (F) Crease pattern with mountain/valley assignment.

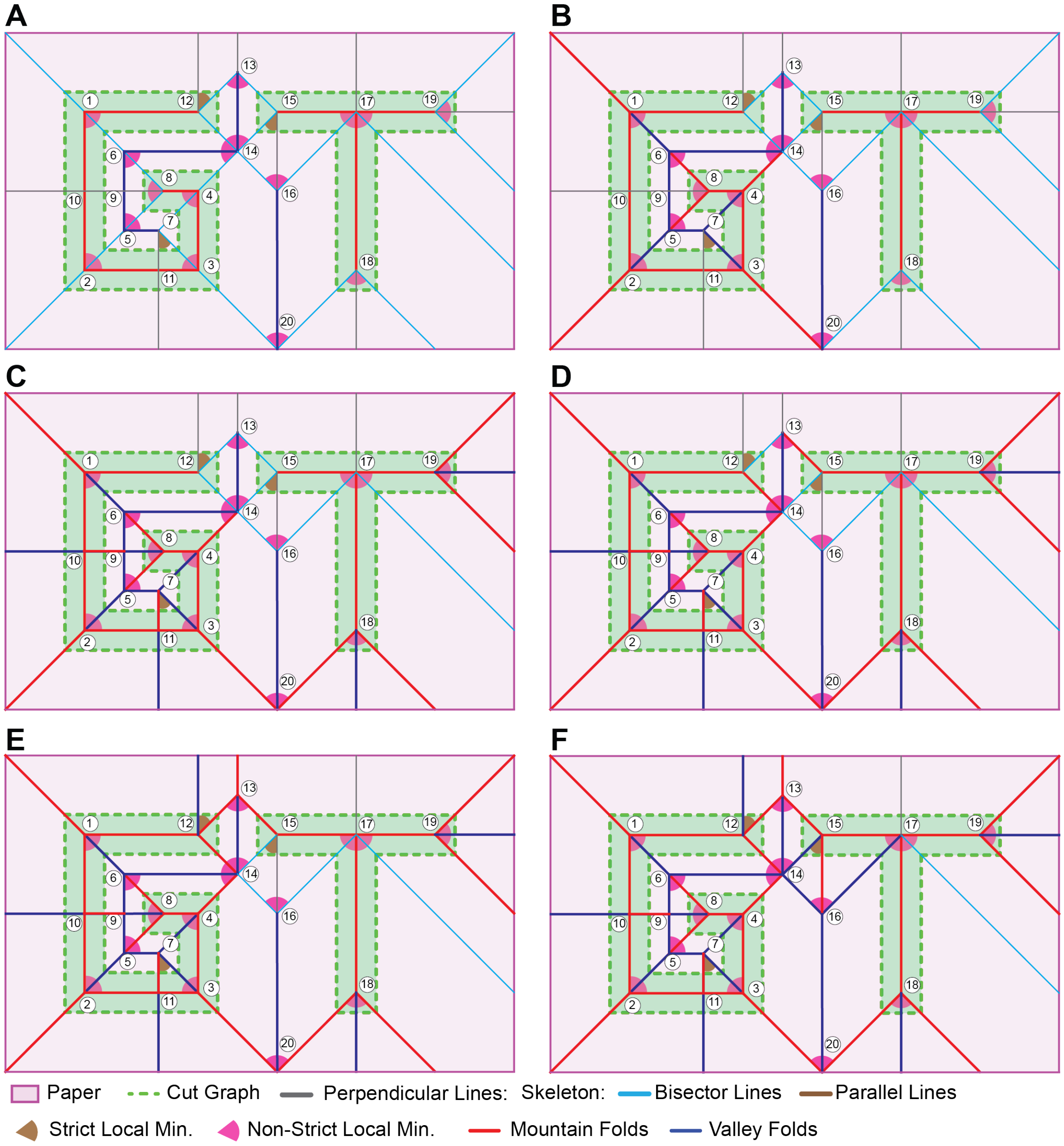

Figure 2.15: (A-F) Mountain/valley assignment Steps.

assigned a valley. Between Vertex #10 and the boundary of the paper, this perpendicular is assigned a mountain. Similarly, we can assign the creases for vertices #7 and #11 (Fig. 2.15(C)).

The remaining vertices do not have unique assignments defined by the flat-foldability theorems, and multiple choices of assignments are possible. For example, Vertices #18 and #19 (Fig. 2.15(B)) have a mountain fold bounding two non-local minimum angles. Thus, we know that those are three-mountain and one-valley vertex. However, because of the non-strict local minimum angles, the valley fold can be assigned to any one of the non-assigned creases. We decide to assign the valley fold to the crease between the two non-strict local minimum angles (Fig. 2.15(C)).

Vertices #12 to #17 (Fig. 2.15(C)) are highly interconnected, meaning that to guarantee a compatible assignment, we must assign those vertices together. From an initial inspection, we see that Vertex #12 and #15 have a pre-assigned mountain fold that does not bound the local minimum angle. Consequently, the creases between vertices #12 and #14, and vertices #13 and #15 have to be assigned as a mountain fold (Fig. 2.15(D)).

At this point, Vertices #12 and #13 impact each other, but not the remaining unassigned creases. We can complete the assignment of those vertices in two ways, and we show one of them in Fig. 2.15(E).

Because of the Maekawa-Justin theorem, the two unassigned creases at Vertex #14 (Fig. 2.15(E)) must have the same assignment. Those creases are connected to Vertex #15 and #16, which are vertices that can accommodate those creases with either assignment. Once again, we have two choices of assignment, and we assign the creases at Vertex #14 as valley folds (Fig. 2.15(F)). As a result and to satisfy the Maekawa-Justin theorem, the crease line between Vertex #15 and #16 has to be a mountain fold, and the crease between Vertex #16 and #17 has to be a valley fold (Fig. 2.15(F)). The only two creases left are the ones connected to the Vertex #17. Because of the Maekawa-Justin theorem, we know that one is a valley and the other is a mountain fold. Because the local minimum theorem was

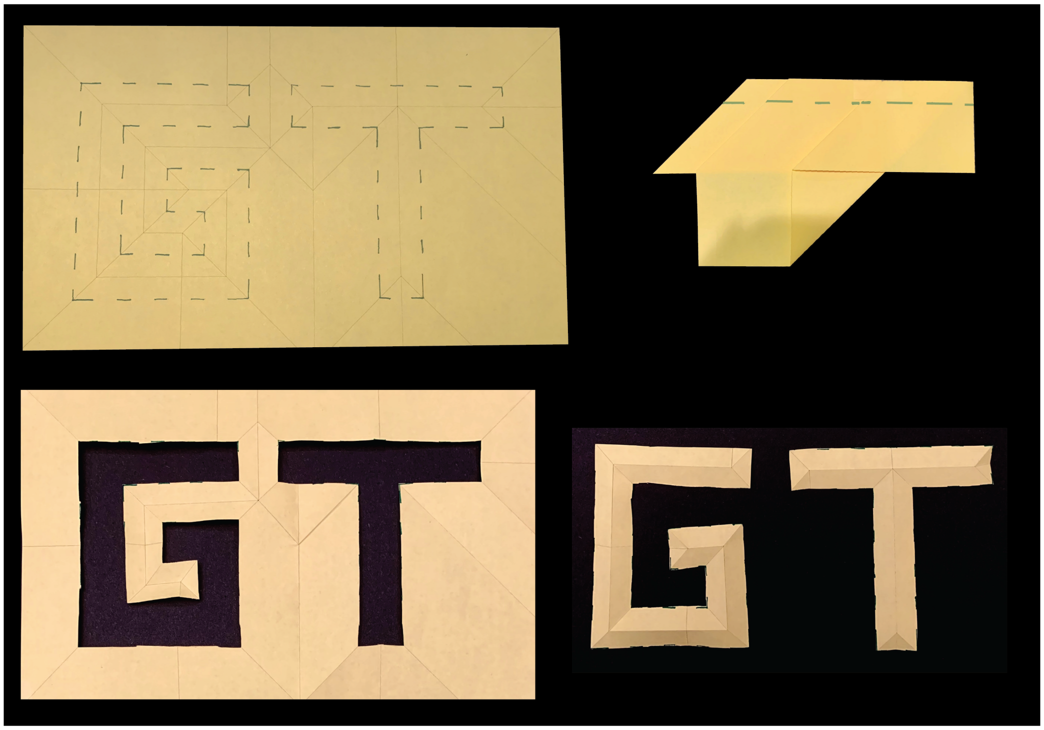

Figure 2.16: Paper with the fold-and-one-cut crease pattern of the simplified version of the Georgia Tech "GT" before and after being folded flat (top), and the resulting cut outs after the single cut (bottom).

already satisfied, any of the two lines can be assigned as a mountain. Fig. 2.14(F) shows the final mountain/valley assignment. In Fig. 2.16 we show the actual fold-and-one-cut of the "GT".

2.5 Example 4: "RICE"

As a final example, we design a crease pattern that will collapse four disconnected polygons in the shape of the letters that compose the word "RICE" (Fig. 2.17).

2.5.1 Step 1: Straight skeleton

As before, we shrink/expand the polygons to find all the skeleton parallel lines and some of the skeleton vertices. Note that interaction between the letters occurs during the expansion, resulting in parallel lines outside the polygons. Besides, the interaction between the letters "C" and "E", creates a square that is later shrunk to a skeleton vertex. Similarly, the

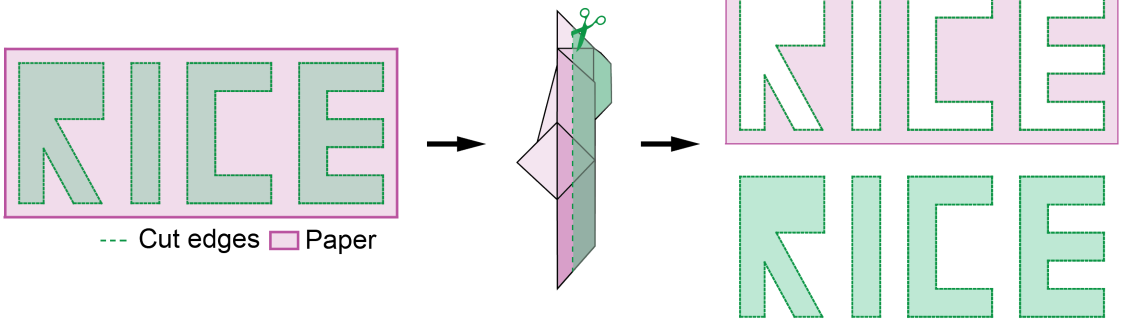

Figure 2.17: Four disconnected polygons forming the word “RICE” to be folded and single cut.

expansion of the letters “R” and “I” creates a triangle that is shrunk into a skeleton vertex (Fig. 2.18). After finding some of the skeleton vertices and all the skeleton parallel lines, we can connect all the vertices formed by offset lines with their respective cut vertex (Fig. 2.18).

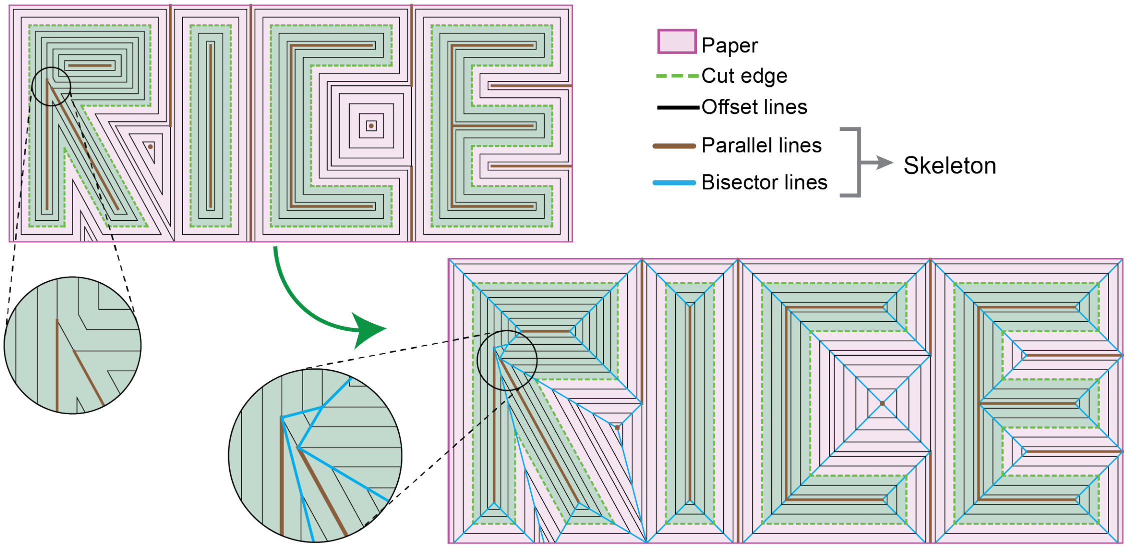

Figure 2.18: Shrinking/expanding of the polygons edges (top) and complete straight skeleton (bottom).

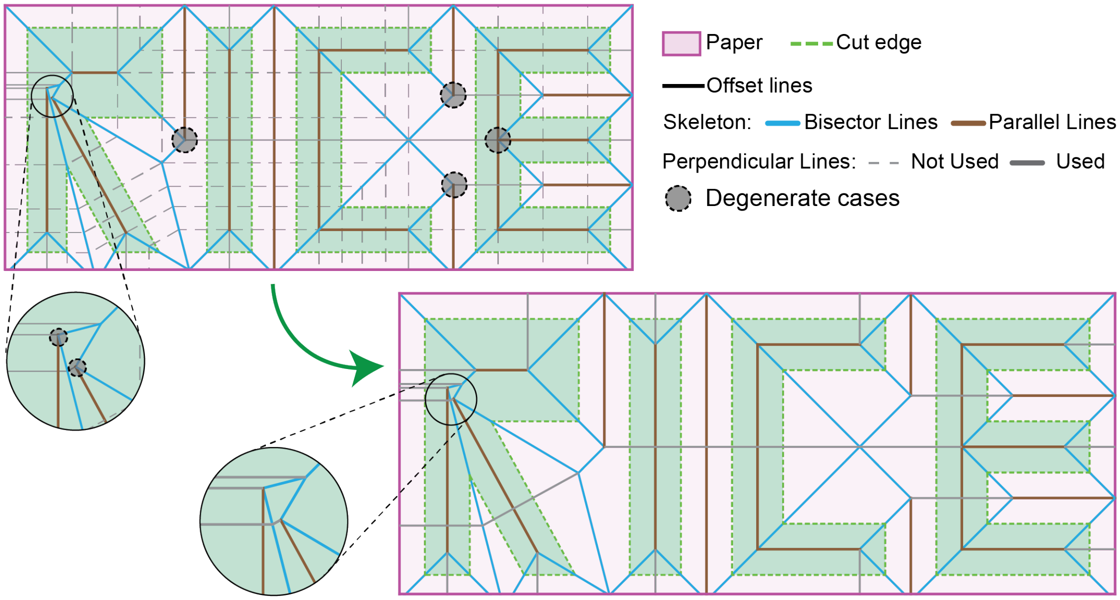

Figure 2.19: Straight skeleton and all possible perpendicular lines (top), and chosen crease pattern (bottom).

2.5.2 Step 2: Perpendiculars

In previous examples, we avoided choosing perpendiculars that cross the skeleton lines and interact with other letters. Unlike previous examples, the degenerated vertices between the letters and the degenerated vertex inside the letter “E” force us to have perpendicular lines that interact with multiple letters (Fig. 2.19). Considering the degenerated vertices, we designed the letters such that the perpendiculars would reach another skeleton vertex (which terminates the perpendiculars) instead of intersecting skeleton lines that reflect them. This strategy is not necessary, but it allows for less dense crease patterns. Fig. 2.19 shows all the possible perpendiculars for each vertex and the chosen perpendiculars. The choice of perpendiculars was made such that we use the perpendiculars with the least number of intersections.

2.5.3 Step 3: Mountain and valley assignment

The mountain and valley assignment is done following previous strategy. That is, we start with the initial guess: *parallel lines inside and outside the polygon are assigned as moun-*

tain and valley folds, respectively. Following, we explain in detail how the creases in Fig. 2.20 were assigned.

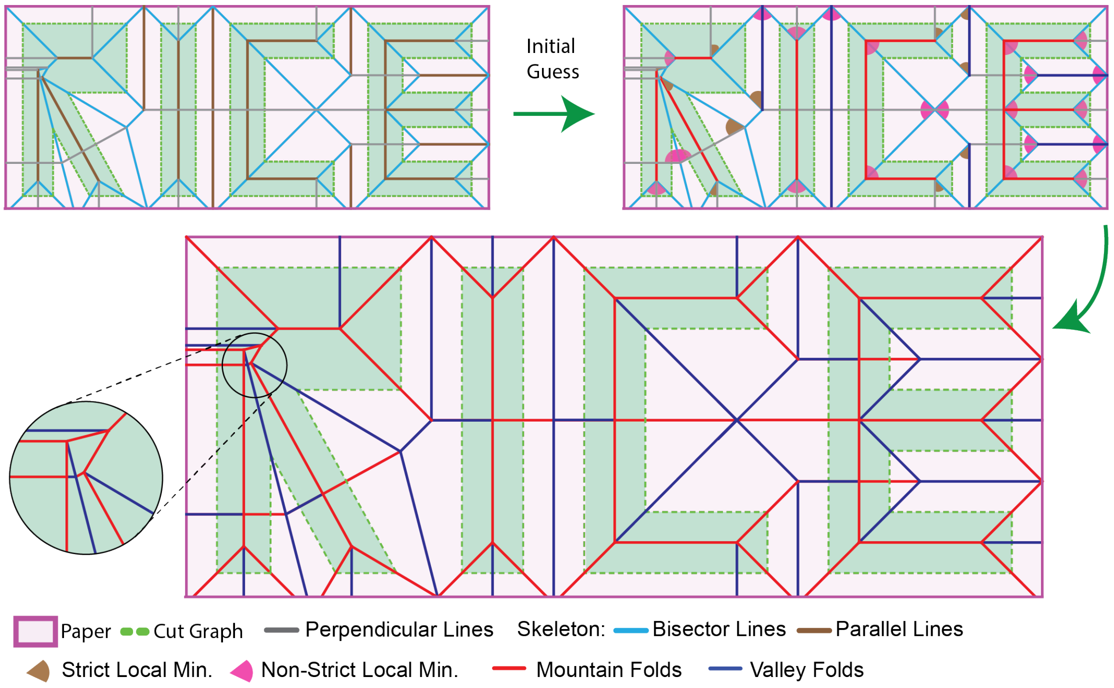

Figure 2.20: Mountain and valley assignment of the “RICE” crease pattern.

Because of the complexity of this crease pattern, we will start inspecting the vertices that have a strict local minimum bounded by an already assigned crease. Because of the local minimum theorem, we know that the other crease bounding the strict local minimum angle must have the opposite assignment. Those are the case of the vertices labeled with the letter *a* in Fig. 2.21(A). After satisfying the local minimum theorem, some vertices are left with a single unassigned crease (vertices *b* in Fig. 2.21(B)). Those creases are assigned by satisfying the Maekawa-Justin theorem ($M - V = \pm 2$). At the vertices *b*, we can assign all the remaining creases. After, we can re-inspect for strict local minimums and assign some of their creases as well, which is the case of vertex *a* in 2.21(B).

Next, we can assign the *independent vertices* (vertices *c* in Fig. 2.21(C)). Those vertices have multiple possible assignments. However, their assignment does not impact other vertices. Fig. 2.21(D)) shows one possible solution. The remaining creases have interaction with multiple vertices. Therefore, we need to choose one vertex either on the left or right side of the paper and ensure that the assignments are compatible between neighboring vertices.

Looking at the letter “R”, we can assign all (but two) crease lines without considering the other letters. We start from vertex #1 (Fig. 2.22(A)). This vertex is a three-mountain and one-valley type and has three possible flat-foldable assignments. For this example, we decided to place the valley fold between the two non-strict local minimum angles. Now, we can assign the crease lines at vertex #2. Because the just assigned mountain fold is not bounding the strict local minimum, we know that this is a three-mountain and one-valley vertex. Thus, the crease between vertex #2 and #3 has to be a mountain. We keep following the vertex sequence from vertex #2 to #6, such that both the Maekawa-Justin theorem and local minimum theorem are always satisfied. Note that if we assign the crease between vertices #1 and #2 as a valley and follow the same procedure that we just described from vertex #1 to #6, we will find another valid assignment.

Vertex #7 (Fig. 2.22(B)) is a three-valley and one-mountain type. Because of the non-strict local minimum, we know that the mountain fold has to be assigned to the crease between vertex #7 and #8. This assignment leaves vertex #8 with one unassigned crease, which has to be valley ($M - V = \pm 2$) (Fig. 2.22(C)). Vertices #9 and # 10 have three and two possible assignments, respectively. Fig. 2.22(C) shows one of the possible assignments. Now, we are left with vertices #11 and #12 and three unassigned creases (Fig. 2.22(C)). By inspecting the vertices, we observe that all the unassigned creases will have the same assignment. We assign all those creases as valley folds such that we can ensure that the magenta portion of the will not be aligned with the cut lines (Fig. 2.22(D)).

Now that all the creases of the letter “R” were assigned, we can inspect the remaining vertices. From Fig. 2.22(E), we observe that we can assign the perpendicular from vertex d_1 to d_4 by satisfying the Maekawa-Justin theorem (Fig. 2.22(F)). Vertex d_4 has multiple possible assignments. In Fig. 2.22(G), we show our choice. This choice leads to a simplified fold and ensures no overlapping of the magenta portion of the paper with the cut edges. Vertex *e* (Fig. 2.22(G)) is left with a single possible assignment, which also determines the assignment of the remaining creases (Fig. 2.22(H)). In Fig. 2.23 we show the actual fold-and-one-cut of the word“RICE”.

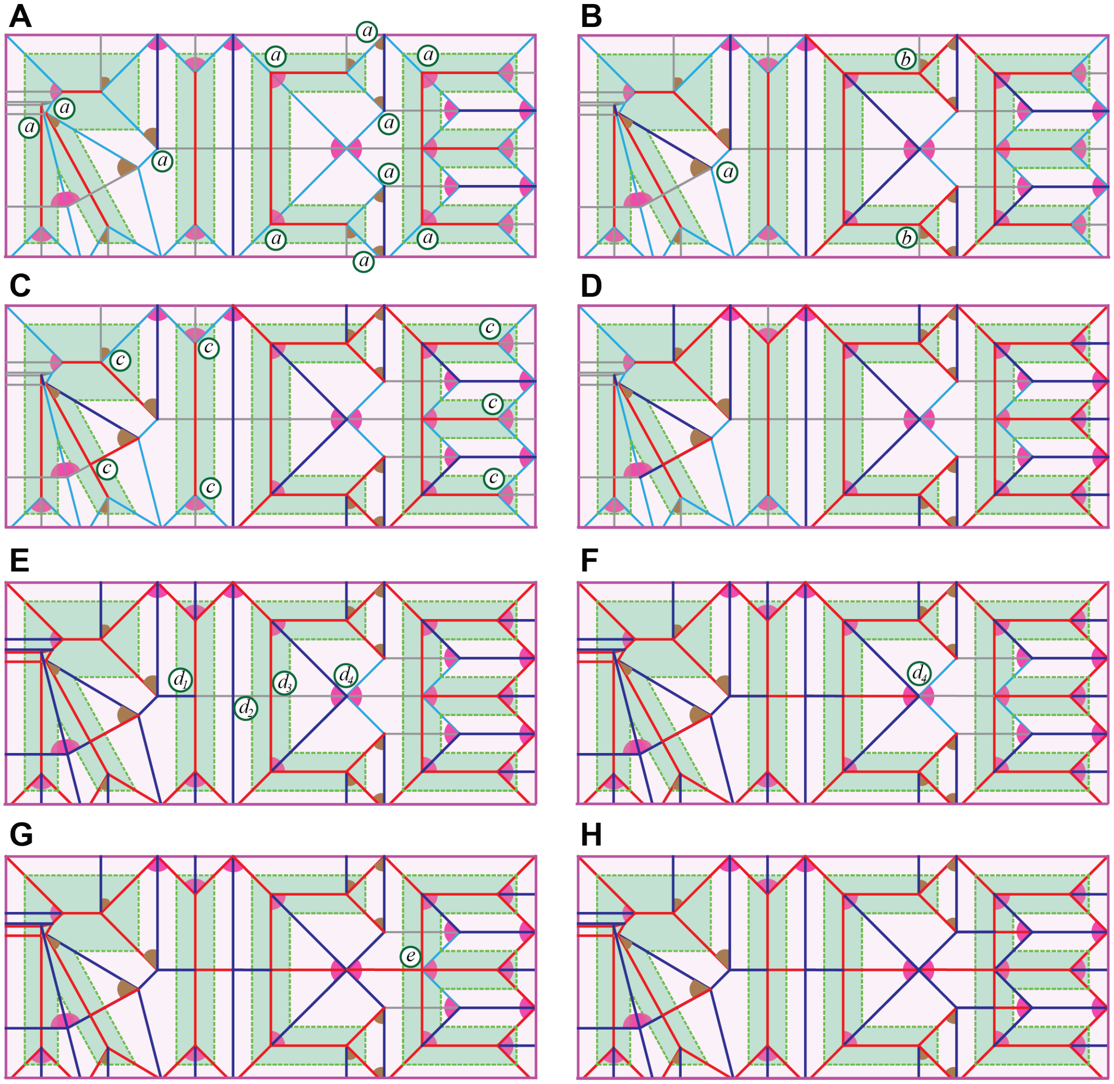

Figure 2.21: (A-H) Steps for the mountain/valley assignment for the crease pattern of “RICE”.

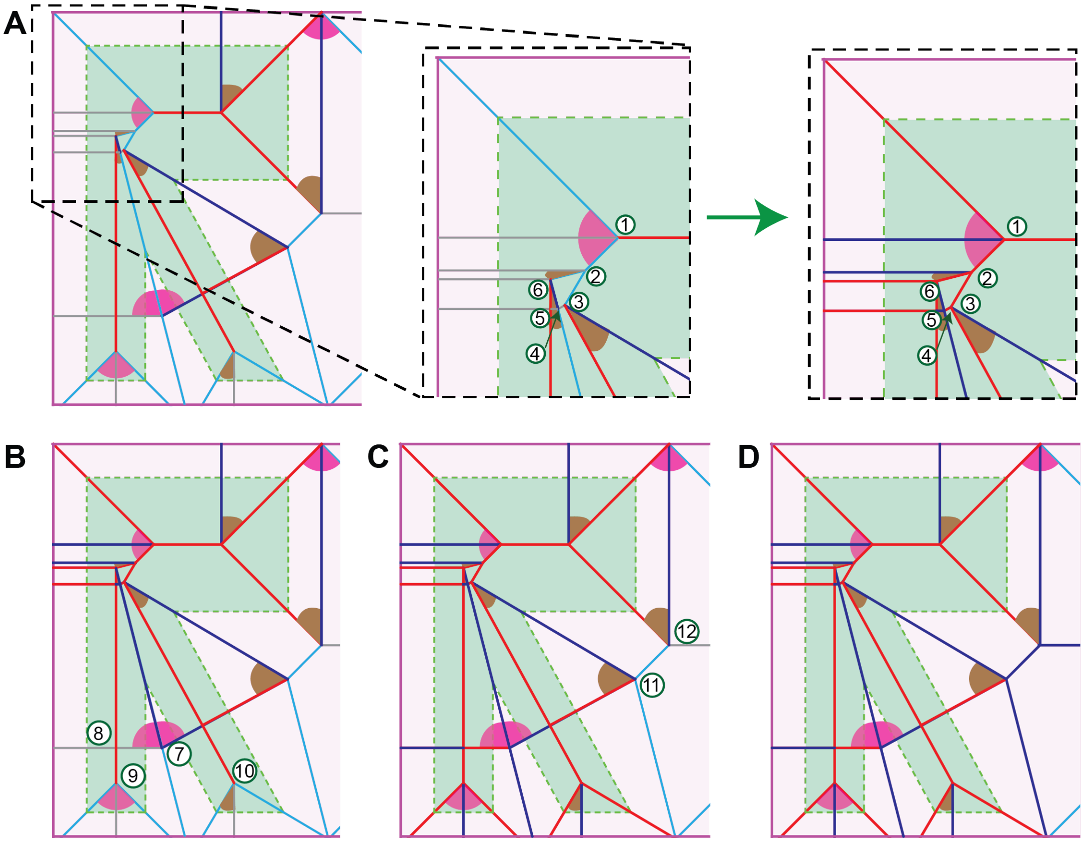

Figure 2.22: (A-D) Steps for the mountain and valley assignment of the letter “R”.

2.6 When does the method fails?

The straight skeleton works almost always. The method fails in specific examples in which perpendicular lines become extremely dense or can never reach the boundary of the paper. In Fig. 2.24, we show an example of dense perpendiculars. We focus on the marked degenerated vertex. This vertex has a single possible perpendicular reflected at the skeleton lines multiple times, creating creases extremely close to each other and making the pattern difficult or even impossible to be folded. Other examples are shown on [27]. In summary, as long as we can ensure that perpendicular lines will not wonder around the pattern, this method will result in a valid solution for the fold-and-one-cut problem.

Figure 2.23: Paper with the fold-and-one-cut crease pattern of the word “RICE” (top), and the resulting cut outs after the single cut (middle and bottom).

2.7 Remarks

Here, we provide a list of remarks, which can be used as a checklist to avoid mistakes in the crease pattern:

- A one-to-one correspondence exists between the skeleton regions and cut edges. Each cut edge belongs to a single skeleton region, and each skeleton region has a single cut edge.

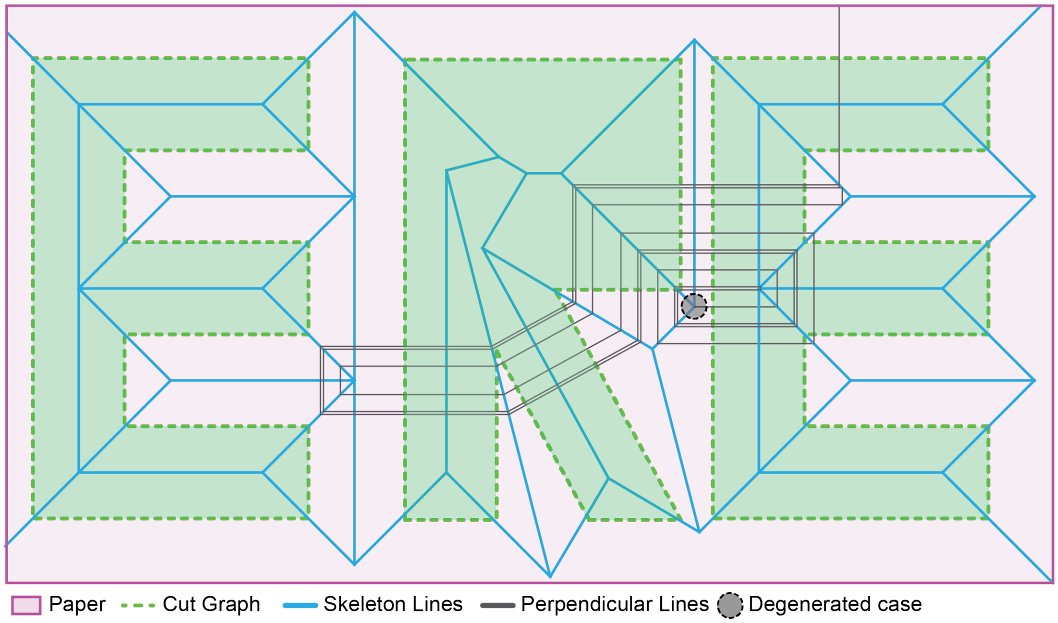

Figure 2.24: Example of a highly dense crease pattern. The black lines represent the only possible perpendicular of the marked degenerated vertex. Although we can still obtain a valid crease, it becomes unrealistic to fold such a pattern.

- The skeleton lines should only cross the cut graph at the cut vertices (never at the cut edges).
- Only perpendiculars can cross the cut edges.
- The sequence of folding is important. If a wrong sequence is used, it may bring material (that should not be cut) to the final cutting line.
- The folds and the mountain/valley assignment are not unique. Our proposed initial guess guides us to a series of possible solutions.

CHAPTER 3

FOLDING AT THE MICRO-SCALE: ENABLING MULTIFUNCTIONAL 3D ORIGAMI-ARCHITECTED METAMATERIALS

Mechanical metamaterials inspired by the Japanese art of paper folding have gained considerable attention because of their potential to yield deployable and highly tunable assemblies. The inherent foldability of origami structures enlarges the material design space with remarkable properties such as auxeticity, high deformation recoverability, and deployability. In this Chapter, we integrate the results of the design, 3D direct laser writing fabrication, and in situ scanning electron microscopic mechanical characterization of microscale origami metamaterials based on the zipper/align coupling of Miura-Ori tubes. The origami-architected metamaterials, achieved by means of microfabrication, display remarkable mechanical properties: stiffness and Poisson's ratio tunable anisotropy, a significant degree of shape recoverability, and reversible auxeticity (i.e., the metamaterial switches Poisson's ratio sign during deformation). Our findings emphasize the scalable and multifunctional nature of origami designs and pave the way toward harnessing the power of origami engineering at small scales.

3.1 Introduction

Architected metamaterials are materials with unusual properties, such as high shape recoverability [36, 37, 38], mechanical cloaking [39], high strength-to-density ratios [40], and mechanical anisotropy [41]. Such properties are dictated by the geometry of the material micro-structure. Thus, origami patterns are excellent candidates for the design of the architecture of metamaterials as some patterns present unusual mechanical properties [42, 43] combined with stacking [1] and space-filling [44] capabilities that are displayed across scales (Figure 3.1). Although origami is a promising tool for many applications, the manu-

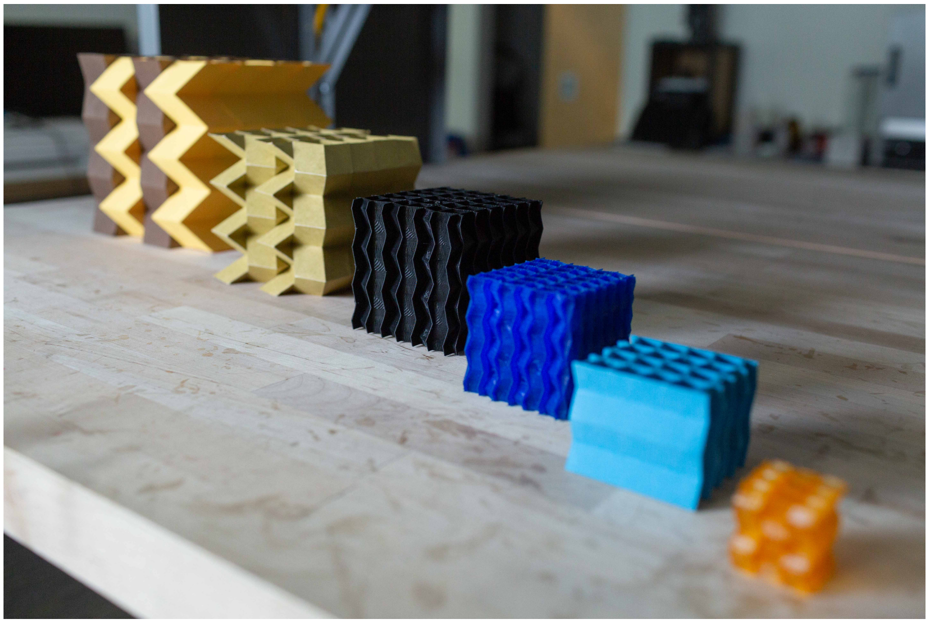

Figure 3.1: Zipper/aligned metamaterial across different scales. In the image, the largest scale model (left) has panels length of 3.8 cm and smallest scale (right) has panels length of 3.8 cm (3D printed model developed by [45]). Photography by Allison Carter

facturing of such structures, specifically at the material level, is still a challenge. Complex origami assemblies have been obtained in the macro-scale using 3D printing techniques, such as digital light processing [45]. However, on a material scale, previous works focused on the behavior of a single unit cell (panel lengths of 20μm [23], and 200μm [46]), rather than on the assembly of more complex functional systems.

In this chapter, we integrate geometric design, micro-fabrication via 3D direct laser writing, and in situ scanning electron macroscopic mechanical testing to reveal remarkable mechanical properties of the zipper/aligned origami assembly [9], which results from the coupling of Miura-Ori tubes with compatible geometries. The tubes are assembled from two mirrored Miura-Ori strips (Fig. 3.2(A,B)). The constructed tube is flat-foldable in two configurations and preserves the one degree of freedom of the Miura-Ori pattern. Thus, under a rigid origami assumption, its kinematics is still described by the intrinsic parameters of the pattern: the panel angle (α) and dimensions (a and b), and a folding angle (such as ψ). The tubes are connected in an aligned and zipper fashion along the z- and y-direction,

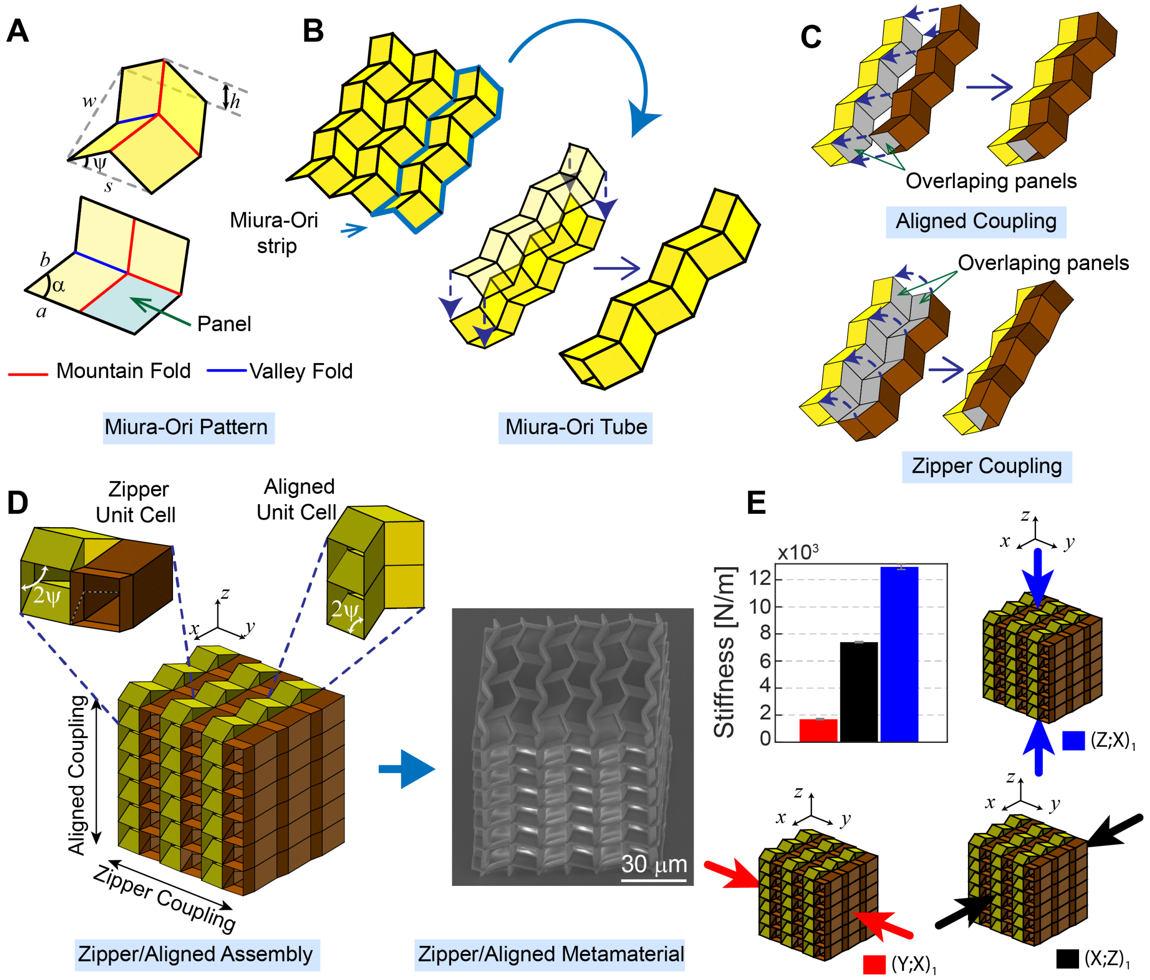

Figure 3.2: Zipper/aligned metamaterial. (A) Partially folded Miura-Ori unit cell and crease pattern. (B) Schematics of the Miura-Ori pattern and tube assembly. (C) Aligned and zipper coupling of Miura-Ori tubes. (D) Schematics and SEM image of the fabricated Zipper/Aligned metamaterial. (E) Initial axial stiffness of the fabricated metamaterial along Cartesian directions.

respectively. The aligned coupling of two Miura-Ori tubes can be understood as a translation, while the zipper coupling also includes a rotation between the tubes (Fig. 3.2(C). The geometry of the cellular assembly is defined in terms of the zipper unit cell, which is replicated along the Cartesian directions. The assembled structure, like the Miura-Ori tube, is deployable in the x- and y-directions (Fig. 3.2(D)). However, because of the zipper assembly, this structure is not deployable in the z-direction.

The zipper/aligned metamaterial behavior has been replicated via 3D printing on a

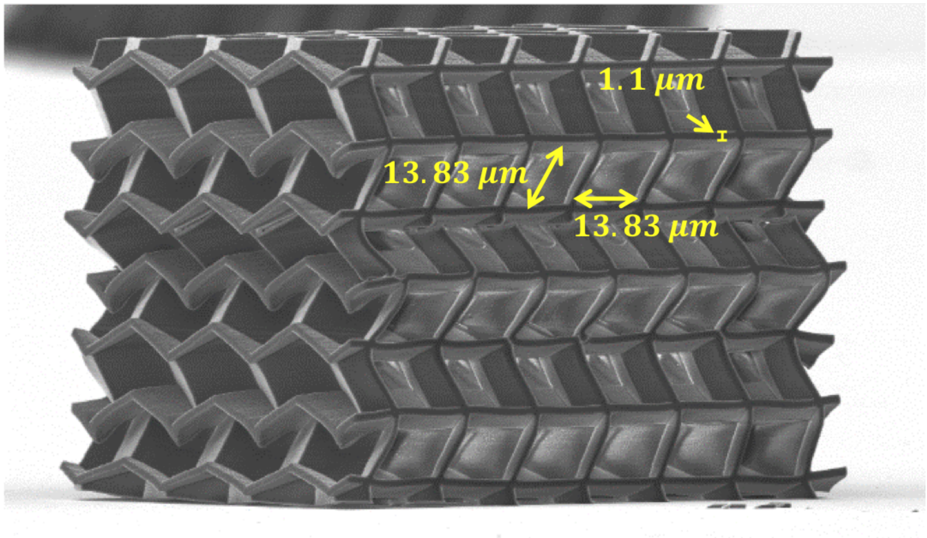

Figure 3.3: Geometry of the fabricated metamaterial.

macro-scale (panel length of 6 mm). The fabricated sample uses a thick origami model that can accommodate the thickness of the panels and provide reduced stiffness at the hinges [45]. However, in the micro-scale, no such complexity has been reported. In this work, we fabricate the zipper/aligned metamaterial at the micro-scale via 3D direct laser writing (DLW) using 2-photon lithography (Nanoscribe, GmbH), producing the smallest 3D origami-architected metamaterial (panel length of 13.83μm and thickness of 1.1μm) (Fig. 3.3). In our fabricated model, we do not use special elements of the thick origami model. Thus, in the fabricated metamaterial, the folds and panels have the same thickness and are made of the same material. While the fabricated metamaterials do not exhibit the same kinematics of the paper model, yet it provides enough foldability and a strong anisotropic mechanical behavior (Fig. 3.2(E)), similar to the one previously predicted computationally [9].

This chapter is organized as follows. First, we provide an introduction to the zipper/aligned geometry and kinematics, and we derive analytical equations for the Poisson's ratio. Next, we will show that the fabricated zipper/aligned metamaterial presents stiffness anisotropy and a large degree of shape recoverability. Following, we will show that based on the initial configuration (i.e., initial folding angle ψ_0), the metamaterial can display either an auxetic behavior or even reversible auxeticity during the axial deformation. Then, we conclude with final remarks.

3.2 Geometry and Mechanics

Under the assumption of rigid origami, we derive analytical expressions to describe the zipper/aligned assembly's kinematics. Thus, considering that the zipper/aligned assembly is composed of tubes with rigid panels and perfectly compliant hinges, the assembly folds rigidly with a single degree of freedom, and the zipper unit cell kinematics (Fig. 3.4(A)) is described by

$$w_x = 2b\sqrt{1 - (\cos^2\alpha / \cos^2\psi)}, \quad w_y = 2a \sin 2\psi, \quad w_z = a, \quad \text{where} \quad \psi[0, \alpha] \tag{3.1}$$

where $a, b,$ and α the panels intrinsic parameters and ψ is the folding angle. Fig. 3.4(B) shows how the geometry of the zipper unit cell changes with the folding angle ψ for a zipper unit cell with $a = b = 13.83\mu$m and $\alpha = 75°$. We also derive the in-plane Poisson's ration ν_{ij}, i.e., the ratio between the strains in the transverse direction j and the loading direction i

$$\begin{gathered} \nu_{xy} = -\frac{dw_y(\psi)/w_y(\psi)}{dw_x(\psi)/w_x(\psi)} = \frac{(\cos^2\psi - \cos^2\alpha)(1 - \tan^2\psi)}{\tan^2\psi \cos^2\alpha}, \\ \nu_{yx} = 1/\nu_{xy}, \quad \nu_{xz} = -\frac{dw_z(\psi)/w_z(\psi)}{dw_x(\psi)/w_x(\psi)} = 0 \end{gathered} \tag{3.2}$$

where $dw_x(\psi)$ and $dw_y(\psi)$ refer to the derivatives of w_x and w_y with respect to ψ. The kinematic model predicts that ν_{xz} is always zero, independent of the folding angle ψ, while ν_{xy} is a function of ψ. In Fig. 3.4(C) we plot ν_{xy} and ν_{yx} as a function of the folding angle. From those plots, we observe that if the panel angle $\alpha < 45°$, the zipper/aligned metamaterial will always have $\nu_{xy} < 0$. However, if $\alpha > 45°$, the Poisson's ration changes sign depending on the configuration (i.e., folding angle ψ).

While forces along the x-direction are capable of promoting the metamaterial's full

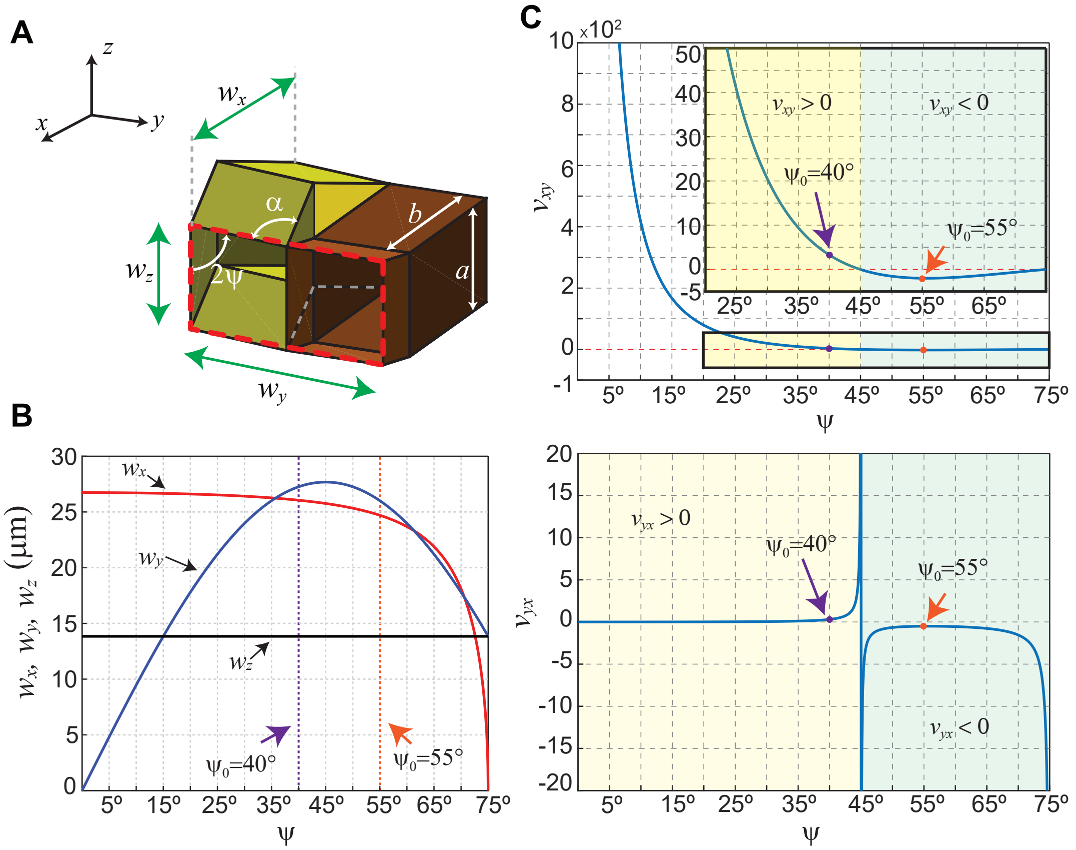

Figure 3.4: Kinematics of the Zipper/aligned metamaterial with panel parameters: $a = b = 13.83\mu m$ and $\alpha = 75°$. (A) Unit cell of the kinematic model of zipper-coupled tubes. Plots showing the (B) Geometry and (C) Poisson's ratio as a function of the folding angle $\psi[0, \alpha]$.

kinematics (ψ can reach values from 0 to α, forces along y-direction have their deployability constrained by the folding angle ψ. At the folding angle $\psi = 45°$, the projection of the panels into the yz-plane are perpendicular to each other. At this point, w_y has its highest dimension and corresponds to an instability/bifurcation point in the architecture kinematics. Further compression along y-direction leads either to a contraction or expansion along the x-direction. This geometric instability produces the sign switching in the Poisson's ratio when we compress the structure along the x-direction. From the kinematic equations, we observe that depending on the choice of intrinsic and extrinsic geometric parameters, we are capable of design a structure with a positive or negative Poisson's ratio, or even a single structure with switching Poisson's ratio sign. Although, in reality, the fabricated structure is not composed of rigid panels and perfectly compliant hinges, we can still use those kinematic equations to describe the geometry of the initial structure and to obtain an insight into the mechanical behavior and design of those structures.

3.3 Results

The single degree-of-freedom kinematic model for the zipper/aligned assembly indicates a geometric instability at the folding angle $\psi = 45°$, where w_y reaches its maximum (Fig. 3.4(B)). Associated with this is a switch in the sign of the Poisson's ratio (Eq. 3.2 and Fig. 3.4(C)). Motivated by this, we investigate two sets of zipper/aligned metamaterials, both with the same panel lengths $a = b = 13.83\mu m$, angle $\alpha = 75°$, and thickness $1.1\mu m$, but with different initial folding angles ψ_0. The initial folding angle can be understood as the natural state (i.e., equilibrium state) and is chosen such that the selected configurations are on opposite sides of the instability point. Thus, we select Configuration A at $\psi_0 = 55°$ and Configuration B at $\psi_0 = 45°$, which are equivalent to 92.4% and 97.4%, respectively, of the total extension of a Miura-Ori tube. The number of unit cells and building direction of the printed metamaterial is dictated by the compression direction in which the structure will be tested. That is, the number of zipper/aligned unit cells is $N_i = 6$ and $N_j = N_k = 3$, where the subscript i indicates the compression/building direction and j, k the perpendicular directions.

3.3.1 Stiffness Response and shape recoverability: Configuration A, $\psi_0 = 55°$

The fabricated zipper/aligned metamaterial exhibit pronounced stiffness anisotropy. The initial stiffness for Configuration A along the z-direction is almost twice the initial stiffness along the x-direction and six times higher than the initial stiffness along the y-direction (Fig. 3.2(E)). This anisotropic behavior results from the folding properties of the origami assembly. That is, in the two flat-foldable directions (x- and y-directions), the metamaterial is softer, while in the non-foldable direction (z-directions), the metamaterial is stiffer.

For the characterization of the stiffness in multiple stages of compression, we subject the metamaterial to an oscillatory compression load along the foldable (x- and y-) directions (see inset in Fig. 3.5). From the stress-strain response of the metamaterial at *Configuration A*, we observe that the fabricated zipper-aligned metamaterial presents distinct stress-strain behaviors in the large deformation regime. Along the x-direction, we observe a high stress plateau over a long strain regime (Figs. 3.5), while along the y-direction, we observe a strain hardening (Fig. 3.6). Note that upon unloading, there is a residual compression that subsequently recovers significantly but not completely. The geometric- and scale-enabled foldability in the x- and y-directions endows the origami assemblies with high shape recoverability under large deformations. After $\approx$30 minutes of relaxation, the structure recovers up to 93% and 94% of its initial configuration after compression in the x- and y-directions, respectively.

Fig. 3.8 reports the tangent stiffness of Configuration A obtained during the oscillatory loading steps at various compression levels, where the colors represent different tested samples. Solid and dashed lines show the stiffness upon the first and second compression cycle, respectively. The second compression cycle was done after the reported viscoelastic recovery. We observe that the response is repeatable for the first and second compression of the same sample. Note that fabrication variances (i.e., laser power, writing speed) can change the polymer's material properties, giving rise to variations in the mechanical response. Thus, consistent fabrication processes are fundamental.

Under compression along the x- and y-direction, we can observe a folding-like behavior of the unit cell layers, while along the z-direction this behavior is not observed. Instead, we observe a local buckling of the vertical panels (parallel to the z-direction), which is a result of the intrinsic unfoldability of the metamaterial along the z-direction (Fig. 3.9). Note that this unfoldable direction is a consequence of the zipper coupling and allows for a higher initial stiffness in the z-direction.

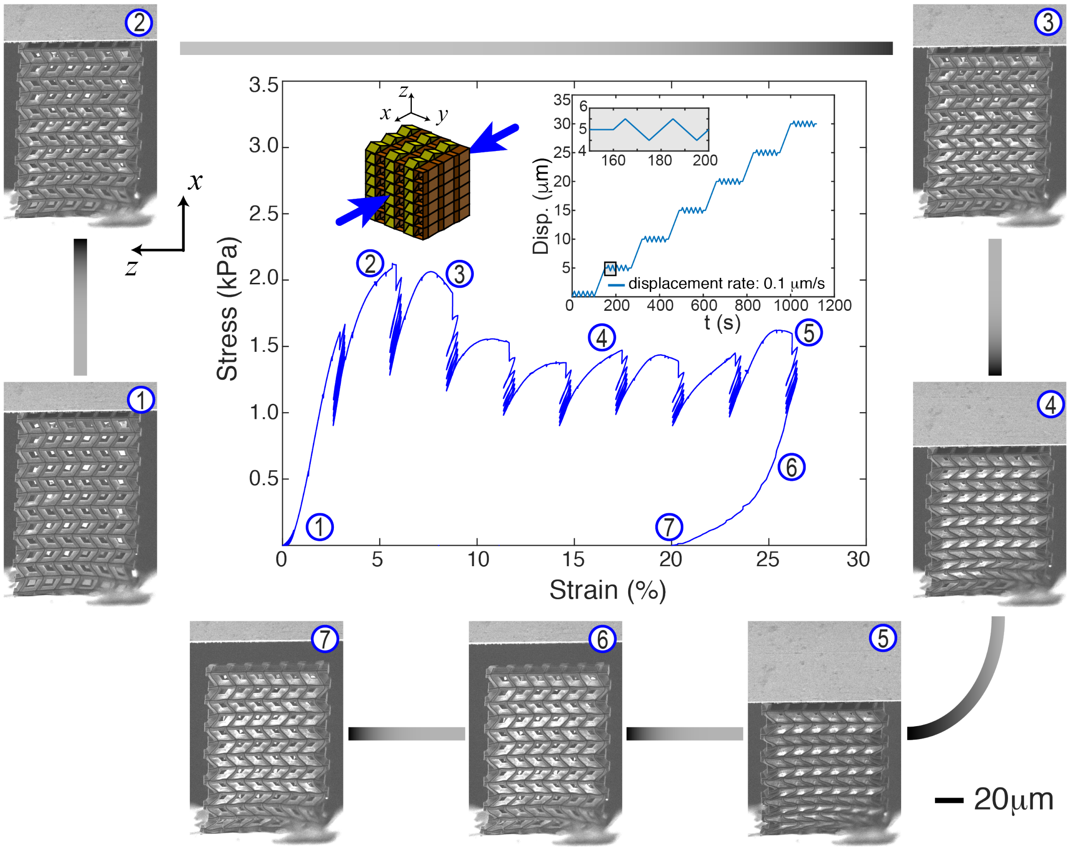

Figure 3.5: Configuration A plateau behavior upon compressive loading and recovery along the x-direction. SEM snapshots during loading (1-4), at maximum compression (5), and during recovery (6-7). Inset shows loading scheme of compression tests.

3.3.2 Poisson's Ratio Anisotropy: Configuration A, $\psi_0 = 55^\circ$

We calculate the Poisson's ratio to quantify the ability of the metamaterial at Configuration A to expand/contract in the transverse directions in response to axial deformation. We measure the change in length by comparative image analysis at two compression stages: zero compression and maximum compression. In this case, the Poisson's ratio should be interpreted as an average instead of an instantaneous value. Owing to the non-uniform deformation of the structures, a consequence of both the folding sequence heterogeneity and end effects, only a region in the middle of the structures was employed to calculate Poisson's ratio, as highlighted in Fig. 3.7. A summary of the measured Poisson's ratios is presented in Table 3.1. The Poisson's ratio of the zipper/aligned origami assemblage for Configu-

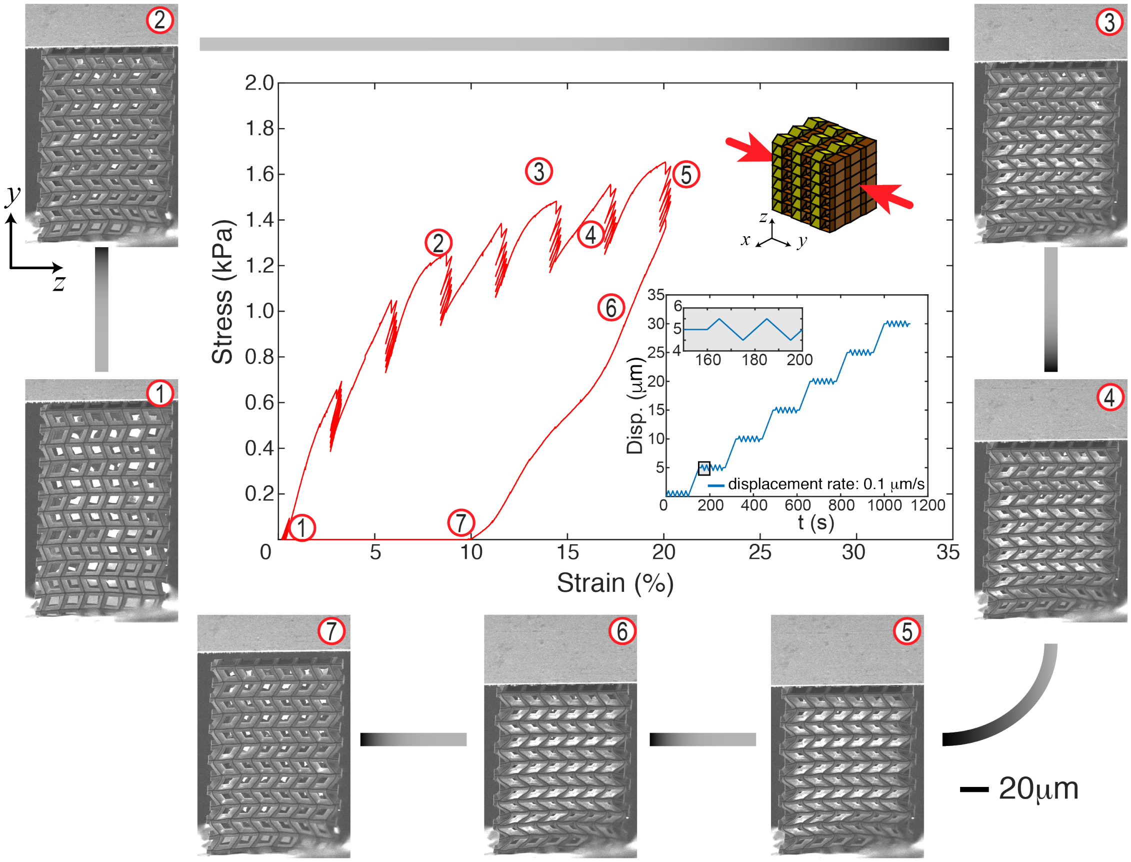

Figure 3.6: Configuration A hardening behavior upon compressive loading and recovery along the y-direction. SEM snapshots during loading (1–4), at maximum compression (5), and during recovery (6–7). Inset shows loading scheme of compression tests.

ration A is clearly anisotropic. When compressed along the x-direction and observe from z-direction, the metamaterial exhibits a negative Poisson's ratio of $\nu_{xy} = -0.55$ (transverse strain measured along the y-direction). However, when observing from y-direction, the metamaterial exhibits a Poisson's ratio of $\nu_{xz} = 0.04$ (transverse strain measured along the z-direction), which is close to the theoretical value of zero. Because of the initial folding angle of Configuration A ($\psi = 55°$), under compression, the metamaterial always exhibits negative Poisson's ratio ν_{xy}. Note the sign of the measured Poisson's ratio agrees with our geometric-based prediction.

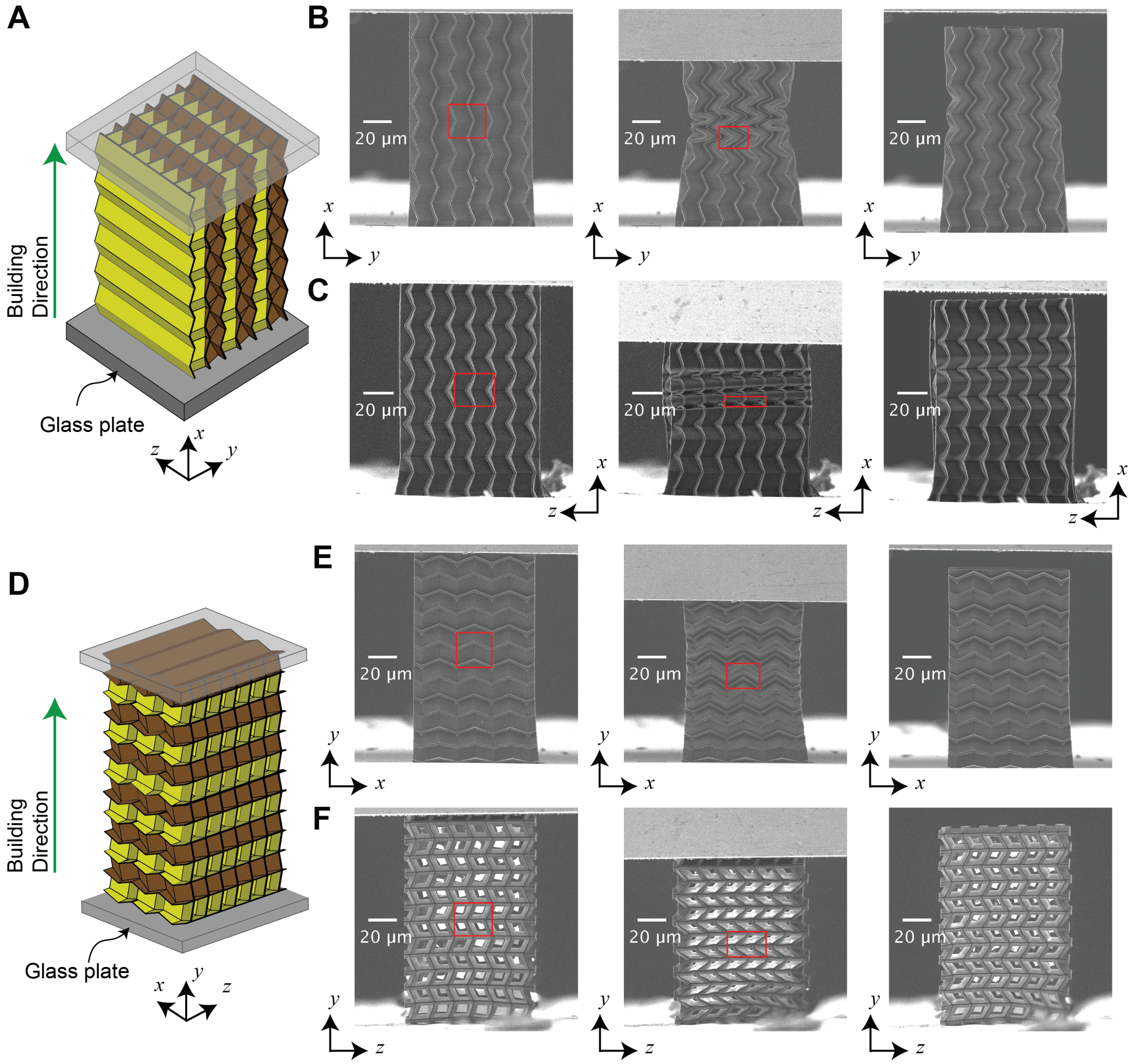

Figure 3.7: Compression of Configuration A. (A) Schematic and SEM images of the metamaterial compressed along the x-direction and observed from (B) the z-direction (sample (X;Z))and (C) the y-direction (X;Y). (D) Schematic and SEM images of the structures compressed along the y-direction and observed from the (E) z-direction (sample (Y;Z)) and (F) x-direction (sample (Y;X)). SEM images show the metamaterial at initial configuration (left), maximum compression (center), and after relaxation (right). Red squares represent regions where the Poisson's ratios were measured.

3.3.3 Poisson's Ratio Reversible Auxeticity: Configuration B, $\psi_0 = 40°$

From the kinematic model of the zipper/aligned metamaterial, we observe that if we compress a metamaterial with an initial folding angle $\psi_0 < 45°$ a switch in the sign of the Poisson's ratio occurs. To investigate this behavior predicted via geometry, we fabricate a

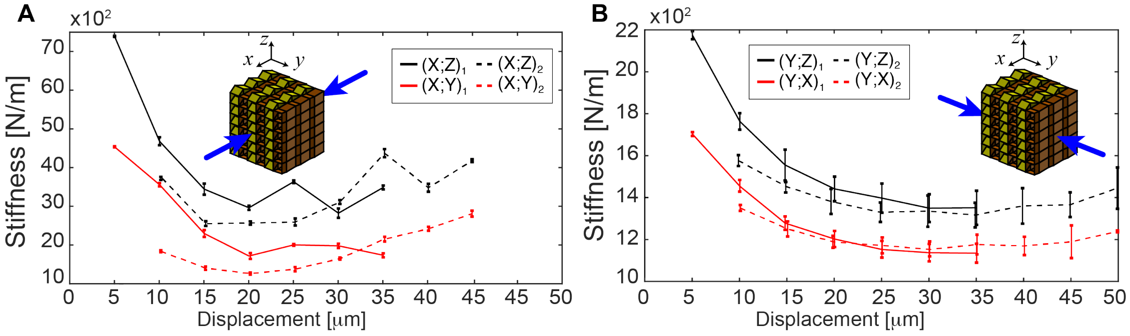

Figure 3.8: Stiffness relationships for non-monotonic loading of Configuration A samples. (A) Compression along x-direction of (X;Y)$_{1,2}$ and (X;Z)$_{1,2}$ samples. (B) Compression along y-direction of (Y;X)$_{1,2}$ and (Y;Z)$_{1,2}$ samples. Where sample (*i;k*)$_m$ corresponds to the samples being compressed along the *i*-direction and observed from the *k*-direction. Subscript m corresponds to the compression cycle.

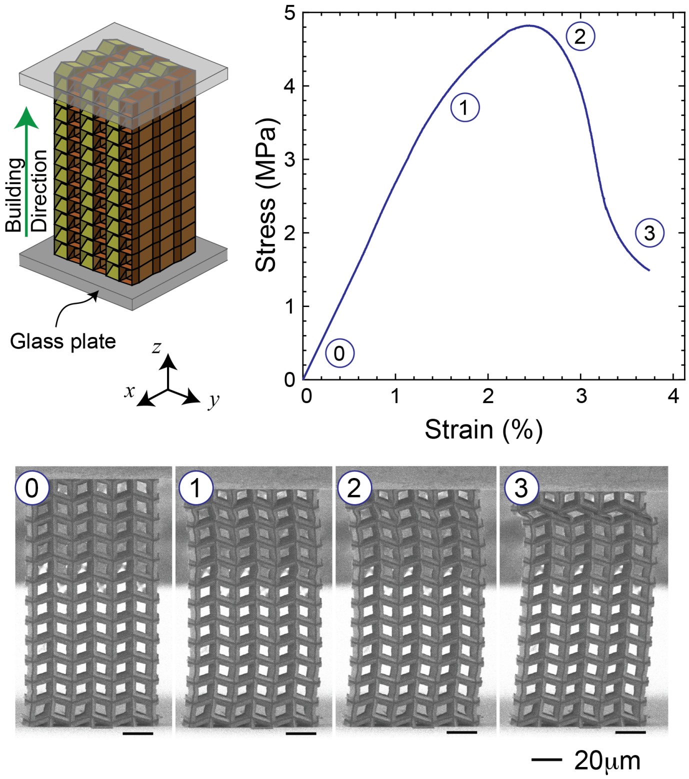

Figure 3.9: Stress-strain curves and SEM snapshots of Configuration A under monotonic compression loading along the unfoldable z-directions.

metamaterial with initial folding angle $\psi_0 < 40^\circ$, named Configuration B. We test the fabricated structure under axial monotonic load applied along the x-direction (Fig. 3.10(A)) and observe it along the z-direction. As the metamaterial is compressed, we measured both

Table 3.1: Measured Poisson's ratios for Configuration A

Compression/ Observation direction	(X;Z)	(X;Y)	(Y;Z)	(Y;X)
Poisson's ratio (ν)	$\nu_{xy} = -0.55$	$\nu_{xz} = 0.04$	$\nu_{yz} = -0.18$	$\nu_{xy} = 0.10$

axial and transverse strains along the x- and y-direction (Fig. 3.10). We observe that the transverse strain initially increases and is positive but subsequently decreases and becomes negative upon increasing compression (Fig. 3.10(B)). This marks a switching in the sign of the Poisson's Ratio ν_{xy} consistent with the kinematic model. Following the gradient definition of the Poisson's ration [47], the sign switch occurs at the peak of the transverse strain (point #2 in Fig. 3.10(B)), which occurs at a critical axial strain $\varepsilon_{crit} = 3.2\%$. Note that while both Configurations A and B exhibit auxetic behavior, the latter stands out because of its ability to exhibit reverse auxeticity.

3.4 Methods

3.4.1 Fabrication

The origami architected metamaterials were fabricated via 3D direct laser writing (DLW), two-photon polymerization technique (Nanoscribe, GmbH), employing a two-photon liquid photoresist (IP-DIP, Nanoscribe). The 3D DLW has a print resolution of 100nm in-plane and 300nm out-of-plane. The structures were printed on top of a glass slide. To enhance the adhesion between the metamaterial structure and the substrate, the glass slide (fused silica substrate) was cleaned using acetone and isopropyl alcohol ($p > 99.5\%$), followed by de-ionized water. A dip-in mode was used wherein a 63X objective lens was immersed into the polymer placed on the substrate (Fig. 3.11) where the metamaterial was vertically printed in a layer-by-layer fashion [48]. To attain high resolution, a writing speed of 50 μm/s and a femtosecond laser power of 4 mW were found to be optimal and used for fabricating the metamaterials. After printing, the structures were developed with

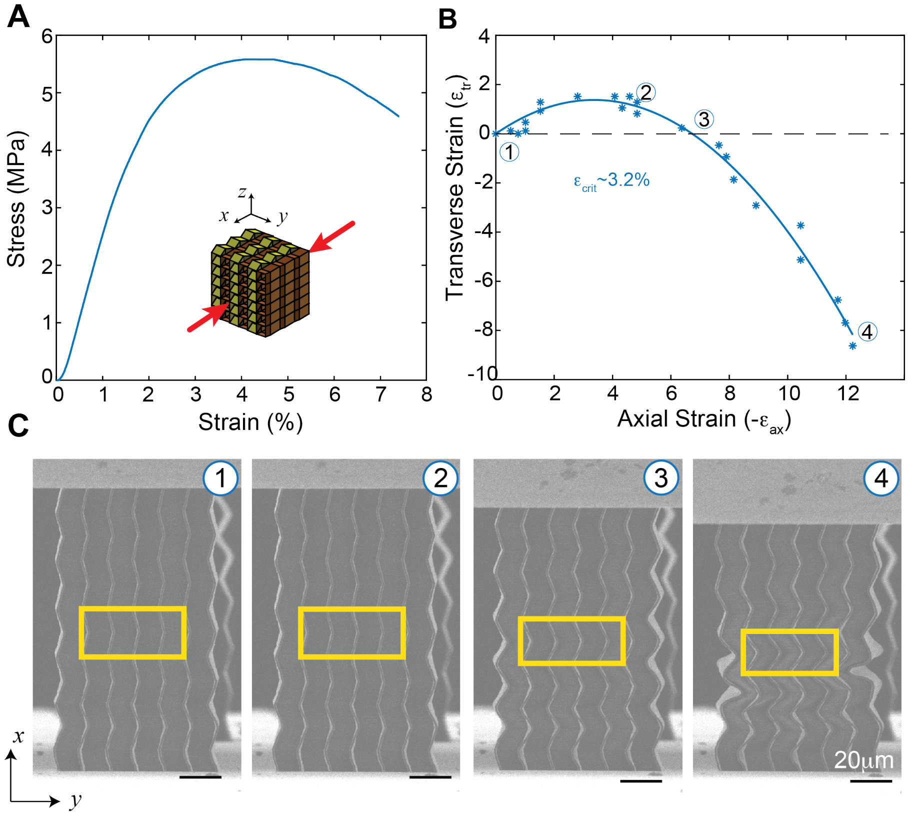

Figure 3.10: Strain dependent Poisson's ratio and reversible auxeticity of Configuration B ($\psi_0 = 40°$). (A) Stress-strain curves from the compression experiments. (B) Measured transverse and axial strains. (C) SEM snapshots correspondent of the points in (B). Yellow rectangles outlining the regions where Poisson's ratio was measured.

propylene-glycol-monomethyl-ether-acetate (PGMEA, $p > 99.5\%$) and rinsed with isopropyl alcohol. Finally, a critical point dryer (Tousimits, SAMDRI-795) was used to dry the structures in a controlled manner to avoid bending.

3.4.2 Mechanical Testing

In situ Scanning Electron Microscopy (SEM) compression tests were performed using a commercial Alemnis nanomechanical test platform (Alemnis AG) set up inside an FEI Nova 600 SEM (Fig. 3.12(A)). Both monotonic and oscillatory displacement profiles were programmed to be exerted by a piezo-driven actuator with a stainless-steel flat punch (1mm diameter). For the oscillatory scheme (Fig. 3.12(B)), applied only to Configuration A, initial loading-unloading cycles were performed with the objective of eliminating any possi-

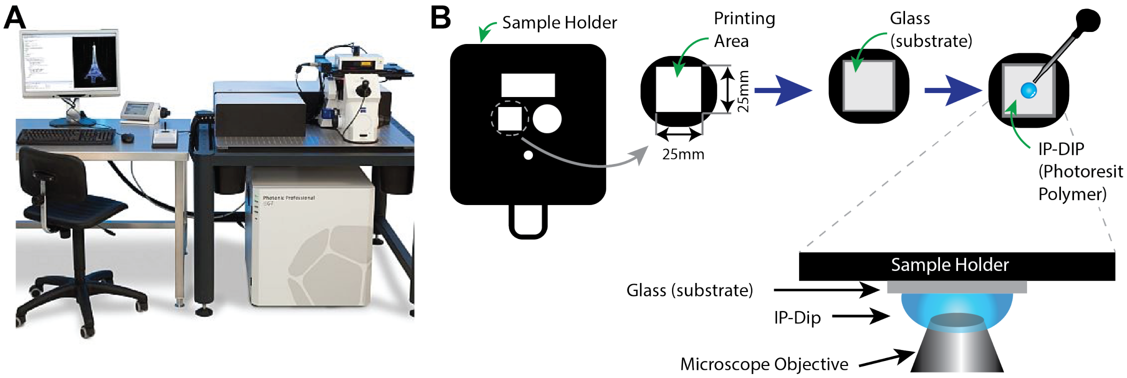

Figure 3.11: Schematics of the fabrication process.(A) Picture Nanoscribe Photonic Professional GT (image source [49]). (B) Schematics of the fabrication process.

ble hysteresis within the system. Subsequent steps sought to probe the structure's elastic response at different levels of compression. Within each load step, the amount of compressive displacement was first increased by $5\mu m$. Following a holding time of 10 seconds, the imposed displacement oscillated with an amplitude of $0.5\mu m$ for five cycles, followed by another 10 seconds of holding. The unloading portion of the five cycles at each compression level was used for stiffness calculations. In all cases, the flat punch speed was prescribed to be $0.1\mu m/s$, and the force was measured by a load cell with 1N capacity and 4μN resolution.

Configuration A specimens were tested under compression in the three orthogonal directions, labeled as x, y, and z in Fig. 3.2(D). For each Cartesian direction, two sets of structures were tested and imaged from different orientations. For instance, the structures compressed in the x-direction were observed from the y- and z-directions, denoted as (X;Y) and (X;Z), respectively. After a waiting time to allow for viscoelastic recovery, the structures compressed in the x- or y-direction were subjected to a second compression test. Numerical subscripts are used to differentiate the results of the first and second (post recovery) tests on a particular printed structure (e.g., $(X;Y)_1$ and $(X;Y)_2$). Configuration B specimens were compressed along the x-direction and observed from the Z-direction. Similar to Configuration A, two sets of samples were printed and in situ SEM tested.

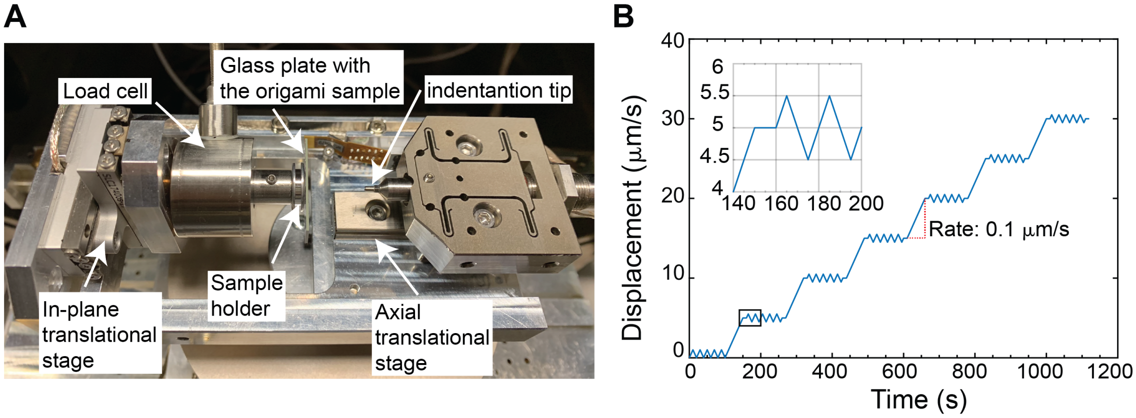

Figure 3.12: Scanning Electron Microscopy (SEM) Compression Tests. (A) Nanomechanical test platform. (B) Oscillatory loading profile.

3.4.3 Micropillar Compression Tests for Material Characterization

We fabricate micro-pillars via two-photon polymerization to characterize the photocured printing polymer's constitutive properties. The Micropillars have a nominal diameter of 8μm and a length-to-diameter ratio of 3:1 (Fig. 3.13(A)). Printing parameters (i.e., laser power, writing speed) and manufacturing steps remained consistent with those in the origami metamaterials' fabrication. The micropillar tests provided information on the nature of the cured polymer's compressive uniaxial stress–strain behavior. Micropillar compression testing was performed on five samples using the Alemnis (Alemnis AG) micromechanical test platform under in-situ SEM conditions, using displacement control at a nominal strain rate of $\approx 1x10^{-4}$ s^{-1} with a flat-tip diamond indenter. Yield stresses and strains were estimated using the 0.2% offset rule. Fig. 3.13(B) shows the stress–strain curves for the micropillar compression experiments described above. Table 3.2 summarizes the mechanical parameters obtained from each test and average values with the corresponding sample standard deviations.

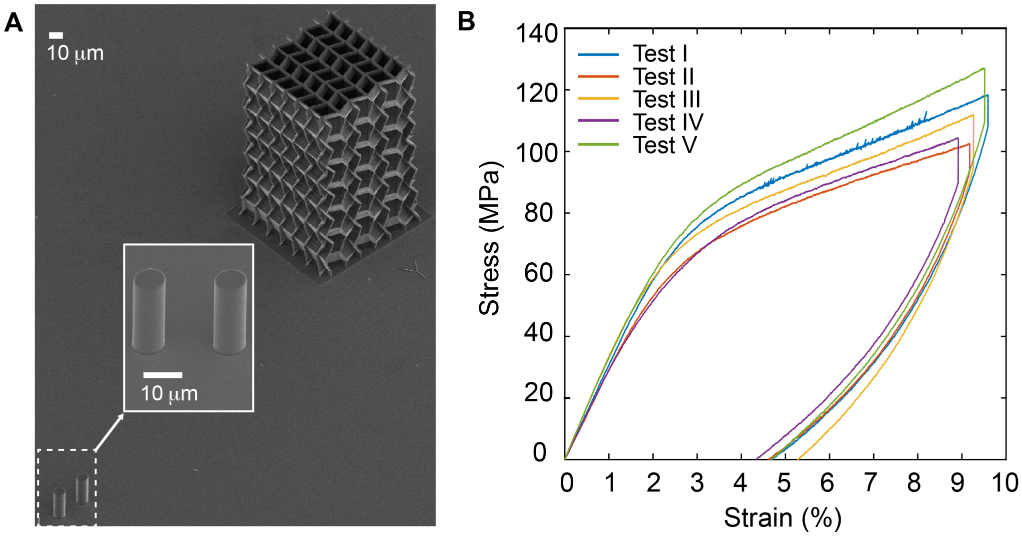

Figure 3.13: (A) Two-photon lithography printed IP-DIP (Nanoscribe, GmbH) micropillars for material mechanical characterization (B) Stress-strain curves from uniaxial compression tests.

Table 3.2: Material properties of IP-DIP from micropillar uniaxial compression tests

Young's Modulus (MPa)	Yield Stress (MPa)	Yield Strain	Tangent Modulus
3030.83	65.76	0.024	564.67
2910.20	53.84	0.021	465.83
3364.74	56.19	0.019	572.16
2860.14	51.50	0.020	502.20
3319.82	61.50	0.021	680.10
Average			
3097.15	57.76	0.021	557.00

3.5 Conclusion

Foldability, the core property underlying origami principles, is natural at the micro- and nanoscale because of reduced bending stiffness, as demonstrated in this Chapter. We have exploited the microscale features (e.g., plate thickness) enabled by two-photon direct laser writing to fabricate 3D origami metamaterials, have measured their mechanical properties using in situ SEM experimentation. The structures, based on the coupling of Miura-Ori tubes, constitute the smallest fabricated origami architected metamaterials exhibiting a combination of mechanical properties without precedents. As such, they promise to influence several applications across a wide range of fields encompassing the nano-, micro- ,and macroscales, leveraging the intrinsic scalability of origami assemblies. For example, in soft microbotics, structural components with highly anisotropic stiffness could be harnessed to carry payloads while maintaining degrees of flexibility for mobility and deployability. The microscale dimension of the developed metamaterials paves the way for applications in the field of medical devices (e.g., deployable stents, microsurgical instruments), energy harvesting (e.g., auxetic boosters), and other areas where size, shape-morphability, and deployability coupled with functionality are requisite attributes.

CHAPTER 4

CONTINUOUS-RANGE TUNABLE MULTI-LAYER FREQUENCY SELECTIVE SURFACES USING ORIGAMI AND INKJET-PRINTING

The tremendous increase in the number of components in typical electrical and communication modules requires low-cost, flexible and multifunctional sensing, energy harvesting, and communication modules that can readily reconfigure depending on changes in their environment. Current reconfigurable systems based on subtractive manufacturing offer limited flexibility (limited finite number of discrete reconfiguration states) and have high fabrication cost and time requirements. Thus, this chapter introduces an approach to solve the problem by combining additive manufacturing and origami principles to realize tunable electrical components that can be reconfigured over continuous state ranges from folded (compact) to unfolded (large surface) configurations. Special "bridge-like" structures are introduced across the crease lines and parallel to the traces, increasing their flexibility, thereby avoiding breakage during folding. These techniques allow creating truly flexible conductive traces that can maintain high conductivity even for large bending angles, further enhancing the states of reconfigurability. To demonstrate the idea, a Miura-Ori pattern is used to fabricate spatial filters – frequency selective surfaces (FSSs) with dipole resonant elements placed along the fold lines. The electrical length of the dipole elements in these structures changes when the Miura-Ori is folded, which facilitates tunable frequency response for the proposed shape-reconfigurable FSS structure. Higher-order spatial filters are realized by creating multi-layer Miura-FSS configurations, which further increase the overall bandwidth of the structure. Such multi-layer Miura-FSS structures feature the unprecedented capability of on-the-fly reconfigurability to different specifications (multiple bands, broadband/narrowband bandwidth, wide-angle of incidence rejection) requiring neither specialized substrates nor highly complex electronics, holding frames, or fabrication processes.

4.1 Introduction

Frequency selective surfaces (FSSs) have found many applications ranging from the design of radomes, reflectors, and spatial filters to reduction of antenna radar cross-section and realization of artificial electromagnetic bandgap materials [50, 51, 52]. FSS structures typically consist of a periodic arrangement of resonant elements on a thin sheet of substrate that reflect, absorb or allow certain electromagnetic waves to pass through them based on their frequency, thus exhibiting either bandpass or band-reject characteristics [53, 54, 55]. These characteristics have made them a subject of extensive research for the past five decades resulting in the evolution of their design from a simple planar array of 2D resonant structures to complex 3D resonant elements printed/etched on thin sheets of substrates [50, 56, 57, 58, 59].

The electromagnetic behavior of a single-layer FSS is primarily determined by the shape, size, and type of resonant elements, as well as their inter-element distances [50]. Moreover, the dielectric substrate's effects can be ignored if its thickness is less than $\lambda/100$, where λ is the wavelength. Typically, single-layer FSS structures suffer from poor selectivity and narrow bandwidth [50]. These characteristics are improved by using multi-layer configurations that are traditionally realized by either placing the resonant element on both sides of a thick substrate or using specialized frames to separate the FSS layer by the required distance [50, 60, 61]. Especially at higher frequencies, both techniques drastically limit the effective realization of the optimum frequency response in terms of the tunable frequency range, angle of incidence rejection range, and other standard performance parameters.

Traditional FSS structures are unable to tune their response according to the environmental changes over an almost continuous multitude of states. Typically, tunable FSS structures are realized by incorporating electronic components such as varactor-diodes [62] and

MEMS switches [63] or by changing the electrical properties [64, 65] or geometric configuration [66] of the substrate. However, these approaches become extremely expensive, laborious, and impractical as the size of the FSS is increased. To address this problem, origami-based structures have been proposed as a solution to create deployable continuous-state tunable structures, in which an origami pattern enables the change in the overall shape of the structure, thereby realizing on-demand reconfigurability [67, 68, 69, 4, 2, 70, 71, 72, 73, 74]. These properties make them a good candidate for terrestrial, outer-space, and electromagnetic cloaking applications over tunable frequency ranges, as well as morphing devices.

Previous work in origami-based FSS [75, 69, 76] has been dedicated to single-layer structures in which the resonating elements were realized by etching copper tape and manually placing them over the flat panels or the fold lines of the Miura-Ori pattern. Nevertheless, the copper tape is prone to peel off with humidity and high temperature, and the manual placement of the resonant elements is a laborious, inefficient, and non-repeatable procedure, limiting its use for practical applications. The unique "continuous-state" reconfigurability feature of a shape-shifting (origami-based) structure can only be fully exploited if the utilized resonators are highly flexible and their shape changes along with the underlying origami structure. Also, a repeatable and accurately controlled manufacturing technology is required. Thus, a preliminary single layer prototype of a Miura-FSS has been realized by inkjet-printing [77], in which the flexible conductive lines are printed using silver nano-particle ink [78].

The folding-induced reduction of the electrical length of the dipole resonators in the FSS structures implies that, without changing the physical length of the dipoles, the folding introduces an additional degree of continuous state reconfigurability through an increase in effective capacitance to the bandstop Miura-FSS structure, resulting in a resonant frequency shift to higher values. Besides, because the Miura-Ori has a negative in-plane Poisson's ratio [42, 1], it proportionally reduces the resonators' electrical length as well as their inter-element spacing to enable a continuous state tunability without the use of any electronic component. Furthermore, it is also a developable pattern (that is, it can be developed from a single 2D sheet) that enables the realization of a full 3D-FSS from a 2D-FSS structure, thereby enhancing the portability while significantly reducing the metalization complexity and the cost typically required by the conventional 3D-FSS structures.

Single-layer Miura-FSS implementations typically result in narrow bandstop frequency responses, limiting their use in practical applications. Thus, this paper introduces two multi-layer Miura-FSS configurations (Fig. 4.1), the mirror stacking and the inline stacking, that feature "on-demand" broad bandwidth with a wide-angle of incidence stability (Figs. 4.2, 4.3). These configurations eliminate the need for a holding frame or a thick dielectric substrate to maintain an accurately controlled inter-layer distance as required by conventional multi-layer FSS structures [50]. Each layer consists of a cellulose paper with inkjet-printed dipole elements folded in the Miura-Ori pattern (Fig. 4.1). Fully inkjet-printed multi-layer tunable Miura-FSS structures are demonstrated and compared with the single-layer Miura-FSS limited performance.

The remainder of this chapter is organized as follows. First, we introduce the geometry of the Miura-FSS unit cell for single- and multi-layer configurations. Next, we present and discuss the frequency response of these structures obtained from an integrated experimental and simulation-based investigation. In addition, we correlate the response of the proposed structures with the intrinsic geometry of the unit cell to provide a systematic methodology for using this approach in applications with arbitrary reconfigurability requirements over a continuous range. We conclude with some final remarks.

4.2 Miura-Ori Based FSS Assemblages

The Miura-Ori pattern has been extensively studied [1, 42] and has found many applications in engineering [79, 9, 4, 2, 80]. Thus, it has been selected as the basis for our origami-based FSS investigation. The Miura-Ori is defined by the geometry of the unit cell rhombic-shaped panels, which are characterized by two lengths, a and b, and the panel angle α (Fig. 4.1(D)). Under assumption of rigid origami model, this pattern features one degree of freedom, meaning that we can fully describe its kinematics using the unit cell intrinsic geometry and one of folding angle, here defined as the dihedral angle θ.

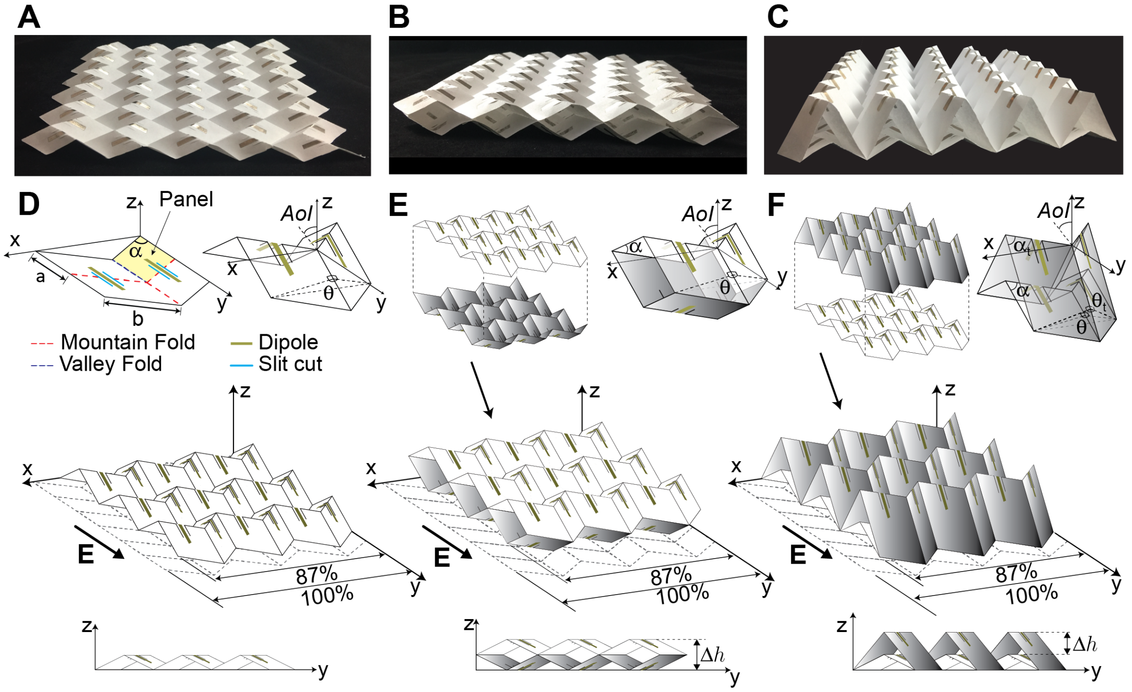

Figure 4.1: Design, assembly, and response of an origami-FSS with dipole elements of dimension 20x2 mm. Prototype of (A) single-layer, (B) mirror-stacked, and (C) inline-stacked Miura-FSS. (D) Miura-FSS unit cell with $a = b = 20$ mm, $\alpha = 45^\circ$ and its folded configuration with folding angle θ. (E) Assembly of two identical Miura-Ori layers ($a = b = 20$ mm, $\alpha = 45^\circ$) into a mirror-stacked configuration and its unit cell. (F) Assembly of two Miura-Ori layers into an inline-stacked configuration and its unit cell, where the intrinsic geometry for the "white" unit cell is defined as $a = b = 20$ mm, $\alpha = 45^\circ$, and for the "shaded" unit cell as $a = 23.3mm$, $b = 20mm$, $\alpha = 52^\circ$. The electric field **E** on the same direction of the dipole elements.

A typical single-layer Miura-FSS consists of a single sheet of the Miura-Ori pattern with two dipole elements per unit cell (Fig. 4.1(A,D)). In this work, the dipole elements are inkjet-printed over the mountain folds and centered along length b to demonstrate the realization of highly flexible conductive traces, which is an essential requirement for origami-inspired tunable electrical/RF structures over a continuous range of states. Dipoles are fundamental electromagnetic structures that help us fully understand the frequency behavior of a Miura-FSS across folding states.

By stacking two Miura-FSS sheets, we realized two multi-layer configurations: the mirror multi-layer stacking (Fig. 4.1(B,E)) and the inline multi-layer stacking (Fig. 4.1(C,F)). The former consists of two identical Miura-FSS layers connected along the valleys in a mirror fashion, and the latter consists of distinct and kinematic compatible layers [1] connected along the valley folds. Both stacking types preserve the flat-foldability and in-plane kinematics of the Miura-Ori (see Appendix A, Section A.1), which is described as a function of the intrinsic geometry and dihedral angle θ (shown in Fig. 4.1(D-F)).

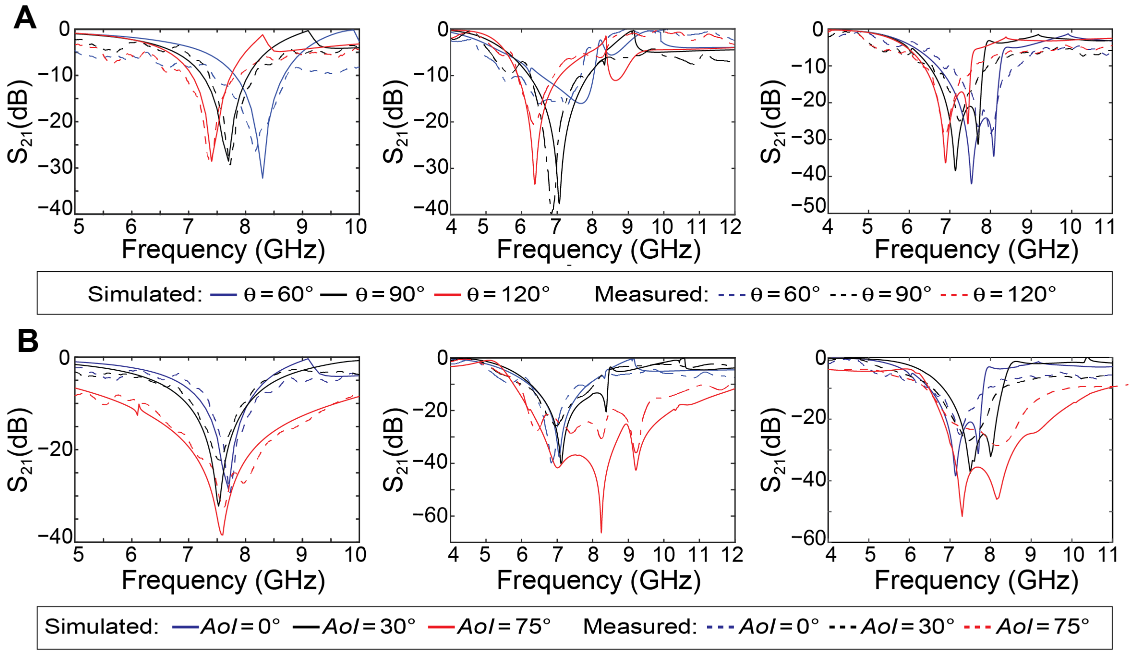

Figure 4.2: (A) Frequency response in terms of transmission coefficient S_{21} for the single-layer, mirror-stacked, and inline-stacked Miura-Ori shown in Fig. 4.1 for folding angles $\theta = 60^\circ, 90^\circ, 120^\circ$ corresponding to extensions of 50%, 71%, 87%, respectively; and considering a perpendicular angle of incidence (*AoI*) and (B) for folding angle $\theta = 90^\circ$ (i.e. 71% extension) and *AoI* = $0^\circ, 30^\circ, 75^\circ$. The electric field **E** on the same direction of the dipole elements.

4.3 Results and Discussion

The single-layer Miura-FSS structure along with its two multi-layer configurations were designed and simulated in Ansys HFSS. To exploit the periodic nature of the Miura-FSS

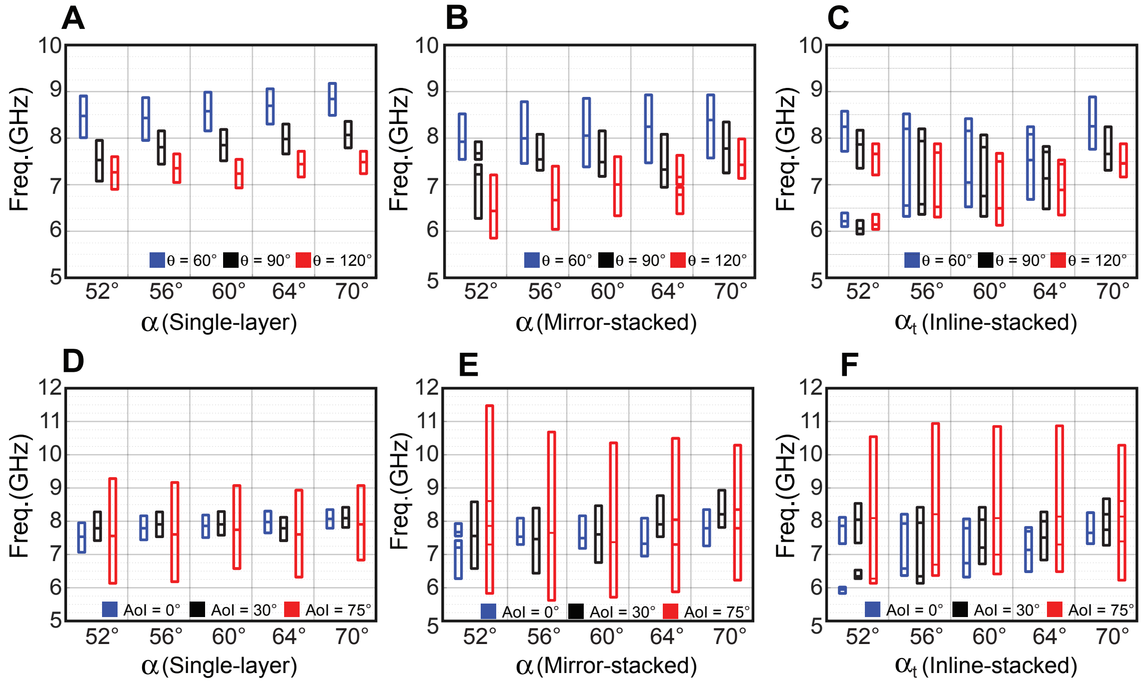

Figure 4.3: Simulated response of the Miura-Ori based FSS, in which the internal lines represent the resonant frequency, and the top and bottom lines represent the cut-off frequencies at -10 dB. Response of the FSS structures with distinct panel angles $\alpha = 52°, 56°, 60°, 64°, 70°$ (in the case of inline-stacking, $\alpha = \alpha_t$, i.e. the angle α for the top layer). (A-C) For a specific angle of incidence $AoI = 0°$ and distinct folding angles $\theta = 60°, 90°, 120°$ for single-layer, mirror-stacked, and inline-stacked Miura-FSS, respectively; (D-F) For a specific folding angle $\theta = 90°$ and distinct $AoI = 0°, 30°, 75°$ considering single-layer, mirror-stacked, inline-stacked Miura-FSS, respectively.

structure while saving computational time and resources, for each configuration, only the unit cell (shown in Fig. 4.1(D-F)) was simulated using master/slave boundary conditions and Floquet port excitation [5]. The simulation results were verified by a bi-static measurement setup consisting of two broadband horn antennas placed in the line-of-sight to each other with the fabricated Miura-FSS structure placed in the middle. To ensure uniform folding angle throughout the Miura-Ori based FSS structure and minimize measurement errors, we 3D printed specialized frames to hold the FSS structures at different folding angles. As shown in Fig. 4.2(A), the simulated and measured insertion loss (S_{21}) for the single and the two multi-layer Miura-FSS configurations display good agreement with each other.

The simulated frequency response for the three Miura-FSS configurations with respect to different folding angles (θ) and panel angles (α) is shown in Fig. 4.3. All Miura-FSS structures resonate at a higher frequency as the folding angle (θ) is decreased. This is because of the reduction in the effective electrical length of the dipole elements as they morph from a flat configuration to a V-shape structure as the Miura-FSS structure is folded. It is also interesting to note here that while the single-layer Miura-FSS structure has a single resonant frequency with a narrow bandwidth ($\leq 15\%$), the two multi-layer Miura-FSS structures feature multiple resonance behavior to realize much broader bandwidth. The frequency response of a typical Miura-FSS can be easily changed on-demand by varying the folding angle (θ) for a given panel angle (α).

Figure 4.2(A) shows that the inline-stacked Miura-FSS configuration features two operating frequencies (modes). The lower frequency is mainly determined by the coupling between the two layers (coupling mode), while the higher frequency is determined by the size of the resonant dipole element and the folding angle (resonant mode). At lower values of the panel angle (α_t), the change in effective interlayer distance is negligible compared to the wavelength of the resonant mode frequency, which results in the same coupling mode frequency for different folding angles. Moreover, the overall electrical length of the dipole element is reduced by decreasing the folding angle (θ), thereby causing a shift in resonant mode frequency to higher values. However, the coupling mode frequency also changes with different folding angles for higher values of α_t since the change in the interlayer distance becomes comparable to the resonant mode frequency. The two resonant frequencies merge at $\alpha_t = 70^0$, which indicates strong coupling between the two layers as shown in Fig. 4.3(C). Furthermore, the inline-stacked Miura-FSS structure features a very stable angle of incidence (*AoI*) frequency response as shown in Fig. 4.3(F). That is, the change in resonant frequency is relatively small and can be compensated by larger filter bandwidth at higher *AoI* [50]. An exception occurs at panel angles that feature weak coupling between the two layers (e.g., $\alpha = 52°$).

In contrast to the inline-stacked Miura-FSS, the inter-layer distance for mirror-stacked

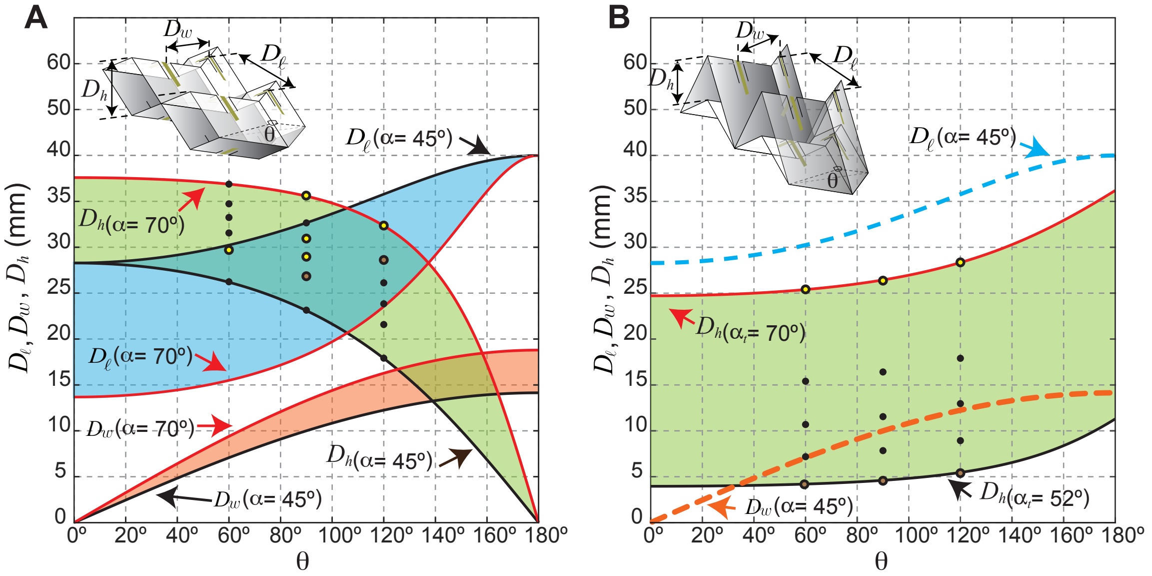

Figure 4.4: Relation between folding angle θ and dipole distances D_w, D_ℓ and Δh for the mirror-stack and inline-stack of the Miura-FSS. (A) For the mirror stacking of identical layers, the shades represent the range of the curves for panel angles α between 45° and 70°. The green, blue and orange shades represent how Δh, D_ℓ, and D_w, respectively, vary with respect to α. (B) For the inline stacking, the green shade represents the variation of Δh for panel angles α_t (subscript t refers to the top layer) between 52° and 70°. The blue and orange dashed lines represent the distances D_ℓ and D_w between the dipoles of the top and bottom layers. In both figures, the yellow dots represent the configurations in which percentage bandwidth $\leq 15\%$ (comparable to single layer Miura-FSS) while black dots represents configurations which can realize broader bandwidth ($> 15\%$), and brown dots represent configurations with multi-band and multi-resonant frequency.

Miura-FSS increases as folding angle θ decreases. This behavior is illustrated in Fig. 4.4, which shows how the distances between the resonant elements change depending on panel angle α and folding angle θ (see Appendix A, Section A.1). By comparing the interlayer distance (Δh) plots for the two multilayer configurations, we see that mirror-stacking offers a relatively higher variation in Δh, causing the structure's frequency response to be more sensitive to the folding angle as opposed to the inline-stacking configuration. However, the optimum inter-layer distance for a given α is difficult to achieve in the mirror configuration for all folding angles θ. Typically, the structure would have a strong resonance with wide bandwidth when $\Delta h \leq n\lambda/2$, where n is a positive integer. In contrast to in-line stacking configuration, mirror-stacked Miura-FSS has good *AoI* rejection only at lower values of α

($\leq 60°$). Because of poor inter-layer coupling at higher values of α, we get unstable *AoI* rejection as shown in Fig. 4.3(E).

4.4 Methods

4.4.1 Sample fabrication

We fabricated each layer of the Miura-FSS by perforating the Miura-Ori pattern on 0.11 mm-thick cellulose paper with a mechanical cutting machine (Silhouette CAMEO, Silhouette America) that perforates and cuts the origami pattern on the paper. The pattern had 6×5 unit cells in the x- and y-directions, respectively. These cells were a modified version of the Miura-Ori unit cell, in which we included slit cuts with no perforation between them to realize "bridge-like" structures that allow for the inkjet-printed dipoles to smoothly bend over the fold lines, thereby avoiding cracks or breakage in the conductive trace during folding (Fig.4.5(A))

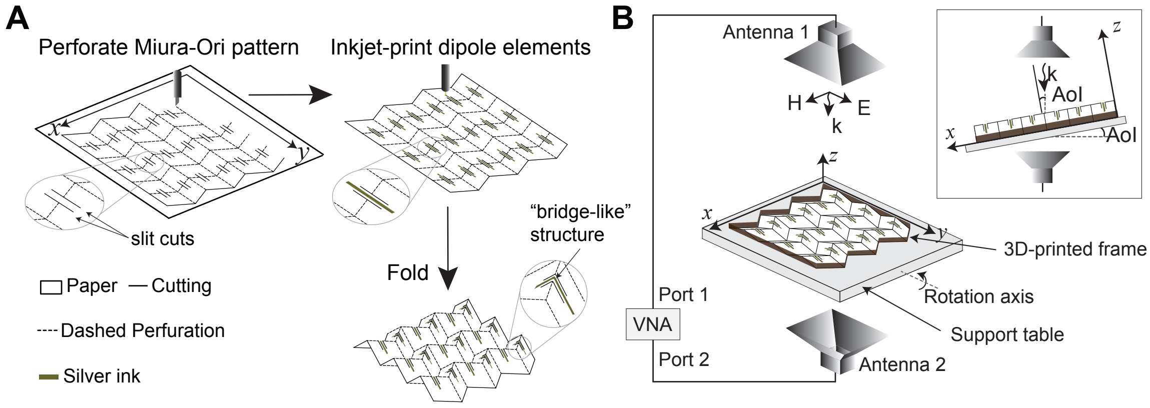

Figure 4.5: Schematics of the general fabrication process and experimental setup. (A) Schematics of the fabrication process of each Miura-FSS layer, which consists of the perforation of the modified Miura-Ori pattern, inkjet-printing of the dipole elements, and manual folding of the pattern. (B) Schematics of the experimental characterization setup. The top box shows a side ("plane of incidence") view of the setup, where *AoI* (angle of incidence) represents how much we tilted the support table, reflecting the relative angle between the incident waves and the normal to the FSS structure plane.

4.4.2 Experimental testing

We tested each prototype in three geometric configurations. For accuracy, we used 3D printed frames to shape the prototype into the desired folding angles ($\theta = 60°, 90°$ and $120°$). Each test consisted of placing the prototype with the 3D printed frame between two horn antennas in the line-of-sight. We attached the horn antennas to a vector network analyzer (VNA), to measure the S_{21} (transmission coefficient) values of the three Miura-FSS configurations. The frequency response of the structures with respect to the folding angle was measured for only normal incidence ($AoI = 0°$). While the angle of incidence rejection capability of the structures was measured by keeping the folding angle fixed ($\theta = 90°$) and rotating the support table about the rotation axis (Fig. 4.5(B) and Fig. A.3).

4.4.3 Mechanical Properties of the Cellulose Paper

The bending stiffness of the panels (K_B) and folding stiffness of hinges (K_F) are essential mechanical properties that dictate the behavior of the Miura-Ori pattern. Thus, to characterize those quantities for the fabricated Miura-FSS, we test individual panels and hinges made of 0.11mm-thick cellulose paper. For the test, we use a custom-build testing bed (detailed description in Appendix B) that mainly consists of a frame with a fixed plate that is attached to the load cell and a movable plate that is responsible for applying displacement (Fig. 4.6). We attach a 3D printed force arm to the fixed plate, and to the movable plate, we attach a spacer. The spacer is responsible for holding the sample and providing clearance for the sample to fold/bend. The spacer and the force arm are placed 20 mm apart (in the x-direction).

To measure the bending stiffness of the panels (K_B), we test five samples with a single 40x20 mm panel surrounded by folded tabs. Those tabs simulate the existence of surrounding panels. We attach one side of the panel to the spacer and apply a total displacement of 5 mm in the y-direction (Fig. 4.7). The spacer moves with the movable plate and presses the sample against the force arm. The arm is attached to the load cell that measures the

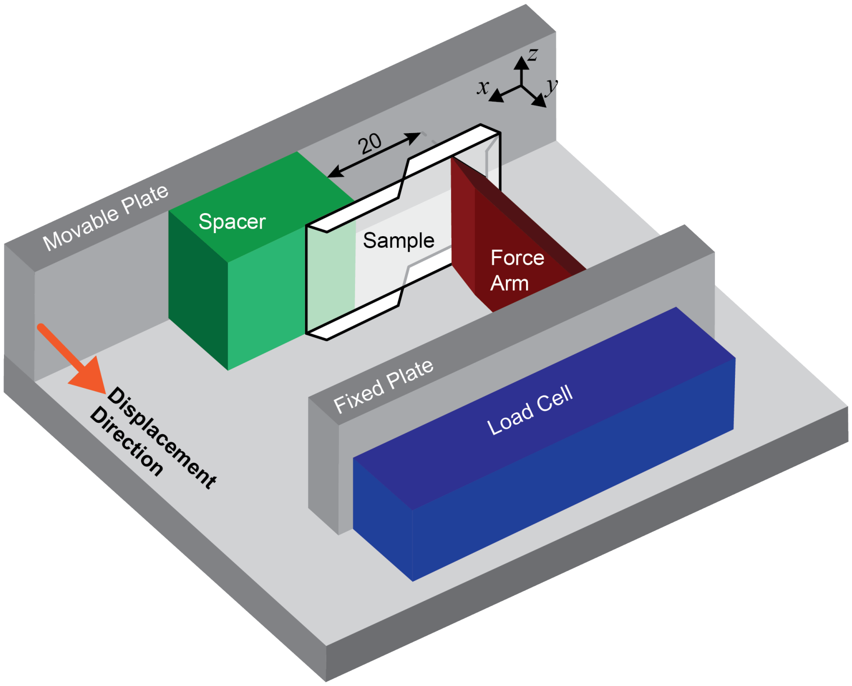

Figure 4.6: Testing setup for the characterization of the bending stiffness of the panels (K_B) and folding stiffness of the hinges (K_F). Distance is shown in mm.

reaction force (F).

For the measurement of the folding stiffness of the hinges (K_F), we test five samples with two 20x20 mm panels. Those panels are also surrounded by folded tabs and are connected by a single hinge. The hinge was fabricated with the same dashed perforation as the Miura-FSS samples. Before the test, each hinge is completely folded and unfolded to the initial position shown in Fig. 4.7. Similar to the panels' test, we attached the sample to the spacer and applied a total displacement of 10 mm in the y-direction.

For each increment of applied displacement (Δu) and measured force (F), we calculate the moment M at the bending/folding regions and the rotation angle ψ as

$$M = d_x F, \quad \psi = \tan^{-1}\left(\frac{u_0}{d_x}\right) - \tan^{-1}\left(\frac{u_0 - \Delta u}{d_x}\right) \tag{4.1}$$

where d_x is the distance between the crease/bending line and the force arm (i.e., $d_x = 10$ mm), and u_0 is the initial distance between the force arm and the spacer in the y-direction.

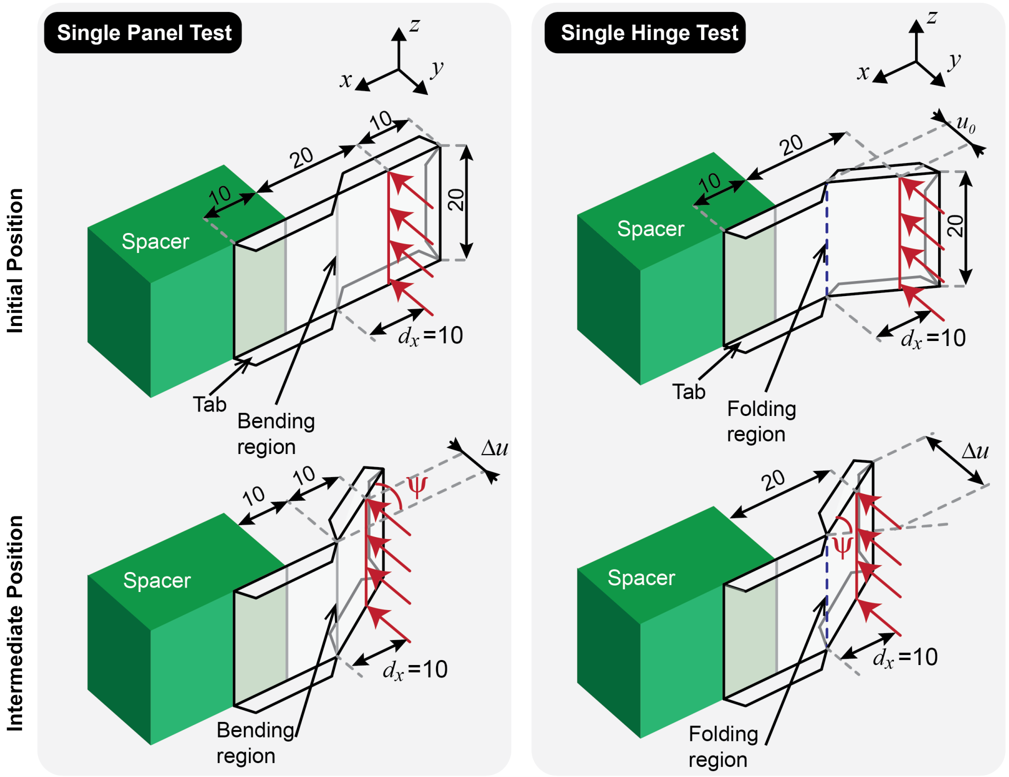

Figure 4.7: Schematics of the single panel (left) and single hinge (right) test for characterization of the bending and folding stiffness, respectively. Here we show only the spacer holding the samples in the initial (top) and intermediate (bottom) position. The red arrows and line represent the region where the displacement is applied (i.e., where the force arm touches the sample). Distances are shown in mm.

For the measurements of bending stiffness, $u_0 = 0$ and for the folding stiffness, $u_0 = 5$ mm.

Fig. 4.8 shows the moment-rotation diagrams of one panel and one hinge sample. From the slope of the fitted curve, we obtained the stiffness of each sample. Table 4.1 shows the stiffness per unit length for each sample. We average the stiffness values and obtained the stiffness ratio $K_r = K_B/K_F = 3.3$. This ratio will be used for the mechanical simulation of the Miura-FSS.

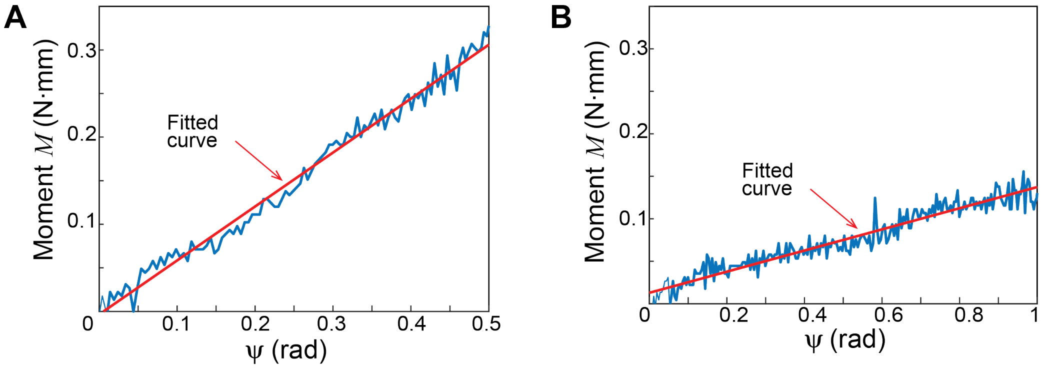

Figure 4.8: Moment M vs. rotation angle ψ of one (A) panel sample and one (B) hinge sample made of cellulose paper. The measured data is plotted in blue lines, and the red lines represent the linear regressions. From the slope of the red line, the rotational stiffness is obtained.

Table 4.1: Cellulose Paper Properties

K_B $\left(\text{N·mm(rad·mm)}^{-1}\right)$	R_B^2	K_F $\left(\text{N·mm(rad·mm)}^{-1}\right)$	R_F^2
0.02432	0.9800	0.01211	0.8734
0.02604	0.9417	0.00602	0.8926
0.02533	0.9631	0.00622	0.9212
0.02630	0.9707	0.01263	0.8959
0.02497	0.9536	0.00478	0.8713
Average			
0.025391	0.96182	0.008353	0.89088

4.4.4 Bar and Hinge Simulation Using Merlin Software

To simulate the electromagnetic response of the Miura-FSS, we assumed that the fabricated structures have the same kinematics as a rigid Miura-Ori. To show that this is a reasonable assumption, we simulate the in-plane mechanical behavior of the fabricated Miura-FSS and compare it to the rigid origami behavior, which is analytically described by the kinematic equations provided in Appendix A, Section A.1.

We simulate the in-plan folding motion of the Miura-FSS using the Merlin software

[81, 82, 83], which is a nonlinear implementation of the bar-and-hinge model [84]. Following the bar-and-hinge discretization, each crease line is modeled as a bar with rotational springs along its length. Similar bars are also added along the panels shortest diagonals (Fig. 4.9(A)). Those additional bars provide an approximation to the bending behavior of the panels. The major material parameter for this analysis is the stiffness of the rotational springs. For the bars that represent the crease lines, the rotational stiffness corresponds to the hinges' folding stiffness (K_F). For the diagonal bars, the rotational stiffness corresponds to the bending stiffness (K_B) of the panels. Note that both values were obtained from the material characterization in section 4.4.3.

To simulate the same folding motion necessary for the reconfigurability of the proposed Miura-FSS, we apply the boundary conditions shown in Fig. 4.9(B) and impose a displacement to the boundary nodes on the right. The total imposed displacement is equivalent to the change in the folding angle from $\theta = 120°$ to $\theta = 60°$ (i.e., total displacement of -62.12 mm in the x-direction). The final configuration (equivalent to $\theta = 60°$) is shown in Fig. 4.9(C), where the brown lines represent the initial configuration. Fig. 4.9(D-F) shows the final configuration obtained from the simulation for single-layer, mirror, and inline stacking, where the red lines represent the position of the crease lines under a rigid origami assumption (i.e., calculated following the parametrization in Eq. A.1). We observe that the boundary unit cells do not behave as rigid origami, but the unit cells in the middle present a behavior close to a rigid origami. Thus, in Fig. 4.9(G-I), we quantitatively compare the values for the parameters calculated from Eq. A.1 and Eq. A.3 (red column) with the parameters measured for each unit cell. The green and blue columns represent the minimum and maximum values obtained from the Merlin simulation, respectively. The percentages indicate the difference between the values obtained from the simulation and the values from Eqs. A.1 and A.3.

Fig. 4.9(J-L) shows the stored energy, where the red line represents the total stored energy. The shaded areas represent the portion of the energy of the hinge folding (red), panels bending (blue), and stretching of the crease lines (magenta). For the single-layer Miura-FSS, we observe that a small portion of the energy corresponds to bending and stretching, while for the multi-layer structures, those are negligible, indicates that deformations occur mainly at the hinges.

4.5 Concluding Remarks

In this work, we created Miura-Ori-based FSS multi-layer structures that feature the unprecedented capability of on-the-fly reconfigurability to different specifications (multiple bands, broadband/ narrowband bandwidth, wide-angle of incidence rejection). By combining additive manufacturing and origami principles, we achieve tunable electrical components that can be reconfigured over continuous state ranges from folded (compact) to unfolded (large surface) configurations on cellulose paper. The use of a highly porous substrate along with the “bridge-like” structures allows the realization of truly flexible resonant elements that maintain high conductivity even for large bending angles, further enhancing the states of reconfigurability. The dipole elements’ electrical length in these structures changes when the Miura-Ori is folded, which is the tuning mechanism for the shape-reconfigurable response of the FSS structure.

We remark that the present approach applies to other developable and non-developable tessellations. Furthermore, multi-layer origami-based-FSS can be developed from layers of tessellations with compatible in-plane kinematics [85], such as Miura-Ori derivatives [86, 87] and kirigami patterns [88, 89]. In addition, the mirror-stacking FSS could be explored considering layers with different intrinsic geometry. In this case, the maximum distance between resonant elements could be better controlled, such that the distance among the resonant elements is finite (no inter-penetration) as the stacked configuration unfolds.

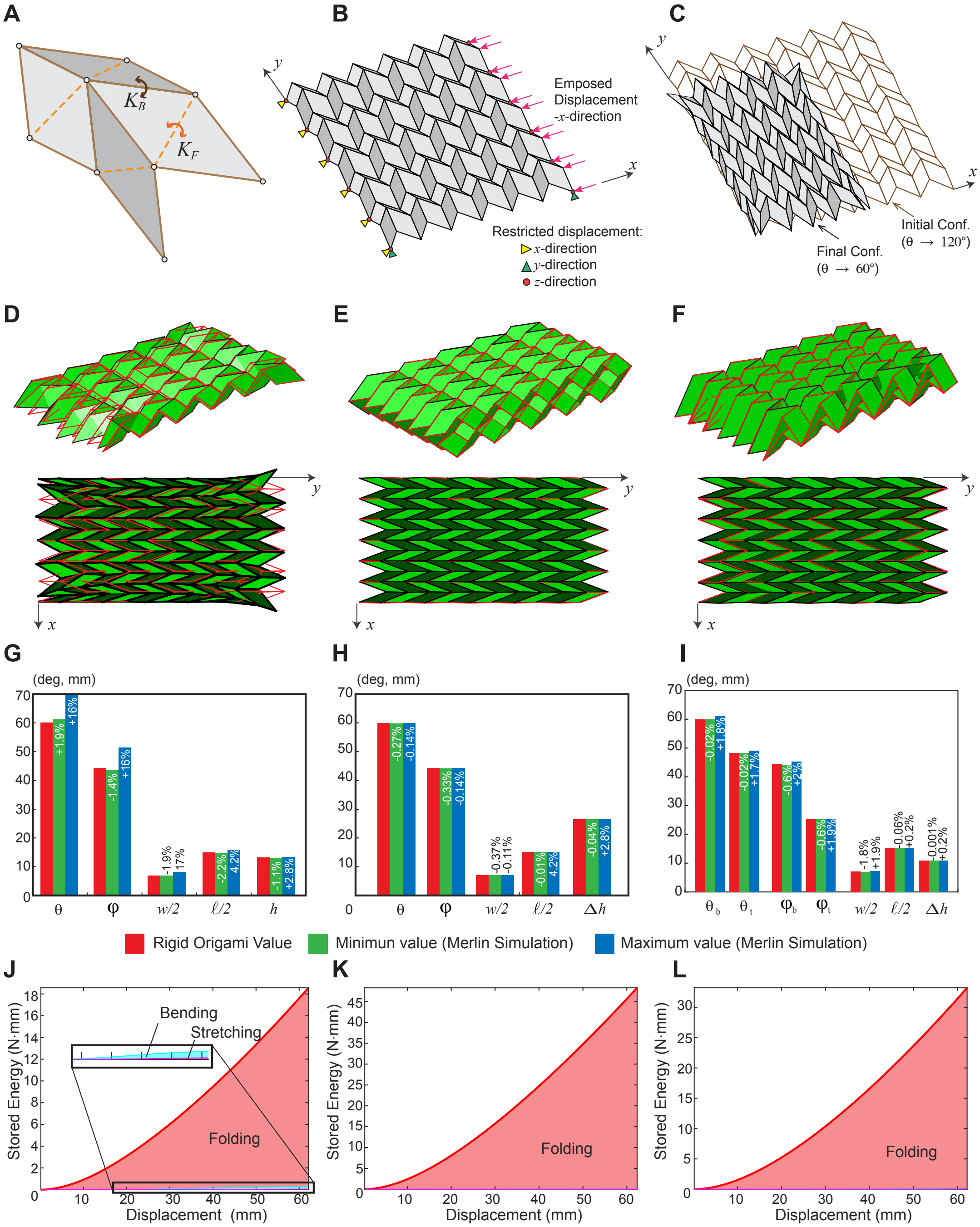

Figure 4.9: Mechanical simulation of the Miura-Ori pattern. (A) Discretization of the unit cell using the bar and hinge model. (B) Applied Boundary conditions. (C) Final configuration after applied displacement from $\theta = 120°$ to $\theta = 60°$. Final configuration of the (D) Single layer and (E) mirror-stacking with $a = b = 20$ mm and $\alpha = 45°$, and (F) Inline-stacking with $a_b = b_b = 20$ mm, $\alpha_b = 45°$ and $\alpha_t = 60°$, where the red lines represents the configuration assuming a rigid origami behavior. (G-I) Comparison of the unit cell parameters for the rigid origami assumption, and Merlin simulation. (J-K) Plot of the stored energy.

CHAPTER 5

UNTETHERED CONTROL OF FUNCTIONAL ORIGAMI MICRO-ROBOTS WITH DISTRIBUTED ACTUATION

Deployability, multifunctionality, and tunability are features that can be explored in the design space of origami engineering solutions. These features arise from the shape-changing capabilities of origami assemblies, which require effective actuation for full functionality. Current actuation strategies rely either on slow, or tethered or bulky actuators (or a combination). To broaden applications of origami designs, we introduce an origami system with magnetic control. We couple the geometrical and mechanical properties of the bi-stable Kresling pattern with a magnetically responsive material to realize the untethered and local/distributed actuation with controllable speed, which can be as fast as a tenth of a second with instantaneous shape locking. We show how this strategy facilitates multi-modal actuation of the multi-cell assemblies, in which any unit cell can be independently folded and deployed, allowing for on-the-fly programmability. In addition, we demonstrate how the Kresling assembly can serve as a basis for tunable physical properties and for digital computing. The magnetic origami systems are applicable to origami-inspired robots, morphing structures and devices, metamaterials, and multifunctional devices with multiphysics responses.

5.1 Introduction

Origami applications take advantage of the shape change capabilities to create tunable, deployable, and multifunctional systems. Naturally, shape changing systems require proper actuation. Unfortunately, the lack of a robust solution for shape actuation is one of the barriers to widespread use of origami-based engineering solutions. While many applications focus on mechanical [20] and pneumatic [16, 17, 18, 19] actuations, those solutions result in bulky assemblages with excessive wiring. Although other solutions exist, where thermo- [21, 22, 13], humidity- [24], and pH-responsive [23] materials are adopted, the actuation speed of the shape transformation is significantly limited by the slow response rate of the materials and/or actuation sources.

By means of origami engineering, kinematic shape change can be synergistically integrated with mechanical instabilities to devise functional mechanisms [90, 91, 19, 92]. Such instabilities may arise from non-rigid foldable patterns with an unstable deformation path leading to a stable state, representing multi-stability and an instantaneous shape locking [17, 2]. The Kresling pattern [93] is an example of a geometrically bi-stable pattern that can be spontaneously generated on a thin cylindrical shell under axial and torsional load, displaying a natural coupling between axial deformation and rotation. For a bi-stable Kresling, the bi-stability represents an instantaneous shape locking of the pattern in the two stable states, which are achieved either by axial forces or torques that are superior to the energy barrier between states. When composed of axially assembled N unit cells, the Kresling assembly can effectively accomplish tremendous height shrinkage, while possessing the capability of achieving 2^N stable states if each unit cell is actuated locally (e.g., Fig. 5.1). Because of those properties, this pattern has been used in several applications, such as metamaterials [94, 95], robot [20], and wave propagation media [96]. However, under currently available actuation methods (e.g., motors, pressure, shape memory polymers, and hydrogels), those Kresling structures are limited by slow actuation or bulky wiring systems. Further, local/distributed control requires multiple actuation sources as well as multiple controllers, leading to increased system complexity.

Recently, magnetic-responsive materials have emerged as a promising alternative for shape control [97, 98], as it allows for untethered ultra-fast and controlled actuation speed, as well as distributed actuation [99, 100]. The magnetic untethered control separates the power source and controller out of the actuator by using field-responsive materials, making applications possible at different scales (e.g., macro, micro, and nano). These features pro-

Figure 5.1: The sixteen stable states of a four-cell Kresling assembly.

mote magnetic actuation as an ideal solution for origami shape transformation, as explored in this chapter. Thus, we attach magnetic-responsive plates to the Kresling unit cells for the application of torsion to a level that triggers the bi-stable state transition (Fig. 5.2(A)). This torsional force is instantaneously generated in the presence of an external magnetic field **B**, which causes the plate to rotate while trying to align its programmed magnetization **M** with **B**. For multi-cell Kresling assembly with a magnetic plate attached on each unit cell, different magnetic torque intensities and directions can be exerted by distinguishing the magnetization directions of the magnetic plates. The unit cells can be actuated simultaneously or independently by utilizing different magnetic torques of the magnetic plates and distinct geometric-mechanical properties of each unit cell. Further, the magnetization directions change with the states of the multi-cell assembly, allowing multi-modal distributed actuation by controlling just the magnetic field.

The remainder of this chapter is organized as follows. First, we present and discuss the design and actuation of the Kresling pattern using different strategies. Next, we provide two

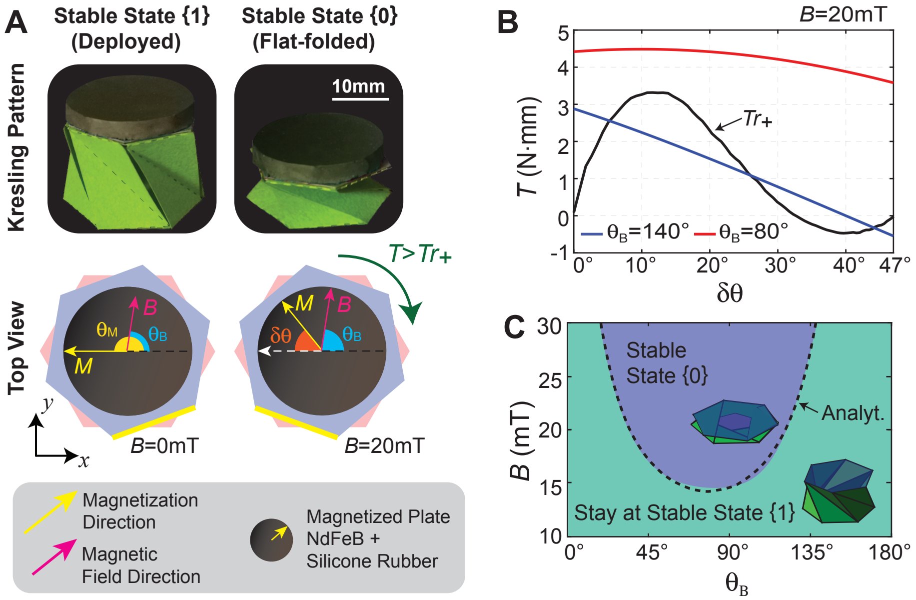

Figure 5.2: Magnetic actuation of the Kresling pattern. (A) Kresling pattern with a magnetic plate at deployed and folded states, where θ_B is the direction of the applied magnetic field $\mathbf{B}$, θ_M is the direction of the plate magnetization $\mathbf{M}$, and $\delta\theta$ is the rotation angle controlled by $\mathbf{B}$. (B) Torque required to fold the unit cell and magnetic torque versus plate rotation angle $\delta\theta$ at given $\mathbf{B}$. (C) Contour plot of the analytical and measured results showing whether the unit cell will switch from stable state $\{1\}$ to stable state $\{0\}$, depending on the direction θ_B and intensity B. Dashed line represents the analytical prediction.

examples of applications of the magnetically actuated Kresling: (1) a Kresling assembly with tunable mechanical property; and (2) a magneto-mechano-electrical Kresling pattern for digital computing. Then, we conclude with final remarks.

5.2 Results and Discussion

5.2.1 Geometry and Magnetic Actuation

The Kresling pattern is a non-rigid foldable origami, meaning deformation is not restricted only to folding hinges but also involves bending and stretching of both panels and hinges. This non-rigid behavior is what allows for unit cell bi-stability. Although, theoretically, all geometrically designed Kresling unit cells present bi-stability, the material plays an important role in whether or not this behavior will be observed in the fabricated unit cell.

Thus, to guarantee bi-stability, the design of the pattern parameters (panel angle α, and lengths a and b in Fig. C.1) are guided both by geometric relations [101] and computational mechanics simulations [81] (Appendix C, Section C.1, Table C.1). The Kresling unit cells are fabricated with cut-relieved hinges [102], that is, we replace diagonal mountain folds by cuts (Fig. C.1). In each unit cell, we add a magnetic-responsive plate with volume V and a programmed magnetization $\mathbf{M}$, whose direction is always in the plane of the plate. In the presence of an external magnetic field $\mathbf{B}$, a magnetic torque $\mathbf{T} = V(\mathbf{M} \times \mathbf{B})$ is generated, which tends to align the plate magnetization direction θ_M with the magnetic field direction θ_B. Note that the direction of the applied magnetic field is also in the plane of the plate so that the induced magnetic torque causes a rotational motion of the plate around the longitudinal axis of the Kresling unit cell. This motion twists the unit cell by an angle $\delta\theta$.

Fig. 5.2(A) shows a single unit cell that folds under a clockwise magnetic torque. Because the unit cell is bi-stable, an energy barrier has to be overcome for the switch from stable state $\{1\}$ (deployed) to $\{0\}$ (folded). We experimentally quantified this energy barrier by obtaining the required torque to fold the unit cell (black curve in Fig. 5.2(B)) via a uniaxial compression (see Methods Section 5.3.3). The magnetic torque has to be both clockwise and larger than the required torque ($Tr+$) for the unit cell to fold. The magnetic torque T with clockwise as the positive direction is computed as $T = BMV \sin(\theta_M - \theta_B)$, where B is the magnetic field intensity, M is the magnetization intensity of the magnetic plate (Appendix C, Section C.2.2), and both directions θ_B and θ_M are defined with respect to the x-axis. Taking the case with magnetization direction $\theta_M = 180°$ at the deployed state, as an example, the Kresling pattern folds when the provided magnetic torque is larger than the required torque during the entire folding process (red curve in Fig. 5.2(B) with $B = 20$mT and $\theta_B = 80°$). Note that the magnetic torque varies during the rotation of the magnetic plate. If the applied magnetic torque is smaller than the required torque at any angle during the entire folding process (blue curve in Fig. 5.2(B) with $B = 20$mT and $\theta_B = 140°$), the Kresling pattern will fail to achieve the folded state and will return

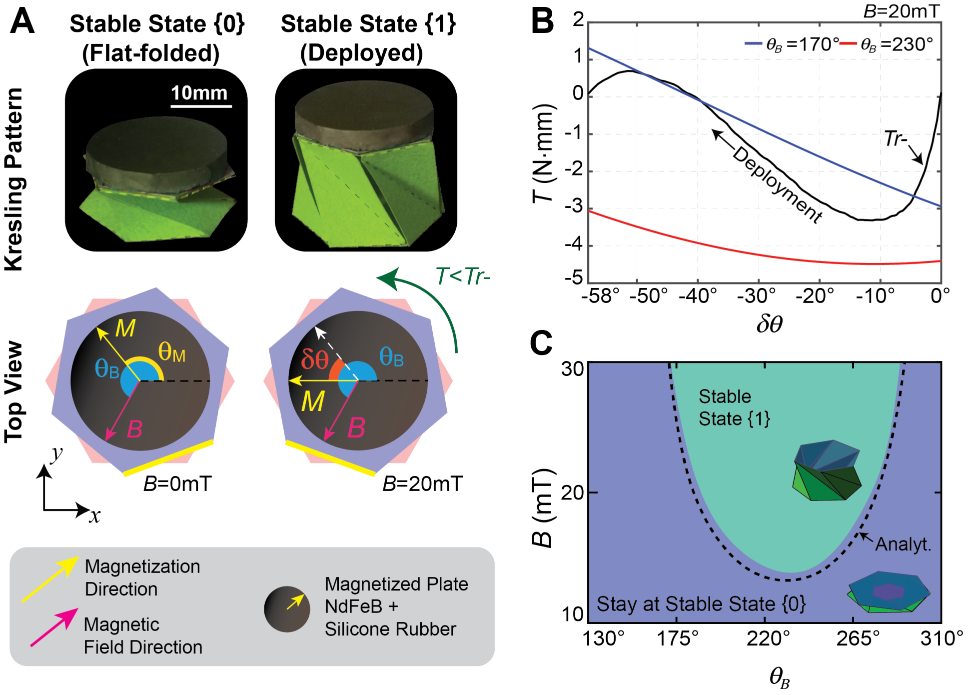

Figure 5.3: Magnetic actuation of the Kresling pattern ($H = 18.2\text{mm}$) from folded state $\{0\}$ to deployed state $\{1\}$ (A) Schematic of the actuation process, where $\theta_B = 240°$ is the direction of the magnetic field $\mathbf{B}$, and the magnetization $\mathbf{M}$ has direction $\theta_M = 129°$. (B) Torque $Tr-$ is required to switch the unit cell stable state, and the torques produced by the magnetic actuation versus the rotation angle $\delta\theta$ (C) Contour plot of the experimental and analytical results for the deployment, showing if the unit cell will switch from stable state $\{0\}$ to stable state $\{1\}$, depending on the direction of the magnetic field θ_B and intensity of the magnetic field B.

to the deployed state when the magnetic field is removed. Because of the tunability of the magnetic field, the actuation speed can be controlled as fast as a tenth of a second. Fig. 5.2(C) shows the required actuation condition (combination of B and θ_B) to fold the Kresling from state $\{1\}$ to $\{0\}$ (Appendix C, Section C.3). For the deployment of the unit cell (switching from state $\{0\}$ to $\{1\}$), a counterclockwise torque $T < Tr-$ throughout the rotation is required. Fig. 5.3 shows the deployment process and required actuation condition.

5.2.2 Distributed Actuation

Rationally designing the individual magnetization on each unit cell of the Kresling assembly allows a distributed torque to be introduced along the longitudinal axis of the assembly and under the applied magnetic field. To explain the concept, Fig. 5.4 show the actuation of a two-cell assembly with equivalent geometries. The global states are defined by a binary code $\{ij\}$, with *i* and *j* denoting the bottom and top unit cells, respectively. For example, global state $\{10\}$ corresponds to the state in which the bottom unit cell is deployed and the top unit cell is folded. Each unit cell behaves differently because of the different magnetization directions of the attached magnetic plates (e.g., 0° and 90° at the folded state $\{00\}$). Tailoring the intensity and direction of the magnetic field, we can precisely actuate the two-cell assembly from, and to, any of the four stable states. In Fig. 5.4, we provide the top view of the unit cells as the assembly switches from the stable state $\{00\}$ to the other three stable states under a 20mT magnetic field.

Starting *from state* $\{00\}$, when a 20mT magnetic field is applied at $\theta_B = 120^\circ$, the torque generated is enough to deploy the bottom unit cell, but not the top one, leading *to a new stable state* $\{10\}$. Note that the torque generated on the top unit cell is determined only by the top magnetic plate, while the torque acting on the bottom unit cell is the vector summation of the magnetic torques from both magnetic plates. Thus, only the bottom unit cell can change state, rotating by $\delta\theta_1$, making the top unit cell rotate with it by rigid body motion (i.e., $\delta\theta_2 = \delta\theta_1$). *From Global State* $\{00\}$ *to* $\{01\}$, the change of state occurs under a magnetic field with intensity $B = 20$mT and direction $\theta_B = 240^\circ$. In the bottom unit cell, the magnetic field induces a clockwise magnetic torque that is opposite to the rotation direction for deployment, preventing the state change ($\delta\theta_1 = 0$). While, in the top unit cell, the magnetic field induces a counterclockwise torque larger than the required torque (i.e., $T < Tr-$), leading to the unit cell deployment with a rotation $\delta\theta_2$. *From Global State* $\{00\}$ *to* $\{11\}$, the change of state occurs under a magnetic field with intensity $B = 20$mT and direction $\theta_B = 180^\circ$. In both bottom and top unit cells, the magnetic field induces a

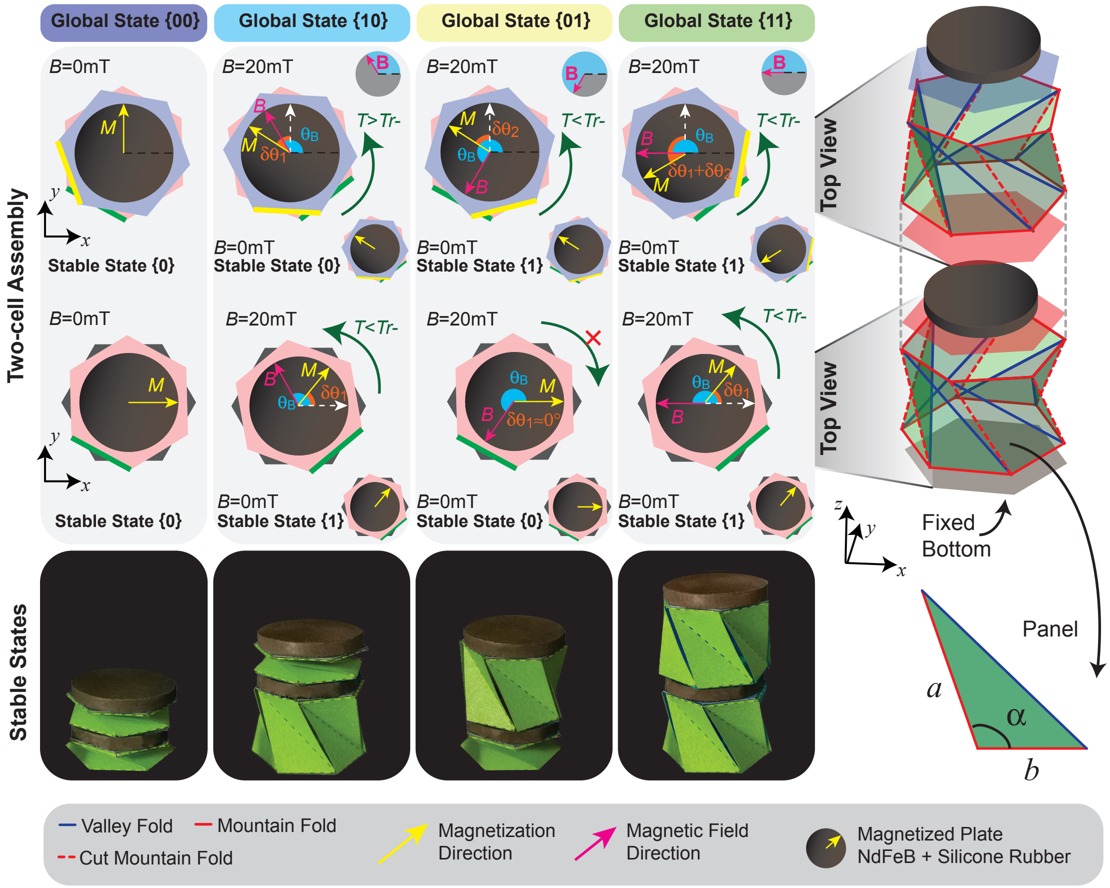

Figure 5.4: Schematics of the magnetic actuation of a two-cell Kresling assembly. The first column represents the initial state of the unit cells and the other three columns show the three different stable states of the assembly after the magnetic actuation. The parameters $\delta\theta_1$ and $\delta\theta_2$ denote the rotation angle of the bottom and top unit cells, respectively. In each column, the corner insets represent the unit cell state after the magnetic field is removed. $Tr+$ and $Tr-$ represent the required torques to fold and deploy the unit cell, respectively. The red cross (on the third column) denotes that the rotation is constrained by the geometry.

counterclockwise torque larger than the required torque (i.e., $T < Tr-$). Thus, the bottom unit cell rotates by $\delta\theta_1$ and the top unit cell rotates by $\delta\theta_1 + \delta\theta_2$. Fig. 5.5(A) shows the contour plot of the magnetic field direction and the intensity needed to keep the global state at $\{00\}$ or to switch to any of the three other stable states (i.e., states $\{10\}$, $\{11\}$, and $\{01\}$). Fig. 5.5(B-D) shows the contour plots for the actuation starting from the stable states $\{10\}$, $\{11\}$, and $\{01\}$, which provides guidance to achieve sequential deformations from a specific state to the others.

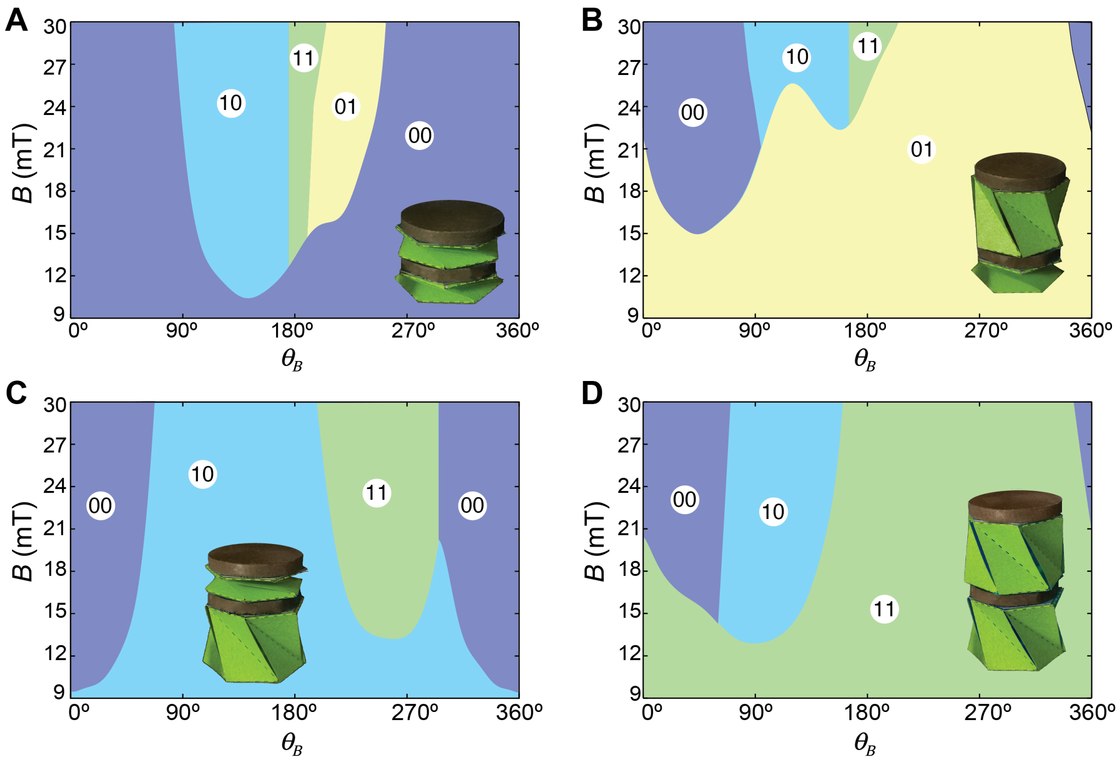

Figure 5.5: Contour plots for the experimental measurements of the magnetic actuation of the two-cell Kresling pattern with same crease direction (Fig. 5.4). Actuation starts from global (A) state $\{00\}$, (B) state $\{01\}$, (C) state $\{10\}$, and (D) state $\{11\}$.

Based on the concept of distributed actuation, we can theoretically achieve 2^N stable states from a Kresling assembly with N unit cells. This multi-stable assembly therefore enables large number of state shifting, which can be further explored for multifunctional applications such as tunable physical properties and logic computing that will be discussed in the following sections.

5.2.3 State Shifting of Kresling Assembly

Taking advantage of distributed actuation, we explore the multiple state shifting behavior of the Kresling with enhanced programmability by assembling unit cells with reverse creases. As shown in Fig. 5.6(A), two assembled unit cells are chiral to each other and have opposite folding rotational direction. The orange unit cell folds under clockwise (CW) rotation, while blue unit cell folds under counterclockwise (CCW) rotation. As an example, we show in Fig. 5.6(B) a four-cell Kresling assembly with chiral unit cells (blue-orange-blue-orange) in which we can program the actuation of the achiral groups (represented by same colors) to fold/deploy together. This strategy also allows for two global actuation modes: (1) purely rotational modes in which the change in global state occurs without axial displacement (represented by switching between states $\{1010\}$ and $\{0101\}$ in Fig. 5.6(B)); and (2) purely axial modes in which the change in global state occurs without the change in global rotation (for example, switching between states $\{1111\}$ and $\{0000\}$ in Fig. 5.6(B)). This occurs because the rotation of the pair of chiral unit cells cancels each other, leading to no rotation between the polygonal panels in the two extremities. The distributed actuation allows us to achieve the fully and selectively folded/deployed states even though we control the unit cells in groups. All the reported actuation strategies are possible because of the local response of the magnetic plates under the two-dimensional magnetic field generated by the setup in Fig. 5.6(C). The setup consists of two pairs of coils along the Cartesian x- and y-directions. Inside the coil assembly, the samples are attached to an acrylic base that kinematically restricts one of the ends, leaving the other end free for any type of displacement. In Fig. 5.6(D), we show the contour plots with the measured actuation parameters (B and θ_B) needed to cyclically switch states $\{11\}$, $\{01\}$, $\{00\}$, $\{10\}$. Although some transformations cannot be attained directly, the actuation actually closes a loop, meaning that we can actuate the Kresling assembly to all the possible global stable states via the ultra-fast magnetic actuation method by controlling applied magnetic field intensity and direction.

5.2.4 Distributed Actuation for Tunable Physical Property

The aforementioned discussion focuses on the Kresling assemblies with the same unit cell geometry (same required torque and energy barrier between stable states). Since their multi-cell assemblies can shift between states under the distributed actuation, we geometrically engineer the energy barriers needed to fold/deploy each unit cell to achieve tunable physical property. In our designs, the polygon size and type are fixed, and only the height

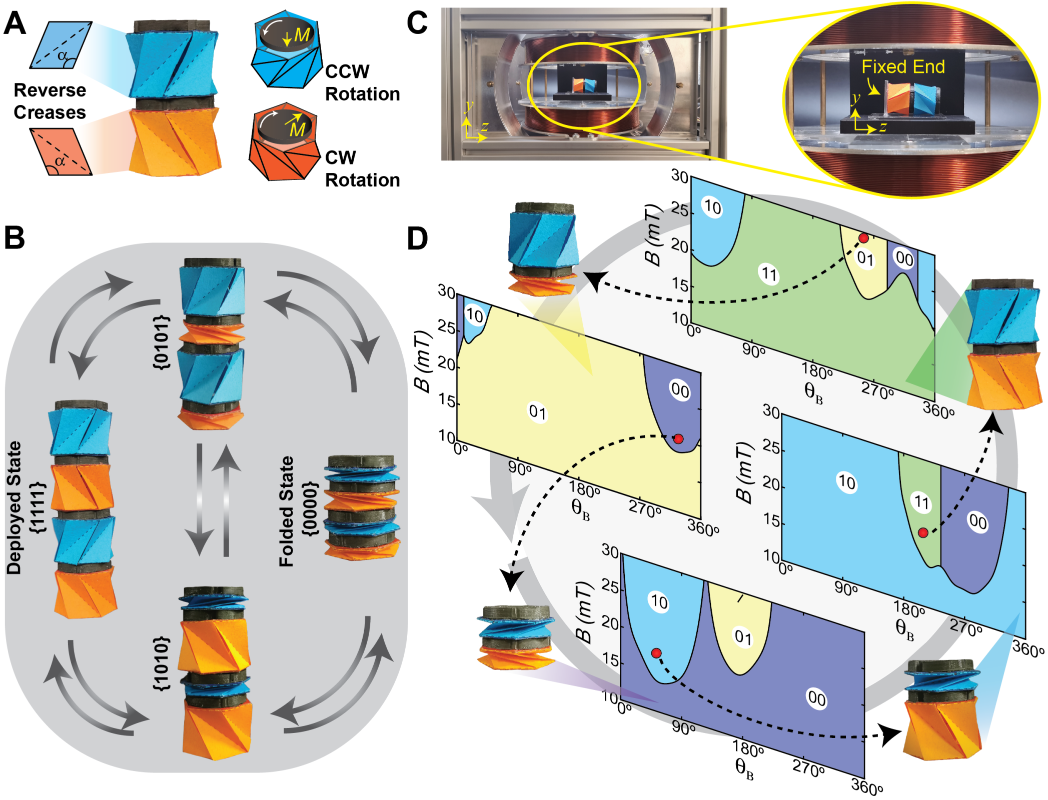

Figure 5.6: Magnetic actuation of generalized reverse creases Kresling assemblies with multiple cells. (A) Two-cell Kresling assembly with reverse creases. (B) Sequential magnetic actuation of unit cells with reverse creases. (C) Magnetic actuation setup used to provide the two-dimensional magnetic field. (D) Magnetic actuation of multi-cell assembly with reversed creases leading to cyclic switch of states {11}, {01}, {00}, {10}, {11}, ... etc. Each contour plot provides the set of actuation parameters (B and θ_B) needed to switch the unit cell from one stable state to the other.

of the unit cell in the deployed state is changed to tune the required energy barrier effectively. From those constraints, the crease pattern parameters are computed (Appendix C, Section C.1). The increase in height relates to the increasing of the energy barrier between states, as shown by the experimentally measured force-displacement curves (Fig. 5.7(A)) and the computed stored energy (Fig. 5.7(B)) of the unit cells under the axial compression load (Methods Section 5.3.2). The samples are fixed at the bottom, which restricts both rotation and axial displacement, and are entirely free at the top (see inset in Fig. 5.7(A)). Because of the specific boundary conditions (fixed-free ends) of the test, we do not obtain (measure) negative forces. Instead, the null forces in Fig. 5.7(A) indicate that the unit cell snaps and loses contact with the load cell. Although the test gives no information about the unit cell during the snapping process, it provides the stored energy before the snapping point and the height change between the states of each unit cell. The initial slope of the force-displacement curve can be further used to calculate the stiffness of each unit cell. From the uniaxial compression, we obtain the required torque needed to actuate each unit cell design (Methods Section 5.3.3, Fig. C.8), which guides the parameter design of the magnetic actuation. Fig. 5.7(C) shows the contour plots with the analytical and experimental values for the actuation parameters. It can be seen that the actuation of unit cells with higher energy barrier requires larger B, meaning that we can use distinct energy barriers for the actuation, where the wide range of magnetic field intensity allows for the local control of assemblies with a larger number of unit cells (e.g., $N > 4$).

The assembly of geometrically different unit cells enables tunable mechanical properties under the distributed magnetic actuation. Because each unit cell presents distinct stiffness, we can conceptualize the assembly as springs in series and compute the system's stiffness in each one of the global states, where the Kresling units are selectively folded/deployed. Fig. 5.7(D) shows the experimental force-displacement curve for the four-cell assembly. In this plot, we observe a sequential compression of the unit cells. In the first linear region, we characterize the stiffness K at the all-deployed state $\{1111\}$. Similarly, we characterize the stiffness of the assembly at the other states and report it in Fig. 5.7(E) together with the theoretical values (See Appendix C, Section C.1.3). From this figure, we observe that by using the proposed distributed actuation, we can tune the stiffness of the assembly by switching between stable states.

5.2.5 Multifunctional Origami for Digital Computing

Origami systems have recently been explored for digital computing because of the potential applications in intelligent autonomous soft robots, integrating the capabilities of actuation, sensing, and computing in the origami assemblies, acting as either basic logic gates [24]

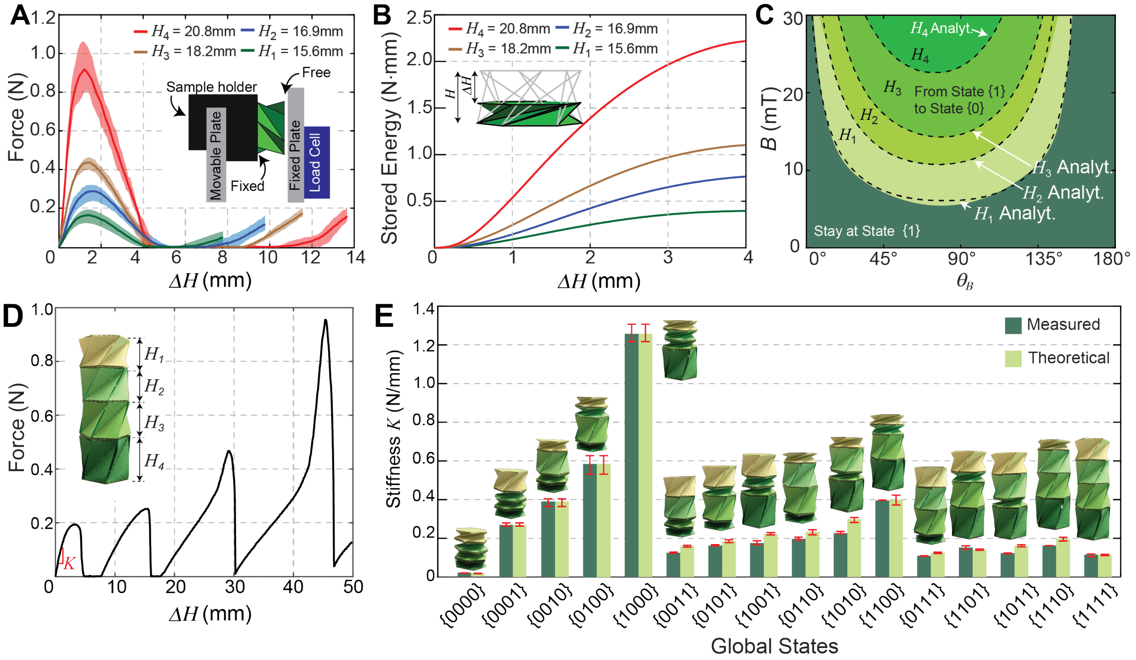

Figure 5.7: Tunable mechanical response of a multi-cell Kresling assembly. (A) Measured force-displacement curves for unit cells with distinct heights. Solid lines represent the average responses and shaded envelopes delimit maximum and minimum response ranges. The inset shows the schematic of the compression setup with fixed-free boundary conditions. (B) Stored energy versus axial displacement, obtained from the averaged force-displacement curves prior to snapping. (C) Contour plot with measured and analytical (dashed lines) conditions for the magnetic actuation depending on each unit cell geometry. (D) Measured force-displacement curve for a four-cell Kresling assembly in the stable state $\{1111\}$. (E) Tunable mechanical response of the four-cell Kresling assembly. From multiple consecutive testing cycles, we obtain the average (columns) and maximum/minimum (error bars) stiffness of the assembly. Theoretical values are approximated by a system of springs in series (see Appendix C, Section C.1.3).

or integrated memory storage devices [95]. The multifunctional origami can eliminate the requirement of conventional rigid electronic components and its stiffness mismatch with compliant origami bodies. The bi-stable nature of the Kresling pattern shows its potential in representing a binary system for digital computing, introducing multifunctionality into our Kresling system that goes beyond structural actuation. To develop a multifunctional Kresling assembly, we employ a magneto-mechano-electric device that incorporates actuation and computing capabilities, which could be further extended to sense external stimulation. The operation of the assembly is based on the distributed actuation of the

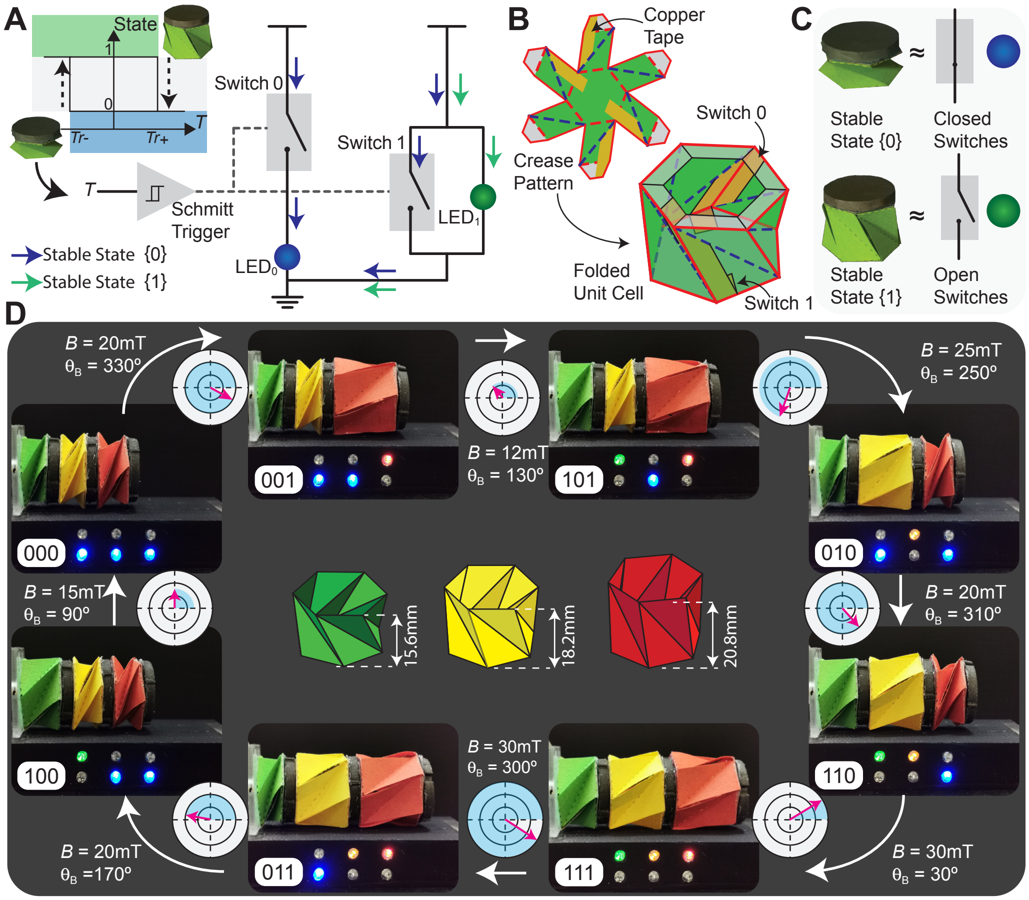

Figure 5.8: Origami logic circuit with LED (A) Schematics of the electric circuit of a single unit cell, where the arrows show the current direction depending on the state of the unit cell. If the unit cell is deployed, both switches are open and the current follow the green arrows, turning on the green light. Otherwise, the switches are closed, and the blue light is on. (B) Schematics showing the placement of the copper tape inside the crease pattern and folded unit cell. (C) Schematic showing how the state of the unit cell controls whether both switches are open or closed. (D) Demonstration of the logic circuit on a multi-cell pattern with unit cells with distinct energy barriers.

Kresling unit cells with distinct, geometrically designed, energy barriers. By treating the applied magnetic torque as the input signal and digitizing the resultant mechanical states of the Kresling pattern as digital output $\{1\}$ (deployed state) or $\{0\}$ (folded state), it can be regarded as a Schmitt Trigger (Fig. 5.8(A)), a basic comparator circuit to convert analog input signal to a digital output signal. The higher and lower thresholds of the "Origami Schmitt Trigger" are the required torques ($Tr+$ and $Tr-$) to change the stable state of the unit cell. Blue and green LEDs are used to represent the folded and deployed stable states, respectively. To construct the circuit, copper tape is attached inside the unit cell to form two switches (Fig. 5.8(B)). Switch 0 is connected to the blue LED in series and Switch 1 is connected to the green LED in parallel (Fig. 5.8(A)). Starting from the deployed state, when $T > Tr+$, the unit cell changes to the folded state $\{0\}$ and both switches are closed (blue paths in Fig. 5.8(A)). The green LED is short-circuited and only the blue LED is turned on (Fig. 5.8(C)). Now, starting from the folded state, if we apply a $T < Tr-$, the unit cell changes to the deployed state $\{1\}$, both switches are open and only the green LED is turned on (green path in Fig. 5.8(A)). If the applied magnetic torque is not enough to change the state of the Kresling pattern, the "Origami Schmitt Trigger" remains in its state and possesses memory. With the concept of "Origami Schmitt Trigger", we design a device for three-bit information storage and display using a three-cell magneto-mechano-electric Kresling assembly that has three different energy barriers and controllable multi-modal distributed actuation (Fig. 5.8(D)). Each unit cell is represented by two LEDs: The blue LED in the lighted state denotes the folded state of the unit cell. The other colored LEDs are green, yellow, and red, whose lighted state denotes the deployed state of the unit cell with the same color. In this way, the state of the Kresling assembly is digitized as three-bit information with real-time display. Fig. 5.8(D) demonstrates the transition between the eight states in a loop by accurately controlling the intensity and direction of the magnetic field (B, θ_B). The initial magnetization directions of the attached magnetic plates are shown in Table C.2. Note that by designing the Kresling geometries and magnetic controlling parameters, this device can be extended to a N-layer assembly with the capabilities of N-bit information storage resulted from the 2^N distinct states. Additionally, because of the differently designed energy barriers in the assembly, the device can passively sense and actively respond to the external load, enabling an intelligent system with integrated actuation, sensing, and computing.

5.3 Methods

5.3.1 Samples Fabrication

We fabricate each unit cell of the Kresling pattern by perforating and cutting the pattern on Tant origami paper (0.1mm thick) with the PLS4.75 laser cutting system (Universal laser systems). The Kresling pattern is modified to a flower-like shape (Fig. C.1(B)) to accommodate the cuts along the mountain folds. Those cuts avoid kinks in the mountain folds, creating samples with similar response on multiple folding cycles [102]. After the pattern is folded, we use 3M Scotch double sided tape to attach the top and bottom polygons (Fig. 5.9). These polygons are made of 160g/m Canson Mi-Teintes paper (0.2 mm thick), a thicker paper meant to provide stiffness and avoid bending of the polygons.

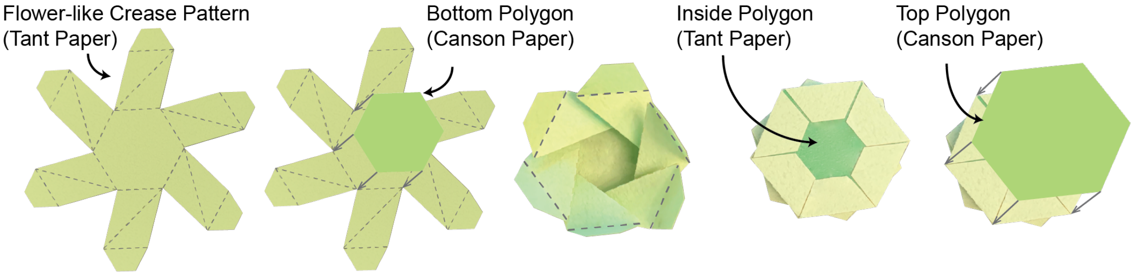

Figure 5.9: Fabrication steps of the Kresling unit cell.

To the top of each unit cell, we attach the magnetized plate using Sil-Poxy silicone adhesive. We fabricate the magnetized plates by first mixing Ecoflex 00-30 silicone rubber and NdFeB particles into a homogeneous mixture with 30% NdFeB volume. This solution is poured into a circular 3D printed mold with 22mm of diameter and 3mm of depth and cured for one hour at 60°C. Next, we magnetize the plates using a magnetizer with an 1.5T impulse magnetic field. In Table C.2, we provide the magnetization directions of the magnetic plates at the folded state with respect to the x-axis and the geometries of the unit cells for the Kresling assembly presented in this Chapter.

We investigate the variability of the mechanical properties over multiple compression cycles. Fig. 5.10 shows the force-displacement response of a unit cell with $H = 18.2$mm

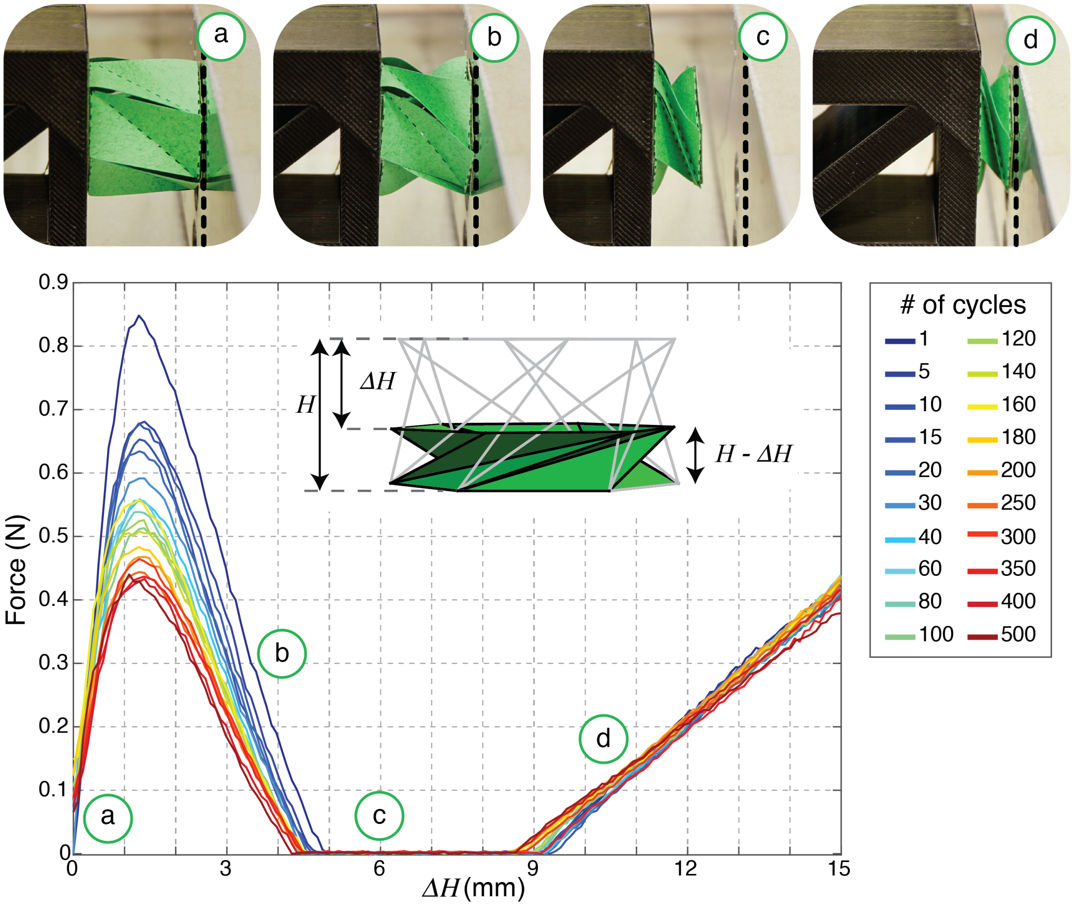

Figure 5.10: Kresling pattern (Design 3, $H = 18.2$mm) responses up to 500 compression cycles and snapshots of the experiment. Points a, b, and d are contact points, while point c is a non-contact point. Note that once the unit cell snaps, it loses contact with the load cell (e.g., point c), resulting on null forces until the contact is restored (e.g., point d).

(design 3 in Table C.1) up to its 500th folding cycle. We observed that the mechanical response stabilizes around the cycle 300. Thus, for consistent results, all the samples were folded and deployed up to 300 times prior to performing the magnetic actuation and mechanical tests reported in this work.

5.3.2 Mechanical Test

We test the mechanical properties of the Kresling unit cells under compression using a customized testing bed (see Appendix B). The setup consists of a metallic frame that integrates two steel plates. One plate is fixed and is connected to a 50N capacity load cell

(RSP1, Loadstar Sensors) with accuracy to 0.02% full scale. The other plate is movable and is controlled by a stepper motor (STP-MTR-23079, SureStep). The testing bed has a safety mechanism that limits the distance between the two plates to be no smaller than 15mm, which is about the size of our samples. To overcome this size limitation, we add a 3D printed sample holder to the setup.

From the experiments, we observe that the stable states of the samples differ from the geometric folded stable state. In reality, the folded stable state is not equivalent to the flat-foldable state (that is, $H_0 > 0$). Similarly, the rotational angles $\delta\theta$ are also different from those geometrically computed $\Delta\psi$ and reported in Table C.1. This difference comes from the fact that the fabricated samples have panels with thickness and hinges with stiffness, while the geometric model assumes panels with zero thickness and hinges with zero stiffness.

Setup #1: Folding of the Unit Cell

For each unit cell design in Table C.1, we test five samples under compression. For the tests, we attach one end of the unit cell to the sample holder, while leaving the other end completely free (Fig. 5.11). The free end is compressed against the fixed plate. Note that because the sample has no physical connection to the fixed plate, once the sample snaps, the free end loses contact with the load cell (see snapshots in Fig. 5.10). This results in the region with zero load in the force-displacement curves. Once the free end reaches the load cell again, we see the load increasing.

Setup #2: Folding and Deployment of the Unit Cell

Because we need to measure the required forces to both fold (compress) and deploy (pull) the unit cell, we modified the boundary conditions of the testing setup. For deployment, we need to constrain both ends of the unit cell, while allowing for rotation of the end in contact with the fixed plate. Thus, we use a wire to attach the crease pattern to a acrylic

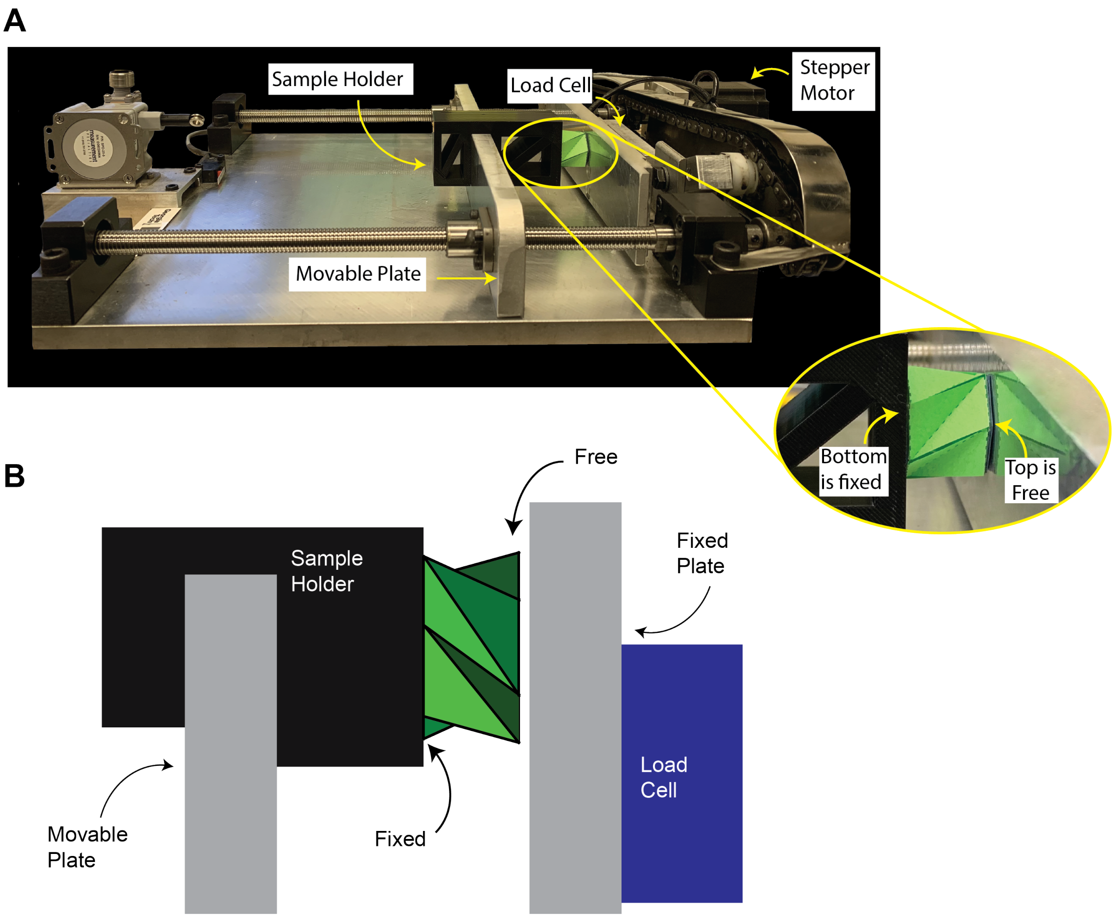

Figure 5.11: Compression test (setup #1). (A) Compression test bed and (B) Schematic of the test with fixed-free boundary conditions.

plate (Fig. 5.12(A)). In the acrylic plate, we laser cut a hole and a slot, allowing for the wire to pass through the plate and to be folded into the slot. This wire connection is enough to constraint the unit cell to the plate, while allowing for it to freely rotate. Once the attachment is done, we fold the unit cell, as described previously (Fig. 5.9). Next, we attach the acrylic plate to the testing bed fixed plate and attach the bottom of the unit cell to the sample holder (Fig. 5.12(B,C)). We first compress (fold) each unit cell from the deployed to the flat-folded state. Because both ends of the unit cell are constrained, the sample will not lose contact with the load cell. Thus, we obtain the entire equilibrium path between the stable states (Fig. 5.13) in which we observe a change in the direction of the axial load (from compression to tension). Once the unit cell reaches the stable state [0], the load changes direction again (from tension to compression) and the unit cell is compressed until it reaches the flat-folded state. After reaching the flat-folded state, we start the deployment of the unit cell. At first, the unit cell deploys without any force being applied (i.e., the unit cell experiences unloading). After a stable state is reached, the unit cell starts to experience tension. Similarly to the folding process, we capture the entire equilibrium path and we observe a change in the direction of force (from tension to compression). Once the unit cell reaches another stable state, further deployment is only possible under tension (Fig. 5.13).

5.3.3 Rotation and Displacement Coupling

Because the Kresling pattern displays a coupling between compression and torsion, we can obtain the required torque to fold the unit cells from the uniaxial compression test. Thus, we use a compression test setup to measure the force needed to transition between the two stable states of the pattern (Fig. 5.7(A)).

From the measured results, we obtain the stored energy. The derivative of the stored energy with respect to the rotation angle variation $\delta\theta$ results on the torque ($Tr+$) required to fold the unit cells. Thus, we express the stored energy as a function of $\delta\theta$, instead of ΔH (Fig. 5.14). With the torque, we compute the parameters (B and θ_B) needed to actuate each one of the unit cell designs (Table C.1), which are provided in Fig. C.8.

Although the Kresling pattern has a coupling between rotation and axial displacement, the relationship between the two is not available from kinematic equations. Because the Kresling Pattern is a non-rigid origami, we only have a geometrical relationship between height ΔH and the rotation angle $\delta\theta$ at the stable states. Thus, we approximate this relationship from the simulation of each unit cell under axial load using the Merlin software [81]. Simulation details are shown in Appendix C, Section C.1.2. From the displacement history of the nodal coordinates, we measure both the axial and rotational displacements of the unit cell. We approximate this data by a polynomial function and use this function to plot the stored energy as a function of the rotation angle.

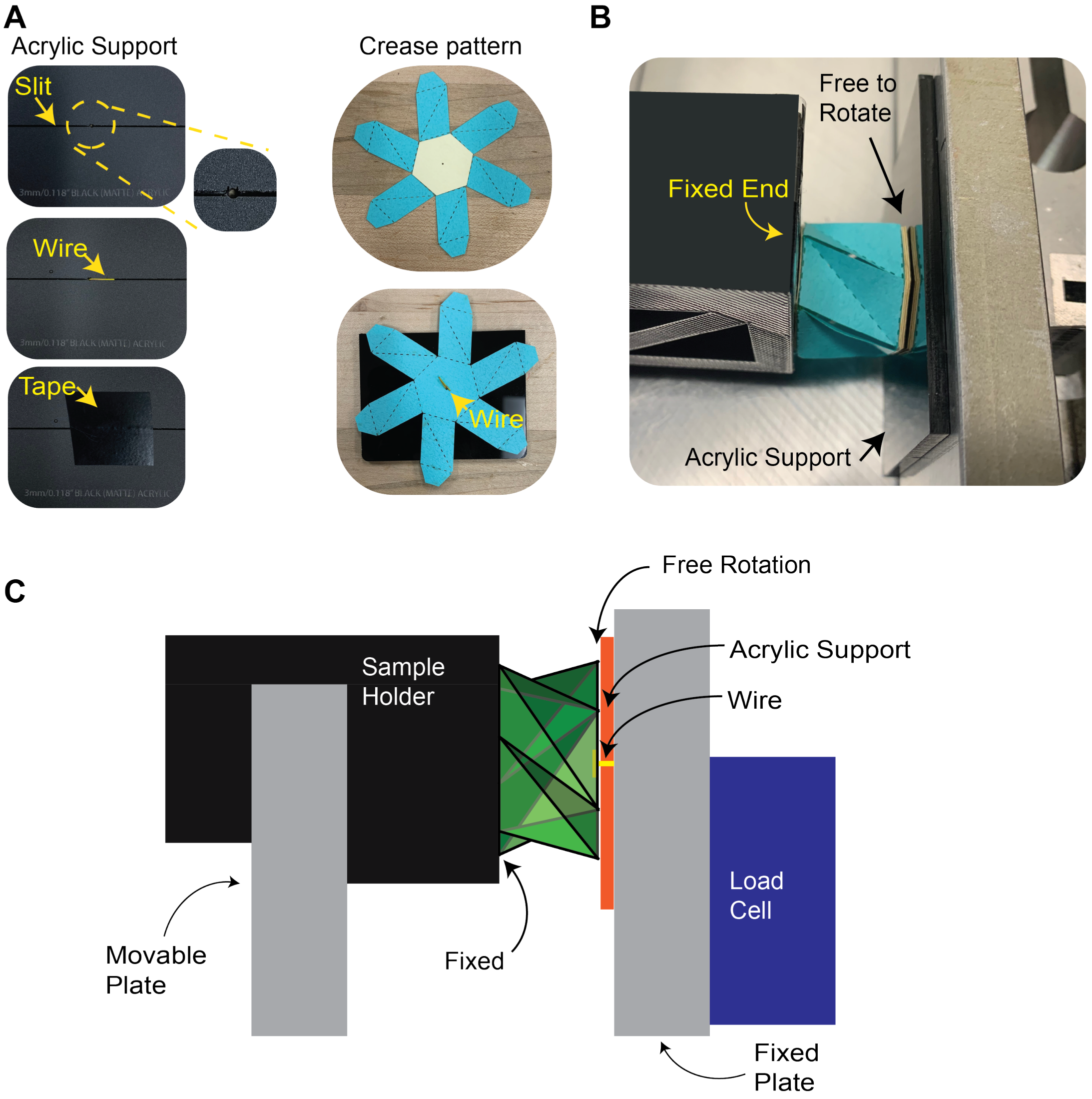

Figure 5.12: Compression and Tension test (setup #2). (A) Modified sample with a wire connection to an acrylic plate. (B) Sample assembled in the test bed. The sample is directly attached to the sample holder and the acrylic support to the fixed plate. (C) Schematic of the test setup.

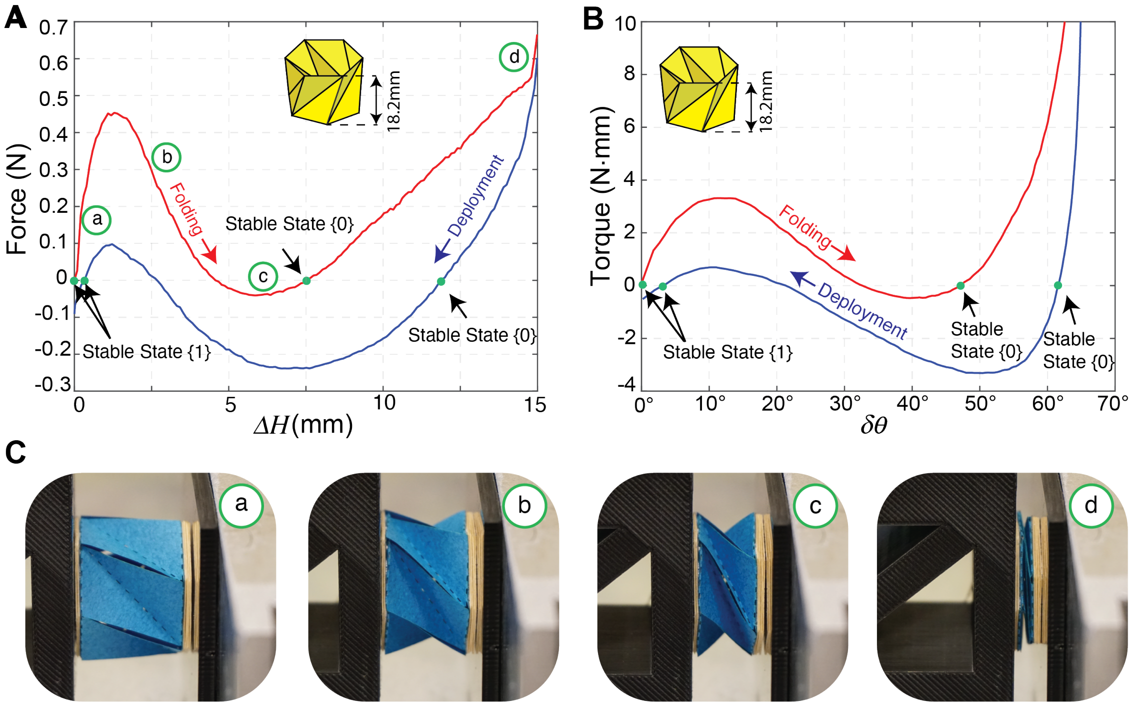

Figure 5.13: (A) Force-displacement curve obtained from the compression/tension test (setup #2) of the Design 3 unit cell. (B) Torque-rotation curve obtained from the derivation of the stored energy. (C) Snapshots of the experiment. Note that the left side of the sample is fixed to the sample holder and the right side uses a wire connection that constrains the unit cell while allowing for free rotation. The constraints at both ends permit the measurement of the entire equilibrium path. Contact at the right-hand-side of the setup is maintained at all times (points a, b, c, d).

5.3.4 Magnetic Actuation Experiment

The Kresling patterns with magnetic plates are actuated within a customized electromagnetic coil system, which can generate a two-dimensional (2D) uniform magnetic field (Fig. 5.15). Two sets of standard Helmholtz coils are configured perpendicularly to each other in the xy-plane. The in-plane magnetic field direction and intensity can be accurately controlled by the current in the coils. The coils can generate 2.7 mT/A and 3.3 mT/A uniform magnetic fields with 60mm and 80mm spacing for the x- and y-axes, respectively.

All Kresling unit cells and multi-cell assemblies are tested in the 2D electromagnetic coils. The Kresling samples are attached to an acrylic support (Fig. 5.15), so that only the bottom polygon is constrained against any type of displacement, and the other end is

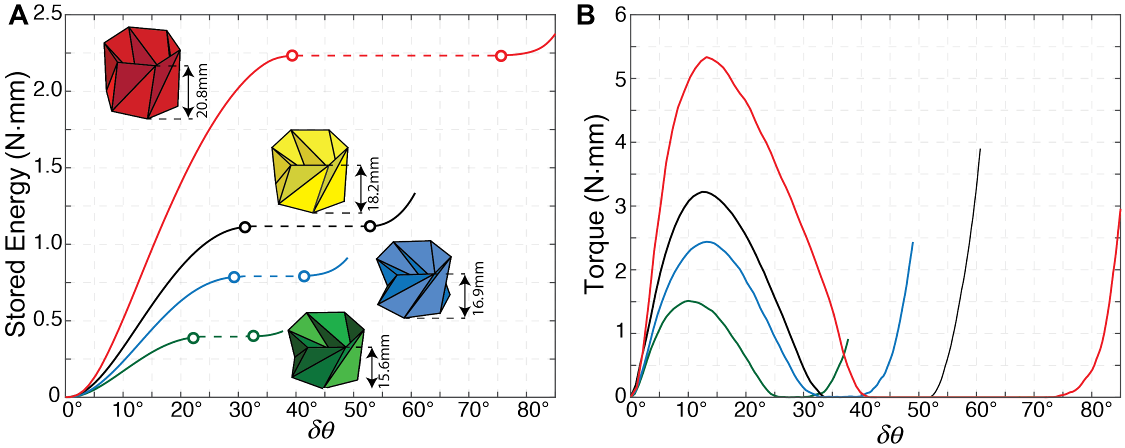

Figure 5.14: Mechanical response obtained from the average of the force-displacement curves (Fig. 5.7(A)) of the unit cells tested with fixed-free boundary condition, i.e., setup #1 (Fig. 5.11). (A) Stored energy and (B) Torque required to fold each designed unit cell, where $\delta\theta$ is the rotation angle. Dashed lines represent the region in which the unit cell loses contact with the load cell.

completely free. All magnetic plates are placed parallel with the xy-plane of the coils. The induced magnetic torque can fold and deploy the patterns along the z-axis. Then, a specific direction of the magnetic field is set, and the amplitude increases from 0 mT to 30 mT at a rate of 1 mT/s. When the Kresling patterns change states, the corresponding magnetic field is recorded. This is the minimum required magnetic field to actuate the Kresling pattern in this specific direction. Then, we change the magnetic field direction and repeat the same procedure. A step of 5° is used to scan the xy-plane from 0° to 360°. We fit the recorded magnetic field direction and amplitude data using the Fourier series and plot the corresponding experimental contours of magnetic actuation (Fig. 5.2(C), Fig. 5.4(B), Fig. 5.6(D), Fig. 5.7(C), Fig. 5.3(C), Fig. 5.5, and Fig. C.8).

5.4 Concluding Remarks

This work closes the gap existing in most origami applications by providing an actuation solution that acts locally and remotely on complex origami assemblies. We propose a coupling between magnetic-responsive materials with a bi-stable origami pattern, eliminating

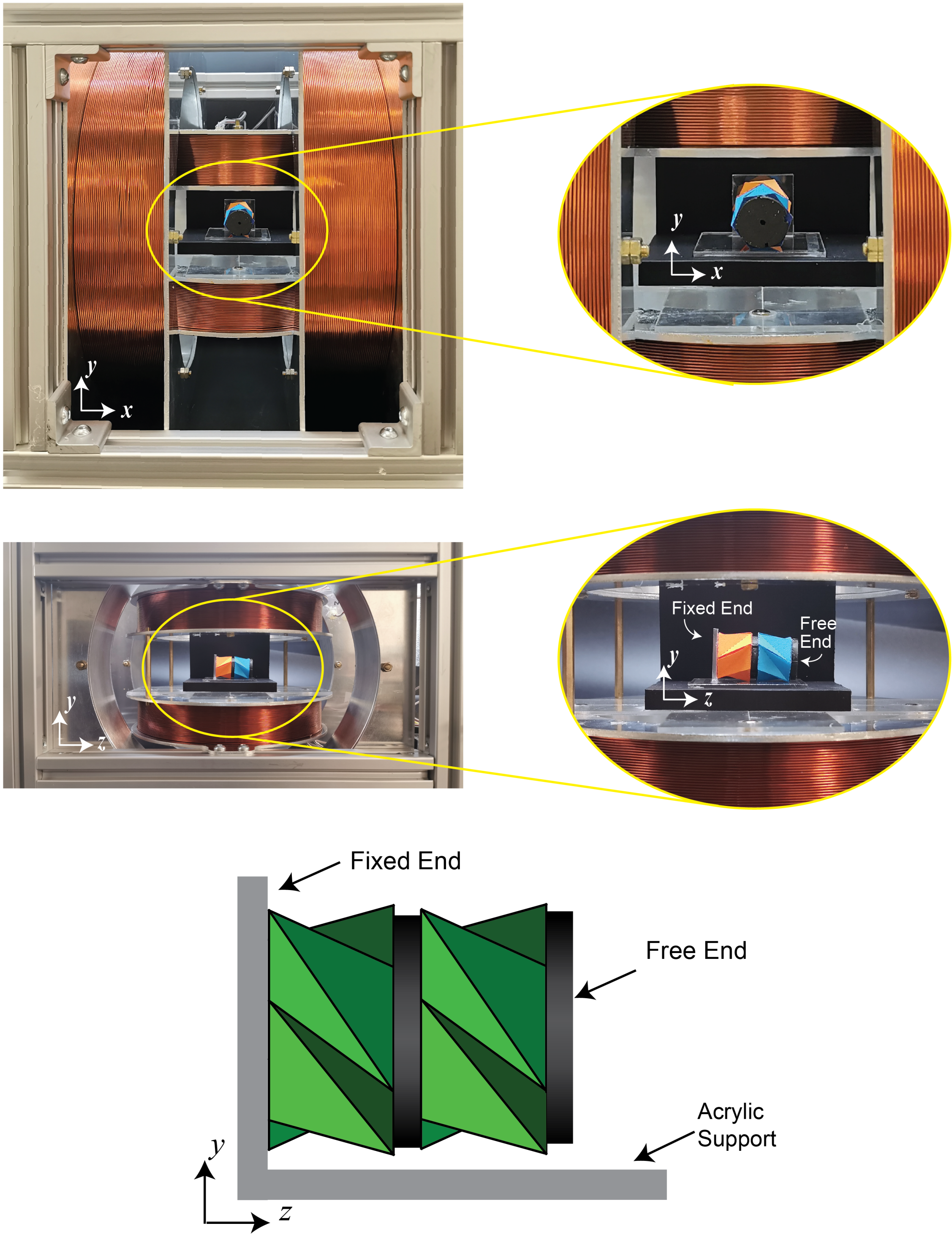

Figure 5.15: Magnetic actuation setup with electromagnetic coils. Bottom schematic shows the boundary conditions of the sample inside the coils.

the need for explicit shape-locking mechanisms, and allowing for a fast shape changing and instantaneous shape-locking of those structures. In addition, we are capable of actuating complex assemblies (as opposed to single or dual unit cells) with local control. That is, each unit cell can fold and deploy independently, on demand. This approach is extendable to other origami materials, as the magnetic material is assembled to the unit cells. Thus, we envision a simple transition to other material systems, including 3D printing, previously used to fabricate origami structures.

CHAPTER 6

BIG INFLUENCE OF SMALL RANDOM IMPERFECTIONS IN ORIGAMI-BASED METAMATERIALS

Origami structures demonstrate great theoretical potential for creating metamaterials with exotic properties. However, there is a lack of understanding of how imperfections influence the mechanical behavior of origami-based metamaterials, which, in practice, are inevitable. For conventional materials, imperfection plays a profound role in shaping their behavior. Thus, in this chapter, we investigate the influence of small random geometric imperfections on the compressive response of the representative Miura-Ori, which serves as the basic pattern for many metamaterial designs, as we showed in previous chapters. Experiments and numerical simulations are used to demonstrate quantitatively how geometric imperfections hinder the foldability of the Miura-Ori, but on the other hand, increase its compressive stiffness. This leads to the discovery that the residual of an origami foldability constraint, given by the Kawasaki theorem, correlates with the increase of stiffness of imperfect origami-based metamaterials.

6.1 Introduction

Mechanical metamaterials exhibit unconventional behavior that is rarely found in natural materials [38, 103, 104, 105]. Their exclusive properties and functionalities arise from carefully architected microscopic structures, for which origami is a rich source of inspiration. Origami-based metamaterials are able to produce negative Poisson's ratio [1, 42, 43], acoustic bandgaps [106], multi-stability, [46, 107, 108, 109, 17], programmable thermal expansion [4], and tunable chirality [70]. However, regarding practical applications of origami-based metamaterials, a few fundamental questions are yet to be answered: *how robust are their special properties, and how these properties may change in the presence of* *imperfections* [110, 111, 112]*?* We focus on a well-known origami pattern, the Miura-Ori, which, together with its variants, is perhaps the most adopted pattern for origami-based metamaterial designs [1, 42, 9, 113, 114, 106, 107, 108, 115, 2, 116, 117, 118, 4, 70, 86]. The special properties of the Miura-Ori are mainly programmed in its geometry [1, 42]. Consequently, irregularities in a Miura-Ori geometry can significantly change its mechanical behavior [118, 119, 120]. For instance, the so-called "pop-through defect" in Miura-Ori, a deterministic and localized interruption of periodic folding, was shown to affect their stiffness towards either stiffening or softening [2]. However, in practice, small random geometric imperfections are perhaps the more likely cause of irregularity in the Miura-Ori geometry. An example of this is reported by Baranger et al. [110]. They showed that local inaccurate crease pattern greatly reduces the global out-of-plane response of origami-like folded core. Additionally, Jianguo et al. [111] found that the influence of the imperfections, modeled by the buckling modes from eigenvalue analysis, strongly affect the folding behavior of the Kresling tubular origami structure that shifts the folding sequence. Therefore, in this chapter, we conduct both experiments and numerical simulations to study the statistical influence of small random geometric imperfections on the mechanical properties of Miura-Ori. The type of imperfection that we are considering is fundamentally different from deterministic variations (or intentional imperfection) of origami geometry that has been studied in the literature [108, 2, 86, 119]. In this research, our main interest is to understand how the presence of random imperfections may hinder or enhance the functionality of origami-based metamaterials, but not to modify the mechanical properties of origami metamaterials by introducing imperfections.

Geometric imperfections are caused by various sources, such as misaligned crease patterns or deterioration during service. To motivate our study, let us fold three Miura-Ori with different degrees of random imperfection. The imperfections are imposed by random perturbations of the nodes on the planar crease pattern to create misalignment. Since the perturbations are small, the three Miura-Ori do not show any notable difference initially.

However, if we try to fold them (in-plane compression) simultaneously, their responses deviate significantly, as shown in Fig. 6.1(A). This example shows that small random geometric imperfections seem to hinder the foldability of Miura-Ori, but on the other hand, increase their stiffness, which is different from geometric imperfections in lattice and thin-walled cellular materials [38, 112, 121, 122].

6.2 Geometry and Stiffness of Standard Miura-Ori

A standard Miura-Ori unit cell is composed of identical parallelogram panels, defined by panel edge lengths a, b, and panel angle α, as shown in Fig. 6.1(B). At each vertex of this pattern, the sum of opposite sector angles equals to π, satisfying a necessary condition for flat-foldability (aka the Kawasaki theorem) as demonstrated Fig. 6.1(C). As a result, the Miura-Ori admits a single degree-of-freedom (DOF) rigid folding mechanism, which can be parametrized by one of the two dihedral angles β and θ. The two angles are related by $\sin^2(\beta/2) = \sin^2(\theta/2)[\cos^2\alpha + \sin^2\alpha \sin^2(\beta/2)]$ [1, 42]. Ideally, when subject to in-plane compression, a Miura-Ori should deform only at the folding creases, which is known as rigid origami behavior. As the functionality of origami-based metamaterials mainly arise from large folding deformations [123, 43, 1, 42, 9, 113], here we focus on the nonlinear response of imperfect origami under in-plane compressive folding (i.e., compression in the x-direction shown in Fig. 6.1). Assuming a simple discretized model (Fig. 6.1(B)) to represent the Miura-Ori unit cell and considering rigid origami behavior, which means that there is no bending deformation and stretching deformation, the reaction force along the x-direction of a Miura-Ori unit cell is derived as [42]:

$$F_x = 2K_F \frac{a(\theta - \theta_0)\cos^2\xi + b(\beta - \beta_0)\cos\alpha}{b\cos^2\xi \sin\alpha \cos(\theta/2)} \tag{6.1}$$

where K_F is the asssigned rotational stiffness of the hinges, $\xi = \sin^{-1}[sin\alpha \sin(\theta/2)]$, β_0 and θ_0 define the initial partially folded configuration, and a, b are the edge length of panels.

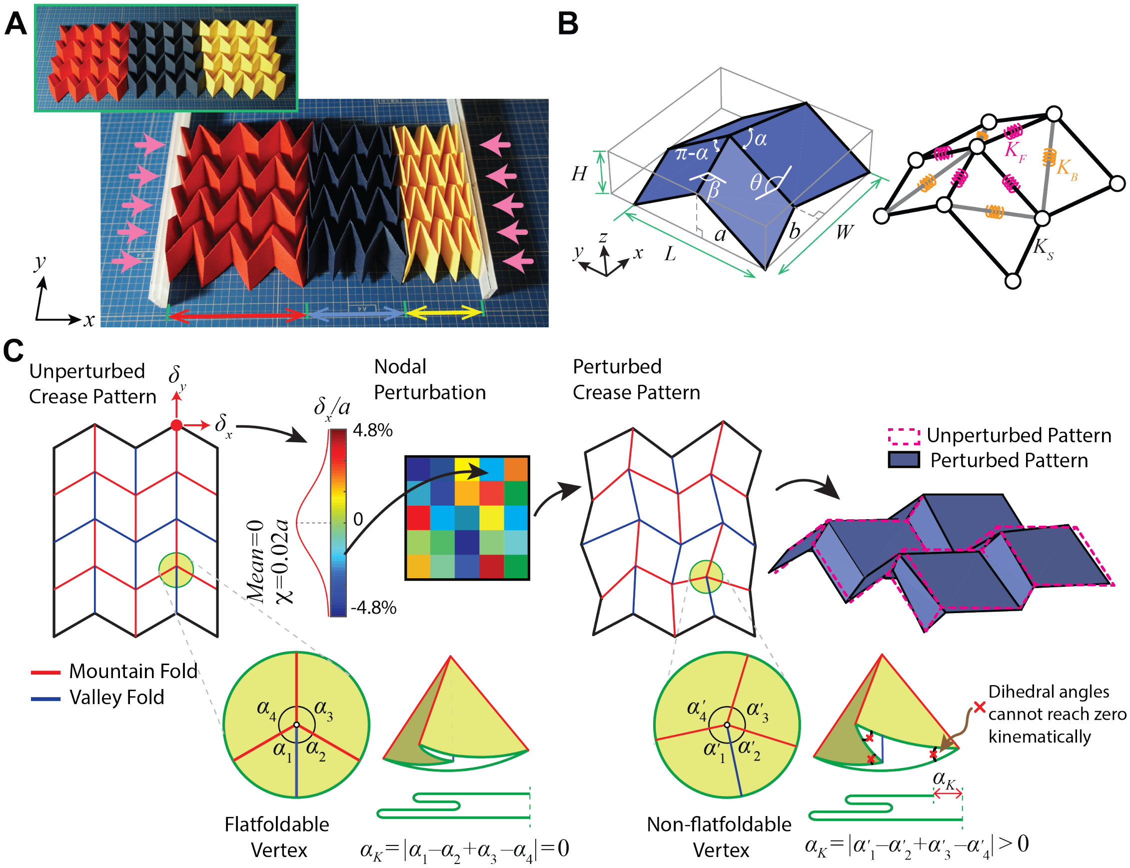

Figure 6.1: Geometric imperfections in origami metamaterials. (A) Three origami sheets under the same load. We fold the yellow one with the perfectly aligned Miura-Ori pattern. The blue one is folded from a slightly misaligned Miura-Ori pattern, and the red one is folded from a pattern with relatively strong misalignment. The inset shows the initial configurations of the three samples. (B) Geometry of the Miura-Ori unit cell (left) and schematic of a bar-and-hinge model as a simplified discretization of the Miura-Ori, which we use later for the numerical simulations (right). We discretize each quadrilateral panel into two triangles by its shorter diagonal. The parameters K_B, K_F, and K_S are bending, folding and stretching stiffness, respectively. (C) Introduction of geometric imperfections by random nodal perturbations. At each node, the perturbation is decomposed into x- and y-directions (denoted as δ_x and δ_y). Folding up a perturbed crease patterns results in an imperfect Miura-Ori, whose geometry slightly deviates from the perfect Miura-Ori as indicated by magenta dashed lines. For each vertex, we compute the Kawasaki excess α_K. When $\alpha_K = 0$, the vertex is flat-foldable, which is the case for all the vertex in a standard Miura-Ori pattern. However, nodal perturbation leads to $\alpha_k > 0$, in which early contact between two panels prevents the whole origami to be flattened, and some dihedral angles (marked by red crosses) cannot reach zero kinematically.

6.3 Experimental Analyses

All experimental samples have 4x4 unit cells, with standard geometry defined by $a = b =$ 25mm and $\alpha = 60^\circ$. To quantitatively examine the effect of geometric imperfections, we fabricate and perform in-plane compression tests on Miura-Ori samples with different degrees of random geometric imperfection. As sketched in Fig. 6.1(C), at each node of the crease pattern, the perturbations along x- and y-direction are sampled independently from a Gaussian distribution with zero mean and standard deviation χ (i.e., $N(0, \chi)$). From such sampling, we make sure that the nodal perturbations are unbiased in direction. Two representative values of χ are used to prepare two groups of perturbed patterns: $\chi = 0.01a$, and $\chi = 0.02a$. The physical samples are fabricated using three different materials: (1) craft paper (160g/m^2 Mi-Teintes, Canson, Young's modulus $E = 1219$MPa, thickness of 0.24mm), (2) polyester film (Grafix Drafting Film, $E = 2449$MPa, thickness of 0.127mm), and (3) composite sheet (260 g/m^2 Durilla Durable Premium Ice Card Stock, $E = 1303$MPa, thickness of 0.30mm), as shown in Fig. 6.2. The composite sheet is made of three layers in a "paper-film-paper" construction.

6.3.1 Characterization of Materials Mechanical Properties

Folding and bending stiffness

Folding and bending stiffness of the sheet materials are important properties when dealing with origami metamaterials. To characterize the bending stiffness of the origami panels K_B, for each material, we prototype five rectangular panels (50x25 mm) with folded flanges that resemble the presence of neighboring panels in an origami pattern (Fig. 6.3(A)). The presence of the flanges leads to localized bending curvatures, similar to deformed origami panels [81]. In a similar fashion, we also prototype five samples per material to characterize the folding stiffness of the paper creases K_F. Each sample has two square panels of dimension 25x25 mm, jointed by a perforated crease line (Fig. 6.3(D)). The crease lines

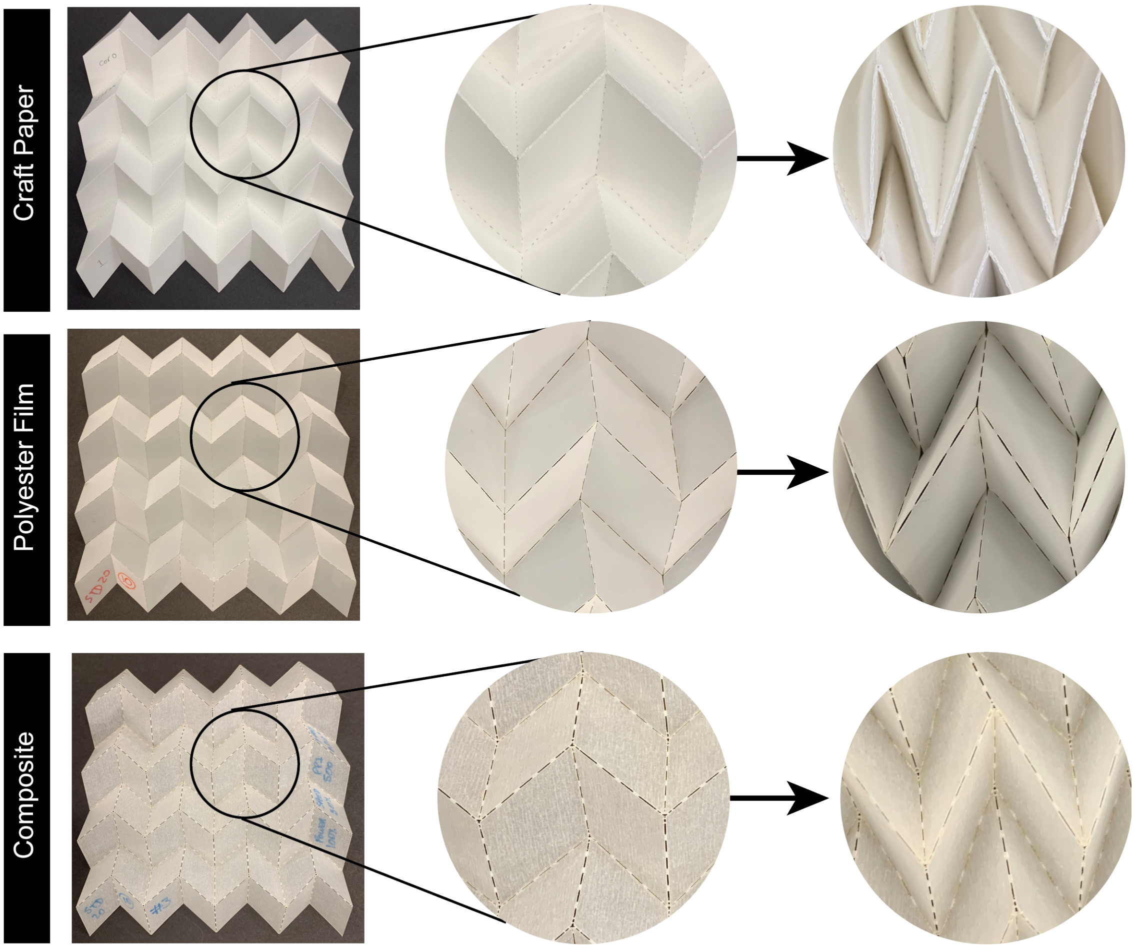

Figure 6.2: Zoom-in view of the creases of Miura-Ori samples made from craft paper (Mi-Teintes, Canson), polyester film (Grafix Drafting Film) and composite (Durilla Durable Premium Ice Card Stock). The right most column shows the deformation of the creases under compressive folding. We can see that the small gaps between creases being pulled open, especially for the polyester film samples.

are first folded completely and then released to a neutral angle prior to the test.

The samples are tested using a custom-built mechanical testing device (see device description in Appendix B), similarly to the material characterization in Chapter 4. That is, we attach a spacer to the movable plate. The spacer holds the sample, while leaving clearance for the free end of the sample to displace freely in space to some extent. Second, we mount a 3D printed force arm to the fixed plate with its center offset 29 mm from the spacer edge. This arm transmits the reaction force from the sample to the load cell. Fig. 6.3(B,E) show the initial setup of the tests to measure bending stiffness and folding stiffness, respectively. Fig. 6.3(C,F) sketch intermediary scenarios during the test.

The moment M at the crease/bending lines and the rotational angle ψ are calculated by Eq. 4.1, where d_x is the distance between the crease/bending line and the force arm (i.e., $d_x = 19$mm), F is the measured force from the load cell, and u_0 is the initial distance between the force arm and the spacer in the y-direction. For the measurements of bending stiffness, $u_0 = 0$, while for the folding stiffness, we see different initial neutral angles after a complete fold. In such cases, u_0 was measured for each sample based on where the force arm touches the sample. Fig. 6.4 shows the moment-rotation diagrams of one bending test and one folding test for the craft paper. The measured rotational stiffness of all samples and materials are collected in Tables 6.1, 6.2, and 6.3 with coefficients of determination (i.e., R_B^2 and R_F^2) included. The coefficients of determination (i.e., R_F^2 and R_B^2) can be used to indicate the linearity of the constitutive relationships of the folding hinges and bending lines. We observe that while the bending constitutive relationships of all three materials are quite linear as all R_B^2's are close to 1.0, the linearity of the folding constitutive relationships is less significant. For the polyester film, the average value of R_F^2 is 0.88, less than the other two materials, which indicates a relatively strong nonlinear behavior of the folding hinges of polyester films. On the contrary, both bending and folding constitutive of the craft paper is quite linear, even for a relatively large range of rotation, as implied by the coefficients of determination, and as shown in Fig. 6.4, which is the reason why later we use the properties of the craft paper to build our numerical models. The mean value of the measured rotational stiffness is normalized by the bending/folding hinge length (i.e., 25mm) to obtain the rotational stiffness per unit length. The ratios between the bending and folding stiffness for the materials used in the experiments are averaged at $K_B/K_F = 6.4$, $K_B/K_F = 1.95$, and $K_B/K_F = 10.7$ for craft paper, polyester film, and the composite sheet, respectively. The ratio of K_B/K_F is a key parameter that determines whether an origami is close to a mechanism (rigid origami) or not. For example, when $K_B/K_F \to \infty$, we approach a situation where rigid panels are connected by zero-stiffness hinges (rigid origami). When $K_B/K_F = 1$, the panels and the folds have the same stiffness (such as molded samples).

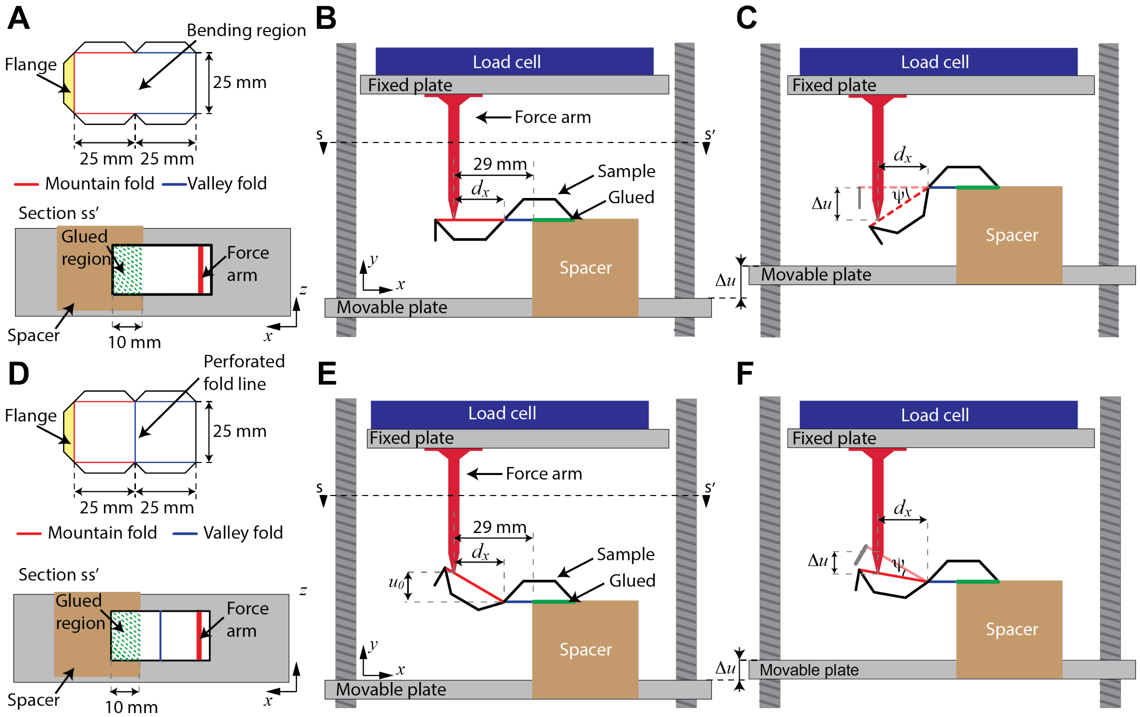

Figure 6.3: Schematics of the bending and folding test. (A-C) Characterization of the bending stiffness of the panels, and (D-F) characterization of the folding stiffness of the perforated crease (fold line).

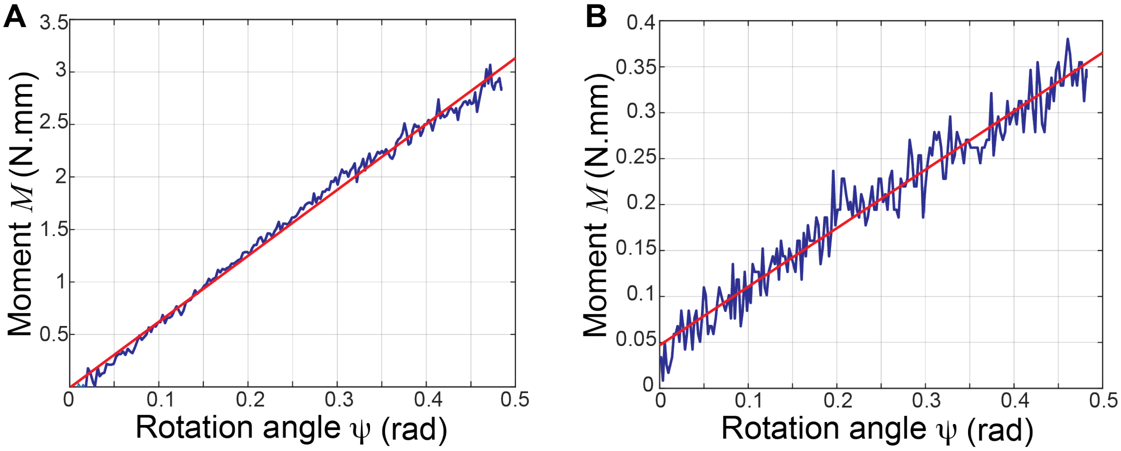

Figure 6.4: Moment M vs. rotation angle ψ for the (A) panel bending and (B) hinge folding from one sample of each made of Canson Mi-Teintes paper. The measured data is plotted in blue lines, and the red lines represent the linear regressions. From the slope of the red line, the rotational stiffness is obtained.

Stretching stiffness

To obtain the Young's modulus (E) of the three sheet materials, we use an Instron model 5566 equipped with a 30kN load cell to perform a tensile test on five samples per material (Fig. 6.5). Each sample has a dimension of 20mmx100mm. From those tests, we take the mean of the results and obtained the Young's modulus E. The data is collected in Tables 6.1, 6.2, and 6.3.

The values presented in the Tables 6.1, 6.2, and 6.3 represent samples tested in one orientation. We did not investigate either consider the anisotropic behavior of the material sheets in this work. In Appendix D, we provide a preliminary study on the investigation of the influence of material anisotropy into the mechanical response of the Miura-Ori patterns. From this study, we observed that the Miura-Ori pattern's behavior is governed by its geometry, and the material anisotropy does not considerably impact it.

6.3.2 Miura-Ori Sample Fabrication

A MATLAB program generates the crease patterns for the samples. We include a reference group consisting of 6 samples folded from a standard Miura-Ori pattern. For each choice of

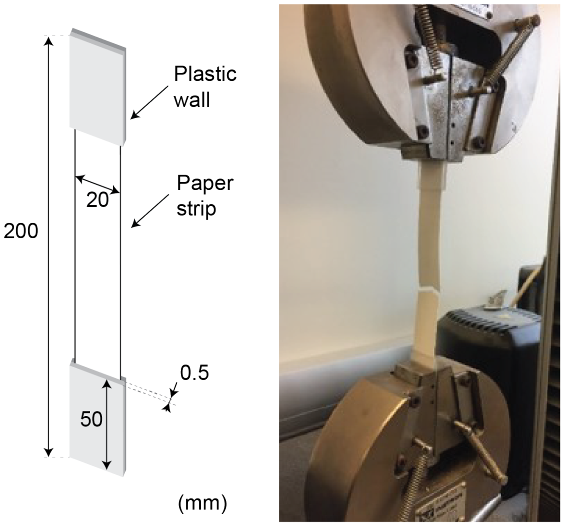

Figure 6.5: Tension test on craft-paper using the Instron machine.

Table 6.1: Canson Mi-Teintes Properties.

E (MPa)	K_B $\left(\text{N}\cdot\text{mm}(\text{rad}\cdot\text{mm})^{-1}\right)$	R_B^2	K_F $\left(\text{N}\cdot\text{mm}(\text{rad}\cdot\text{mm})^{-1}\right)$	R_F^2
1313.3	0.2513	0.9800	0.0375	0.9226
1114.3	0.2078	0.9417	0.0322	0.9280
1287.0	0.2465	0.9631	0.0225	0.9520
1201.9	0.2141	0.9707	0.0434	0.9621
1180.5	0.2194	0.9536	0.0445	0.9489
Average				
1219.4	0.2278	0.9868	0.0366	0.9427

Table 6.2: Drafting Film Properties.

E (MPa)	K_B $\left(\text{N}\cdot\text{mm}(\text{rad}\cdot\text{mm})^{-1}\right)$	R_B^2	K_F $\left(\text{N}\cdot\text{mm}(\text{rad}\cdot\text{mm})^{-1}\right)$	R_F^2
2476.5	0.0809	0.9896	0.0401	0.8413
2480.5	0.0765	0.9904	0.0396	0.7753
2408.6	0.0896	0.9921	0.0466	0.9821
2423.0	0.0938	0.9839	0.0458	0.9310
2455.5	0.0900	0.9857	0.0481	0.9077
Average				
2448.8	0.0862	0.9883	0.0441	0.8875

standard deviation for random perturbations, a group of 10 different crease patterns is generated. A mechanical cutting machine (Silhouette CAMEO, Silhouette America) is used to fabricate samples from the craft paper, and a PLS4.75 laser cutting system (Universal laser systems) is used to fabricate samples from the polyester film and the composite sheet.

Table 6.3: Durilla Durable Premium Ice Card Stock Properties

E (MPa)	K_B $\left(\text{N·mm(rad·mm)}^{-1}\right)$	R_B^2	K_F $\left(\text{N·mm(rad·mm)}^{-1}\right)$	R_F^2
1317.1	0.7667	0.9895	0.0827	0.9797
1323.5	0.7587	0.9886	0.0623	0.9132
1298.3	0.7866	0.9892	0.0620	0.9323
1277.2	0.7729	0.9889	0.0690	0.9377
1297.0	0.7952	0.9841	0.0875	0.9032
Average				
1302.6	0.7760	0.9881	0.0727	0.9332

Creases were patterned by cutting perforated lines with equal lengths of material and gaps. All samples are then carefully folded by hand, according to the same folding procedure. Samples are first folded to approximately 20% of the full extension of the crease pattern before mechanical testing and then fit into a mold of partially folded configuration with a width of $W_0 = 152mm$ for approximately seven days to release the residual stresses. This results in a nominal rest fold angle at $\beta_0 = 95°$.

6.3.3 Experimental Tests on the Miura-Ori Samples

Each Miura-Ori sample is tested a single time under in-plane compression. For the tests, we use the custom-build mechanical testing device described in Appendix B. The testing frame consists of two steel plates. One of the plates is fixed and mounted on a high-sensitivity load cell (50N); a stepper motor controls the other to apply prescribed displacement load (Fig. 6.6). We configure the initial setup by separating the two steel plates by a distance of 152mm and placing the sample between the plates. All samples are subject to a displacement load of 110mm with a speed of 1mm/s. The displacement and force data are simultaneously recorded by a custom LabVIEW program and stored for later analysis.

The samples are uniaxially compressed along the x-direction, as shown in Fig. 6.7(A,B). The behavior of the samples is recorded by the compressive strain ($\varepsilon_x = \Delta W/W_0$) and bulk stress ($\sigma = F/H_0L_0$, where F is the measured force, and H_0, L_0, and W_0 are the dimensions of the initial configuration). As shown in Fig.6.8, all samples behave almost linearly up to a small strain around 2%. The metamaterials continue to deform at slowly increasing stress for a large range of deformation (plateau), until the stress rises with a notably increasing slope (densification).

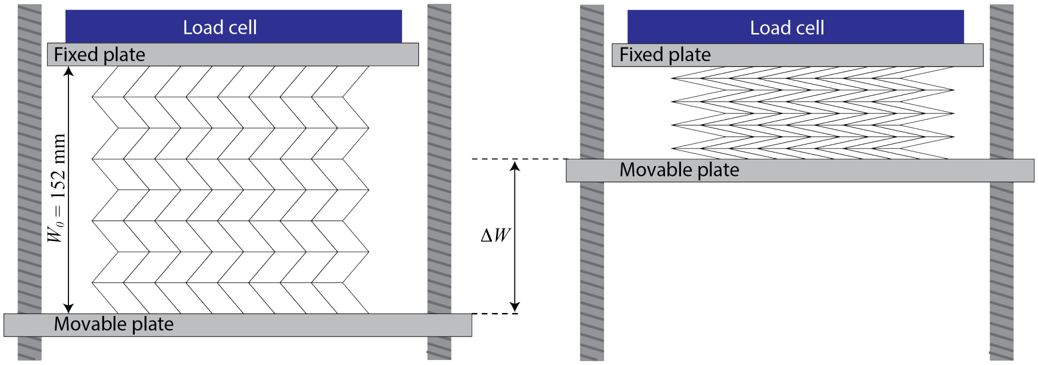

Figure 6.6: Schematics of the in-plane compression test setup for the Miura-Ori samples at the initial (left) and final position (right). W_0 is the initial length the sample, and ΔW is the total in-plane displacement applied.

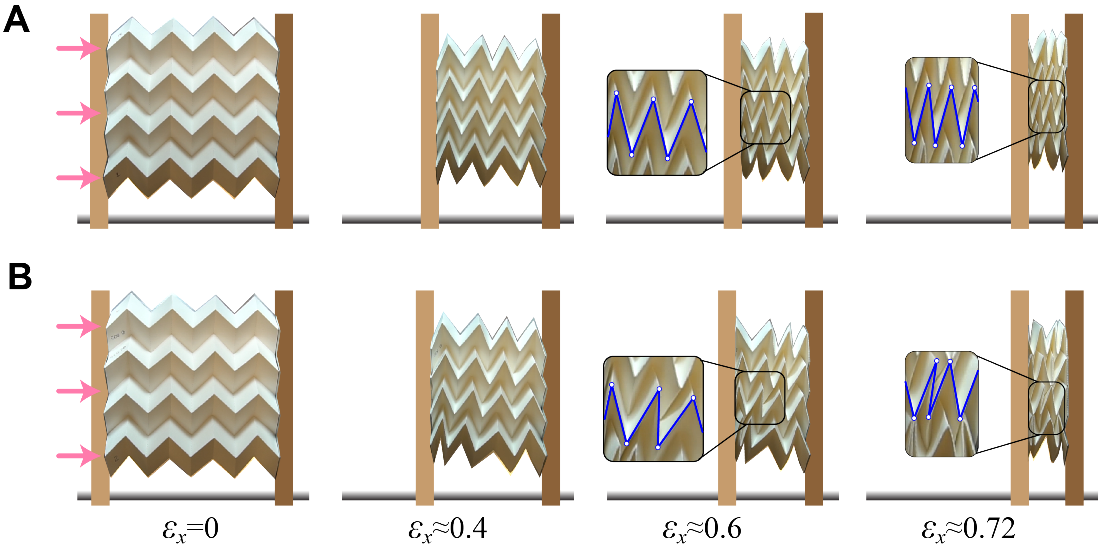

Figure 6.7: Experimental quantification of the effect of geometric imperfections. Snapshots from experiments of craft paper samples with (A) an unperturbed crease pattern and (B) a perturbed crease pattern with $\chi = 0.02a$ under increasing compressive strain. The blue lines outline a row of vertices.

To quantitatively compare the constitutive behavior of Miura-Ori, we define the initial linear modulus E_{lin}, computed as the slope of the stress-strain curve between zero and 2%

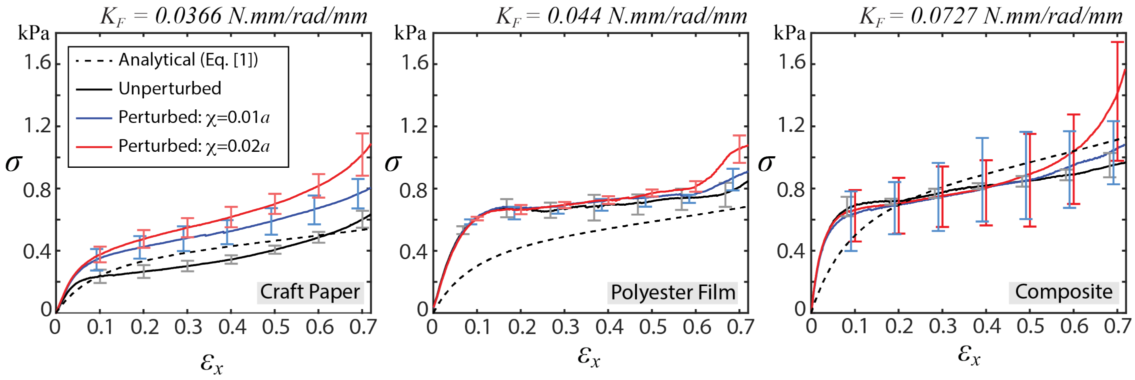

Figure 6.8: Bulk stress σ (kPa) vs. compressive strain ε_x for samples made of different materials. The solid lines represent mean responses. The error bars show the maximum and minimum values of the measured σ data. Plotting the min/max values can show that our data suggests no significant skewness, as the min and max values are about equidistant from the mean. The dashed line is the response of ideal Miura-Ori according to Eq. 6.1, where K_F is obtained by mechanical test on single creases.

strain, and the plateau stress $\sigma_{0.65}$ as the stress at 65% strain, as illustrated in Fig. 6.9(A). The plateau stress is defined as the end-of-plateau stress. The representative strain of 65% is based on our observation on all curves as the approximate end point of the plateau stage before densification.

Let's denote $\langle\cdot\rangle$ as the mean value operator. The reference groups of unperturbed samples have: $\langle E_{lin,ref}\rangle = 4.93$kPa and $\langle\sigma_{0.65,ref}\rangle = 0.52$kPa for the craft paper, $\langle E_{lin,ref}\rangle = 11.11$kPa and $\langle\sigma_{0.65,ref}\rangle = 0.76$kPa for the polyester film, and $\langle E_{lin,ref}\rangle = 18.33$kPa and $\langle\sigma_{0.65,ref}\rangle = 0.92$kPa for the composite sheet. Based on the results, we see that for all three materials, as χ increases, the Miura-Ori become stiffer, as shown in Fig. 6.8 and 6.9(B). Compared to the reference groups: for the craft paper samples, $\langle E_{lin}\rangle$ increases up to 38% and $\langle\sigma_{0.65}\rangle$ increases up to 72%; for the polyester film samples, $\langle E_{lin}\rangle$ remains almost unchanged, but $\langle\sigma_{0.65}\rangle$ increases by 22%; for the composite samples, $\langle\sigma_{0.65}\rangle$ increases by 27%. We notice that the average value of linear moduli of the three types of experimental samples is less sensitive to geometric imperfections compared to the plateau stress. However, geometric imperfection increases their variances. This is likely caused by material variability, such as the variances of K_F. Also, the edges of the imperfect Miura-

Ori samples are jagged, not as straight as the standard pattern. Hence, when the moving plate applies the in-plane compression, it is possible that the compression is not applied uniformly to the sample, in the beginning, causing localized deformation of the protrusions first near the boundary before affecting the entire sample, which may appear a softer response on the load record.

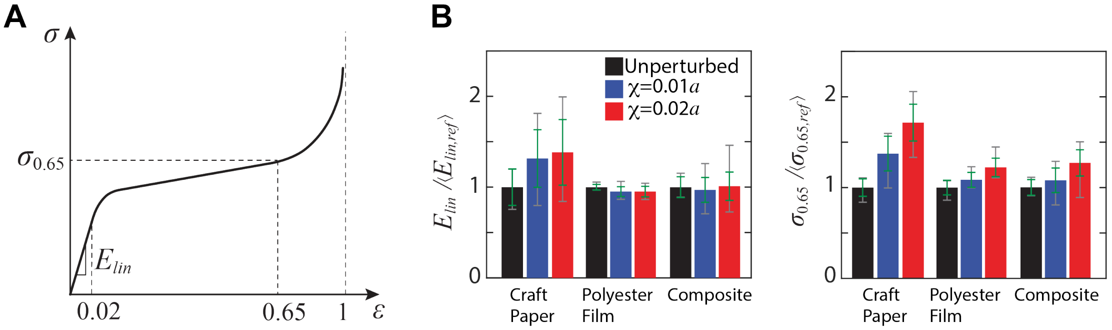

Figure 6.9: Experimental quantification of the effect of geometric imperfections. (A) Illustration of the constitutive model. (B) E_{lin} and $\sigma_{0.65}$ for different sample groups, where $E_{lin,ref}$ and $\sigma_{0.65,ref}$ refers to unperturbed sample group. The gray error bars show standard deviations, and the green error bars indicate extrema of data.

Besides the difference in the global responses between perturbed and unperturbed samples, a significant difference is also observed at the local level (Fig. 6.7). The unit cells of the unperturbed pattern uniformly deform with the lattice structure of vertices remaining relatively ordered and periodic throughout the compressive folding process. The perturbed samples, however, display non-uniform deformation among unit cells, with severely distorted lattice structures, especially under higher compressive strains.

6.3.4 Numerical Analyses

The variability of the mechanical properties of the physical samples comes from not only random geometric imperfections, but also material variabilities. To study the pure effect of geometric imperfections, we would like to exclude material variabilities as much as possible. Hence, we perform numerical simulations using a reduced order bar-and-hinge model of origami [81, 124], as introduced earlier in Fig. 6.1(B). The bar-and-hinge model represents the behavior of an origami structure by a triangulated bar frame with constrained rotational hinges, capturing three essential deformation modes of origami structures: in-plane stretching (modeled by K_S), folding (modeled by K_F), and panel bending (modeled by K_B). With only a few degrees of freedom, the bar-and-hinge model predicts well the overall mechanical behavior of elastic origami structures [1, 9, 125, 122, 81], offering the generality and computational efficiency that is needed to reveal statistical trends of the influence of random geometric imperfections. The numerical simulations are performed using the MERLIN software [81] that implements the bar-and-hinge model. We use the data collected from the craft paper to tune K_B and K_S of the bar and hinge model, and vary K_F to assess the effect of hinge compliance. The folding stiffness K_F is calculated based on different prescribed ratios of K_B/K_F.

Using numerical models, we are able to assign constant material properties and impose random imperfections under precise probability distributions. Omitting the process of folding, we configure the numerical models directly in 3D (Fig. 6.10) and impose random nodal perturbation onto the 3D model. This is to keep the study general because not all origami metamaterials are made by folding from a flat piece of sheet. Some are directly assembled to partially folded state by pieces of panels, yet they also carry geometric imperfections. Moreover, some types of imperfections, such as distortion induced by non-uniform thermal effect, may display strong spatial correlation. Thus, we introduce spatially correlated random fields [126] to generate the nodal perturbations. The random perturbations follow zero-mean Gaussian fields with an exponential covariance function [127] characterized by standard deviation χ and correlation length ℓ:

$$C(x_i, x_j) = \chi^2 \exp\left(-\frac{||x_j - x_i||}{\ell}\right) \tag{6.2}$$

where $||x_j - x_i||$ is the Euclidean distance between two nodes whose coordinates are x_i and x_j. Larger ℓ indicates stronger spatial correlation between random nodal perturbations, as shown in Fig. 6.10. For the experimental samples presented earlier, the imposed perturbations follow random fields with $\ell = 0$. We prepare, in total, sixteen groups of perturbed samples with four different χ's and four different ℓ's. We assume that the random field is homogeneous, because typically spatial variability in isotropic materials follows a homogeneous covariance law (depends only on spatial separation) [127]. In addition, some imperfections may be non-Gaussian in nature. Therefore, the adoption of Gaussian random field in this work is an idealized (and first attempt) approximation that intends to provide some insight into the influence of geometric imperfections.

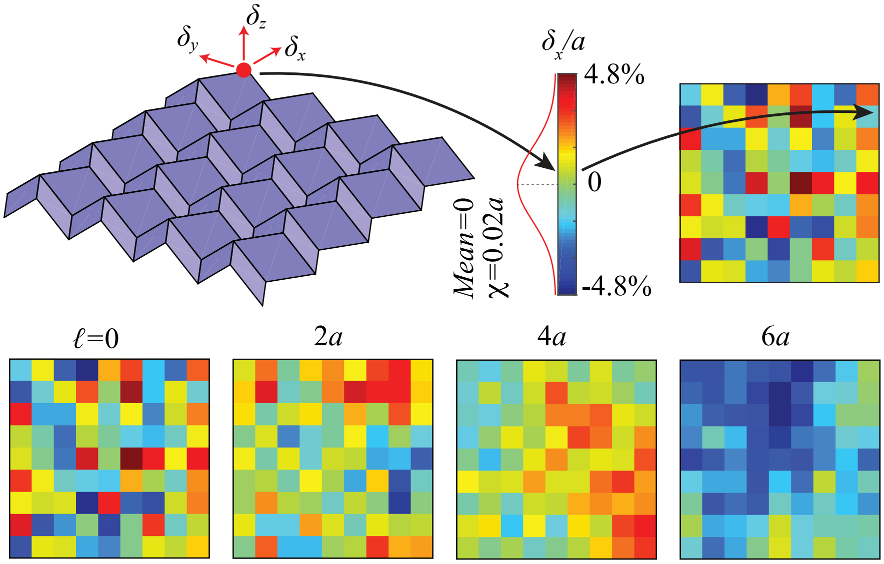

Figure 6.10: Modeling of random geometric imperfections by random fields of nodal perturbations. At each node, the perturbation is decomposed into x-, y-, and z-directions (denoted as δ_x, δ_y, and δ_z), as we assume no directional preference of the geometric imperfections. The perturbations δ_x, δ_y, and δ_z are samples independently from three random fields generated by the same statistical parameters, i.e., mean ($= 0$), standard deviation χ, and correlation length ℓ. The four colored maps demonstrate how ℓ affects spatial correlation between nodal perturbations.

For a group with a given combination of χ and ℓ, the number of samples are determined to ensure the estimated mean of $\sigma_{0.65}$ has 95% confidence to be within ± 0.1kPa from the true mean, using the following formula [127]:

$$N \geq \frac{\tilde{\chi}^2_{\sigma_{0.65}}}{w^2}\left(\Phi^{-1}\left(1-\frac{h}{2}\right)\right)^2 \tag{6.3}$$

where, $w = 0.1$, $h = 0.05$ (for 95% confidence), $\tilde{\chi}_{\sigma_{0.65}}$ is the measured standard deviation of $\sigma_{0.65}$ of the samples, and $\Phi^{(-1)}$ is the inverse of the standard normal cumulative distribution function. Based on the variance of the measure samples, the number of samples of each group could be different. The number of samples increase by multiples of 8 to utilize parallel computation on 8 cores. Each group has a minimum of 8 samples and a maximum of 240 samples. For all cases, $a = b = 25$mm, $\alpha = 60^\circ$, and $\beta_0 = 70^\circ$.

A uniform displacement load is applied to compress the numerical samples. As shown in Fig. 6.11, the σ-ε_x curves of the numerical samples display a similar trend as the physical samples. While the change of $\sigma_{0.65}$ due to imperfection has the same trend as in the experimental data, the influence of imperfection on the linear modulus E_{lin} is more obviously presented in the numerical data, as shown in Fig. 6.11. The deformation of imperfect numerical samples also displays obvious local disorder, as shown in Fig. 6.12(A). The variances shown by the error bars come from the complex effect of random imperfections on origami-based metamaterials, as each numerical sample in the same group is imposed with different nodal perturbations drawn as one realization from the same underlying random field. We remark that the larger the standard deviation of the input random nodal perturbations, the larger the variances of the observed properties of the imperfect origami metamaterials, in agreement with the experimental data.

6.3.5 Relation Between Geometry and Mechanical Response

Both the experimental and numerical results reveal that the magnitude of nodal perturbations positively correlates to the stiffness of Miura-Ori (see Fig. 6.9(B) and Fig. 6.13). Furthermore, the numerical samples show that the spatial correlation between nodal perturbations contributes negatively to the increase of stiffness, as shown in Fig. 6.13. To quantitatively describe geometric imperfections, we need a parameter that provides a consistent and continuous measure that reflects the effects of magnitude and spatial correlation. We could use (ℓ/χ) as the measure of geometric imperfection, as shown in Fig. 6.14. This

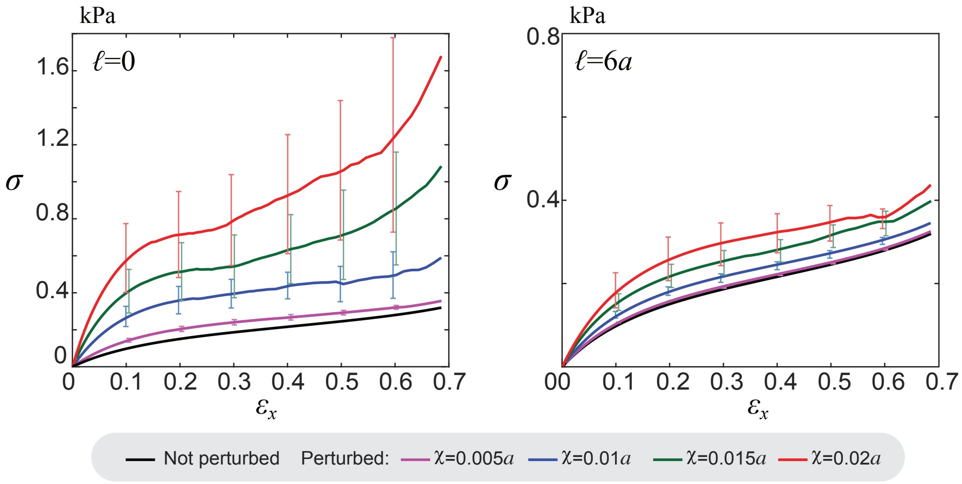

Figure 6.11: Numerical quantification of the effect of geometric imperfections. Bulk stress σ vs. compressive strain ε_x for numerical samples with $K_B/K_F = 10$. Each solid line shows the mean response of a group of samples and the error bars extend to one standard deviation.

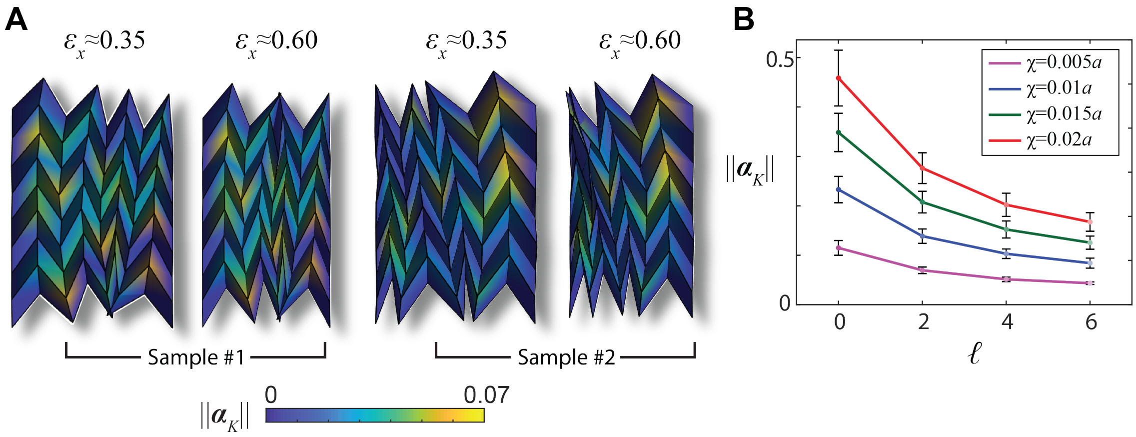

Figure 6.12: Quantification of geometric imperfections in terms of Kawasaki excess. (A) Snapshots from numerical simulation of a perturbed sample with $\chi = 0.02a$ and $\ell = 0$. The varying color indicates the absolute value of Kawasaki excess $||\alpha_K||$ at each vertex. (B) Change of global Kawasaki excess $||\alpha_K||$ as χ and ℓ vary. The error bars extend to one standard deviation. For all cases, $\alpha = 60°$, $\beta_0 = 70°$.

ratio is independent of the size of the origami (quantified by panel edge length a), however, such measure may lead to ambiguities among sample groups with $\ell = 0$.

Owing to its simplicity and relevance, the Kawasaki excess [101] offers a good measure of the random geometric imperfection (as introduced in Fig. 6.1(C)). The Kawasaki theorem states that the flat-foldability of an origami vertex is equivalent to $\alpha_K = 0$ [101].

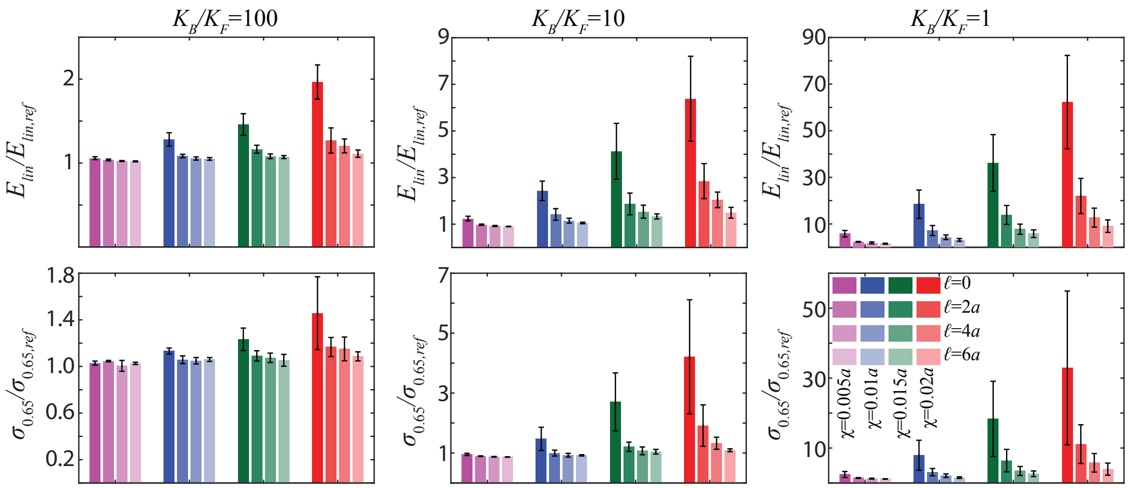

Figure 6.13: E_{lin} and $\sigma_{0.65}$ of sample groups with different material parameters. Each black error bar extends to one standard deviation. The ratio of K_B/K_F reflects the relative stiffness between bending and folding deformations. For all cases, $a = b = 25$mm, $\alpha = 60°$, and $\beta_0 = 70°$.

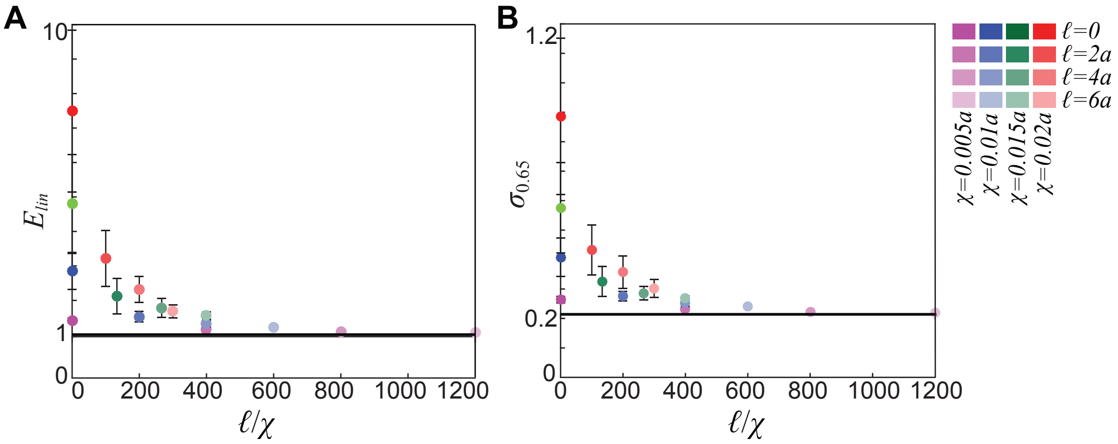

Figure 6.14: Mechanical properties vs. relative imperfection measured as ℓ/χ. Each solid dot shows the mean response of a group of samples and the error bars extend to one standard deviation. The black solid line refers to the obtained values from the unperturbed Miura-Ori. All samples have $\alpha = 60°$, $\beta_0 = 70°$, and $K_B/K_F = 10$. The E_{lin} and $\sigma_{0.65}$ are in units of kPa.

For a multi-vertex origami, we collect the vertex-wise α_K into a vector $\boldsymbol{\alpha_K}$, and define the Kawasaki excess of an multi-vertex origami as the L2-norm of the Kawasaki excess vector (i.e., $||\boldsymbol{\alpha_K}||$). It is sufficient that if $||\boldsymbol{\alpha_K}|| \neq 0$, the pattern loses global flat-foldability. As shown in Fig. 6.12(B), $||\boldsymbol{\alpha_K}||$ increases as χ increases, and decreases as ℓ increases,

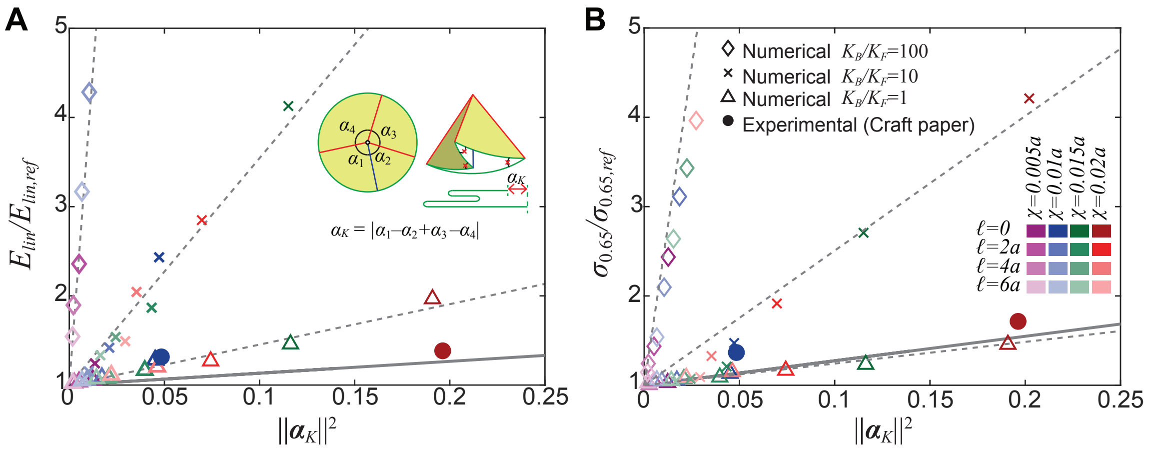

Figure 6.15: Connection between origami geometric design constraint with metamaterial mechanical properties. (A) The square of Kawasaki excess $||\alpha_K||^2$ vs. the normalized mean values of E_{lin}. Each straight line is obtained from linear regression of all data points belonging the samples with the same material properties. The slopes of the linear trend lines are given by: $S_{(E,\diamond)} = 283.20$ ($K_B/K_F = 100$), $S_{(E,\times)} = 25.44$ ($K_B/K_F = 10$), $S_{(E,\triangle)} = 4.54$ ($K_B/K_F = 1$), $S_{(E,Exp)} = 1.33$ (Craft paper). Each marker represents the mean value $\langle E_{lin} \rangle$ of a certain group of samples. (B) The square of Kawasaki excess $||\alpha||^2$ vs. the normalized mean values of $\sigma_{0.65}$. We obtain $S_{(\sigma,\diamond)} = 142.92$, $S_{(\sigma,\times)} = 15.07$, $S_{(\sigma,\triangle)} = 2.42$, and $S_{(\sigma,Exp)} = 2.74$. Inset legend in (B) explains the colors and shapes of the markers in both (A) and (B). Note that the linear regression is performed on all data points of a material (i.e., entire cluster), however, the dots only show the means of the clusters.

reflecting similar effect of χ and ℓ on E_{lin} and $\sigma_{0.65}$. For an imperfect Miura-Ori, as we keep compressing, the origami metamaterial becomes very stiff before it can be folded flat, indicating that its flat-foldability is destroyed by the random imperfections. Furthermore, as shown in Fig. 6.12(A), at the local level, we can clearly see that origami vertices with higher Kawasaki excess appear to be stiffer in folding than vertices with smaller Kawasaki excess, contributing to the increase of global stiffness. Therefore, we may conjecture that flat-foldability is a geometric feature that causes the change of mechanical properties of imperfect Miura-Ori metamaterials.

Indeed, we discover that both $\langle E_{lin} \rangle$ and $\langle \sigma_{0.65} \rangle$ (normalized by the reference values based on unperturbed samples) correlate with the square of Kawasaki excess $||\alpha_K||^2$, as shown in Fig. 6.15. The slope of each line reflects the sensitivity of samples made with the same materials to random geometric imperfections. Therefore, the average compressive modulus and plateau stress of geometrically imperfect Miura-Ori can be estimated as

$$\frac{\langle E_{lin} \rangle}{E_{lin,ref}} = S_E ||\alpha_K||^2 + 1, \frac{\langle \sigma_{0.65} \rangle}{\sigma_{0.65,ref}} = S_\sigma ||\alpha_K||^2 + 1 \tag{6.4}$$

The samples with higher K_B/K_F ratio are more sensitive to geometric imperfections. The response of the craft paper samples (with $K_B/K_F = 6.8$) is expected to be between the lines of $K_B/K_F = 1$ and $K_B/K_F = 10$ from the numerical data (tuned by the properties of the craft paper), which is true for $\langle \sigma_{0.65} \rangle$ of the craft paper samples. However, the sensitivity of experimental samples is generally lower than what we expected for both $\langle \sigma_{0.65} \rangle$ and $\langle E_{lin} \rangle$. There are several possible reasons. First, in the numerical models, the creases always hold their continuity, while in the physical models, the perforated creases (especially their intersecting nodes) can be pulled apart by small gaps, which compensate for the violation of strong kinematic constraint imposed by the geometric continuity, and thus mitigate the effect of geometric imperfection (Fig. 6.2). Second, the numerical models are elastic while the physical models are inelastic. Lastly, the material variabilities could also be a contributing factor for this discrepancy, as it reduces the statistical significance of observations related to geometric imperfections. Although not compared with the numerical model as the material parameters (i.e., K_S and K_B) in the numerical models are tuned only with the craft paper, similar linear correlation is seen in the polyester film samples and composite samples, as shown in Fig. 6.16. For the experimental samples made with three different materials, the correlations between the pair of $\langle E_{lin} \rangle$ and $||\boldsymbol{\alpha_K}||^2$ are not as strong as the pair of $\langle \sigma_{0.65} \rangle$ and $||\boldsymbol{\alpha_K}||^2$, while the numerical samples present clear correlations for both pairs. This discrepancy seems to suggest that the influence of material variabilities is larger at small strains but not at large strains.

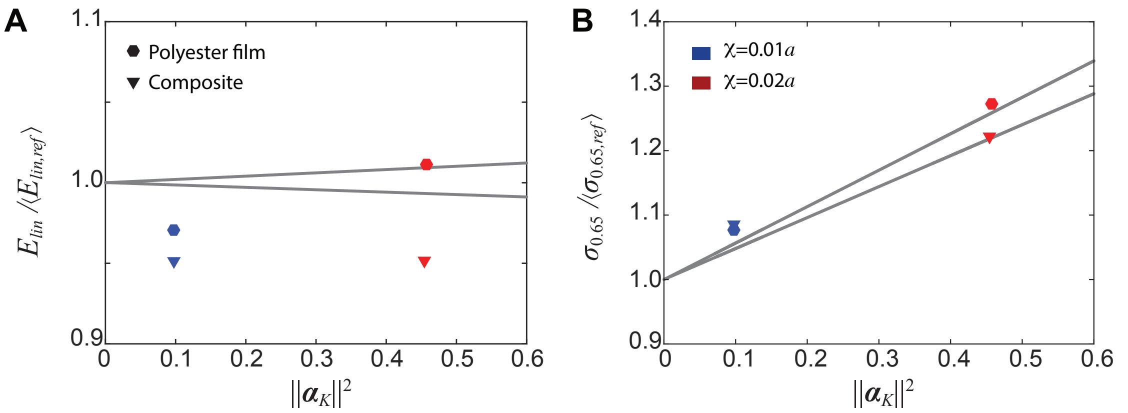

Figure 6.16: The normalized mean values of (A) E_{lin} and (B) $\sigma_{0.65}$ vs. the square of Kawasaki excess $||\boldsymbol{\alpha_K}||^2$ for the polyester film samples and composite samples. The linear regression is performed on all data points of a material (i.e. entire cluster), however, the dots only show the means of the clusters.

6.3.6 Other observations related to geometric imperfections

Another interesting phenomenon that we observed is that relatively large degree of random geometric imperfections may lead to instability, as we observe strain softening from some numerical samples, which is also recorded in a few polyester film samples and composite samples (see Fig. 6.17). Such phenomenon shows a connection with the observations by Dudte et al. [117] that the flat-foldability residual (defined similarly to the Kawasaki excess) enables energy barrier between two configurations during form-find of curved Miura-Ori patterns.

We find no significant change of effective global in-plane Poisson's ratio due to imperfections, based on the numerical analyses. However, it is difficult to make a clear argument about the effect on Poisson's ratio, as the local distortion can be quite large (Fig. 6.7). As a result, based on the size of the local region over which the Poisson's ratio is defined, we could reach at different conclusions. However, we remark that these are not the main focus of this study, they are mentioned here to demonstrate the complex influence of random geometric imperfections on the behavior of origami-based metamaterials.

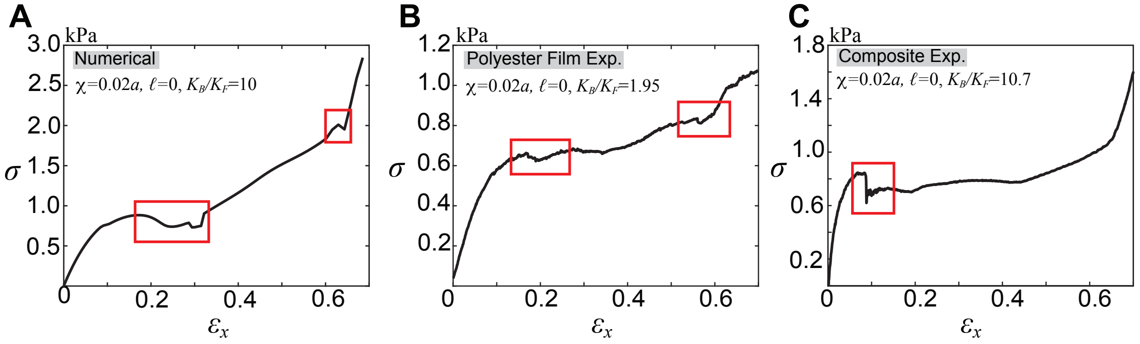

Figure 6.17: Examples of unstable strain softening, highlighted by red boxes, on perturbed Miura-Ori metamaterials from (A) numerical and (B,C) experimental measurements. For perturbed samples with small χ or large ℓ, this phenomenon is rarely seen. Instability seems to be induced by relatively large geometric imperfections.

6.4 Concluding Remarks

We conclude that *small random geometric imperfections change the mechanical properties of origami-based metamaterials*. In this work, a quantitative investigation is carried out by a representative case study on the popular Miura-Ori, which serves as the building block for many origami-based metamaterials. Therefore, our results have direct implications on all Miura-Ori based metamaterials. Moreover, the conceptual framework introduced in this research can potentially be extended to other patterns, such as the metric of Kawasaki excess for flat-foldable patterns. For non-flat-foldable patterns, the Kawasaki excess may be rewritten as the difference between the Kawasaki excess of an imperfect pattern and its standard version. However, to obtain the exact properties of a piece of imperfect origami-based metamaterial, a thorough case study is always needed.

We conduct experimental and numerical analyses to reveal that small geometric imperfections may significantly increase the compressive stiffness of Miura-Ori. Owing to the random nature of the geometric imperfections, we notice relatively large standard deviations in observations, which is part of the physics of the problem being investigated. Because it is not representative to look at specific properties of each individual imperfect sample, in this research, we focus on the statistical average behavior of imperfect samples.

Indeed, we are able to find shared trends among imperfect samples made with different materials, both experimentally and numerically, which help us to make general predictions on the influence of geometric imperfections. In particular, we find that the linear modulus and plateau stress of imperfect Miura-Ori metamaterial correlate to the square of its Kawasaki excess, which is a purely geometric metric based on the vertex sector angles that reflect the degree of imperfections.

We notice that a higher degree of random geometric imperfections significantly amplifies the variance of origami-based metamaterials' mechanical properties, which is, in general, undesirable and has to be considered cautiously in applications. However, for applications such as energy storage and dissipation [128, 129], geometric imperfections may be beneficial as they raise stored energy (i.e., area below the $\sigma - \varepsilon_x$ curve). Furthermore, one may exploit random geometric imperfections to purposely modify the behavior of origami-based metamaterials, similar to intentional imperfections [2, 119]. For example, we can introduce unevenly distributed imperfections to achieve functionally graded stiffness (Fig. 6.1(A)), or create designated local deformations (Fig. 6.18). Moving forward, much work remains to be done, for instance, investigating the effect of geometric imperfections for other deformation modes and origami patterns, in order to bring the theoretical advantages of origami [129] to real applications.

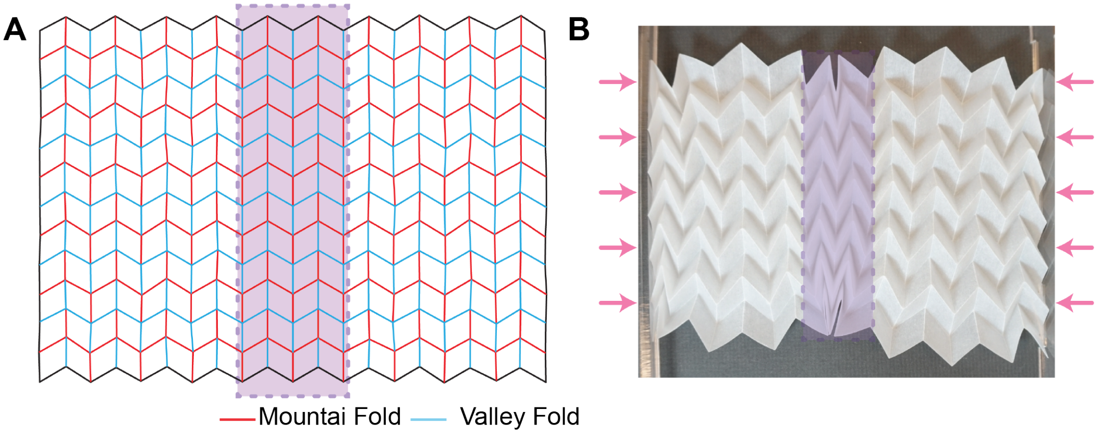

Figure 6.18: Purposely induced local deformation concentration by random perturbations. (A) Crease pattern, where the purple region represents the unperturbed portion. (B) The folded pattern under in-plane compression. Notice that the unperturbed region contracts more in the lateral direction than the perturbed portion because of the negative Poisson's ratio of Miura-Ori.

CHAPTER 7
CONCLUSIONS AND FUTURE WORK

In this thesis, we investigated origami systems from a practical point of view and proposed solutions for challenges that have limited the application of those systems in material, electrical, civil, aerospace, biomedical, and other engineering fields. The challenges we addressed include effect of geometric imperfections, actuation strategy, and manufacturing across scales. Throughout the thesis, we designed, fabricated, and tested multifunctional origami systems, including architected materials with remarkable mechanical properties (e.g., stiffness and Poisson's ratio tunable anisotropy, large degree of shape recoverability, and reversible auxeticity), tunable electromagnetic structures, and untethered robots capable of computing and sensing. In this final chapter, we summarize the main contributions of this thesis and provide suggestions for future work.

7.1 Summary

In *Chapter 1*, we introduced Origami Engineering and its challenges. We also introduce the key ideas that are investigated in the following chapter. In this chapter, important concepts and theorems are used in the subsequent chapters are also introduced.

In *Chapter 2*, we presented a didactic approach for the understanding and solution of the fold-and-one-cut problem. This educational chapter presents examples with increasing complexity, allowing for the gradual understanding of the problem. Our educational approach proposes an initial guess that leads to a systematic approach for the mountain/valley assignment of the crease lines. This approach significantly simplifies the decision process for crease assignment.

In *Chapter 3*, we took advantage of the intrinsic scalability of origami assemblies and the microscale features (e.g., plate thickness) enabled by two-photon direct laser writing to design and fabricate a micro-origami metamaterial that displays a combination of mechanical properties without precedents: stiffness and Poisson's ratio tunable anisotropy, a significant degree of shape recoverability, multistability, and even reversible auxeticity. We showed that the mechanical properties obtained via in situ SEM experimentation match our purely geometric predictions. By deriving the analytical expression for the Poisson's Ratio of the metamaterial, we could geometrically design metamaterials with reversible auxeticity (i.e., the metamaterial switches Poisson's ratio sign during deformation).

In *Chapter 4*, we showed a tunable frequency selective surfaces that uses origami as a substrate and that changes its response as we fold and deploy the origami pattern. We showed that stacking multiple layers of those structures results in a broader bandwidth. Also, we provided a prototyping process that takes advantage of the pattern developability and allows for repeatability. We created Miura-Ori-based FSS structures that feature the unprecedented capability of on-the-fly reconfigurability to different specifications (e.g., multiple bands, broadband/ narrowband bandwidth, wide-angle of incidence rejection). Although we focused on the Miura-Ori pattern as a substrate for the dipole elements, we believe that the same approach applies to other developable tessellations to create tunable FSS. Non-developable tessellations can be fabricated with our approach. However, the manufacturing process becomes cumbersome and less precise because these patterns need to be assembled and glued. Furthermore, multi-layer origami-based-FSS can be developed from developable tessellation with compatible in-plane kinematics [85], which is the case for some Miura-Ori derivatives [86] and some kirigami patterns[88].

In *Chapter 5*, we closed the gap that exists in most origami applications by providing an actuation solution that acts locally and remotely on complex origami assemblies. We propose a coupling between magnetic-responsive materials with a bi-stable origami pattern, eliminating the need for explicit shape-locking mechanisms and allowing for a fast shape-changing and instantaneous shape-locking of those structures. Besides, we are capable of actuating complex assemblies (as opposed to single or dual unit cells) with local control.

That is, each unit cell can fold/deploy independently and on-demand. This approach is extendable to other origami materials, as the magnetic material is assembled to the unit cells. Thus, we envision a simple transition to other material systems used to fabricate origami structures, including 3D printing.

In *Chapter 6*, we study the impact of geometric imperfections that can occur during the fabrications process and/or service of origami systems. We showed from experiments and numerical simulations that *small random geometric imperfections change the mechanical properties of origami-based metamaterials*. Our analyses revealed that such imperfections might significantly increase the compressive stiffness of the origami system. Although the work is focused on the Miura-Ori, a pattern that is directly connected to many origami systems proposed in this thesis, we believe that the conceptual framework introduced in this research can potentially be extended to other patterns [85, 86, 88].

In summary, this thesis showed the potential of origami to create tunable, deployable, and multi-functional systems. We leveraged different aspects of origami patterns (e.g., scalability, developability, bi-stability, and flat-foldability) to enrich the design space by including multi-functionality and adaptability for otherwise non-tunable systems.

7.2 Future Work

This thesis provides multiple examples of how origami can be used in engineering while solving key issues that relate to the practical application of origami systems. In particular, in Chapter 6, we study the impact of geometric imperfections in origami systems. This work opened the door for new questions and possible research paths, such as:

- **General impact of geometric imperfections across patterns:** In Chapter 6, we observe that geometric imperfections can change the mechanical properties of the Miura-Ori pattern, which raises the following question: Would other origami patterns also behave in the same way? Would other patters also experience the same behavior as the Miura-Ori? To answer this question, we need a more general study that considers representative patterns with distinct features.

- **Designed geometric imperfections:** In Chapter 6, our objective was not to modify patterns to enhance or tune material properties. However, our investigations showed that this could be a path for future work. By introducing geometric imperfections in a deterministic fashion, we potentially would be able to design the patterns to display a target stiffness or even a functionally graded stiffness.

- **Geometric imperfections and multiple loading cycles:** In Chapter 6, all the samples were tested under a single load cycle. However, from Chapter 5, we see that the origami pattern's mechanical behavior can be significantly impacted over multiple loading cycles. Thus, an investigation of the influence of geometric imperfection under multiple load cycles should be performed.

- **Anisotropic sheets and Geometry:** The effect of the material anisotropy in origami patterns has not been thoroughly studied. In Appendix D, we did a preliminary study for the Miura-Ori pattern. However, a more representative study with multiples tests and distinct patterns would be beneficial for the origami community. Such a study will reveal if material anisotropy needs to be considered in the origami design.

Appendices

APPENDIX A

SINGLE AND MULTI-LAYER MIURA-FSS DESIGN

A.1 Miura-Ori Geometry

The Miura-Ori is a rigid foldable origami tessellation defined by the geometry of its rhombic-shaped panels, each of which is characterized by the two lengths a and b and the acute angle α. This pattern presents one degree of freedom, meaning that we describe its kinematics by one of the dihedral angles between panels, defined as the folding angle. Our parametrization for the Miura-Ori unit cell follows [42], where θ is used as folding angle (Fig. A.1):

$$w = 2b\xi, \quad \ell = 2a\zeta, \quad v = b(1-\xi^2)^{1/2}, \quad h = a\zeta tan(\alpha)cos(\theta/2) \tag{A.1}$$

where

$$\xi = sin(\alpha)sin(\theta/2), \quad \zeta = cos(\alpha)(1-\xi^2)^{-1/2} \tag{A.2}$$

In addition, the dihedral angle φ (Fig. A.1), which is the dihedral angle between the folded dipoles, is also expressed as a function of θ,

$$\varphi = 2\sin^{-1}(\zeta\sin(\theta/2)) \tag{A.3}$$

Multiple layers of the Miura-Ori pattern with compatible in-plane kinematics can be stacked. This compatibility is achieved if the dimensions w, ℓ and v are the same for all the layers, leaving h as an independent dimension [1, 85] (Fig. A.1). Those conditions result in the design constraints on Eq. A.4.

$$a_t = a_b\frac{cos(\alpha_b)}{cos(\alpha_t)}, \quad b_t = b_b \tag{A.4}$$

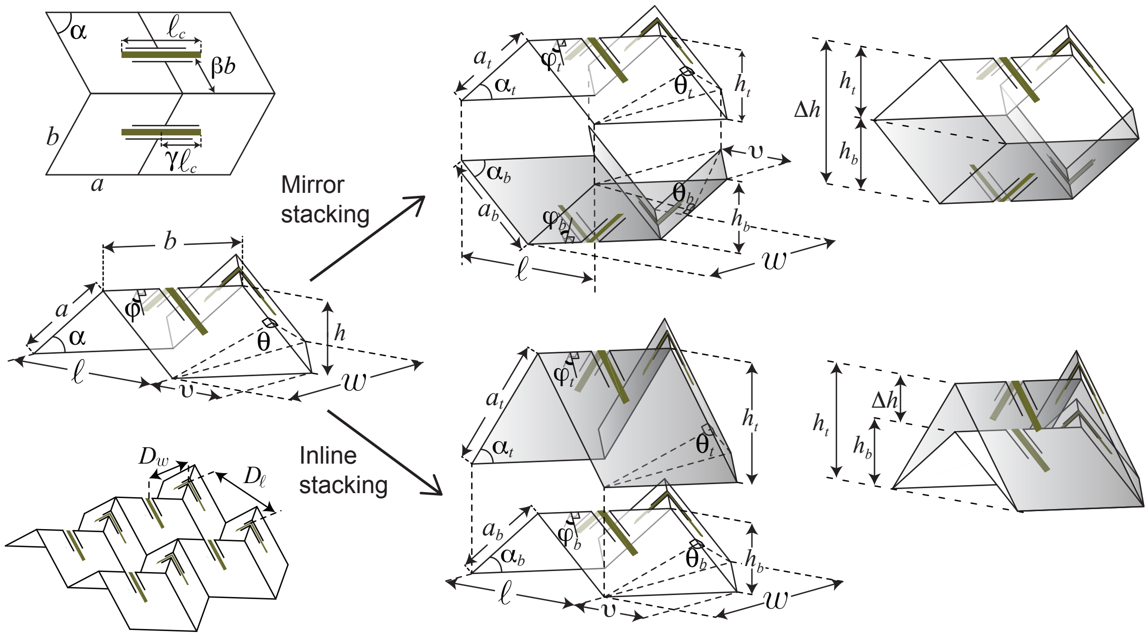

Figure A.1: Schematics of the single- and multi-layer Miura-FSS unit cells.

where, the subscript *b* and *t* represent the bottom and top layer a given Miura design parameter. In addition, because the stacking preserves the in-plane kinematics, a single dihedral angle can still be used to describe the kinematics of the stacking, thus the folding angle θ_t of the top layer can be written in terms of the bottom layer

$$sin(\theta_t/2) = \frac{sin(\alpha_b)}{sin(\alpha_t)} sin(\theta_b/2) \tag{A.5}$$

Multi-layer structures retain the flat-foldability of the Miura-Ori, that is, they can still be fully folded (i.e, folding angles $\theta_t = \theta_b = 0$). However, structures with distinct layers have the total extension of the largest layer limited by the smallest layer.When the smallest layer is fully extended ($\theta = 180°$), all the other layers will be restrained to further expansion and that will be the maximum expansion of those. Therefore, a Miura-Ori with layers with distinct geometry cannot be unfolded into a flat configuration, but it is still flat-foldable.

The maximum folding angle of each layer is defined by

$$\theta_t = 2sin^{-1}\left(\frac{sin(\alpha_b)}{sin(\alpha_t)}\right) \tag{A.6}$$

The design constraints on Eq. A.4 and the relationship between folding angles on Eq. A.5 are valid for both types of stacking. For inline stacking, we followed the Eq. A.4 to design compatible top layers for a bottom layer with fixed intrinsic geometry $a_b = 20$ mm, $b_b = 20$ mm and $\alpha_b = 45°$. On Table A.1, we report the length a_t of the panel for each panel angle α_t studied in this work. For the mirror stacking, we used identical layers, therefore the design constraints are automatically satisfied.

Table A.1: Parameters α_t and a_t of the top layer with $b_t = 20$ mm for a kinematic compatibility with a bottom layer with $a_b = 20$ mm, $b_b = 20$ mm, $\alpha_b = 45°$.

α_t	52°	56°	60°	64°	70°
a_t	22.97 mm	25.29 mm	28.28 mm	32.26 mm	41.35 mm

While in theory the mirror stacking and the bottom layer of the inline stacking are able to completely unfold, in practice, for the paper prototype, this unfolding is not trivial because of the plasticity of paper at the hinges. However, this plasticity acts in our favor because it allows the pattern to keep the angle engaged (i.e. retains the mountain and valley assignment, which is fundamental for the pattern actuation. (Fig. A.2). It is important to notice that, the use of other materials as substrate and other approaches to create hinges are possible, in which the complete unfolding is achievable.

The distances between conductor elements, D_w and D_ℓ, changes with the folding angle θ and these can be expressed in terms of the parameters w and ℓ of the unit cell, the length of the conductor line l_c, and the line position within the unit cell.

$$D_w = \beta w, \quad D_\ell = \psi \ell \tag{A.7}$$

where $\psi = \ell_c/2a$ and β is the design parameter that provides the conductor position in the

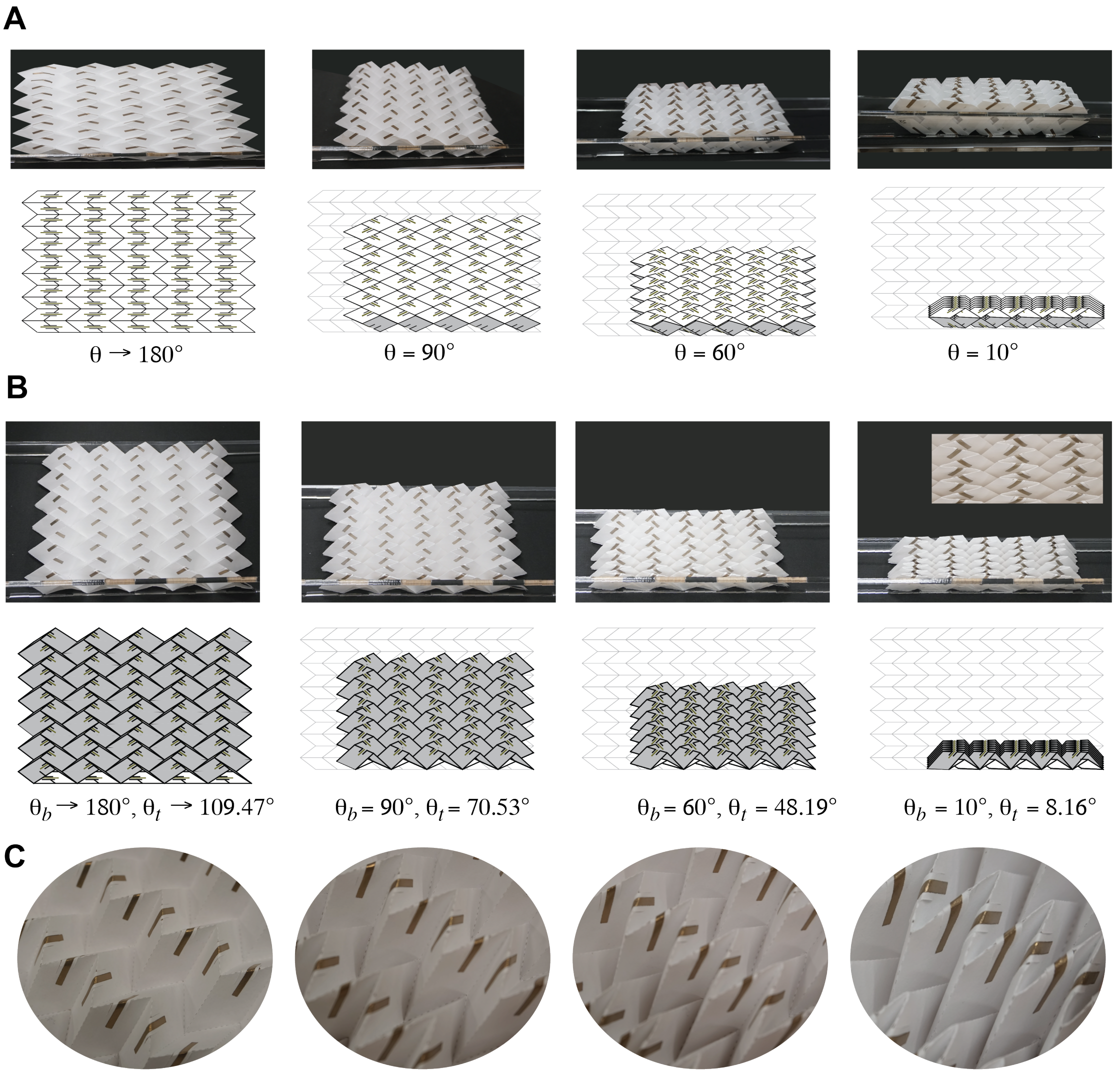

Figure A.2: Illustration of the kinematics of the (A) mirror and (B) inline stacking, and (c) Bridge-like structures in different folding stages.

unit cell (Fig. A.1). When considering multi-layer structures, the extrinsic parameters w and ℓ on Eq. A.9 are expressed in terms of the bottom layer parameters (i.e., a_b, b_b, α_b), while β and ψ refers to the specific layer where the conducts are located. For multi-layer configurations, the inter-layer distance is defined by an extra extrinsic parameter Δh. For the in-line stacking, this is expressed as

$$\Delta h = h_t - h_b \tag{A.8}$$

and for the mirror stacking

$$\Delta h = h_t + h_b \tag{A.9}$$

where for identical layers, $\Delta h = 2h_b$.

A.2 Experimental Setup

The measurement setup used to verify the simulation results consisted of a customized Miura-FSS sample holder with an integrated 3D printed frame, which was placed in the middle of two constant gain horn antennas as shown in Fig. A.3. The antennas were placed in line-of-sight of each other to realize maximum power transfer between them and were connected to a vector network analyzer (VNA) using coaxial cables. The distance between the two antennas was kept far enough such that the Miura-FSS sample was in far-field of each antenna, this is a key criterion for an FSS measurement to ensure that it is excited by a plane wave.

It is also important to note here that the fabricated Miura-FSS structure comprised of finite number of unit cells (hence finite FSS size) as opposed to the simulation setup, in which infinite array was assumed. Therefore, the fabricated Miura-FSS was made large enough such that it encloses the main beam of the antenna thereby mitigating the edge effects introduced by a finite FSS and realizing constant current distribution along resonant elements in the same fashion as in an infinite FSS [130].

One of the key challenges for the measurements of a Miura-FSS is to ensure that each Miura unit cell features the same folding angle. This was realized by using a 3D printed frame for each folding angle (i.e. $\theta = 60^\circ, 90^\circ, 120^\circ$) as shown in Fig. A.3. Moreover, the 3D printed frame along with the Miura-FSS sample was secured firmly to the rotating table so that the Miura-FSS sample was parallel to the antenna aperture for normal incidence and excited by plane waves. Finally, measurements for different angles of incidence (AoI) were made by rotating the FSS structure around $y-$axis as shown in Fig. A.3.

In this work, a two-step calibration was performed to incorporate system errors and shift the reference plane to the surface of the Miura-FSS structure. First, the effects of the VNA and coaxial cables were eliminated by using a conventional 2-port Short-Open-Load-Through (SOLT) calibration technique at the end of the coaxial cables that would be connected to the antennas. Next, a free-space Gate-Reflect-Line (GRL) calibration was performed to de-embed the region between the antennas and Miura-FSS structure. This was done by first finding the location of the Miura-FSS in time domain by comparing the return loss (as a function of time) of an empty sample holder with a metal sheet using the VNA. Then a proper time-domain gated function (according to the width of the reflected pulse) was applied to filter out any unwanted reflections. Therefore, making sure that the Miura-FSS structure was only excited by direct line-of-sight plane waves. Finally, the calibration was completed by taking reflect and line measurements by respectively placing and replacing a metal sheet with given thickness on sample holder. The quality of calibration was further improved by placing absorbers around the measurement setup to mitigate the effect of unwanted reflections from objects in its surroundings as shown in Fig. A.3.

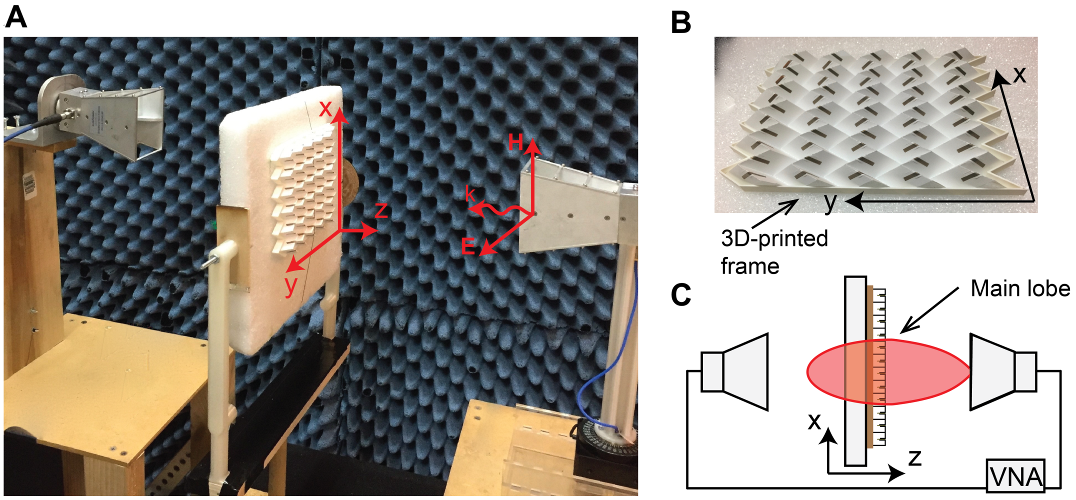

Figure A.3: Experimental setup and prototyped Miura-FSS. (A) Experiment setup, where k, **E**, and **H** are the direction of propagation, the Electric field, and the magnetic field, respectively, of the electromagnetic wave (B) Prototype with the 3D printed frame (C) Schematics of the position of the prototype relative to the main lobe of the source

A.3 Dipole position

A.3.1 Dipoles along the V-shaped creases

The unique feature of printing dipoles on the mountain creases is that in this configuration, the electrical length and the inter-element distances between the dipoles (along $y-$axis) varies linearly. This results in a very systematic, predictable and quantifiable frequency response. On the other hand, Miura-Ori geometry does not allow comparable linear shrinkage in the y-axis that would result in wider inter-element distances as the Miura-Ori geometry is folded. Therefore, the dipoles printed on the V-shaped creases may have a reduced electrical length but inter-element distances would become larger than the λ (wavelength of the operational frequency) with folding. This means that the real and imaginary part of the dipole impedance will change for different values of angle of incidence (as compared to only real part variation in the mountain fold dipoles presented in the paper) resulting in an unstable angle of incidence rejection.

Second, the shape of the dipole on the V-shaped creases is also critical. Let's consider the sub cases below:

- **Straight dipoles:** In this case, the dipoles are printed along one mountain and one valley fold (i.e., the folds parallel to the y-axis) folds of the Miura-Ori unit cell and are parallel to the x-axis as shown in Fig. A.4(A). In the folded configuration, the dipole on the mountain fold folds upwards while the one on the valley fold, folds inwards. This means that they would experience different phases from the incoming field. The phase variation would become even more pronounced at lower values of the folding angle θ where dipoles would have reduced electrical length (higher resonant frequency) and wider inter-element distances. Thereby further complicating quantification of the electromagnetic behavior of the FSS structure. The non-linearity of such FSS can be seen in Fig. A.4(C), where the resonance frequency at $\theta = 60^\circ$ is lower than the one at $\theta = 90^\circ$ even though the electrical length of the dipole is shorter for the former case. Moreover, the change in resonance frequency with folding angle is also not linear. Last, the bandwidth also decreases with folding which is primarily due to the wider inter-element distances [50]. As mentioned earlier, the wider inter-element distances give rise to an unstable angle of incidence rejection as shown in Fig. A.4(E,G) for $\theta = 180°$ and $120°$, respectively.

- **V-shape Dipoles:** In order to minimize the phase difference of the two dipoles at the two folds, a V-shaped dipole can be used as shown in Fig. A.4(B). This can introduce linear variation in the frequency response of the Miura-FSS with folding angle as shown in Fig. A.4(D). However, inter-element distance (along y-axis) is still much larger for the given dipole length used in the paper and it becomes even larger (compared to resonant frequency wavelength) as the structure is folded. This results in unstable frequency response with angle of incidence [50] as shown in Fig. A.4(F,H).

- **One dipole on V-shaped crease and one parallel to $y-$axis:** In view of the detailed explanation on the effects of inter-element distance on the FSS frequency response, we can conclude that if we place one dipole on V-shaped crease and one parallel to $y-$axis neither of them would have required inter-element distance. Thus, would also have narrow-band and unstable angle of incidence frequency response.

As a conclusion, one of the limitations of Miura-FSS structure is that it does not realize linear shrinkage in both axes. This can be realized by using other origami structures with a positive Poisson's ratio, such as the egg-box pattern. However, the egg-box is a non-developable pattern, meaning that it cannot achieve a flat sheet configuration, making the ink-jet printing of the dipoles complicated.

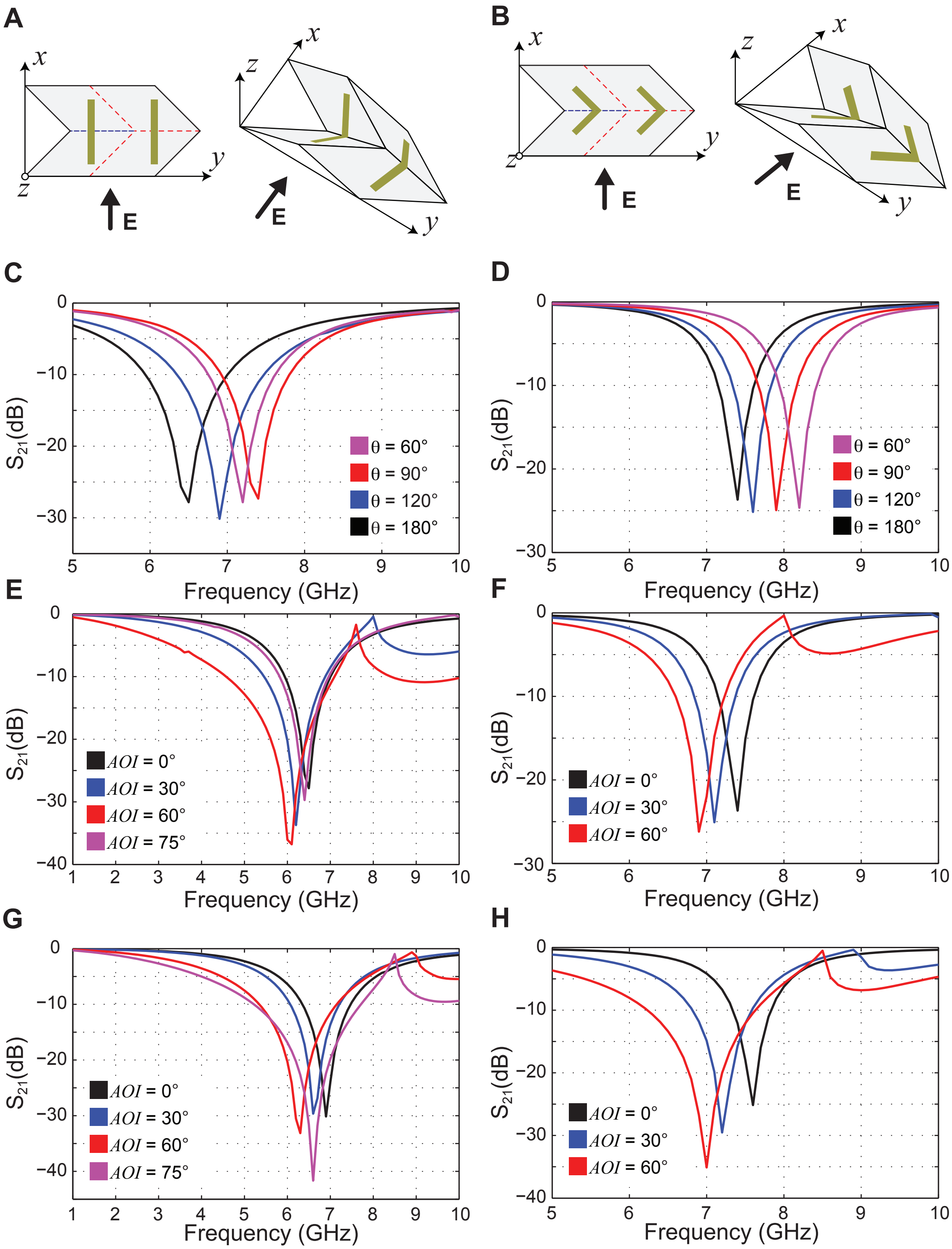

Figure A.4: Unit cell of single-layer Miura-FSS with (A) straight and (B) V-shaped dipoles placed along the V-crease mountain fold in unfolded and folded configuration ($\alpha = 45°$, $a = b = 20$ mm). Simulated S_{21} frequency response for single-layer Miura-FSS with (C) straight and (D) V-shaped dipoles for different values of folding angle θ. Simulated S_{21} frequency response for Miura-FSS with (E,G) straight and (F,H) V-shaped dipoles for different values of angle of incidence (AoI) at flat configuration $\theta = 180°$ and folded configuration $\theta = 120°$, respectively.

A.4 Specimens sensitivity

Variation in frequency response due to change in folding angle is the key to realize continuous-range frequency tunability for the proposed structure. Therefore, a quantitative measure of tolerance due to variation of folding angle across the sample is important. Typically, the complete frequency response of FSS structures is defined by both its resonance frequency and the bandwidth. For our structures (band-stop filters), maximum reflection occurs at the resonance frequency while the bandwidth is defined at the two points where the transmission curve intersects the -10dB level. That is the structure reflect at least 90% of the incident power at all frequencies points within the bandwidth of the filter. Thus, a slight shift in resonant frequency can be compensated as long as the desired resonant frequency is within its bandwidth. For example, lets consider the frequency response of a typical single-layer bandstop filter with resonance frequency f_c as shown in Fig. A.5(A) with the respective bandwidth highlighted in grey. Now if the resonant frequency shifts at f_2 we can still get good reflection as f_c lies within the (shifted) bandwidth. However, this would not be the case if the resonant frequency shifts to f_1 as value of S_{21} for f_c is more than -10dB. Therefore, the system can compensate for the shift in resonant frequency as long as its magnitude is less than -10dB. That is why very narrow band FSS are generally undesirable because it would not only require a system with very high frequency resolution (thereby increasing its cost) but would also be prone to failure with slight variation in the structure.

In order to quantify the tolerances for the proposed structure with respect to variation in folding angle long the Miura-FSS structure, we fabricated a graded Miura-Ori [131] with dipole elements. The grading allows for a Miura-FSS with different folding angles across the unit cell. We use the intrinsic parameter c (see Fig. A.5(B)) to define the grading as follows

$$c_i = (1 + (i-1)P)c_1, \quad i = 1..N \tag{A.10}$$

where i refers to the numbering of the unit cells in the x-direction, N is the total number of unit cells in the x-direction and P is the percentage of increasing. We prototype and tested models with $P = 0.02$ and $P = 0.1$ (i.e., 2% and 10% graded). We design the structure such that all the unit cells have different extension w_i in the x-direction and the same dimension ℓ, v, and h (see Figure S1). This results in the following design constraints

$$\alpha_i = \cos^{-1}\left(\frac{b_1}{b_i} cos(\alpha_1)\right), \quad i = 1..N \tag{A.11}$$

where $\alpha_1 = 45°$, $a = 20$ mm, $b_1 = 20$ mm, and $b_i = (c_1^2 + c_i^2 - b_1^2)^{1/2}$.

The folding angle of all the unit cells is defined as a function of the folding angle θ_1 of the smallest unit cell (i.e., unit cell number 1)

$$\theta_i = \sin^{-1}\left(\sin(\rho)\frac{\sin(\alpha_1)}{\sin(\alpha_i)}\right), \quad i = 1..5 \tag{A.12}$$

where

$$\rho = \cos^{-1}\left(\frac{\sin(\theta_i/2)\cos(\alpha_1)}{(1 - (\sin(\alpha_1)\sin^2(\theta_1/2))^{1/2}}\right) \tag{A.13}$$

The simulated and measured results of 0% (uniform Miura-FSS), 2% and 10% graded Miura-FSS are shown in Fig. A.5(D) with folding angle $\theta_1 = 90°$. It can be seen that the resonant frequency for uniform (0% graded) Miura-FSS can be filtered even if folding angle of each neighboring cell varies up to 10%.

A.5 Applications of shape-reconfigurable Miura-FSS

Shape-reconfigurable Miura-FSSs are good candidates for terrestrial, outer-space and electromagnetic cloaking applications over tunable frequency ranges, as well as morphing devices. Reconfigurable FSS allows a designer to use the same structure for different operational frequencies. This also helps re-tune the frequency response of the structure effectively compensating for manufacturing or installation errors or failure of some radiating elements due to environmental factors. One of the most common methods to achieve reconfigurability is to use electronic components such as diodes and varactors that become

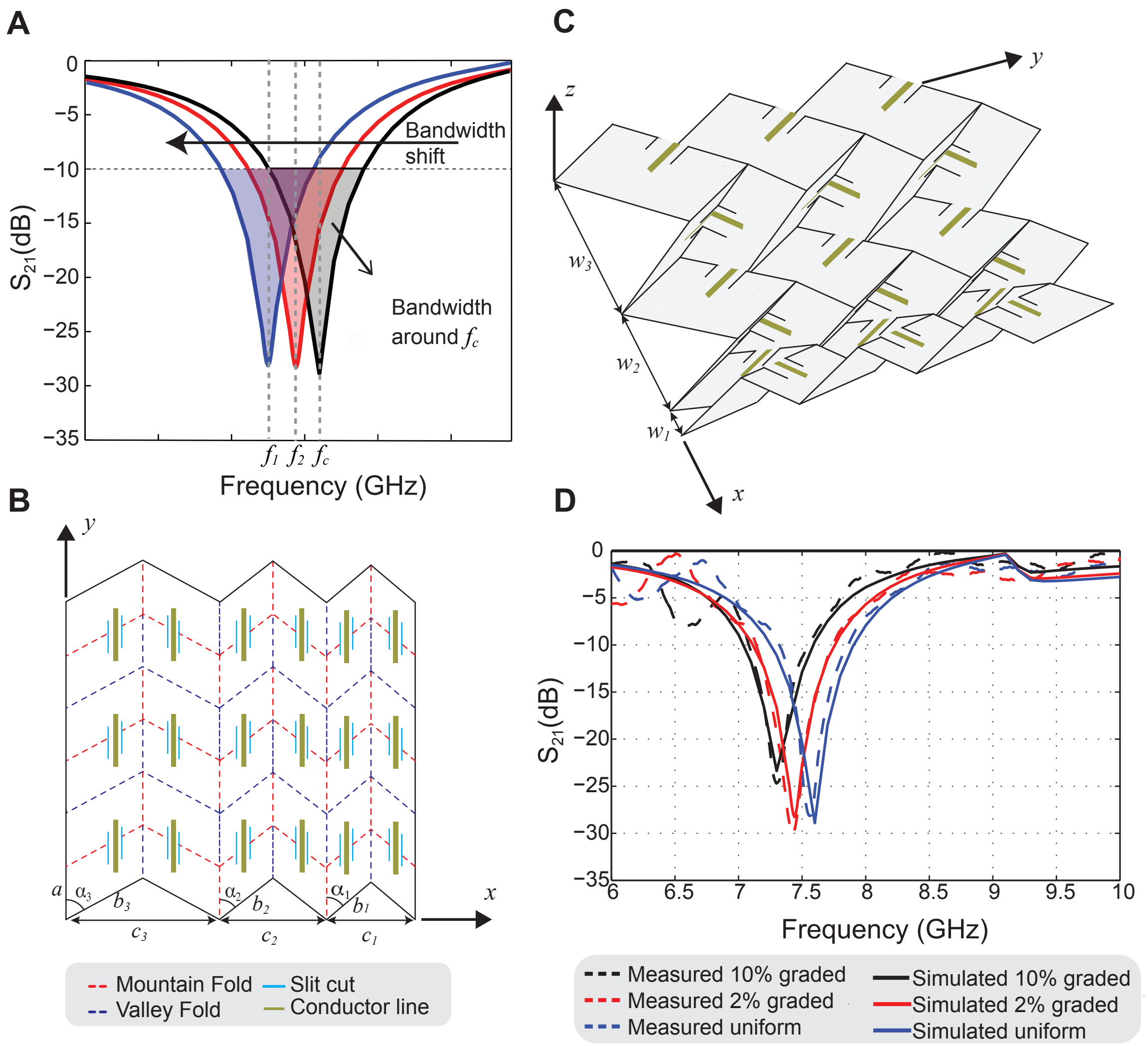

Figure A.5: (A) Schematics of the sensitivity of band-stop filters, (B) Crease pattern and (C) Miura-FSS. (D) Simulated S_{21} frequency response for a graded Miura-FSS.

expensive and complicated for increasing sizes of the FSS structure. Since these are non-linear devices, they make the overall response of the structure non-linear as well. Therefore, Miura-FSS presents a more robust mechanism to change, on-the-fly, the electromagnetic response of FSS structures without using any non-linear electronic components.

In addition to the electromagnetic reconfigurability of Miura-FSS structures, their ability to be stowed in small spaces and on-demand deployability makes them extremely important for terrestrial and outer-space applications. For example, one of the key components of the space-to-ground communication systems is the parabolic reflector that ensures high signal fidelity due to its large gain. However, its typically large size and high manufacturing cost makes it a very expensive payload especially for modern cubesats. That is why modern satellites use reflectarrays due to their planar design and ability to reflect the desired band of frequencies in a given direction. The operation principle of reflectarrays is similar to FSS except that the size of each neighboring element of a reflectarray is varied such that there is a progressive phase difference between them as opposed to FSS where the phase difference is constant between each neighboring element [132]. The amount of phase difference dictates the beam scanning ability of the reflectarrays. One of the key drawbacks of these structures is their inability to reconfigure the size of each element on-the-fly thereby limiting its beam scanning ability. On the contrary, the proposed Miura-FSS would enable us to change the size of these radiating elements on-demand by simply changing its folding angle. This would allow us to realize a deployable reflectarray with wider beam scanning ability and lower failure rate as compared to traditional reflectarrays.

Similarly, FSS structures are also used for electromangetic cloaking of metallic structures. A common figure of merit to detect the electromagnetic size of RF structures (such as antennas) for a given band of freqencies, is its radar cross-section (RCS). Typically, RCS of an antenna is reduced by either placing FSSs at the aperture (of horn antenna) or using them as a ground plane (for planar antennas e.g. patch antenna) [133]. The frequency band can be varied by using tunable FSS structures. However, traditional flat FSSs are harder to mount, complicated to reconfigure and additional biasing network for electronic reconfigurable FSS structures may not be desirable for some applications [134]. Since Miura-Ori geometry provides higher mechanical strength as well as wider frequency tunability range as compared to flat FSS, the presented Miura-FSS structures would be a better alternative in a sandwich configuration [135]. Moreover, multi-layer configuration is typically required for wide-band RCS reduction applications, which is much easier to realize using the approach presented in this work than the traditional multi-layer FSSs.

Another key application could be the design of a universal "morphing" radome that can be optimized for various operational frequencies without modifying its design. Typical radomes feature a curved or a flat configuration. While the curved radomes are extremely costly to fabricate and harder to mount, the flat radomes (comprising of FSS structures) do not offer high reconfigurability and suffer from non-linear affects mentioned earlier. On the other hand, curved Miura structures can be easily realized by varying the shape of the unit cell. This makes mass-production of radomes possible and with their ability to be stowed in small spaces, they can be transported much easily as compared to the traditional radomes. Similarly, due to their higher mechanical strength and wider frequency tunability, they can be used as the filling material in the dry walls for shielding or structural health monitoring purposes [136] that could find applicability in a variety of scenarios e.g. hospitals, radiation rooms, homes (to create localized wifi zones). From the aforementioned, there is a broad range of applications of shape-reconfigurable Miura-FSS.

APPENDIX B

MECHANICAL TESTING DEVICE

In Chapters 4, 5 and 6, we characterized the mechanical behaviour of the origami patterns, the bending stiffness of the panels, and the folding stiffness of the hinges using the customised mechanical testing bed shown in Figures B.1 and B.2. The setup consists of two parts: (1) A test frame (Fig. B.1) that offers a vertical support for the sample and that integrates two steel plates, a stepper motor (STP-MTR-23079, SureStep), and a 50N capacity load cell (RSP1, Loadstar Sensors) with accuracy of 0.02% full scale and its I/O module (DI-1000U, Loadstar Sensors), and (2) a hardware component box (Fig. B.2) that integrates the microstepping drive (STP-DRV-6575, SureStep), the stepper motor power supply (STP-MTR-23079, SureStep), and the data acquisition device (DAQ) (National Instruments). Note that although the machine is equipped with a string pot, we did not use it to measure the applied displacement. Instead, we collect the displacement based on the number of rotations done by the stepper motor. We use a Lab-VIEW program to control the system and acquire data.

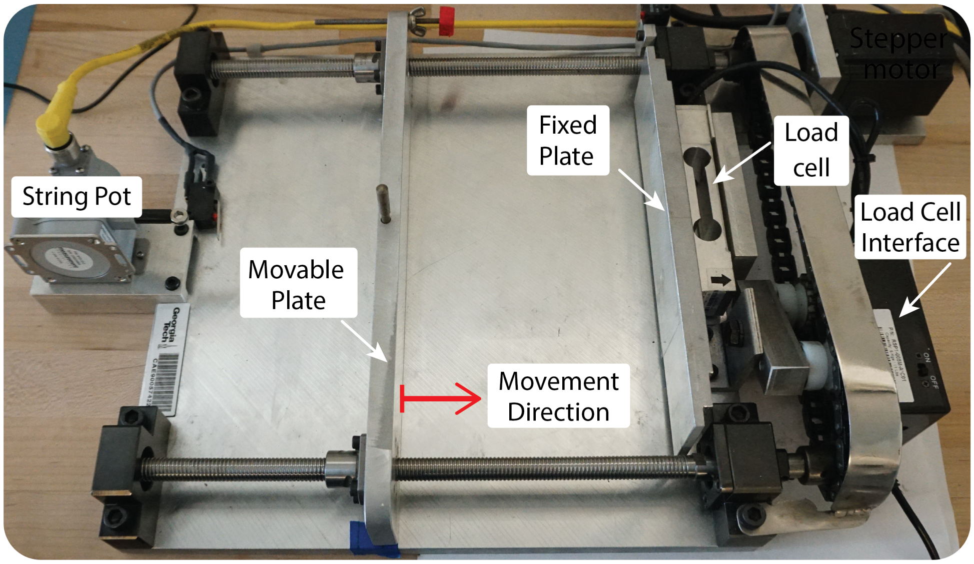

Figure B.1: Testing frame of the customised mechanical testing bed.

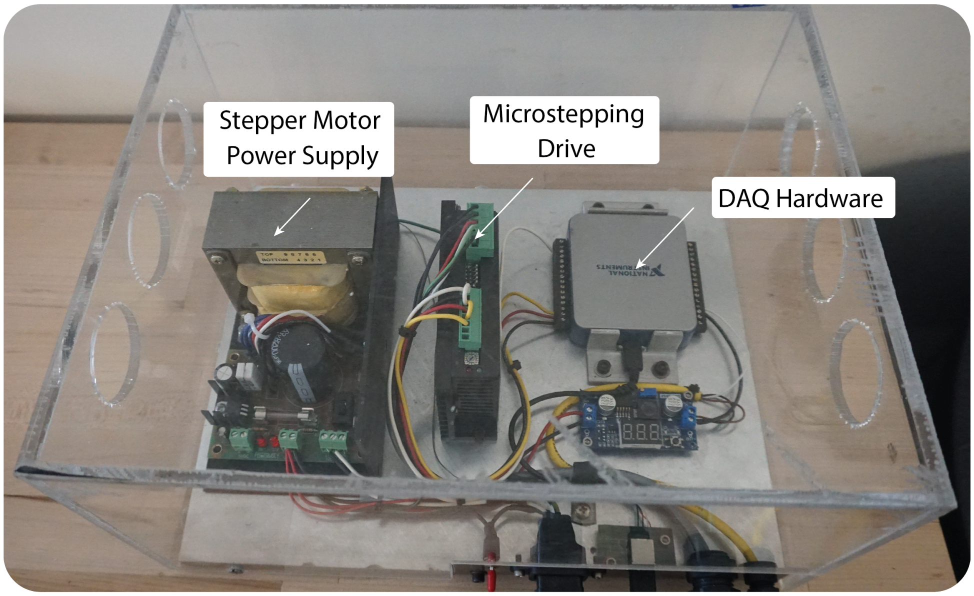

Figure B.2: Hardware components of the customised mechanical testing bed.

APPENDIX C

KRESLING PATTERN GEOMETRY, DESIGN, AND MAGNETIC ACTUATION

C.1 Kresling Pattern Geometry and Design

C.1.1 Geometry

We engineer the Kresling pattern [137, 93] to obtain desired mechanical properties and precise actuation. From a geometry perspective, the Kresling pattern is a non-rigid origami and presents two stable states per unit cell. That means that each unit cell cannot transition between those two stable states through the folding of the hinges alone. Each unit cell is tessellated with triangulated panels of equal geometry, that is, same panel angle α and lengths a and b (Fig. C.1). The geometrical assemblages are composed of multiple unit cells N, with the same or distinct geometry, that behave independently from each other. In fact, because each unit cell has two stable states, we can have 2^N stable states.

The vertices of the triangles, when folded, all lie on the top and bottom polygon circumscribed circles. Those polygons twist in relation to each other, and the angle between them is the twisting angle (ψ). This angle varies from ψ_1 (deployed) to ψ_0 (folded) as the unit cell is folded, showing the coupling between rotation and axial displacement. The Kresling pattern is designed based on the height of the unit cell in the two stable states (i.e., H_0 and H), number n of polygon edges, and corresponding edge lengths, b. From those parameters, we compute the design parameters of the crease pattern. That is, panel length a and angle α, as provided in [101]

$$\alpha = \cos^{-1}\left(\frac{x_2(x_2 - \cot(\pi/n))}{\sqrt{((x_2^2+1)(h_0^2(x_2^2+1) + x_2^2\csc(\pi/n)^2))}}\right) \tag{C1}$$

$$a = b\sqrt{h_0^2 + \frac{x_2^2 \csc(\pi/n)^2}{(x_2^2+1)}} \tag{C2}$$

$$c = b\frac{\sqrt{(h_0^2(x_2^2+1)^2 + x_2^3\cot(\pi/n)(x_2\cot(\pi/n)+2) + x_2^2)}}{(x_2^2+1)} \tag{C3}$$

where $h_0 = H_0/b$, $h = H/b$, and

$$x_1 = 2\sin(\pi/n)\frac{(\sin(\pi/n)\sqrt{(\cot(\pi/n)^2\csc(\pi/n)^2 - (h^2-h_0^2)^2)} - \cos(\pi/n))}{1 + h^2 - h_0^2 + (1 - h^2 + h_0^2)\cos(2\pi/n)} \tag{C4}$$

$$x_2 = 2\sin(\pi/n)\frac{(\sin(\pi/n)\sqrt{(\cot(\pi/n)^2\csc(\pi/n)^2 - (h^2-h_0^2)^2)} - \cos(\pi/n))}{1 - h^2 + h_0^2 + (1 + h^2 - h_0^2)\cos(2\pi/n)} \tag{C5}$$

The twisting angles in the two stable configurations are computed as

$$\psi_1 = 2\tan^{-1}x_1, \quad \psi_0 = 2\tan^{-1}x_2 \tag{C6}$$

When the twisting angle between bottom and top vertices of a valley fold is equal to $180°$, that is $\psi_0 = \pi - 2\pi/n$, the valley folds meet at the center, making this a critical design. If $\psi_0 > \pi - 2\pi/n$, the pattern will experience contact among its panels and will not be able to reach the folded stable state. This angle restriction results in a design constraint on the choice of the height difference between stable states [101],

$$|H^2 - H_0^2| \leq b^2\cot^2(\pi/n) \tag{C7}$$

Because we work with compact assemblies that have large changes in geometry, we opt for flat-foldable designs, that is, we design the unit cells to have zero height on the folded state ($H_0 = 0$). In addition, all the designs are based on hexagons ($n = 6$) with sides length

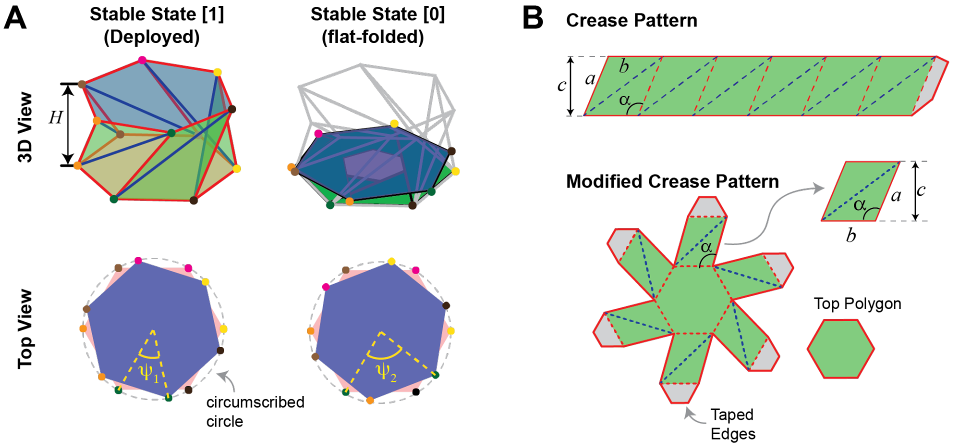

Figure C.1: Kresling pattern (A) geometry and (B) crease pattern.

Table C.1: Geometry of the Kresling Unit Cells

Design	H (mm)	α	c (mm)	a (mm)	ψ_1	ψ_0	$\Delta\psi$
1	15.6	107.72°	16.66	17.34	35.44°	84.56°	49.12°
2	16.9	105.40°	17.60	18.26	30.80°	89.20°	58.40°
3	18.2	102.77°	18.61	19.08	25.54°	94.46°	68.92°
4	20.8	96.18°	20.87	20.99	12.35°	107.65°	95.30°

$b = 13$mm, resulting on height restriction of $H_{crit} = 22.52$mm. Respecting this design constraint, we investigate unit cells with $H = 15.6$mm, 16.9mm, 18.2mm, and 20.8mm (see Table C.1). For each unit cell, we define the folded and deployed stable states as state $\{0\}$ and state $\{1\}$, respectively (Fig. C.1(A)).

C.1.2 Mechanics

Geometrically, the Kresling pattern always presents bi-stability, with an energy barrier correlated to the height of the unit cell. However, this statement is only valid under the assumption of hinges with zero stiffness. In reality, the crease lines store energy as we fold the pattern, making the existence of bi-stability dependent on the material properties of both hinges and panels.

To guide our design, we simulate the unit cells with distinct heights (Fig. C.2) using the MERLIN software [81]. This software uses a non-linear formulation combined with the modified generalized displacement control method [138], which allows tracking of the complete equilibrium path, even for structures displaying snap-type behavior, as is the case of the Kresling pattern. The MERLIN software uses a reduced order model (know as the bar-and-hinge model) [1, 124] that considers the crease lines as bars with rotational springs along them. For non-triangular (quadrilateral) panels, this model adds an extra bar along the panels' shortest diagonals to avoid mechanisms and to approximate the bending of the panels. However, because the Kresling pattern is already tessellated by triangles, the simulation will not consider any bending of the panels and consider that all the deformation occurs either by the folding of the hinges or stretching of the crease lines and panels. The reduced order model provides information on the global behavior of the unit cell and how the geometry is correlated with the energy barrier between stable states [81].

C.1.3 Mechanical Properties of the Four-Cell Kresling Assembly

We investigate the mechanical tunability of the four-cell Kresling assembly (Fig. 5.7(D,E)) by axial compression of the assembly at all sixteen stable states. The assembly is composed of unit cells with designs 1 to 4 (top to bottom) presented in Table C.1. However, because the folded unit cells (state $\{0\}$) are not completely flat-folded during the experiments, we decided to remove them for a better quantification of the stiffness of the assembly in each state. Thus, we test only the unit cells that are deployed. For example, the quantification of the stiffness of the stable state $\{1001\}$ involves testing the assembly using only the unit cells with design 1 and 4.

For each one of the sixteen stable states, we test the same assembly sample under compression three times using the experiment setup #1. That is, the assembly has one end attached to the sample holder, and the other end is free. The legend in Fig. C.3 refers to the stable state of the unit cells (from bottom to top), and it is in this figure that we show the averaged force-displacement curves for all three tests in each of the stable states.

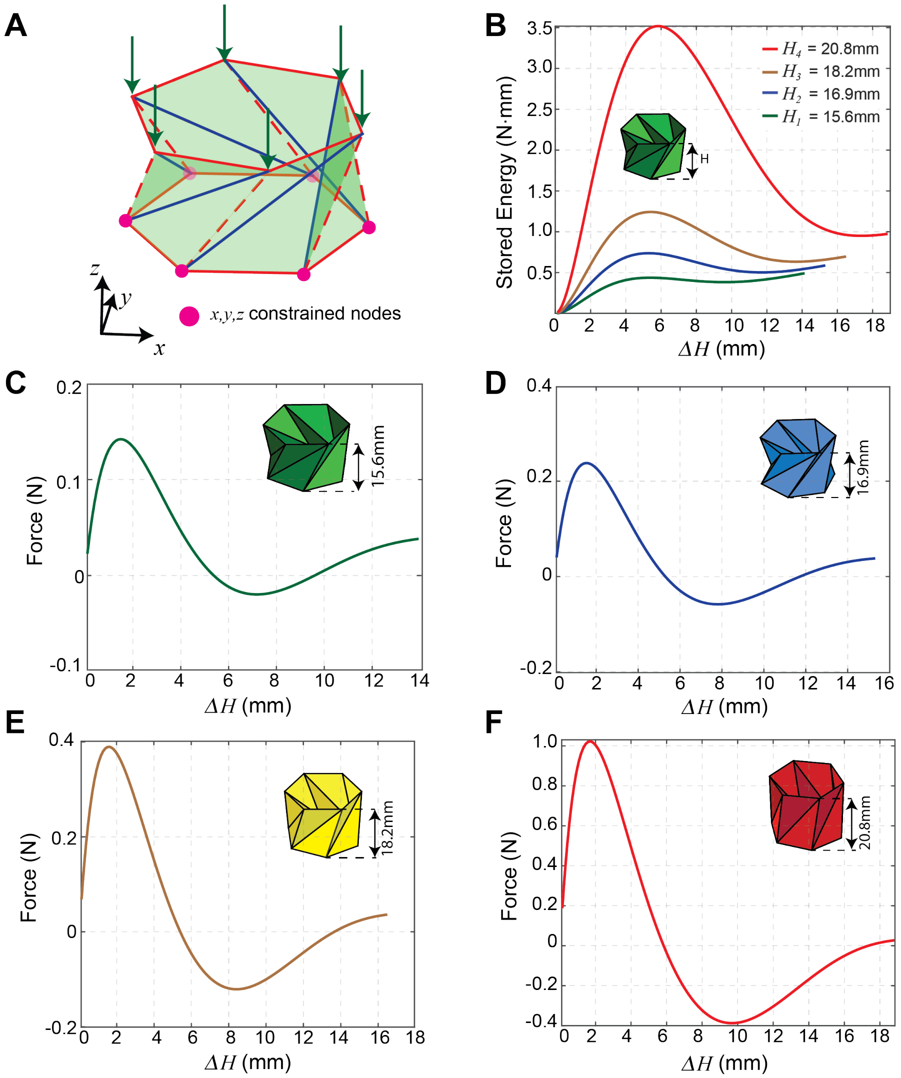

Figure C.2: Simulation of the Kresling unit cell used to guide the geometric design. (A) Bar-and-hinge model representing the unit cell. Valley folds (blue lines) are modeled by bars with area $A \approx t \times b$, where the paper thickness $t = 0.1$mm and $b = 13$mm, and rotational springs with stiffness $k_f = 2.4 \times 10^{-3}$N·mm/mm/rad. Mountain folds with slit cuts (dashed lines) are modeled as bars with area $A_{slit} \approx 0.5A$ and rotational springs with stiffness $k_{slit} \approx 0.01k_f$. Arrows represent the direction of applied displacement $0.9H_i$ $(i = 1..4)$. (B) Stored energy vs. displacement curve. Force-displacement curves for (C) Design 1 ($H_1 = 15.6$mm), (D) Design 2 ($H_2 = 16.9$mm), (E) Design 3 ($H_3 = 18.2$mm), and (F) Design 4 ($H_4 = 20.8$mm).

By comparing those curves, we observe a dramatic change in the mechanical behavior between some of the stable states, showing that we can use our actuation method to tailor the mechanical properties of a Kresling metamaterial.

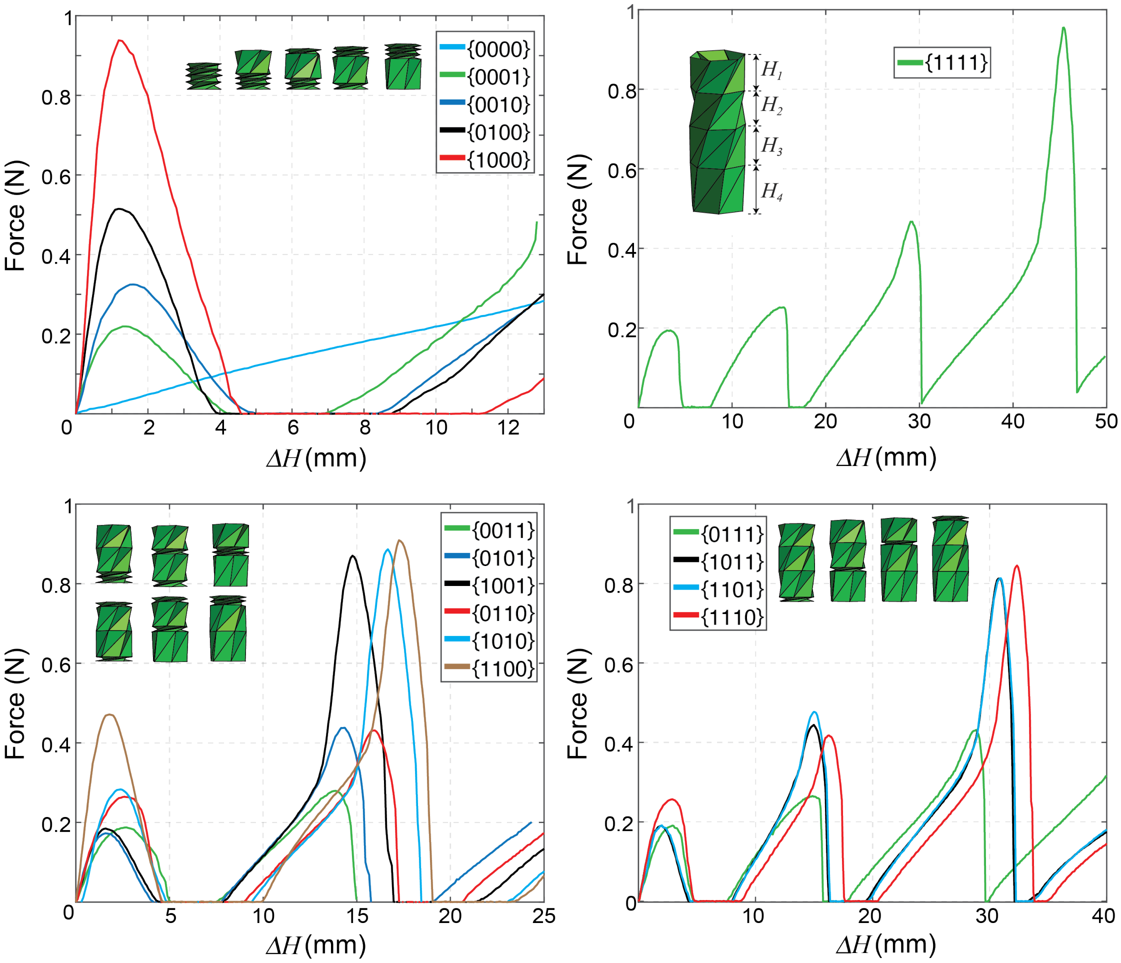

Figure C.3: Average force-displacement curves of the sixteen stable states of the four-cell Kresling assembly, where $H_1 = 15.6$mm, $H_2 = 16.9$mm, $H_3 = 18.2$mm, and $H_4 = 20.8$mm. For this test, we use setup #1 (Fig. 5.11). Legend refers to the state of each unit cell (bottom to top).

From the force-displacement curves, we obtain the stiffness K. This stiffness is defined as the slope of the first linear region of the force-displacement curves. In Fig. 5.7(E), we compare theoretical values of the equivalent stiffness for each state with the measured values. The theoretical values are obtained from the simplification of the four-cell assembly to a system of springs in series, where the stiffness of each spring corresponds to the stiffness of each unit cell that is obtained from the compression test. Thus, we compute the theoretical stiffness K_{eq} as

$$\frac{1}{K_{eq}} = \sum_{i=1}^{N} \frac{1}{K_i}, \tag{C8}$$

where K_i is the stiffness of each spring (i.e., unit cell) i in the deployed state and N is the number of deployed unit cells. Because the values of K_i are obtained experimentally, in Fig. 5.7(E), we provide the theoretical values computed with the averaged (columns), maximum and minimum (error bars) stiffness values. The averaged measured values for single unit cells are $K_1 = 0.25$N/mm, $K_2 = 0.39$N/mm, $K_3 = 0.59$N/mm, and $K_4 = 1.26$N/mm.

In Fig. C.4, we provide a comparison of the modulus E of each state, which is defined as the slope of the first linear region of the stress-strain (σ-ϵ) curves, being expressed as

$$E = \frac{\sigma}{\epsilon} = \frac{F}{A}\frac{H}{\Delta H} \tag{C9}$$

where F is the measured force, A is the area of the unit cell polygon, ΔH is the applied displacement, and H is the sum of the heights of the deployed unit cells. The averaged measured values for single unit cells are $E_1 = 0.86 \times 10^{-2}$N/mm^2, $E_2 = 1.4 \times 10^{-2}$N/mm^2, $E_3 = 2.4 \times 10^{-2}$N/mm^2, and $E_4 = 5.9 \times 10^{-2}$N/mm^2.

C.2 Material Characterization

C.2.1 Mechanical Properties

To measure the stiffness of the hinges, we test samples with a primary hinge manufactured with the same process as the valley folds of the Kresling unit cell samples. That is, the hinge is cut with a dashed line pattern and is folded and deployed for 300 cycles. Parallel to the primary hinge, we add secondary hinges that are made weaker than the primary one, making the stiffness at those hinges close to zero.

Each end of the sample is attached to an acrylic plate. Those plates have a slit cut,

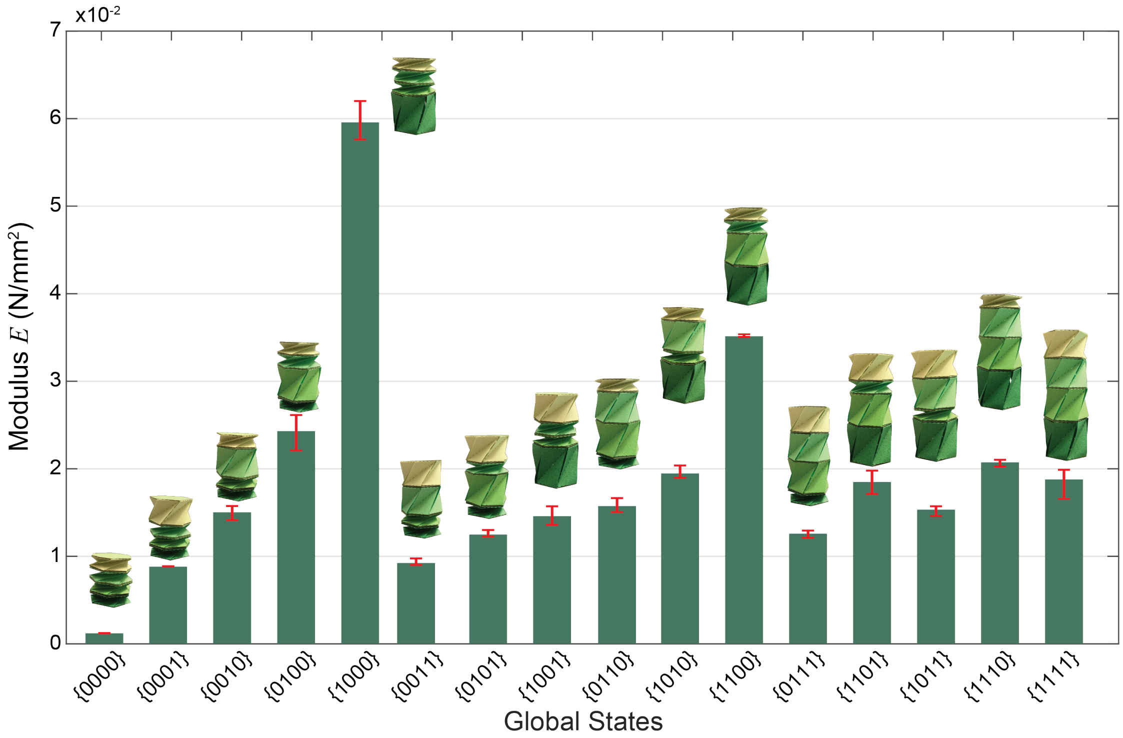

Figure C.4: Tunable mechanical response of the four-cell Kresling assembly. From multiple consecutive testing cycles, we obtain the average (columns) and maximum/minimum (error bars) values of the modulus E (Eq. C.9)

allowing for the edges of the sample to pass through it and be folded and taped on the other side. The acrylic plates are assembled to the test bed shown in Fig. 5.11, such that one plate is attached to the sample holder and the other to the fixed plate (Fig. C.5). From the experiment, we measure the displacement d and force F, and with this information, we calculate the bending moment M_b and the change in folding angle $\delta\phi$ as

$$M_b = F\delta\ell, \quad \delta\phi = 2\sin^{-1}(d_0/2b) - 2\sin^{-1}(\delta d/2b) \tag{C10}$$

where $\delta\ell$ is the vertical distance between the edges and the hinge, $b = 13mm$ is the panel size, $d_0 = 21$mm is the initial opening of the hinge, and $\delta d = d_0 - d$ (Fig. C.5(B)). From the slope of the bending moment versus folding angle curves, we obtain the rotational stiffness of the hinges. This value is divided by the length of the hinge, that is 50mm, resulting on an average stiffness of $k_f = 2.4 \times 10^{-3}$ N·mm(rad·mm)$^{-1}$.

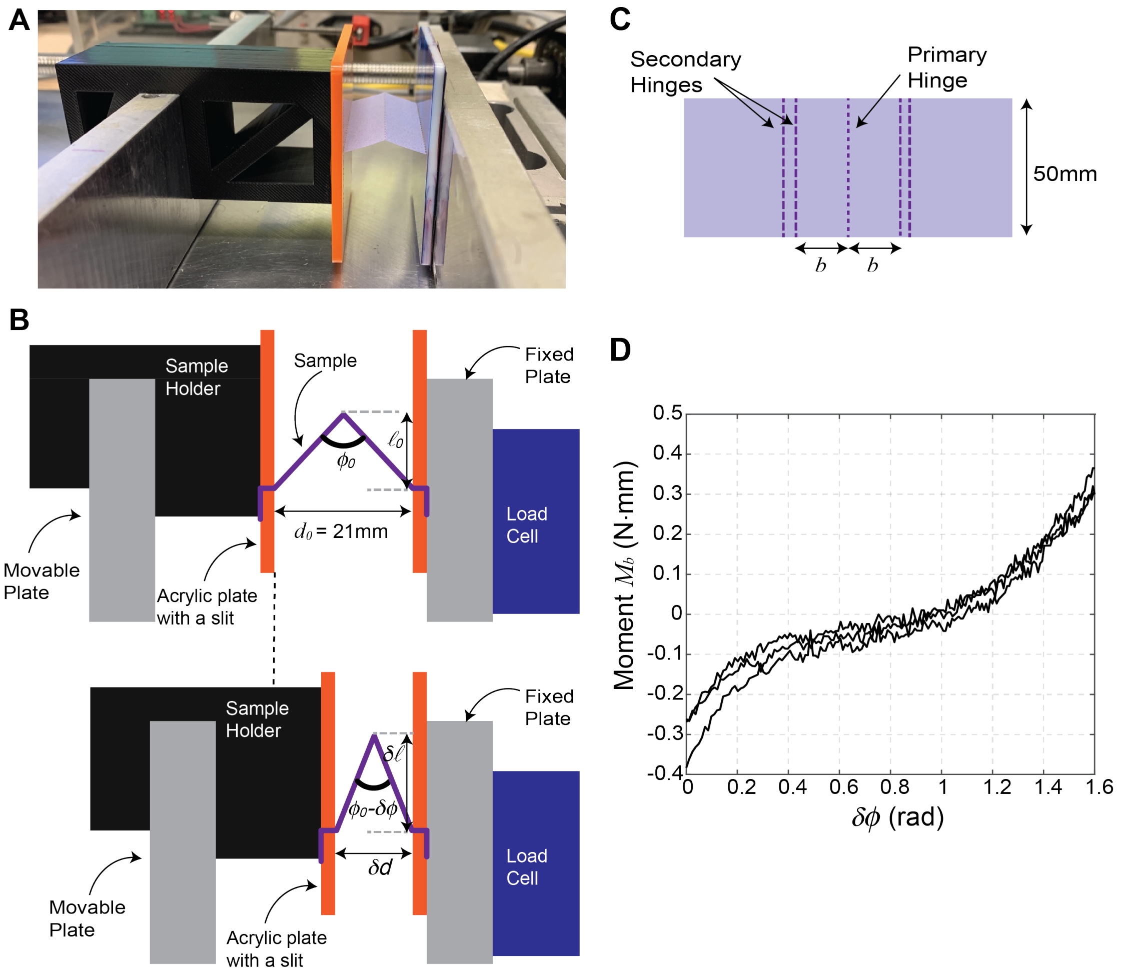

Figure C.5: Characterization of the rotational stiffness of the hinges. (A) Testing setup and (B) schematics. (C) Tested sample, where $b = 13\text{mm}$. (D) Measured bending moment vs. rotation at the primary hinge, with each curve corresponding to one tested sample. From those curves, we obtain an average rotational stiffness $k_f = 2.4 \times 10^{-3}$N·mm/mm/rad.

C.2.2 Magnetic Properties

The magnetic properties of the magnetic material for the plates are measured on a Vibrating Sample Magnetometer (VSM, 7400A series, Lake Shore Cryotronics, Inc., Chicago, IL, USA). The magnetic moments of the material under external magnetic field (B) from -1.5T to 1.5T are scanned and recorded. The corresponding magnetic moment densities (M) are calculated from the magnetic moments by dividing by the sample volume. From the measured M-B curve in Fig. C.6, the remanent magnetic moment density (M_r) is

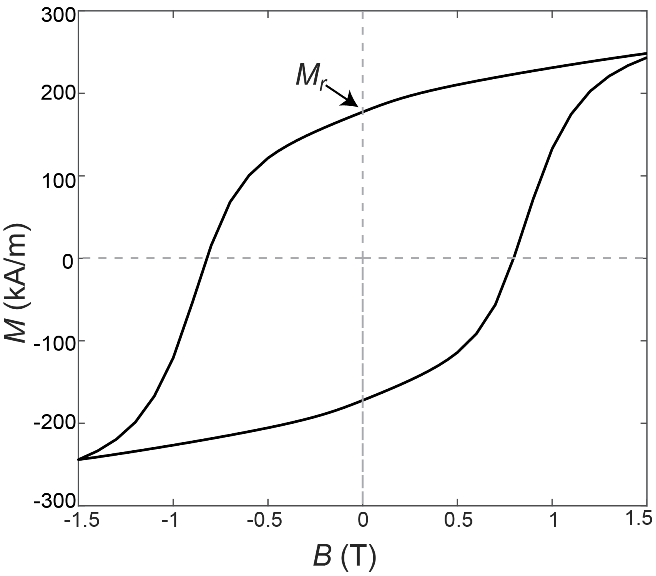

Figure C.6: The M-B curve of the magnetic material

177.39 kA/m and will be used as the magnetization intensity M for analyzing the magnetic actuation performance in the next section.

C.3 Analytical Calculation for Magnetic Actuation

Under a homogeneous magnetic field, the magnetic torque (T) will be induced to align the magnetization direction of the magnetic material to the external magnetic field and is calculated as

$$T = BMV \sin(\theta_M - \theta_B) \tag{C11}$$

where V is the volume of the magnetic plate, B is the magnetic field intensity, θ_M and θ_B are the directions of the magnetization and the external magnetic field, respectively. With the folding process of a Kresling pattern as an example in Fig. 5.2(A), the Kresling pattern will rotate clockwise. The angles of $\delta\theta$s and $\delta\theta$ are defined as the angle difference between two stable states and the real-time rotation angle during the actuation process, respectively. The Kresling pattern can be changed to state $\{0\}$ (folded) when the magnetic torque (T) is larger than the required torque ($Tr+$) at any angle $\delta\theta$ (Fig. 5.2(B)). In the analytical calculations, 0.1° is chosen as the angle step.

The state of the Kresling pattern under a specific magnetic field direction and amplitude will be determined as in the flowchart shown in Fig. C.7, and the states of the Kresling patterns under different magnetic field directions can be predicted numerically with the same flow. The analytical results shown in Fig. 5.2(C), Fig. 5.3(C), and Fig. C.8 display good agreement with the experimental results.

Table C.2: Unit cells design and actuation

Structure (Fixed to Free end)	Geometry	Magnetization direction Folded
Unit cell (Fig. 5.2, Fig. 5.3)	Design 3	$\theta_M = 129^\circ$
Two-cell assembly (Fig. 5.4, Fig. 5.5)	Design 3 (bottom)	$\theta_M = 0^\circ$
	Design 3 (top)	$\theta_M = 90^\circ$
Reversed creases assembly (Fig. 5.6)	Design 3 (orange)	$\theta_M = 0^\circ$
	Design 3 (blue)	$\theta_M = -90^\circ$
LED assembly (Fig. 5.8)	Design 1 (green)	$\theta_M = 0^\circ$
	Design 3 (yellow)	$\theta_M = 90^\circ$
	Design 4 (red)	$\theta_M = 180^\circ$

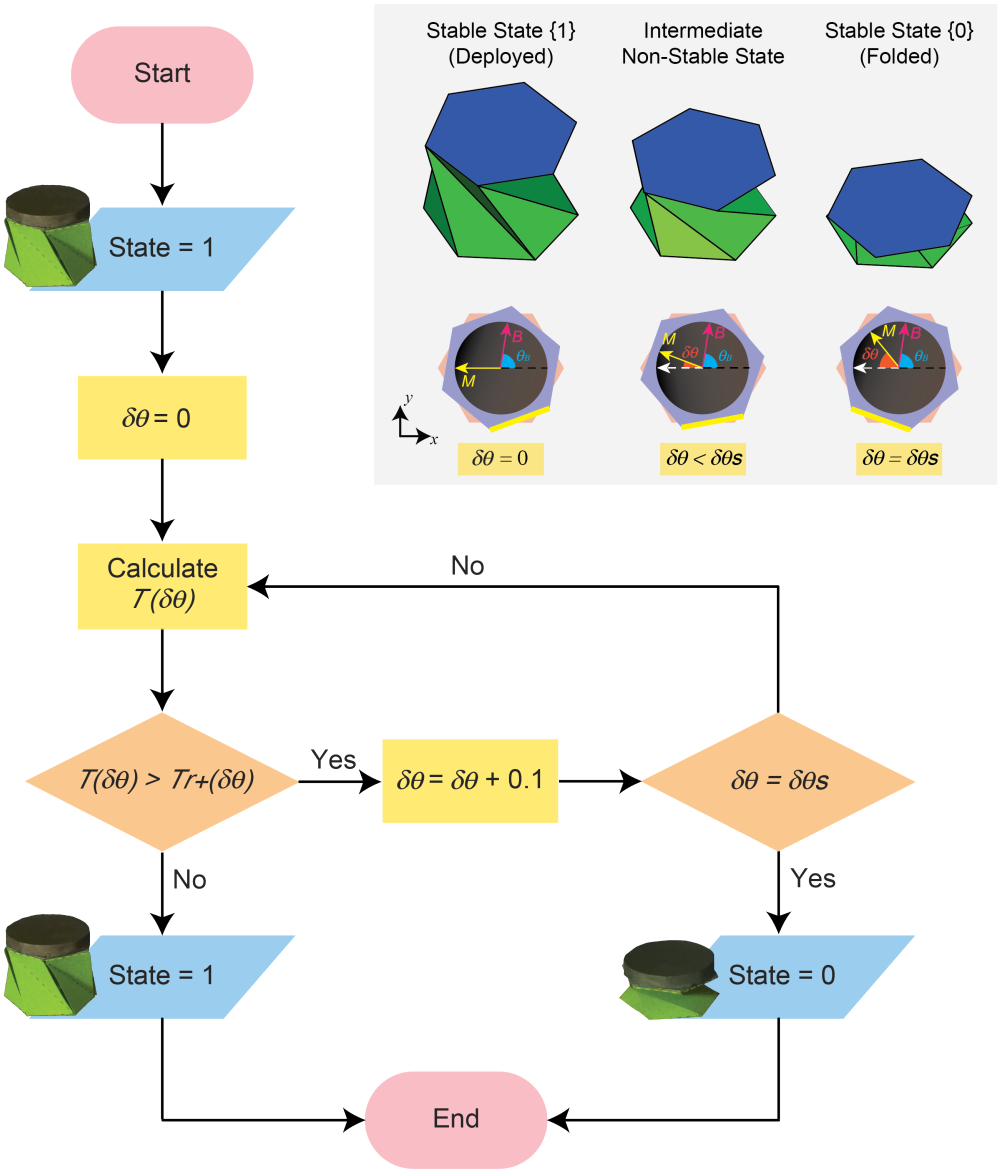

Figure C.7: Flowchart of the analytical calculation algorithm for the magnetic actuation of single unit cell with initial state $\{1\}$. Inset shows three different stages of the Kresling Pattern.

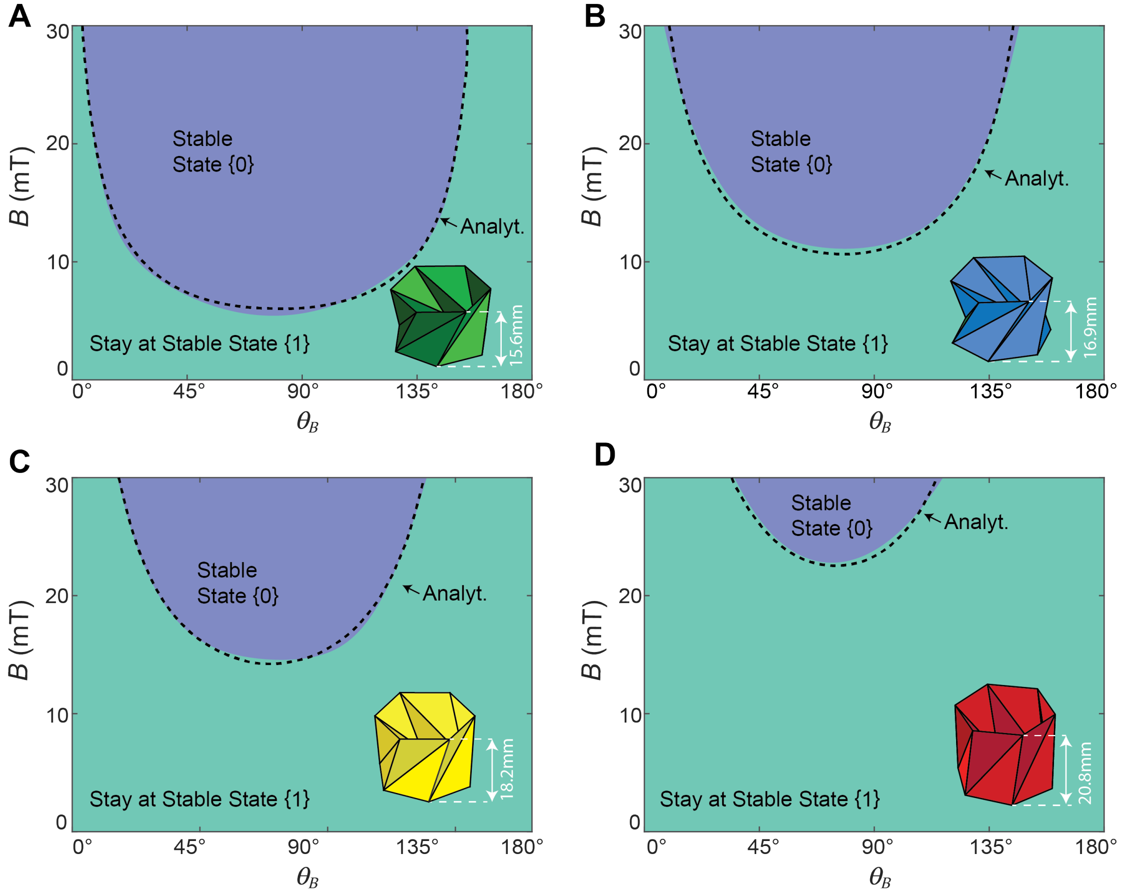

Figure C.8: Magnetic actuation contours for unit cells with geometries in Table C.1. (A) Design 1 ($H_1 = 15.6$mm). (B) Design 2 ($H_2 = 16.9$mm). (C) Design 3 ($H_3 = 18.2$mm). (D) Design 4 ($H_4 = 20.8$mm).

APPENDIX D

MATERIAL ANISOTROPY AND GEOMETRY

In this Appendix, we provide a preliminary investigation on the influence of material anisotropy on the mechanical behaviour of the Miura-Ori pattern. For this investigation, we study the composite material used in Chapter 6 (Durilla Durable Premium Ice Card Stock, 0.30 mm-thick). First, we provide a characterization of the anisotropic behaviour of the composite material. That is, the modulus E and the folding stiffness of the hinges K_F in different directions. Next, we characterize the mechanical response of Miura-Ori pattern under in-plane compression considering different orientations of the crease pattern with respect to the composite sheet.

D.1 Composite Material Characterization

To obtain the Young's modulus (E) of the the composite material, we use an Instron model 5566 equipped with a 30kN load cell to perform a tensile test on the fabricated samples (Fig. D.1). Sample dimension is shown in Fig. D.1(A). Note that the top and bottom of the samples are folded to increase the thickness of the sample at the edges. We fabricate the samples in two orientations with respect to the composite sheet. ***Samples type (1)*** have the fibers of the composite sheet parallel to the direction of the applied axial load, which provides the modulus E_1 and ***samples type (2)*** have the fibers of the composite sheet perpendicular to the applied axial load, which provides the modulus E_2 (Fig. D.1(B)). From the tests, we obtain the modulus for both sample types. The data for all the samples is collected in Table D.1.

For the characterization of the folding stiffness K_F, we fabricate and test two set of samples: ***Samples type (1)*** with the fibers of the composite are perpendicular to the perforated crease lines, which provides the folding stiffness K_{F_1} and ***samples type (2)*** with the

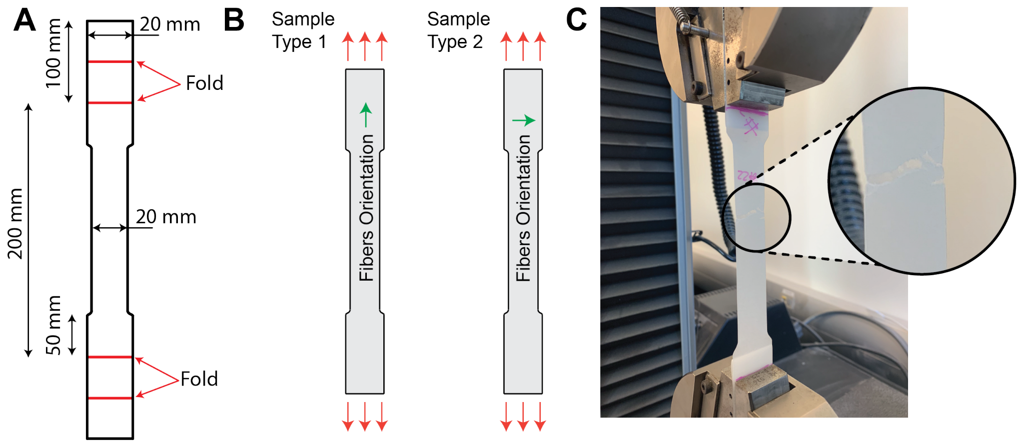

Figure D.1: Tensile test of the composite material. (A) Sample dimension (B) Sample types differentiated by the material orientation. (C) Tensile test setup

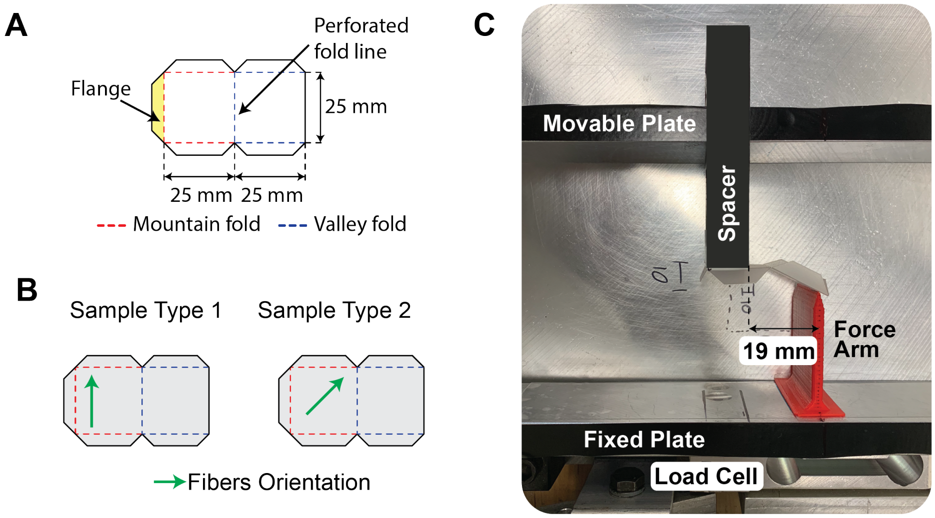

Figure D.2: Characterization of the folding stiffness of the composite material. (A) Sample dimension (B) Sample types differentiated by the material orientation. (C) Composite material folding test.

fibers of the composite sheet with an angle of $45°$ to the the perforated crease lines, which provides modulus K_{F_2}. The samples have the same dimensions and are tested in the same way as the samples in Chapter 6 (Fig. D.2). In Table D.1, we report the data collected from the experiments.

Table D.1: Durilla Durable Premium Ice Card Stock Anisotropic Properties

E_1 (MPa)	E_2 (MPa)	K_{F_1} $\left(\text{N}\cdot\text{mm}(\text{rad}\cdot\text{mm})^{-1}\right)$	$R^2_{F_1}$	K_{F_2} $\left(\text{N}\cdot\text{mm}(\text{rad}\cdot\text{mm})^{-1}\right)$	$R^2_{F_2}$
1317.1	777.7	0.0827	0.9797	0.1121	0.9803
1323.5	805.5	0.0623	0.9132	0.1141	0.9457
1298.3	813.5	0.0620	0.9323	0.0905	0.9171
1277.2	797.6	0.0690	0.9377	0.1012	0.9382
1297.0	794.7	0.0875	0.9032	0.1008	0.9620
Average					
1302.6	797.8	0.7760	0.9881	0.1037	0.9487

D.2 Miura-Ori Mechanical Characterization

The mechanical properties that we obtained indicate that the composite material has an anisotropic behaviour (Table D.1). Our question now is "How the behaviour of the material impacts the global response of the origami pattern?" To try to answer this question, we fabricated three set of Miura-Ori patterns with the same geometry, but oriented in three different ways within the material sheet (Fig. D.3(A,B)). We use a LS4.75 laser cutting system (Universal laser systems) to create equally spaced dashed-gap-dashed crease lines and to fully cut out the sample from the composite sheet. After, we fold each sample individually. Before being tested, the samples are flat-folded to ensure that all hinges are equally pre-folded and will display similar stiffness.

For each orientation, we test three samples under in-plane compression using the custom-build machine described in Appendix B and following the experimental procedure described in Chapter 6, Section 6.3.3. Fig. D.3(C) shows the averaged force-displacement of each set. Although further investigation is still needed, our preliminary investigation shows that the mechanical response of the Miura-Ori pattern is governed by its geometry, and the anisotropic behaviour has little influence on it.

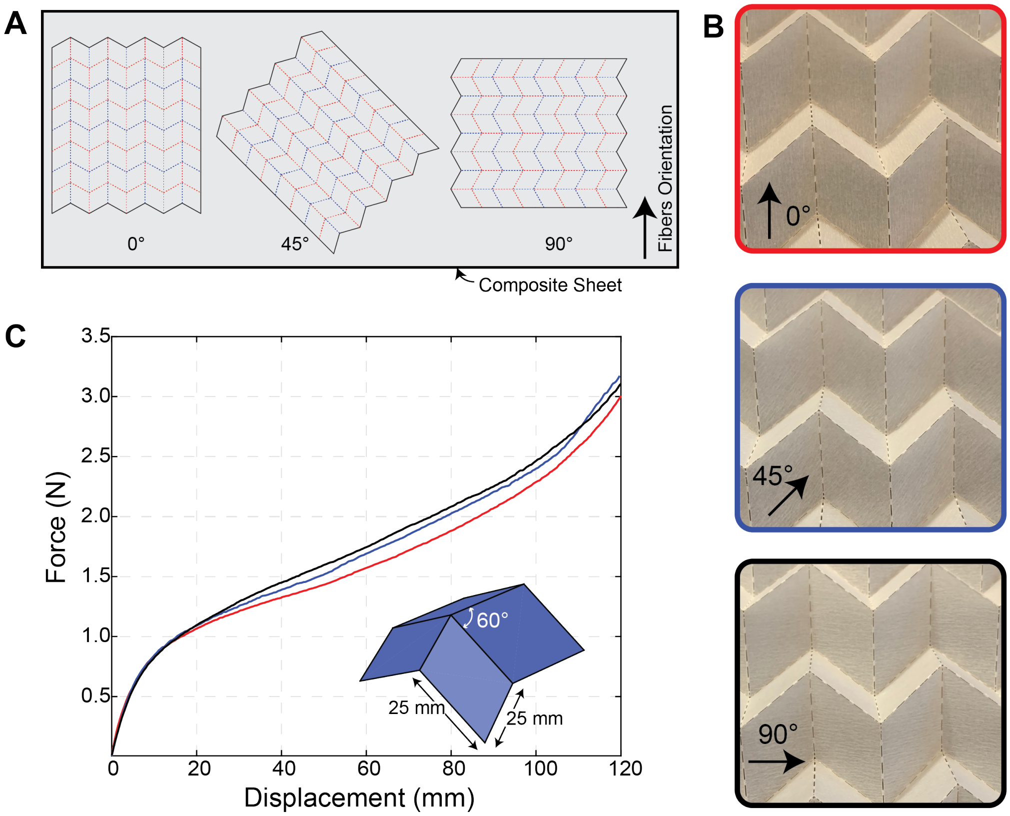

Figure D.3: (A) Orientations of the samples in the sheet of the composite material. (B) Zoom-in of the samples printed with three different orientations in the composite paper. (C) Force-displacement curve for samples with different orientations. Each curve represents the averaged response of three samples.

REFERENCES

[1] M. Schenk and S. D. Guest, “Geometry of Miura-folded metamaterials,” *Proceedings of the National Academy of Sciences*, vol. 110, no. 9, pp. 3276–3281, 2013.

[2] J. L. Silverberg, A. A. Evans, L. McLeod, R. C. Hayward, T. Hull, C. D. Santangelo, and I. Cohen, “Using origami design principles to fold reprogrammable mechanical metamaterials,” *Science*, vol. 345, no. 6197, pp. 647–650, 2014.

[3] Z. Lin, L. S. Novelino, H. Wei, N. A. Alderete, G. H. Paulino, H. D. Espinosa, and S. Krishnaswamy, “Folding at the microscale: Enabling multifunctional 3D origami-architected metamaterials,” *Small*, p. 2 002 229, 2020.

[4] E. Boatti, N. Vasios, and K. Bertoldi, “Origami metamaterials for tunable thermal expansion,” *Advanced Materials*, vol. 29, no. 26, 2017.

[5] S. A. Nauroze, L. S. Novelino, M. M. Tentzeris, and G. H. Paulino, “Continuous-range tunable multilayer frequency-selective surfaces using origami and inkjet printing,” *Proceedings of the National Academy of Sciences*, vol. 115, no. 52, pp. 13 210–13 215, 2018.

[6] X. Liu, S. Yao, S. V. Georgakopoulos, B. S. Cook, and M. M. Tentzeris, “Reconfigurable helical antenna based on an origami structure for wireless communication system,” in *2014 IEEE MTT-S International Microwave Symposium (IMS2014)*, IEEE, 2014, pp. 1–4.

[7] L. S. Novelino, S. A. Nauroze, M. M. Tentzeris, and G. H. Paulino, “Multiphysics origami: Achieving tunable frequency selective surfaces from origami principles,” in *Origami 7: Seventh International Meeting of Origami Science, Mathematics, and Education*, Tarquin, vol. 4, 2018, pp. 1167–1182.

[8] C. L. Zekios, X. Liu, M. Moshtaghzadeh, E. Izadpanahi, H. R. Radnezhad, P. Mardanpour, and S. V. Georgakopoulos, “Electromagnetic and mechanical analysis of an origami helical antenna encapsulated by fabric,” in *International Design Engineering Technical Conferences and Computers and Information in Engineering Conference*, American Society of Mechanical Engineers, vol. 59247, 2019, V05BT07A045.

[9] E. T. Filipov, T. Tachi, and G. H. Paulino, “Origami tubes assembled into stiff, yet reconfigurable structures and metamaterials,” *Proceedings of the National Academy of Sciences*, vol. 112, no. 40, pp. 12 321–12 326, 2015.

[10] P. M. Reis, F. L. Jiménez, and J. Marthelot, "Transforming architectures inspired by origami," *Proceedings of the National Academy of Sciences*, vol. 112, no. 40, pp. 12 234–12 235, 2015.

[11] S. A. Zirbel, R. J. Lang, M. W. Thomson, D. A. Sigel, P. E. Walkemeyer, B. P. Trease, S. P. Magleby, and L. L. Howell, "Accommodating thickness in origami-based deployable arrays," *Journal of Mechanical Design*, vol. 135, no. 11, p. 111 005, 2013.

[12] S. A. Zirbel, B. P. Trease, S. P. Magleby, and L. L. Howell, "Deployment methods for an origami-inspired rigid-foldable array," 2014.

[13] T. Chen, O. R. Bilal, R. Lang, C. Daraio, and K. Shea, "Autonomous deployment of a solar panel using elastic origami and distributed shape-memory-polymer actuators," *Physical Review Applied*, vol. 11, no. 6, p. 064 069, 2019.

[14] S. Li, D. M. Vogt, D. Rus, and R. J. Wood, "Fluid-driven origami-inspired artificial muscles," *Proceedings of the National Academy of Sciences*, vol. 114, no. 50, pp. 13 132–13 137, 2017.

[15] K. Kuribayashi, K. Tsuchiya, Z. You, D. Tomus, M. Umemoto, T. Ito, and M. Sasaki, "Self-deployable origami stent grafts as a biomedical application of ni-rich tini shape memory alloy foil," *Materials Science and Engineering: A*, vol. 419, no. 1-2, pp. 131–137, 2006.

[16] J. T. Overvelde, T. A. De Jong, Y. Shevchenko, S. A. Becerra, G. M. Whitesides, J. C. Weaver, C. Hoberman, and K. Bertoldi, "A three-dimensional actuated origami-inspired transformable metamaterial with multiple degrees of freedom," *Nature Communications*, vol. 7, no. 1, pp. 1–8, 2016.

[17] J. A. Faber, A. F. Arrieta, and A. R. Studart, "Bioinspired spring origami," *Science*, vol. 359, no. 6382, pp. 1386–1391, 2018.

[18] W. Kim, J. Byun, J.-K. Kim, W.-Y. Choi, K. Jakobsen, J. Jakobsen, D.-Y. Lee, and K.-J. Cho, "Bioinspired dual-morphing stretchable origami," *Science Robotics*, vol. 4, no. 36, 2019.

[19] Y. Tang, Y. Chi, J. Sun, T.-H. Huang, O. H. Maghsoudi, A. Spence, J. Zhao, H. Su, and J. Yin, "Leveraging elastic instabilities for amplified performance: Spine-inspired high-speed and high-force soft robots," *Science Advances*, vol. 6, no. 19, eaaz6912, 2020.

[20] P. Bhovad, J. Kaufmann, and S. Li, "Peristaltic locomotion without digital controllers: Exploiting multi-stability in origami to coordinate robotic motion," *Extreme Mechanics Letters*, vol. 32, p. 100 552, 2019.

[21] K. Liu, J. Wu, G. H. Paulino, and H. J. Qi, "Programmable deployment of tensegrity structures by stimulus-responsive polymers," *Scientific Reports*, vol. 7, no. 1, pp. 1–8, 2017.

[22] J.-H. Na, A. A. Evans, J. Bae, M. C. Chiappelli, C. D. Santangelo, R. J. Lang, T. C. Hull, and R. C. Hayward, "Programming reversibly self-folding origami with micropatterned photo-crosslinkable polymer trilayers," *Advanced Materials*, vol. 27, no. 1, pp. 79–85, 2015.

[23] M. Z. Miskin, K. J. Dorsey, B. Bircan, Y. Han, D. A. Muller, P. L. McEuen, and I. Cohen, "Graphene-based bimorphs for micron-sized, autonomous origami machines," *Proceedings of the National Academy of Sciences*, vol. 115, no. 3, pp. 466–470, 2018.

[24] B. Treml, A. Gillman, P. Buskohl, and R. Vaia, "Origami mechanologic," *Proceedings of the National Academy of Sciences*, vol. 115, no. 27, pp. 6916–6921, 2018.

[25] T. Hull, *Project origami: activities for exploring mathematics*. CRC Press, 2012.

[26] J. O'Rourke, *How to fold it: the mathematics of linkages, origami, and polyhedra*. Cambridge University Press, 2011.

[27] E. D. Demaine and J. O'Rourke, *Geometric folding algorithms: linkages, origami, polyhedra*. Cambridge university press, 2007.

[28] Z. Lin, L. S. Novelino, H. Wei, N. A. Alderete, G. H. Paulino, H. D. Espinosa, and S. Krishnaswamy, "Mechanical Metamaterials: Folding at the Microscale: Enabling Multifunctional 3D Origami-Architected Metamaterials (Small 35/2020)," *Small*, vol. 16, no. 35, p. 2 070 192, 2020.

[29] K. Liu, L. S. Novelino, P. Gardoni, and G. H. Paulino, "Big influence of small random imperfections in origami-based metamaterials," *Proceedings of the Royal Society A*, vol. 476, no. 2241, p. 20 200 236, 2020.

[30] H. Houdini, "Paper magic," *EP Dutton & Company*, pp. 176–177, 1922.

[31] G. M. Loe, *Paper Capers*. Magic, 1955.

[32] M. Gardner, "Paper cutting," *New Mathematical Diversions (Revised Edition), Spectrum Series*, pp. 58–69, 1995.

[33] E. D. Demaine, M. L. Demaine, and A. Lubiw, "Folding and cutting paper," in *Japanese Conference on Discrete and Computational Geometry*, Springer, 1998, pp. 104–118.

[34] M. Bern, E. Demaine, D. Eppstein, and B. Hayes, "A disk-packing algorithm for an origami magic trick," in *Origami 3: Third International Meeting of Origami Science, Mathematics, and Education*, 2002, pp. 17–28.

[35] O. Aichholzer, F. Aurenhammer, D. Alberts, and B. Gärtner, "A novel type of skeleton for polygons," in *J. UCS The Journal of Universal Computer Science*, Springer, 1996, pp. 752–761.

[36] T. A. Schaedler, A. J. Jacobsen, A. Torrents, A. E. Sorensen, J. Lian, J. R. Greer, L. Valdevit, and W. B. Carter, "Ultralight metallic microlattices," *Science*, vol. 334, no. 6058, pp. 962–965, 2011.

[37] L. R. Meza, S. Das, and J. R. Greer, "Strong, lightweight, and recoverable three-dimensional ceramic nanolattices," *Science*, vol. 345, no. 6202, pp. 1322–1326, 2014.

[38] L. R. Meza, A. J. Zelhofer, N. Clarke, A. J. Mateos, D. M. Kochmann, and J. R. Greer, "Resilient 3D hierarchical architected metamaterials," *Proceedings of the National Academy of Sciences*, vol. 112, no. 37, pp. 11 502–11 507, 2015.

[39] T. Bückmann, M Thiel, M Kadic, R Schittny, and M Wegener, "An elasto-mechanical unfeelability cloak made of pentamode metamaterials," *Nature Communications*, vol. 5, no. 1, pp. 1–6, 2014.

[40] J. Bauer, A. Schroer, R. Schwaiger, and O. Kraft, "Approaching theoretical strength in glassy carbon nanolattices," *Nature Materials*, vol. 15, no. 4, pp. 438–443, 2016.

[41] C. M. Portela, A Vidyasagar, S. Krödel, T. Weissenbach, D. W. Yee, J. R. Greer, and D. M. Kochmann, "Extreme mechanical resilience of self-assembled nanolabyrinthine materials," *Proceedings of the National Academy of Sciences*, vol. 117, no. 11, pp. 5686–5693, 2020.

[42] Z. Y. Wei, Z. V. Guo, L. Dudte, H. Y. Liang, and L Mahadevan, "Geometric mechanics of periodic pleated origami," *Physical Review Letters*, vol. 110, no. 21, p. 215 501, 2013.

[43] P. P. Pratapa, K. Liu, and G. H. Paulino, "Geometric mechanics of origami patterns exhibiting poisson's ratio switch by breaking mountain and valley assignment," *Physical Review Letters*, vol. 122, no. 15, p. 155 501, 2019.

[44] K. C. Cheung, T. Tachi, S. Calisch, and K. Miura, "Origami interleaved tube cellular materials," *Smart Materials and Structures*, vol. 23, no. 9, p. 094 012, 2014.

[45] Z. Zhao, X. Kuang, J. Wu, Q. Zhang, G. H. Paulino, H. J. Qi, and D. Fang, "3D printing of complex origami assemblages for reconfigurable structures," *Soft matter*, vol. 14, no. 39, pp. 8051–8059, 2018.

[46] J. L. Silverberg, J.-H. Na, A. A. Evans, B. Liu, T. C. Hull, C. D. Santangelo, R. J. Lang, R. C. Hayward, and I. Cohen, "Origami structures with a critical transition to bistability arising from hidden degrees of freedom," *Nature Materials*, vol. 14, no. 4, pp. 389–393, 2015.

[47] G. M. Swallowe, *Mechanical Properties and Testing of Polymers: an A–Z reference*. Springer Science & Business Media, 1999, vol. 3.

[48] H. Wei and S. Krishnaswamy, "Polymer micro-ring resonator integrated with a fiber ring laser for ultrasound detection," *Optics Letters*, vol. 42, no. 13, pp. 2655–2658, 2017.

[49] Georgia Tech Institute for Electronics and Nanotechnology [Online]. Available: `https://dev.ien.gatech.edu/top-20-tools`.

[50] B. A. Munk, *Frequency selective surfaces: theory and design*. Wiley Online Library, 2000, vol. 29.

[51] T. Wu, *Frequency Selective Surface and Grid Array*, ser. Wiley Series in Microwave and Optical Engineering. Wiley, 1995, ISBN: 9780471311898.

[52] D. J. Kern and D. H. Werner, "A genetic algorithm approach to the design of ultra-thin electromagnetic bandgap absorbers," *Microwave and Optical Technology Letters*, vol. 38, no. 1, pp. 61–64, 2003.

[53] R. Panwar and J. R. Lee, "Progress in frequency selective surface-based smart electromagnetic structures: A critical review," *Aerospace Science and Technology*, vol. 66, pp. 216–234, 2017.

[54] R. Mittra, C. H. Chan, and T. Cwik, "Techniques for analyzing frequency selective surfaces-a review," *Proceedings of the IEEE*, vol. 76, no. 12, pp. 1593–1615, 1988.

[55] K. Sarabandi and N. Behdad, "A frequency selective surface with miniaturized elements," *IEEE Transactions on Antennas and Propagation*, vol. 55, no. 5, pp. 1239–1245, 2007.

[56] A. K. Rashid, B. Li, and Z. Shen, "An overview of three-dimensional frequency-selective structures," *IEEE Antennas and Propagation Magazine*, vol. 56, no. 3, pp. 43–67, 2014.

[57] S. N. Azemi, K. Ghorbani, and W. S. Rowe, "3D frequency selective surfaces," *Progress in Electromagnetics Research*, vol. 29, pp. 191–203, 2012.

[58] E. A. Parker, "Convoluted array elements and reduced size unit cells for frequency-selective surfaces," *IEE Proceedings H (Microwaves, Antennas and Propagation). (IET)*, vol. 138, no. 1, pp. 19–22, 1991.

[59] G. Q. Luo, W. Hong, Q. H. Lai, K. Wu, and L. L. Sun, "Design and experimental verification of compact frequency-selective surface with quasi-elliptic bandpass response," *IEEE Transactions on Microwave Theory and Techniques*, vol. 55, no. 12, pp. 2481–2487, 2007.

[60] A. H. Abdelrahman, A. Z. Elsherbeni, and F. Yang, "Transmission phase limit of multilayer frequency-selective surfaces for transmitarray designs," *IEEE Transactions on Antennas and Propagation*, vol. 62, no. 2, pp. 690–697, 2014.

[61] C. Antonopoulos, R. Cahill, E. A. Parker, and I. Sturland, "Multilayer frequency-selective surfaces for millimetre and submillimetre wave applications," *IEE Proceedings-Microwaves, Antennas and Propagation*, vol. 144, no. 6, pp. 415–420, 1997.

[62] T. K. Chang, R. J. Langley, and E. A. Parker, "Active frequency-selective surfaces," *IEE Proceedings-Microwaves, Antennas and Propagation*, vol. 143, no. 1, pp. 62–66, 1996.

[63] B. Schoenlinner, L. C. Kempel, and G. M. Rebeiz, "Switchable RF mems Ka-band frequency-selective surface," *Microwave Symposium Digest, 2004 IEEE MTT-S International*, vol. 2, pp. 1241–1244, 2004.

[64] T. Chang, R. J. Langley, and E. A. Parker, "Frequency selective surfaces on biased ferrite substrates," *Electronics Letters*, vol. 30, no. 15, pp. 1193–1194, 1994.

[65] A. C. Lima, E. A. Parker, and R. J. Langley, "Tunable frequency selective surface using liquid substrates," *Electronics Letters*, vol. 30, no. 4, pp. 281–282, 1994.

[66] D. S. Lockyer and C. Vardaxoglou, "Reconfigurable FSS response from two layers of slotted dipole arrays," *Electronics Letters*, vol. 32, no. 6, pp. 512–513, 1996.

[67] S. Yao, X. Liu, and S. V. Georgakopoulos, "A mode reconfigurable Nojima origami antenna," *Antennas and Propagation & USNC/URSI National Radio Science Meeting, 2015 IEEE International Symposium. (IEEE)*, pp. 2237–2238, 2015.

[68] S. Yao, S. V. Georgakopoulos, B. Cook, and M. Tentzeris, "A novel reconfigurable origami accordion antenna," *Microwave Symposium (IMS), 2014 IEEE MTT-S International. (IEEE)*, pp. 1–4, 2014.

[69] K. Fuchi, P. R. Buskohl, G. Bazzan, M. F. Durstock, J. J. Joo, G. W. Reich, and R. A. Vaia, “Spatial tuning of a RF frequency selective surface through origami,” *Automatic Target Recognition XXVI. (International Society for Optics and Photonics)*, vol. 9844, 98440W, 2016.

[70] Z. Wang, L. Jing, K. Yao, Y. Yang, B. Zheng, C. M. Soukoulis, H. Chen, and Y., “Origami-based reconfigurable metamaterials for tunable chirality,” *Advanced Materials*, vol. 29, no. 27, 2017.

[71] B. Treml, A. Gillman, P. Buskohl, and R. Vaia, “Origami mechanologic,” *Proceedings of the National Academy of Sciences*, vol. 115, no. 27, pp. 6916–6921, 2018.

[72] S. Li, D. M. Vogt, D. Rus, and R. J. Wood, “Fluid-driven origami-inspired artificial muscles,” *Proceedings of the National Academy of Sciences*, vol. 114, no. 50, pp. 13 132–13 137, 2017.

[73] P. M. Dodd, P. F. Damasceno, and S. C. Glotzer, “Universal folding pathways of polyhedron nets,” *Proceedings of the National Academy of Sciences*, vol. 115, no. 29, E6690–E6696, 2018.

[74] Z. Zhai, Y. Wang, and H. Jiang, “Origami-inspired, on-demand deployable and collapsible mechanical metamaterials with tunable stiffness,” *Proceedings of the National Academy of Sciences*, vol. 115, no. 9, pp. 2032–2037, 2018.

[75] K. Fuchi, J. Tang, B. Crowgey, A. R. Diaz, E. J. Rothwell, and R. O. Ouedraogo, “Origami tunable frequency selective surfaces,” *IEEE Antennas and Wireless Propagation Letters*, vol. 11, pp. 473–475, 2012.

[76] D. Sessions, K. Fuchi, S. Pallampati, D. Grayson, S. Seiler, G. Bazzan, G. Reich, P. Buskohl, and G. H. Huff, “Investigation of fold-dependent behavior in an origami-inspired FSS under normal incidence,” *Progress in Electromagnetics Research*, vol. 63, pp. 131–139, 2018.

[77] S. A. Nauroze, L. Novelino, M. M. Tentzeris, and G. H. Paulino, “Inkjet-printed “4D” tunable spatial filters using on-demand foldable surfaces,” in *Microwave Symposium (IMS), 2017 IEEE MTT-S International*, IEEE, 2017, pp. 1575–1578.

[78] S. A. Nauroze, J. Hester, W. Su, and M. M. Tentzeris, “Inkjet-printed substrate integrated waveguides (SIW) with “drill-less” vias on paper substrates,” *Microwave Symposium (IMS), 2016 IEEE MTT-S International*, pp. 1–4, 2016.

[79] K. Miura, “Method of packaging and deployment of large membranes in space,” *The Institute of Space and Astronautical Science report*, vol. 618, p. 1, 1985.

[80] M. Schenk, S. D. Guest, and G. J. McShane, “Novel stacked folded cores for blast-resistant sandwich beams,” *International Journal of Solids and Structures*, vol. 51, no. 25-26, pp. 4196–4214, 2014.

[81] K. Liu and G. H. Paulino, “Nonlinear mechanics of non-rigid origami: An efficient computational approach,” *Proceedings of the Royal Society A*, vol. 473, no. 2206, p. 20 170 348, 2017.

[82] K. Liu and G. H. Paulino, “MERLIN: A MATLAB implementation to capture highly nonlinear behavior of non-rigid origami,” in *Proceedings of IASS Annual Symposia*, International Association for Shell and Spatial Structures (IASS), vol. 2016, 2016, pp. 1–10.

[83] K. Liu and G. H. Paulino, “Highly efficient nonlinear structural analysis of origami assemblages using the MERLIN2 software,” in *Origami 7: Seventh International Meeting of Origami Science, Mathematics, and Education*, Tarquin, vol. 4, 2018, pp. 1167–1182.

[84] M. Schenk and S. D. Guest, “Origami folding: A structural engineering approach,” in *Origami 5: Fifth International Meeting of Origami Science, Mathematics, and Education*, CRC Press, Boca Raton, FL, 2011, pp. 291–304.

[85] Y. Klett and P. Middendorf, “Kinematic analysis of congruent multilayer tessellations,” *Journal of Mechanisms and Robotics*, vol. 8, no. 3, p. 034 501, 2016.

[86] X. Zhou, S. Zang, and Z. You, “Origami mechanical metamaterials based on the Miura-derivative fold patterns,” *Proc. R. Soc. A*, vol. (The Royal Society) 472, p. 20 160 361, 2016.

[87] J. M. Gattas and Z. You, “Miura-base rigid origami: Parametrizations of curved-crease geometries,” *Journal of Mechanical Design*, vol. 136, no. 12, p. 121 404, 2014.

[88] M. Eidini and G. H. Paulino, “Unraveling metamaterial properties in zigzag-base folded sheets,” *Science Advances*, vol. 1, no. 8, e1500224, 2015.

[89] M. Eidini, “Zigzag-base folded sheet cellular mechanical metamaterials,” *Extreme Mechanics Letters*, vol. 6, pp. 96–102, 2016.

[90] P. M. Reis, “A perspective on the revival of structural (in) stability with novel opportunities for function: From buckliphobia to buckliphilia,” *Journal of Applied Mechanics*, vol. 82, no. 11, 2015.

[91] A. Rafsanjani, Y. Zhang, B. Liu, S. M. Rubinstein, and K. Bertoldi, "Kirigami skins make a simple soft actuator crawl," *Science Robotics*, vol. 3, no. 15, eaar7555, 2018.

[92] Y. Zhang, Z. Yan, K. Nan, D. Xiao, Y. Liu, H. Luan, H. Fu, X. Wang, Q. Yang, J. Wang, *et al.*, "A mechanically driven form of kirigami as a route to 3D mesostructures in micro/nanomembranes," *Proceedings of the National Academy of Sciences*, vol. 112, no. 38, pp. 11 757–11 764, 2015.

[93] B. Kresling, "Folded tubes as compared to kikko ("Tortoise-Shell") bamboo," in *Origami 3: Third International Meeting of Origami Science, Mathematics, and Education*, CRC Press, 2002, p. 197.

[94] Z. Zhai, Y. Wang, and H. Jiang, "Origami-inspired, on-demand deployable and collapsible mechanical metamaterials with tunable stiffness," *Proceedings of the National Academy of Sciences*, vol. 115, no. 9, pp. 2032–2037, 2018.

[95] H. Yasuda, T. Tachi, M. Lee, and J. Yang, "Origami-based tunable truss structures for non-volatile mechanical memory operation," *Nature Communications*, vol. 8, no. 1, pp. 1–7, 2017.

[96] H. Yasuda, Y. Miyazawa, E. G. Charalampidis, C. Chong, P. G. Kevrekidis, and J. Yang, "Origami-based impact mitigation via rarefaction solitary wave creation," *Science advances*, vol. 5, no. 5, eaau2835, 2019.

[97] J. Cui, T.-Y. Huang, Z. Luo, P. Testa, H. Gu, X.-Z. Chen, B. J. Nelson, and L. J. Heyderman, "Nanomagnetic encoding of shape-morphing micromachines," *Nature*, vol. 575, no. 7781, pp. 164–168, 2019.

[98] G. Z. Lum, Z. Ye, X. Dong, H. Marvi, O. Erin, W. Hu, and M. Sitti, "Shape-programmable magnetic soft matter," *Proceedings of the National Academy of Sciences*, vol. 113, no. 41, E6007–E6015, 2016.

[99] S. Wu, Q. Ze, R. Zhang, N. Hu, Y. Cheng, F. Yang, and R. Zhao, "Symmetry-breaking actuation mechanism for soft robotics and active metamaterials," *ACS Applied Materials & Interfaces*, vol. 11, no. 44, pp. 41 649–41 658, 2019.

[100] Q. Ze, X. Kuang, S. Wu, J. Wong, S. M. Montgomery, R. Zhang, J. M. Kovitz, F. Yang, H. J. Qi, and R. Zhao, "Magnetic shape memory polymers with integrated multifunctional shape manipulation," *Advanced Materials*, vol. 32, no. 4, p. 1 906 657, 2020.

[101] R. J. Lang, *Twists, tilings, and tessellations: Mathematical methods for geometric origami*. CRC Press, 2017.

[102] N. Nayakanti, S. H. Tawfick, and A. J. Hart, "Twist-coupled kirigami cells and mechanisms," *Extreme Mechanics Letters*, vol. 21, pp. 17–24, 2018.

[103] D. Z. Rocklin, B. G.-g. Chen, M. Falk, V. Vitelli, and T. Lubensky, "Mechanical weyl modes in topological maxwell lattices," *Physical Review Letters*, vol. 116, no. 13, p. 135 503, 2016.

[104] K. H. Matlack, A. Bauhofer, S. Krödel, A. Palermo, and C. Daraio, "Composite 3D-printed metastructures for low-frequency and broadband vibration absorption," *Proceedings of the National Academy of Sciences*, vol. 113, no. 30, pp. 8386–8390, 2016.

[105] K. Bertoldi, V. Vitelli, J. Christensen, and M. Van Hecke, "Flexible mechanical metamaterials," *Nature Reviews Materials*, vol. 2, no. 11, pp. 1–11, 2017.

[106] P. P. Pratapa, P. Suryanarayana, and G. H. Paulino, "Bloch wave framework for structures with nonlocal interactions: Application to the design of origami acoustic metamaterials," *Journal of the Mechanics and Physics of Solids*, vol. 118, pp. 115–132, 2018.

[107] S. Waitukaitis, R. Menaut, B. G.-g. Chen, and M. van Hecke, "Origami multistability: From single vertices to metasheets," *Physical Review Letters*, vol. 114, no. 5, p. 055 503, 2015.

[108] H. Fang, K. Wang, and S. Li, "Asymmetric energy barrier and mechanical diode effect from folding multi-stable stacked-origami," *Extreme Mechanics Letters*, vol. 17, pp. 7–15, 2017.

[109] L.-C. Wang, W.-L. Song, Y.-J. Zhang, M.-J. Qu, Z. Zhao, M. Chen, Y. Yang, H. Chen, and D. Fang, "Active reconfigurable tristable square-twist origami," *Advanced Functional Materials*, vol. 30, no. 13, p. 1 909 087, 2020.

[110] E. Baranger, P.-A. Guidault, and C. Cluzel, "Numerical modeling of the geometrical defects of an origami-like sandwich core," *Composite Structures*, vol. 93, no. 10, pp. 2504–2510, 2011.

[111] C. Jianguo, D. Xiaowei, Z. Yuting, F. Jian, and Z. Ya, "Folding behavior of a foldable prismatic mast with kresling origami pattern," *Journal of Mechanisms and Robotics*, vol. 8, no. 3, 2016.

[112] B. Wang and C. Zhou, "The imperfection-sensitivity of origami crash boxes," *International Journal of Mechanical Sciences*, vol. 121, pp. 58–66, 2017.

[113] H. Yasuda and J. Yang, "Reentrant origami-based metamaterials with negative poisson's ratio and bistability," *Physical Review Letters*, vol. 114, no. 18, p. 185 502, 2015.

[114] C. Lv, D. Krishnaraju, G. Konjevod, H. Yu, and H. Jiang, "Origami based mechanical metamaterials," *Scientific Reports*, vol. 4, p. 5979, 2014.

[115] M Thota, S Li, and K. Wang, "Lattice reconfiguration and phononic band-gap adaptation via origami folding," *Physical Review B*, vol. 95, no. 6, p. 064 307, 2017.

[116] H. Fang, S.-C. A. Chu, Y. Xia, and K.-W. Wang, "Programmable self-locking origami mechanical metamaterials," *Advanced Materials*, vol. 30, no. 15, p. 1 706 311, 2018.

[117] L. H. Dudte, E. Vouga, T. Tachi, and L Mahadevan, "Programming curvature using origami tessellations," *Nature Materials*, vol. 15, no. 5, pp. 583–588, 2016.

[118] K. Saito, A. Tsukahara, and Y. Okabe, "Designing of self-deploying origami structures using geometrically misaligned crease patterns," *Proceedings of the Royal Society A: Mathematical, Physical and Engineering Sciences*, vol. 472, no. 2185, p. 20 150 235, 2016.

[119] H. Fang, S. Li, and K. Wang, "Self-locking degree-4 vertex origami structures," *Proceedings of the Royal Society A: Mathematical, Physical and Engineering Sciences*, vol. 472, no. 2195, p. 20 160 682, 2016.

[120] J. Ma, J. Song, and Y. Chen, "An origami-inspired structure with graded stiffness," *International Journal of Mechanical Sciences*, vol. 136, pp. 134–142, 2018.

[121] D. D. Symons and N. A. Fleck, "The imperfection sensitivity of isotropic two-dimensional elastic lattices," *Journal of Applied Mechanics*, vol. 75, no. 5, 2008.

[122] L. Liu, P. Kamm, F. García-Moreno, J. Banhart, and D. Pasini, "Elastic and failure response of imperfect three-dimensional metallic lattices: The role of geometric defects induced by selective laser melting," *Journal of the Mechanics and Physics of Solids*, vol. 107, pp. 160–184, 2017.

[123] K. Liu, T. Tachi, and G. H. Paulino, "Invariant and smooth limit of discrete geometry folded from bistable origami leading to multistable metasurfaces," *Nature Communications*, vol. 10, no. 1, pp. 1–10, 2019.

[124] E. T. Filipov, K Liu, T Tachi, M Schenk, and G. H. Paulino, "Bar and hinge models for scalable analysis of origami," *International Journal of Solids and Structures*, vol. 124, pp. 26–45, 2017.

[125] J. T. Overvelde, J. C. Weaver, C. Hoberman, and K. Bertoldi, “Rational design of reconfigurable prismatic architected materials,” *Nature*, vol. 541, no. 7637, pp. 347–352, 2017.

[126] H. Xu and P. Gardoni, “Improved latent space approach for modelling non-stationary spatial–temporal random fields,” *Spatial Statistics*, vol. 23, pp. 160–181, 2018.

[127] E. Vanmarcke, *Random fields. Analysis and synthesis*. MIT Press, 1983.

[128] A. Ajdari, H. Nayeb-Hashemi, and A. Vaziri, “Dynamic crushing and energy absorption of regular, irregular and functionally graded cellular structures,” *International Journal of Solids and Structures*, vol. 48, no. 3-4, pp. 506–516, 2011.

[129] J. Ma, D. Hou, Y. Chen, and Z. You, “Quasi-static axial crushing of thin-walled tubes with a kite-shape rigid origami pattern: Numerical simulation,” *Thin-walled structures*, vol. 100, pp. 38–47, 2016.

[130] B. A. Munk, *Finite antenna arrays and FSS*. John Wiley & Sons, 2003.

[131] R. Xie, J. Li, and Y. Chen, “The graded origami structures,” in *ASME 2015 International Design Engineering Technical Conferences and Computers and Information in Engineering Conference*, American Society of Mechanical Engineers, 2015, V05BT08A026–V05BT08A026.

[132] D. Pozar and T. Metzler, “Analysis of a reflectarray antenna using microstrip patches of variable size,” *Electronics Letters*, vol. 29, no. 8, pp. 657–658, 1993.

[133] G. Q. Luo, W. Hong, H. J. Tang, J. X. Chen, X. X. Yin, Z. Q. Kuai, and K. Wu, “Filtenna consisting of horn antenna and substrate integrated waveguide cavity FSS,” *IEEE transactions on Antennas and Propagation*, vol. 55, no. 1, pp. 92–98, 2007.

[134] D. Ferreira, I. Cuiñas, R. F. Caldeirinha, and T. R. Fernandes, “3-D mechanically tunable square slot FSS,” *IEEE Transactions on Antennas and Propagation*, vol. 65, no. 1, pp. 242–250, 2017.

[135] Y. Klett, P. Middendorf, W. Sobek, W. Haase, and M. Heidingsfeld, “Potential of origami-based shell elements as next-generation envelope components,” in *Advanced Intelligent Mechatronics (AIM), 2017 IEEE International Conference on*, IEEE, 2017, pp. 916–920.

[136] S.-D. Jang, B.-W. Kang, and J. Kim, “Frequency selective surface based passive wireless sensor for structural health monitoring,” *Smart Materials and Structures*, vol. 22, no. 2, p. 025 002, 2012.

[137] B. Kresling, “Natural twist buckling in shells: From the hawkmoth’s bellows to the deployable kresling-pattern and cylindrical Miura-ori,” in *Proceedings of the 6th International Conference on Computation of Shell and Spatial Structures*, J. F. Abel and J. R. Cooke, Eds., Ithaca, NY, 2008, pp. 1–4.

[138] S. E. Leon, E. N. Lages, C. N. De Araújo, and G. H. Paulino, “On the effect of constraint parameters on the generalized displacement control method,” *Mechanics Research Communications*, vol. 56, pp. 123–129, 2014.